

ADDRESS OF PUBLISHER
& EDITOR'S OFFICE:

GDĄŃSK UNIVERSITY
OF TECHNOLOGY

Faculty of Ocean Engineering
& Ship Technology
G. Narutowicza 11/12
80-233 Gdańsk, POLAND

EDITORIAL STAFF:

Wiesław Tarełko
| Editor in Chief
Janusz Kozak
| Deputy Editors-in-Chief
Wojciech Litwin
| Deputy Editors-in-Chief

Price:
single issue: 25 PLN

Prices for abroad
single issue:
- in Europe EURO 15
- overseas USD 20

WEB:
pg.edu.pl/pmr

e-mail : pmr@pg.edu.pl

ISSN 1233-2585

CONTENS

- | | |
|----|---|
| 5 | Anna Witkowska, Tacjana Niksa Rynkiewicz
<i>DYNAMICALLY POSITIONED SHIP STEERING MAKING USE OF BACKSTEPPING METHOD AND ARTIFICIAL NEURAL NETWORKS</i> |
| 13 | Lifei Song, Zhuo Chen, Yunsheng Mao, Zaopeng Dong, Zuquan Xiang
<i>ERROR MITIGATION ALGORITHM BASED ON BIDIRECTIONAL FITTING METHOD FOR COLLISION AVOIDANCE OF UNMANNED SURFACE VEHICLE</i> |
| 21 | Zhiquan Liu
<i>ADAPTIVE SLIDING MODE CONTROL FOR SHIP AUTOPILOT WITH SPEED KEEPING</i> |
| 30 | Józef Lisowski
<i>OPTIMIZATION METHODS IN MARITIME TRANSPORT AND LOGISTICS</i> |
| 39 | Habib Choukri Lamraoui, Zhu Qidan
<i>PATH FOLLOWING CONTROL OF FULLY ACTUATED AUTONOMOUS UNDERWATER VEHICLE BASED ON LADRC</i> |
| 49 | Burak Kundakçi, Selçuk Nas
<i>MAPPING MARINE TRAFFIC DENSITY BY USING AIS DATA: AN APPLICATION IN THE NORTHERN AEGEAN SEA</i> |
| 59 | Krzysztof Bikonis, Jerzy Demkowicz
<i>MEMS TECHNOLOGY QUALITY REQUIREMENTS AS APPLIED TO MULTIBEAM ECHOSOUNDER</i> |
| 65 | Daewon Kim
<i>ESTIMATION OF HYDRODYNAMIC COEFFICIENTS FROM RESULTS OF REAL SHIP SEA TRIALS</i> |
| 73 | Paweł Bielski, Leszek Samson, Oskar Wysocki, Jacek Czyżewicz
<i>SIMPLE COMPUTATIONAL METHODS IN PREDICTING LIMIT LOAD OF HIGH-STRENGTH COLD-FORMED SECTIONS DUE TO LOCAL BUCKLING: A CASE STUDY</i> |
| 83 | Hui-Min Hou, Guo-Hai Dong, Tiao-Jian Xu, Yun-Peng Zhao, Chun-Wei Bi
<i>DYNAMIC ANALYSIS OF EMBEDDED CHAINS IN MOORING LINE FOR FISH CAGE SYSTEM</i> |
| 98 | Ozgur Ozguc
<i>ESTIMATION OF BUCKLING RESPONSE OF THE DECK PANEL IN AXIAL COMPRESSION</i> |

**ADDRESS OF PUBLISHER
& EDITOR'S OFFICE:**

**GDAŃSK UNIVERSITY
OF TECHNOLOGY**

**Faculty of Ocean Engineering
& Ship Technology
G. Narutowicza 11/12
80-233 Gdańsk, POLAND**

- 106 Fei Wang, Xiong Deng, Yuqiong Li**
*ELASTIC-PLASTIC ANALYSIS FOR CIRCUMFERENTIAL THROUGH CRACK
AT BOUNDARY OF SEMI'S BRACE UNDER BEAM WAVE*
- 114 Grzegorz Skorek**
*STUDY OF LOSSES AND ENERGY EFFICIENCY OF HYDROSTATIC DRIVES
WITH HYDRAULIC CYLINDER*
- 130 Jerzy Girtler**
*A CONCEPT OF DETERMINING THE RELATION BETWEEN LOAD AND WEAR
OF TRIBOLOGICAL SYSTEMS OF SHIP MAIN SELF-IGNITION ENGINES BY
USING PROBABILISTIC APPROACH*
- 139 Jianhua Zhang, Won-Hee Kang, Chunwei Zhang, Ke Sun**
*RELIABILITY BASED ANALYSIS AND DESIGN OF A TRIPOD OFFSHORE WIND
TURBINE STRUCTURE ASSURING SERVICEABILITY PERFORMANCE*
- 149 Maciej Niedostatkiwicz**
*DEGRADATION OF THE CONCRETE RAILWAY TRACK BED LOCATED IN THE
VICINITY OF THE LOADING WHARF*

Editorial

POLISH MARITIME RESEARCH is the scientific journal with a worldwide circulation. This journal is published quarterly (four times a year) by Gdansk University of Technology (GUT). On September, 1994, the first issue of POLISH MARITIME RESEARCH was published. The main objective of this journal is to present original research, innovative scientific ideas, and significant findings and application in the field of :

Naval Architecture, Ocean Engineering and Underwater Technology,

The scope of the journal covers selected issues related to all phases of product lifecycle and corresponding technologies for offshore floating and fixed structures and their components.

All researchers are invited to submit their original papers for peer review and publications related to methods of the design; production and manufacturing; maintenance and operational processes of such technical items as:

- all types of vessels and their equipment,
- fixed and floating offshore units and their components,
- autonomous underwater vehicle (AUV) and remotely operated vehicle (ROV).

We welcome submissions from these fields in the following technical topics:

- ship hydrodynamics: buoyancy and stability; ship resistance and propulsion, etc.,
- structural integrity of ship and offshore unit structures: materials; welding; fatigue and fracture, etc.,
- marine equipment: ship and offshore unit power plants: overboarding equipment; etc.

Scientific Board

Chairman : Prof. JERZY GIRTLEK - Gdańsk University of Technology, Poland

Vice-chairman : Prof. CARLOS GUEDES SOARES, Universidade de Lisboa, Lisbon, Portugal

Vice-chairman : Prof. MIROSŁAW L. WYSZYŃSKI - University of Birmingham, United Kingdom

Prof. POUL ANDERSEN Technical University of Denmark Kongens Lyngby, Denmark	Prof. STOJCE DIMOV ILCEV Durban University of Technology Durban, South Africa	Prof. JERZY EDWARD MATUSIAK Aalto University Espoo, Finland
Prof. JIAHN-HORNG CHEN National Taiwan Ocean University Keelung, Taiwan	Prof. YORDAN GARBATOV, Universidade de Lisboa Lisbon, Portugal	Prof. JERZY MERKISZ Poznan University of Technology Poznan, Poland
Prof. VINCENZO CRUPI University of Messina, Messina, Italy	Prof. STANISŁAW GUCMA Maritime University of Szczecin Szczecin, Poland	Prof. VALERI NIEKRASOV Admiral Makarov National University of Shipbuilding Mikolaiv, Ukraine
Prof. MAREK DZIDA Gdansk University of Technology Gdansk, Poland	Prof. ANTONI ISKRA Poznan University of Technology Poznan, Poland	Prof. JOZEF SZALA UTP University of Science and Technology Bydgoszcz, Poland
Prof. ODD MAGNUS FALTINSEN Norwegian University of Science and Technology Trondheim, Norway	Prof. JAN KICINSKI Institute of Fluid-Flow Machinery - Polish Academy of Sciences Gdansk, Poland	Prof. TADEUSZ SZELANGIEWICZ Maritime University of Szczecin Szczecin, Poland
Prof. MASSIMO FIGARI University of Genova Genova, Italy	Prof. ZBIGNIEW KORCZEWSKI Gdansk University of Technology Gdansk, Poland	Prof. DRACOS VASSALOS University of Strathclyde Glasgow, United Kingdom
Prof. HASSAN GHASSEMI Amirkabir University of Technology Tehran, Iran	Prof. JOZEF LISOWSKI Gdynia Maritime University Gdynia, Poland	

DYNAMICALLY POSITIONED SHIP STEERING MAKING USE OF BACKSTEPPING METHOD AND ARTIFICIAL NEURAL NETWORKS

Anna Witkowska

Gdańsk University of Technology

Tacjana Niksa Rynkiewicz

Gdańsk University of Technology

ABSTRACT

The article discusses the issue of designing a dynamic ship positioning system making use of the adaptive vectorial backstepping method and RBF type artificial neural networks. In the article, the backstepping controller is used to determine control laws and neural network weight adaptation laws. The artificial neural network is applied at each time instant to approximate nonlinear functions containing parametric uncertainties. The proposed control system does not require precise knowledge of the model of ship dynamics and external disturbances, it also eliminates the problem of analytical determination of the regression matrix when designing the control law with the aid of the adaptive backstepping procedure.

Keywords: backstepping, neural networks, RBF, dynamic ship positioning

INTRODUCTION

Issues related with automatic control of ship motion at sea still remain the area of active research, due to new and more complicated operational tasks to be undertaken by ships. Ship control is usually executed using a multi-layer control structure. The highest layer in this structure is the supervisory control system, which is responsible for planning the desired ship trajectory [10] from the initial point to the set destination point, based on the data achieved from navigation devices [13]. Here, algorithms are proposed in the literature which make use of the game theory [12], or artificial intelligence methods, including evolutionary algorithms [19,20] or fuzzy neural systems [15].

The next control layers are composed of algorithms responsible for ship's motion along the set trajectory, manoeuvring, and keeping the set heading and speed parameters, or position and heading parameters. These tasks are executed depending on the speed of the moving ship. Currently, a large number of watercrafts are equipped with dynamic positioning (DP) systems [17]. The list of those watercrafts includes drilling platforms, floating cranes, cable ships, store ships, fire boats, research and passenger ships, underwater work assistance ships used, for instance, for laying underwater pipelines, warships, reloading terminals, etc. The basic task of the DP systems is maintaining the set ship position and heading, or assistance in ship manoeuvring at low speed (up to 2 m/s), in the presence of environmental

disturbances acting on the ship hull. This task is executed by controlling ship's movements in three degrees of freedom (DOF's): surge, sway, and yaw, with the aid of propellers and rudders. An overview of essential research and technological development in designing DP controllers is presented in [17].

The majority of the presently used DP control methods is based on equations describing the mathematical model of dynamics and kinematics of the object. When maintaining the set position and heading of the DP ship, nonlinear damping forces, Coriolis forces, and centripetal forces can be neglected due to their small effect on ship dynamics, and the nonlinearity can be only taken into account in the kinematic model. On the other hand, tracking the set trajectory at low ship speed consists in simultaneous control of ship heading and its longitudinal and transverse position. Changes of the operating point of the system and hydrodynamic phenomena are the sources of nonlinearities and varying coefficients in equations of ship dynamics and kinematics. Controlling nonlinear systems with uncertainties is the area which still needs further research. At present, two basic approaches, referred to as robust and adaptive control, are applied to deal with system uncertainties. Robust control methods, such as sliding mode control [21] or H^∞ control [8], consist in designing a controller with fixed structure which ensures proper performance in the entire range of process changes. Adaptive control methods, in turn, such as backstepping and its modifications: Dynamic Surface Control (DSC) [18], and Active Direct Surface Control (ADSC) [14] provide opportunities for designing a dynamically changing feedback loop.

The basic idea of designing an adaptive control law consists firstly in assessing the value of the unknown parameter and determining its estimate. Then, the static part of the controller, which contains the estimated parameters, is continuously updated to reflect changing conditions of system operation.

Currently, backstepping is one of basic methods used to design nonlinear control systems with uncertainties. It belongs to the group of recursive methods based on the theory of Lyapunov functions [9]. The structure of both the control law with feedback, and the accompanying Lyapunov function for systems with unknown parameters is systematised.

A complex system is firstly divided into lower-dimension subsystems. Then, the Lyapunov function and the intermediate virtual control inputs are determined for each subsystem. Designing is done recursively until the entire system reaches the real control input. This way the goal of control can be achieved at reduced control effort [22]

The basic limitation in the use of the adaptive backstepping method is the need for analytical calculation of the time derivative of the "virtual control signal" [9] at each procedure step, which leads to a complicated algorithm requiring much computational effort. What is more, the level of complicity of controller's structure increases with the increase of the system order. To eliminate the need for calculating complex derivatives, first- and second-order filters are frequently used [24]. The other limitation of the standard adaptive backstepping method is the assumption that the

functions with uncertainties are to be linear with respect to unknown parameters and, consequently, are able to be presented in the form of the regression model. Determining the regression matrix requires laborious analysis. Moreover, the complexity of the regression matrix and the number of unknown parameters increase in consecutive backstepping procedure steps, thus generating the so-called effect of overparametrization [9].

Some attempts to solve this problem which can be found in the literature make use of fuzzy systems or artificial neural networks [1, 6]. The latter approach can be applied at each step of the backstepping procedure. Neural networks are used for assessing nonlinear functions, the form of which depends on the values of the estimated parameters. This method makes it possible to design the control law in which the analytical form of the regression matrix and the assumption of linearity with respect to parameters are not required.

This paper presents a multidimensional nonlinear DP controller designed using the adaptive vectorial backstepping method and Radial Basic Function (RBF) type artificial neural networks in the feedback loop. When designing the control law, the presence of parametric uncertainties was assumed in the matrices of damping, Coriolis forces, and environmental disturbances. The artificial RBF type neural network was used at each time instant to approximate nonlinear functions with parametric uncertainties. The network weight adaptation laws were determined based on the Lyapunov's theory of stability, depending on the operating point of the system. This way, the neural network does not require preliminary offline weight tuning.

The applied radial network is the structure consisting of three layers: input, hidden, and output. The architecture of the network is relatively simple. The input signals are given to the input layer, while the radial neurons are accumulated in the hidden layer. The neurons play a special role, as they map radially the space surrounding the set points. The output layer usually comprises only one neuron, the role of which is to combine the weighted signals coming from the hidden layer. This approach makes it possible to map the entire space of points.

Unlike the already existing DP systems, the proposed control system does not require detailed knowledge of the model of object's dynamics and external disturbances, thus eliminating the problem of analytical calculation of derivatives and the regression matrix.

The use of the theory of Lyapunov functions and RBF networks makes that the designed feedback loops ensure the convergence of ship position and heading to the set values, and the boundedness of signals in the closed control system loop [11].

STRUCTURE OF CONTROL SYSTEM

A structurally simplified general working scheme of the DP system is shown in Fig. 1. The set values of ship position and heading, composing the ship position vector, are introduced

to the system via user's interface, while the estimated vectors of current ship position and speed are calculated based on the navigation reference system and the state observer. The position error vector, being the difference between the set vector and the estimated vector, is passed to the DP controller, which then calculates forces and torque required to minimise deviations from the set values.

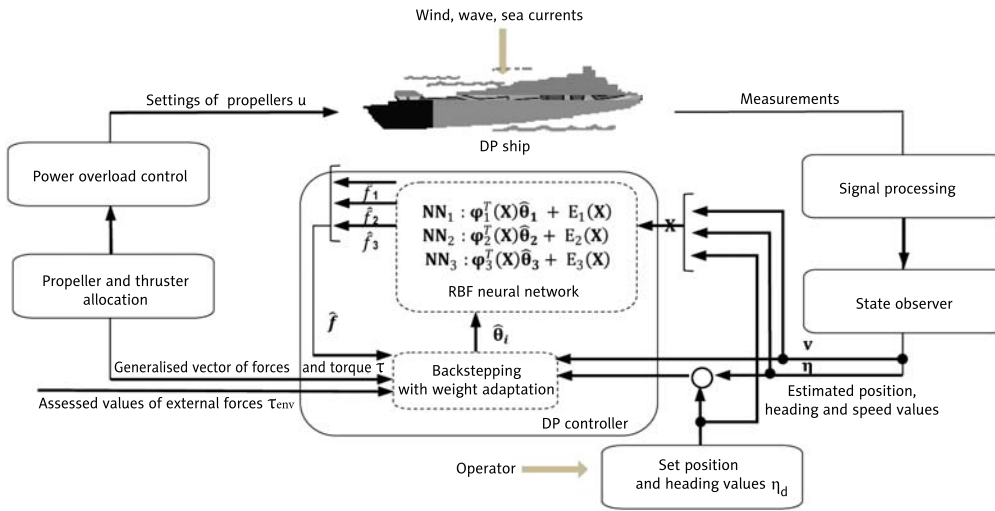


Fig. 1. Structure of DP control system with backstepping controller and RBF type neural network

The resultant vector of forces and torque is passed to the allocation control system, where the set values of forces and torque are converted to control signals for actuator settings, at the same time minimising the energy needed to execute the control task. The actuator settings refer to rotational speeds of main propellers and azimuth and tunnel thrusters, and rudder angles.

Bearing in mind the required precision and safety of control executed by a DP system, the number of actuators is, as a rule, larger than the number of the controlled degrees of freedom of ship motion. This over-actuation is the reason why the conversion of forces and torque to control signals and their allocation into individual actuators is not always unambiguous. In those cases, it can be approximated in the square optimisation process with limitations placed on maximal amplitude and rate of changes of actuator settings, at simultaneous minimisation of economic losses resulting from excessive activity of propellers and rudders.

PROBLEM FORMULATION

This research aimed at designing a controller which would perform basic tasks of dynamic ship positioning: manoeuvres of ship position and heading change or ship stabilisation at a point, in the case of inaccurate data on the mathematical model of the object used for designing the control law. This means that the designed control system meets the condition of control error convergence to zero after change

of the operating point of the system and/or environmental conditions.

The DP controller was synthesised using the adaptive vectorial backstepping method and artificial RBF type neural networks. The artificial neural networks were applied to approximate nonlinear functions with uncertainties, while the backstepping method was used to determine the control laws and the RBF network weight adaptation mechanism.

MATHEMATICAL MODEL OF DP SHIP

When designing the control law based on the backstepping method and neural networks, the mathematical model of a ship dynamically positioned in the horizontal plane was adopted. This model is given by the following system of differential equations (1)-(2).

$$\dot{\eta} = J(\eta)v \quad (1)$$

$$M(v)\dot{v} = \tau + J(\eta)^T b - D(v)v - C(v)v \quad (2)$$

where $\tau = [\tau_x, \tau_y, \tau_z]^T$ is the generalised vector of forces and torque acting on the ship, $\eta = [x, y, \psi]^T$ is the vector of ship position and heading, and $v = [u, v, r]^T$ is the vector of longitudinal, lateral and angular ship velocity components. The matrices $M \in \mathbb{R}^{3 \times 3}$, $D \in \mathbb{R}^{3 \times 3}$, $C \in \mathbb{R}^{3 \times 3}$, and $J(\eta) \in \mathbb{R}^{3 \times 3}$ represent, respectively, the matrices of inertia, damping, and Coriolis forces, and the state dependent matrix which converts coordinates from the system fixed to the ship's centre of gravity to the Earth fixed system. The vector $b = [b_1, b_2, b_3]^T$ represents unmodelled slowly varying environmental disturbances.

The ship model takes into account three degrees of freedom of ship motion: longitudinal motion (surge), transverse motion (sway), and change of ship heading angle.

The model equations have the following properties [7]:

$$M^T = M \Rightarrow x^T M x > 0, x \neq 0, \quad (3)$$

$$J^{-1}(\eta) = J^T(\eta), \|J(\eta)\| = 1, \quad (4)$$

$$\frac{d}{dt} \mathbf{J}(\boldsymbol{\eta}) = -r \mathbf{S} \mathbf{J}(\boldsymbol{\eta})^T, \text{ where } \mathbf{S} = \begin{bmatrix} 0 & -1 & 0 \\ 1 & 0 & 0 \\ 0 & 0 & 0 \end{bmatrix}, \mathbf{s} = -\mathbf{S}^T \quad (5)$$

$$\mathbf{z}_1^T(t) \mathbf{S} \mathbf{z}_1(t) = \mathbf{0}, \mathbf{S} = -\mathbf{S}^T. \quad (6)$$

The system (1)-(2) has a cascaded structure. The control input given to the system is the vector $\boldsymbol{\tau}$, while the “virtual control output” is the vector \mathbf{v} , being simultaneously the “virtual control input” for the first subsystem (1). The control output from the entire system is the ship position and heading vector $\boldsymbol{\eta}$.

When designing the control law, it was assumed that the model of ship dynamics contains parametric uncertainties in matrices \mathbf{D} , \mathbf{C} , and \mathbf{M} , and that the components of the vector \mathbf{b} are unknown but slowly varying. Moreover, it was assumed that all state variables are bounded and measurable (or estimable). The set position and heading trajectories $\boldsymbol{\eta}_d = [x_d, y_d, \psi_d]^T$ and their first- and second-order derivatives are smooth and bounded in time.

STRUCTURE OF RBF TYPE NETWORK

A special variation in the family of artificial neural networks (NN) is the group of networks with radial basic functions (RBF). The hidden layer in this network consists of neurons bearing the name of basic or radial neurons [2]. A radial neuron represents a hypersphere in which circular division around the central point x_i , where $i = 1 \dots l$ [4,16], takes place. The vector of radial functions $\boldsymbol{\varphi}(\mathbf{x}) = [\varphi_1(\mathbf{x}), \varphi_2(\mathbf{x}), \dots, \varphi_l(\mathbf{x})]$ is determined in the space of input signals. It is assumed that there exists the vector $\boldsymbol{\theta}^T \boldsymbol{\varphi}(\mathbf{x})$, which represents the border between two classes, and its value indicates belongingness to a given class, as $\boldsymbol{\theta}^T \boldsymbol{\varphi}(\mathbf{x}) < 0$ or $\boldsymbol{\theta}^T \boldsymbol{\varphi}(\mathbf{x}) > 0$. That means that the space division is nonlinearly φ -separable.

In [4], the authors have proved that each set of patterns randomly distributed in the multidimensional space is φ -separable with probability equal to 1 if only a sufficiently large dimension l of the projection space is assumed.

It is stressed in the literature that assuming a sufficiently large number l of radial neurons in the hidden layer ensures correct solution when using three network layers: the input layer, the hidden layer in which the vector $\boldsymbol{\varphi}(\mathbf{x})$ is executed, and the output layer consisting of one linear neuron described by the weight vector $\boldsymbol{\theta}$. The operation of the network can be described by formula (7)

$$\bar{F}(x) = \sum_{i=1}^K \boldsymbol{\theta}_i \mathbf{G}(\|\mathbf{x} - \mathbf{x}_i\|) \quad (7)$$

Selecting the type of norm can be arbitrary. In the proposed approach, the Euclidean norm was used together with Green's functions of Gauss type [2,3,16] (8).

$$\mathbf{G}(x; \mathbf{x}_i) = \exp\left(-\frac{\|\mathbf{x} - \mathbf{x}_i\|^2}{2\sigma_i^2}\right) = \exp\left(-\frac{1}{2\sigma_i^2} \sum_{k=1}^N (x_k - x_{ki})\right) \quad (8)$$

Here, \mathbf{x}_i is the vector of mean values (centres) and σ_i^2 is the variance. When creating the radial neural network to the presented problem, the number K of basic functions had to be assumed. The initial values of the centres \mathbf{x}_i of the radial functions were selected using the Fuzzy C-Means (FCM) algorithm, which is used and described in the literature [5].

A simplified scheme of RBF network structure is shown in Fig 2.

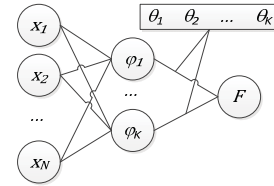


Fig. 2. Simplified scheme of RBF network structure

The approximation task consists in selecting appropriate Green's functions $\mathbf{G}(\mathbf{x}, \mathbf{x}_i)$ and weights $\boldsymbol{\theta}_i$. The nonlinear radial function for each hidden neuron has different parameters \mathbf{x}_i and σ_i . The argument of the radial function is the distance of the given sample \mathbf{x} from the centre \mathbf{x}_i .

DP CONTROLLER

In accordance with the backstepping methodology, for the system (1)-(2), new state variables were defined in the form of control errors $\mathbf{z}_1(t) \in \mathbb{R}^{3 \times 1}$ and $\mathbf{z}_2(t) \in \mathbb{R}^{3 \times 1}$, and the vector $\boldsymbol{\alpha} \in \mathbb{R}^{3 \times 1}$ of functions stabilising the first subsystem. In the coordinate system fixed to the moving ship, the control errors take the following form:

$$\mathbf{z}_1 = \mathbf{J}(\boldsymbol{\eta})^T (\boldsymbol{\eta} - \boldsymbol{\eta}_d) \quad (9)$$

$$\mathbf{z}_2 = \mathbf{v} - \boldsymbol{\alpha} \quad (10)$$

The vector of stabilising functions will be determined when designing the control law.

Based on the kinematics and dynamics equations (1)-(2) and taking into account the model property (5), the control error derivatives were determined as:

$$\dot{\mathbf{z}}_1 = -r \mathbf{S} \mathbf{z}_1 + \mathbf{z}_2 + \boldsymbol{\alpha} - \mathbf{J}(\boldsymbol{\eta})^T \dot{\boldsymbol{\eta}}_d \quad (11)$$

$$\mathbf{M} \dot{\mathbf{z}}_2 = \boldsymbol{\tau} + \mathbf{f}(\boldsymbol{\eta}, \mathbf{v}, \boldsymbol{\eta}_d, \mathbf{v}_d) \quad (12)$$

Denoting the matrix dependent on state variables by $\mathbf{X} = [\boldsymbol{\eta}, \mathbf{v}, \boldsymbol{\eta}_d, \mathbf{v}_d]$, the function $f \in \mathbb{R}^{3 \times 1}$ takes the form:

$$f(\mathbf{X}) = -\mathbf{C}\mathbf{v} - \mathbf{D}\mathbf{v} + \mathbf{J}(\boldsymbol{\eta})^T \mathbf{b} - \mathbf{M}\dot{\boldsymbol{\alpha}} \quad (13)$$

This function contains unknown model parameters.

To determine the adaptation laws for parameters of matrices \mathbf{M} , \mathbf{D} , \mathbf{C} and vector \mathbf{b} , the function f is to be presented in the form of the regression model, after which the standard backstepping procedure can be applied. This approach is labour-intensive, requires huge computational effort, and leads to an excessively large number of estimated parameters, as stated in [23]. Instead, the components of the function $f = [f_1, f_2, f_3]^T$ can be approximated using three artificial RBF type neural networks NN_i with the number of neurons $l > 1$. The outputs $\hat{f} = [\hat{f}_1, \hat{f}_2, \hat{f}_3]^T$ from these networks have the form of the following regression model:

$$\hat{f}_i(\mathbf{X}_i) = \boldsymbol{\varphi}_i^T(\mathbf{X}_i) \boldsymbol{\theta}_i; \quad i = 1..3 \quad (14)$$

In Equation (14), \mathbf{X}_i is the input vector to network NN_i , $\mathbf{X}_i = [\boldsymbol{\eta}(i), \mathbf{v}(i), \boldsymbol{\eta}_d(i), \mathbf{v}_d(i)]^T \in \mathbb{R}^{4 \times 1}$, while $\boldsymbol{\theta}_i$ is the determined vector of weights between the second and third layer in network NN_i , $\boldsymbol{\theta}_i = [\theta_{i1}, \theta_{i2}, \dots, \theta_{il}]^T \in \mathbb{R}^{l \times 1}$. The vector $\boldsymbol{\varphi}_i$ represents the set of basic function values in network NN_i , $\boldsymbol{\varphi}_i = [\varphi_{i1}, \varphi_{i2}, \dots, \varphi_{il}]^T \in \mathbb{R}^{l \times 1}$.

Each RBF network has a predefined number l of radial neurons. The selection of their weights is made in the process of control system adaptation to changing operating conditions. In the proposed system, the number of radial neurons was determined experimentally as equal to $l = 4$.

After complementing with the RBF network equations, Equation (6) of control error dynamics takes the form:

$$\mathbf{M}\dot{\mathbf{z}}_2 = \boldsymbol{\tau} + \boldsymbol{\varphi}^T(\mathbf{X})\boldsymbol{\theta} \quad (15)$$

The regression vector, i.e. the vector of RBF network weights, is defined as $\boldsymbol{\theta} = [\boldsymbol{\theta}_1^T, \boldsymbol{\theta}_2^T, \boldsymbol{\theta}_3^T]^T \in \mathbb{R}^{3 \times l}$, while the regression matrix $\boldsymbol{\varphi}^T \in \mathbb{R}^{3 \times 3l}$ has the form:

$$\boldsymbol{\varphi}^T = \begin{bmatrix} \boldsymbol{\varphi}_1^T(\mathbf{X}) & \mathbf{0}_{1 \times l} & \mathbf{0}_{1 \times l} \\ \mathbf{0}_{1 \times l} & \boldsymbol{\varphi}_2^T(\mathbf{X}) & \mathbf{0}_{1 \times l} \\ \mathbf{0}_{1 \times l} & \mathbf{0}_{1 \times l} & \boldsymbol{\varphi}_3^T(\mathbf{X}) \end{bmatrix} \quad (16)$$

The task of the backstepping controller is to determine: the indirect control law $\boldsymbol{\alpha}$ which stabilises the first subsystem (1), the control law $\boldsymbol{\tau}$ which stabilises the entire system, and the adaptation law for the weight vector $\boldsymbol{\theta}$ with respect to the Lyapunov function of the system.

Applying the certain equivalence principle [9], the vector $\boldsymbol{\theta}$ in Equation (15) was replaced by the sum of the vectors of estimates and estimation errors, $\hat{\boldsymbol{\theta}} + \tilde{\boldsymbol{\theta}}$.

$$\mathbf{M}\dot{\mathbf{z}}_2 = \boldsymbol{\tau} + \boldsymbol{\varphi}^T(\mathbf{X})\hat{\boldsymbol{\theta}} + \boldsymbol{\varphi}^T(\mathbf{X})\tilde{\boldsymbol{\theta}} \quad (17)$$

The control law was determined with respect to the Lyapunov function V_a being the sum of squares of control errors and the term related with the error of estimation of the unknown weight vector $\boldsymbol{\theta}$.

$$V_a = \frac{1}{2} \mathbf{z}_1^T \mathbf{z}_1 + \frac{1}{2} \mathbf{z}_2^T \mathbf{M} \mathbf{z}_2 + \frac{1}{2} \tilde{\boldsymbol{\theta}}^T \boldsymbol{\Gamma}^{-1} \tilde{\boldsymbol{\theta}} \quad (18)$$

where: $\boldsymbol{\Gamma} > 0$ is the diagonal matrix of controller gains, $\dim \boldsymbol{\Gamma} = 3l \times 3l$.

Assuming that the estimated parameters are slowly varying, i.e. the equation $\dot{\tilde{\boldsymbol{\theta}}} = -\tilde{\boldsymbol{\theta}}$ is fulfilled, the derivative of the Lyapunov function V_a (18) takes the form:

$$\dot{V}_a = \mathbf{z}_1^T \dot{\mathbf{z}}_1 + \mathbf{z}_2^T \mathbf{M} \dot{\mathbf{z}}_2 - \tilde{\boldsymbol{\theta}}^T \boldsymbol{\Gamma}^{-1} \dot{\tilde{\boldsymbol{\theta}}} \quad (19)$$

Substituting the error dynamics equations (11) and (17) into equation (19) and eliminating the term $\mathbf{z}_1^T(t) \mathbf{S} \mathbf{z}_1(t) = 0$ (6) gives:

$$\begin{aligned} \dot{V}_a &= \mathbf{z}_1^T [\boldsymbol{\alpha}_1 - \mathbf{J}(\boldsymbol{\eta})^T \dot{\boldsymbol{\eta}}_d] \\ &+ \mathbf{z}_2^T [\mathbf{z}_1 + \boldsymbol{\tau} + \boldsymbol{\varphi}^T(\mathbf{X})\hat{\boldsymbol{\theta}}] \\ &+ \tilde{\boldsymbol{\theta}}_1^T (\boldsymbol{\varphi}(\mathbf{X})\mathbf{z}_2 - \boldsymbol{\Gamma}^{-1} \dot{\tilde{\boldsymbol{\theta}}}) \end{aligned} \quad (20)$$

The control laws $\boldsymbol{\alpha}$, $\boldsymbol{\tau}$ were selected such that the Lyapunov function (20) in the system of new variables was negative semidefinite:

$$\dot{V}_a = -\mathbf{z}_1^T \mathbf{K}_1 \mathbf{z}_1 - \mathbf{z}_2^T \mathbf{K}_2 \mathbf{z}_2 \leq 0 \quad (21)$$

Here, $\mathbf{K}_j \in \mathbb{R}^{3 \times 3}$, $j = \{1, 2\}$ is the diagonal and positive definite matrix of controller gains. Comparing (20) and (21), the following relationships can be determined:

- weight adaptation mechanism:

$$\dot{\tilde{\boldsymbol{\theta}}} = \boldsymbol{\Gamma} \boldsymbol{\varphi}(\mathbf{X}) \mathbf{z}_2 \quad (22)$$

- vector of stabilising functions, $\boldsymbol{\alpha}$, independent of the vector of estimates $\hat{\boldsymbol{\theta}}$:

$$\boldsymbol{\alpha} = -\mathbf{K}_1 \mathbf{z}_1 + \mathbf{J}(\boldsymbol{\eta})^T \dot{\boldsymbol{\eta}}_d \quad (23)$$

- vector of controls, $\boldsymbol{\tau}$, dependent of the vector of estimates $\hat{\boldsymbol{\theta}}$ (RBF network weights) calculated in accordance with (19), under the assumption that the network has a sufficient number of neurons,

$$\boldsymbol{\tau} = -\mathbf{K}_2 \mathbf{z}_2 - \mathbf{z}_1 - \boldsymbol{\varphi}^T(\mathbf{X}) \hat{\boldsymbol{\theta}} \quad (24)$$

If rapidly varying disturbances do not occur in the system, then the control law (24) together with the adaptation law (22) ensure asymptotical convergence of ship position and heading to their set values, $\boldsymbol{\eta}(t) \rightarrow \boldsymbol{\eta}_d(t)$, when $\mathbf{v}(t) \approx 0$. They also ensure the boundedness of changes of signals $\boldsymbol{\eta}(t)$ and $\mathbf{v}(t)$, $t \rightarrow \infty$, at bounded changes of estimated parameter values.

SIMULATION TESTS

The computer simulations were performed on the control system with the structure shown in Fig.1. In these simulations, the issues of power overload and state observer control were not analysed, assuming that all state variables are bounded and measurable (estimable).

The simulation tests were performed using the mathematical model of a store ship with length of $L=76.2$ m and mass of 4591 [t]. The ship motion equation was analysed by controlling the ship motion in 3 degrees of freedom with the aid of two main propellers with rudders, bow tunnel thruster, and rotating azimuth bow thruster.

The following dimensionless parameters of the model (1)-(2), determined in the Bis scaling system, were assumed [7]:

$$\begin{aligned} \mathbf{C}''(\mathbf{v}) &= [0 \ 0 \ -1.8902v'' + 0.0744r''; \\ &\quad 0 \ 0 \ 1.1274 u''; \\ &\quad 1.8902v'' - 0.0744r'' \ -1.1274 u'' \ 0], \\ \mathbf{D}'' &= [0.0414 \ 0 \ 0; \ 0 \ 0.1775 \ -0.0141; \\ &\quad 0 \ -0.1073 \ 0.0568], \\ \mathbf{M}'' &= [1.1274 \ 0 \ 0; \ 0 \ 1.8902 \ -0.0744; \\ &\quad 0 \ -0.0744 \ 0.1278]. \end{aligned}$$

During manoeuvring operations, the set ship position and heading trajectories $\boldsymbol{\eta}_d$ and their derivatives $\dot{\boldsymbol{\eta}}_d$ were generated in accordance with the reference model (25) to determine smooth and bounded set signals for the DP controller. Assuming that $\xi = 0.8$ and $\omega_n = 0.05$ rad/s, the value of $G_f(s)$ was calculated from formula (22):

$$G_f(s) = \frac{\omega_n^2}{(s^2 + 2\xi\omega_n s + \omega_n^2)}. \quad (25)$$

The DP controller was defined by the control law (24), the neural network with radial basic functions (7), and the weight adaptation law (22). In the simulations, the initial ship position and heading, and the initial estimated weight values were assumed equal to zero.

The nonlinear function of the backstepping controller was approximated using the RBF network, due to its properties described in Section 5 and the possibility to present the output in the form of regression model (7).

The proposed system was designed and constructed in MatLab environment. Three RBF networks were created. For each network, 4 sets of input signals were given, and each time one output signal was obtained as a result of its operation. The number of basic neurons was chosen experimentally. The centres of basic functions were set using the FCM algorithm. The RBF network structure underwent preliminary verification by using it as an ordinary function approximator (13). After selecting its parameters, the network was implemented in the control structure with adaptive controller, shown in Fig. 1.

The tests with adaptive controller included programmable inertial changes of set position and heading values in the presence of slowly varying environmental disturbances, modelled using the Markov process [7].

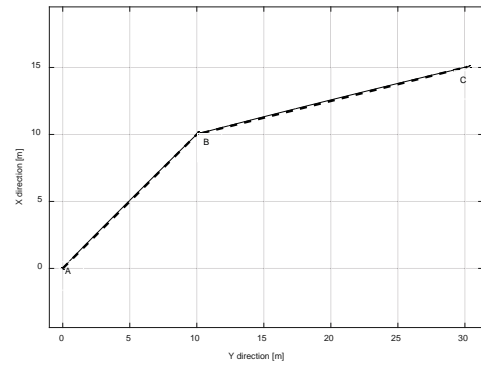


Fig. 3. Set (--) and real (-) trajectory (x, y) of DP ship

Fig. 3 shows the set and real trajectory of the ship. At time zero, the ship is at point A. Then it begins the manoeuvre of position and heading change to the set position B. After time $t_1 = 1115.4$ s, the next change of the set ship position and heading takes place (towards point C). The robustness of the controller with radial neural network was analysed by introducing a disturbance signal after time $t_2 = 836.55$ s. This signal was added to the forces acting on the ship in yaw direction. Based on the results of the performed simulations and the obtained time-histories, it can be concluded that the ship's position and heading track the set trajectory with good accuracy (Fig. 4).

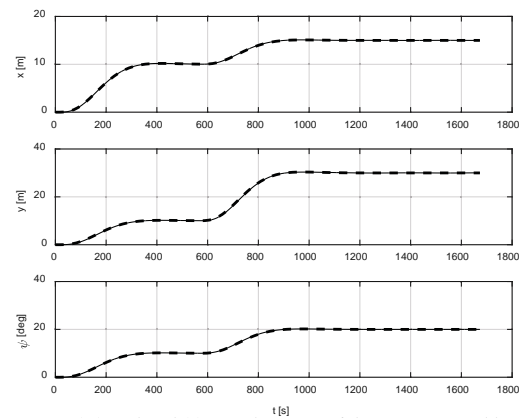


Fig. 4. Set (--) and real (-) time-histories of ship position and heading

The control errors tend asymptotically to zero, without over-regulation in three degrees of freedom of ship motion. This result has been obtained for the system without a priori knowledge of ship model parameters and slowly varying environmental disturbances. The normalised control inputs are shown in Figure 5.

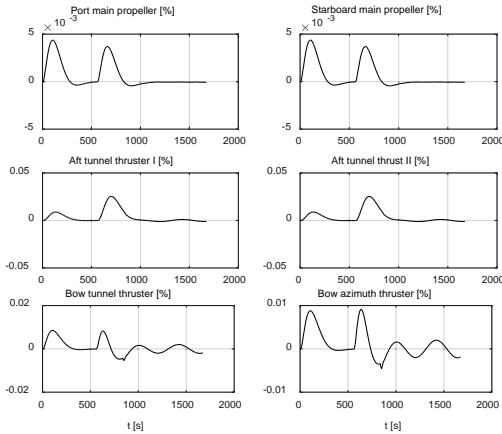


Fig. 5. Control inputs normalised in Bis system

These values become saturated after exceeding 1 and compensate the effect of environmental disturbances. As shown in Fig. 4, small tracking errors were recorded, but they did not exceed acceptable limits.

The present study did not aim at analysing properties of the neural network. Better performance of the DP system can be achieved by further tuning the updating gains and/or by increasing the number of neurons. The present study only demonstrates the possibility of using neural networks for approximating the dynamics of a DP ship with the aid of the theory of Lyapunov functions when designing the control law and when estimating online the RBF network weights.

In a general case, the backstepping method ensures that the values of estimates change in a limited manner and are approximately constant in steady-state conditions (Fig. 6).

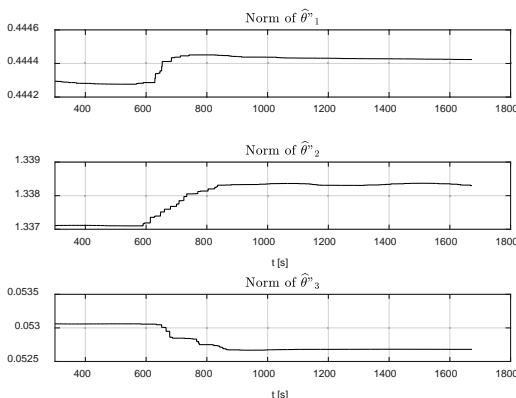


Fig. 6. Norm of RBF network weight vector ($\hat{\theta}_i$ - weight vector for NNi network, $i=1..3$ in Bis system)

The obtained results confirm correct operation of the DB system with model and disturbance uncertainties at the analysed operating points.

CONCLUSIONS

The control system with adaptive backstepping controller was designed for a DP ship. In this system, the RBF neural network was used to estimate the nonlinear function of ship model. The performance of the system was checked in simulation tests. The proposed system does not require a priori knowledge of parameters of matrices of ship damping, Coriolis forces, and/or inertia. It neither requires precise modelling of slowly varying environmental disturbances. The use of the RBF network significantly simplifies designing a backstepping controller, as it does not require analytical description of the regression matrix. Determining the weight adaptation law makes preliminary network tuning unnecessary, as a consequence of which the network can be used online. The performed simulation tests have proved that the adaptive controller tracks the set position and heading trajectory with acceptably small error, at the same time ensuring the boundedness of signals in the closed loop of the control system. Thus, the results of computer simulations illustrate high operating effectiveness of the proposed control method making use of RBF neural networks.

BIBLIOGRAPHY

1. Boulkroune, A., N. Bounar, M. M'Saad, M. Farza: Indirect adaptive fuzzy control scheme based on observer for nonlinear systems: A novel SPR-filter approach, *Neurocomputing*, 135, 2014 pp. 378–387.
2. Buhmann, M.D.: *Radial basis functions: theory and implementations*, Cambridge University Press 2003.
3. Chan, A.K., G.A. Becus: Online adaptation of RBF centers for adaptive control, in: *Proceedings of 1995 American Control Conference - ACC'95*, American Autom Control Council, 1995 pp. 3770–3774.
4. Cover, T.M.: *Geometrical and Statistical Properties of Systems of Linear Inequalities with Applications in Pattern Recognition*, *IEEE Transactions on Electronic Computers* 1965, pp. 326-334.
5. Cpałka, K.: *Design of Interpretable Fuzzy Systems*, Springer 2017.
6. Du, J., X. Hu, H. Liu, C.L.P. Chen: Adaptive robust output feedback control for a marine dynamic positioning system based on a high-gain observer, *IEEE Transactions on Neural Networks and Learning Systems*, 26, 2015 pp. 2775–2786.

7. Fossen, T.I., S.P. Berge: Nonlinear vectorial backstepping design for global exponential tracking of marine vessels in the presence of actuator dynamics, in: Proceedings of the 36th IEEE Conference on Decision and Control, IEEE, 1998 pp. 4237–4242.
8. Katebi, M.R., M.J. Grimble, Y. Zhang: Hinf robust control design of dynamic ship positioning, Ieee Process Control Theory Applicatron. 144 1997, pp. 110–120.
9. Krstić, M., I. Kanellakopoulos, P. Kokotović: Nonlinear and adaptive control design, Wiley 1995.
10. Kuczkowski, Ł., R. Śmierchalski: Path planning algorithm for ship collisions avoidance in environment with changing strategy of dynamic obstacles, in: Springer, Cham 2017: pp. 641–650.
11. Kwan, C., F.L. Lewis: Robust backstepping control of nonlinear systems using neural networks, Systems, Man and Cybernetics, Part A: Systems and Humans, IEEE Transactions on. 30, 2000 pp. 753–766.
12. Lisowski, J.: Game control methods in avoidance of ships collisions, Polish Maritime Research. 19 2012, pp. 3–10.
13. Lisowski, J., A. Lazarowska: The radar data transmission to computer support system of ship safety, Solid State Phenomena. 196 2013, pp. 95–101.
14. Mingyu, F., X. Yujie, Z. Li: Bio-inspired Trajectory Tracking Algorithm for Dynamic Positioning Ship with System Uncertainties, Proceedings of the 35th Chinese Control Conference, 2016 pp. 4562–4566.
15. Niksa-Rynkiewicz, T., Szłapczyński R.: A framework of a ship domain – based near-miss detection method using mamdani neuro-fuzzy classification., Polish Maritime Research, (in review) 2018.
16. Orr, M.J.L.: Introduction to Radial Basis Function Networks 1996.
17. Sorensen, A.: A survey of dynamic positioning control systems, Annual Reviews in Control . 35 2011 pp. 123–136.
18. Swaroop, D., J.K. Hedrick, P.P. Yip, J.C. Gerdes: Dynamic surface control for a class of nonlinear systems, IEEE Transactions on Automatic Control. 45 2000, pp. 1893–1899.
19. Szczypka, J., A. Przybył, K. Cpałka: Some Aspects of Evolutionary Designing Optimal Controllers, in: Springer, Berlin, Heidelberg 2013 pp. 91–100.
20. Szłapczyński, R., J. Szłapczyńska: Customized crossover in evolutionary sets of safe ship trajectories, International Journal of Applied Mathematics and Computer Science. 22 2012.
21. Tannuri, E.A., A.C. Agostinho, H.M. Morishita, L. Moratelli: Dynamic positioning systems: An experimental analysis of sliding mode control, Control Engineering Practice. 18, 2010 pp. 1121–1132.
22. Witkowska, A.: Control design for slow speed positioning, Proceedings - 27th European Conference on Modelling and Simulation, ECMS 2013 pp. 198–204.
23. Witkowska, A., R. Śmierchalski: Designing a ship course controller by applying the adaptive backstepping method, Int. J. Appl. Math. Comput. Sci. 22 2012 pp. 985–997.
24. Yang, Y., J. Du, G. Li, W. Li, C. Guo: Dynamic Surface Control for Nonlinear Dynamic Positioning System of Ship, in: Advances in Intelligent and Soft Computing, Springer, Berlin, Heidelberg 2012: pp. 237–244.

CONTACT WITH THE AUTHORS

Anna Witkowska

e-mail: anna.witkowska@pg.edu.pl

Gdańsk University of Technology

Gabriela Narutowicza 11/12

80-233 Gdańsk

POLAND

Tacjana Niksa Rynkiewicz

e-mail: tacniksa@pg.edu.pl

Gdańsk University of Technology

Gabriela Narutowicza 11/12

80-233 Gdańsk

POLAND

ERROR MITIGATION ALGORITHM BASED ON BIDIRECTIONAL FITTING METHOD FOR COLLISION AVOIDANCE OF UNMANNED SURFACE VEHICLE

Lifei Song^{1,2}

Zhuo Chen²

Yunsheng Mao²

Zaopeng Dong²

Zuquan Xiang²

¹ School of Transportation, Wuhan University of Technology, Wuhan, China

² Key Laboratory of High Performance Ship Technology (Wuhan University of Technology) Ministry of Education, Wuhan, China

ABSTRACT

Radars and sensors are essential devices for an Unmanned Surface Vehicle (USV) to detect obstacles. Their precision has improved significantly in recent years with relatively accurate capability to locate obstacles. However, small detection errors in the estimation and prediction of trajectories of obstacles may cause serious problems in accuracy, thereby damaging the judgment of USV and affecting the effectiveness of collision avoidance. In this study, the effect of radar errors on the prediction accuracy of obstacle position is studied on the basis of the autoregressive prediction model. The cause of radar error is also analyzed. Subsequently, a bidirectional adaptive filtering algorithm based on polynomial fitting and particle swarm optimization is proposed to eliminate the observed errors in vertical and abscissa coordinates. Then, simulations of obstacle tracking and prediction are carried out, and the results show the validity of the algorithm. Finally, the method is used to simulate the collision avoidance of USV, and the results show the validity and reliability of the algorithm.

Keywords: Unmanned Surface Vehicle; Position prediction; Error mitigation; Autoregressive model; Particle Swarm Optimization

INTRODUCTION

An Unmanned Surface Vehicle (USV) is a ship that navigates on water in an autonomous manner. Its autonomous collision avoidance capability is the basis for safe navigation and undertaking maritime tasks [1]. A USV uses the Automatic Identification System (AIS) and radars to access environmental information [2]. Among them, radars are the basic devices for USV to obtain obstacle information [3]. The International Maritime Organization (IMO) specifies that the maximum ranging error of radar should be 1% of the range or 30 m and that the azimuth error should be within 1° [4]. However, radars present unstable accuracy because of the complexity of sea conditions and existence of clutters and exhibit unacceptable detection errors [5]. Given that the collision avoidance planning of

USV is based on the accurate tracking of obstacle targets [6], the errors of the latter may significantly affect the result of the former [7].

The estimation and prediction of position, velocity, and information for maneuvering target are important issues in target tracking area and are closely relevant to information fusion [8]. Boats, which may suddenly change their acceleration and turning, are principal obstacles that can be difficult to avoid for USVs. For an effective target tracking, the motion of target should be modeled first and then the state of target should be estimated by filtering [9]. However, the filter and motion models of target are often mismatched owing to the uncertainty and variability of motion modeling, thereby degrading the effect of estimation [10]. Therefore, filtering the motion data of target by using a simple algorithm, weakening the influence of observation error, and accurately estimating

the target motion are crucial tasks in maneuvering target tracking technology [11].

The Wiener filtering method tracks a target on the basis of input signals and noises, and this method has significantly contributed to the application and development of filter theory. The effect of filtering degrades when the priori information deviates from the hypothesis [12]. Widrow and Hoff [13] of the Stanford University proposed the least mean squares adaptive algorithm based on the Wiener filter and Kalman filter (KF) theory and laid the foundation of adaptive filtering theory [14]. Compared with the Wiener filtering, this algorithm can adjust the parameters of the filter by self-learning without knowing the prior information of input signals and noises and can thus obtain optimal estimation. However, the effect of adaptive filtering is difficult to be controlled [15]. Unlike the traditional Wiener filtering and KF algorithms, algorithms based on the least squares criterion, such as the recursive least squares method [16], and QR decomposition of the minimum method, regard the minimum squared error sum as the optimization target. However, the principle of the methods determines that they can only be applied in the estimation or approximation of long-term statistical properties. Singer [17] proposed a time-dependent model (the Singer model) that assumes noises as colored and considers the targeted acceleration to be a uniform time-dependent process, the process is subject to a zero-mean uniform distribution. However, the model causes large errors for maneuvering target, thereby leading to an undesirable result of estimation. The Jerk model algorithm that considers the order of the state vector derivative as the main reason that affects tracking performance, and the Jerk term (acceleration rate) are introduced into a system model to achieve an accurate estimate of acceleration [18]. However, when the input Jerk term is a step transition, the model algorithm produces some definite steady-state errors. The model parameters also cannot be adjusted adaptively with the change in the target maneuverability, thereby affecting the tracking accuracy of the algorithm. The interacting multiple model has been developed to a complete interactive multi-model algorithm on the basis of the generalized pseudo-Bayesian algorithm. The model has also been combined with cubature KF [19] or linear quadratic regulator [20]. To obtain an ideal effect, the model needs a wide range of

maneuvering forms. This requirement means a substantial increase in computing.

The advantages and limitations of the above-mentioned methods are listed in Table 1.

The autoregressive model is a convenient prediction algorithm that describes variables at later times with the linear combination of variables given in advance [21]. The unfiltered information for target obtained by the autoregressive model results in great perturbations. To solve the problem, a computationally fast algorithm for filtering is proposed in this study in consideration of the requirements of timeliness in the avoidance of USV. First, the sampling points of target are fitted as a polynomial curve by using the least squares method to reduce the longitudinal errors. Thereafter, an improved Particle Swarm Optimization (PSO) algorithm is used to fit the horizontal data of sampling position on the basis of the modified curve. A penalty function is introduced in the PSO algorithm to limit the fitting range and thus keep all the modified points in a reasonable area. After the bidirectional fitting, the radar errors can be effectively reduced. The proposed algorithm can be used in the collision avoidance of USVs.

The paper is organized as follows. In Section 1, the autoregressive model is introduced and the problem of the significant effect of detection errors on the accuracy of motion prediction is analyzed. In Section 2, an error mitigation algorithm based on the bidirectional fitting method that uses polynomial and Particle Swarm Optimization [22] is proposed. In Section 3, simulations of trajectory prediction and obstacle avoidance are carried out, and the results are analyzed in detail to verify the effectiveness of the algorithm. Finally, conclusion is remarked in the last section.

PROBLEM FORMULATION

We predict the moving position using the autoregressive model.

We assume that, at moment t , the position of obstacle is $p(t)$, $p = (x \ y)^T$. After the obstacle enters the detection area of radar, the continuous position sequence of this obstacle can be obtained.

Tab. 1. Schematic diagram of mass point

Methods Name	Advantages	Limitations
Wiener filtering method	It can be used in continuous and discrete models	The effect of filtering degrades when the priori information deviates from the hypothesis
Least mean squares (LMS) adaptive algorithm	It can adjust the parameters of the filter by self-learning without knowing the prior information of input signals and noises	The effect of adaptive filtering is difficult to be controlled
Recursive least squares method	It can converge much faster than the LMS algorithm	It can only be applied in the estimation of long-term statistical properties
Singer model	It is a global statistical model and can be used for filtering in various tracking methods	The model causes large errors for high maneuvering target. Inaccurate noise statistics can also cause low precision
Jerk model	It improves the accuracy by adding the jerk dimension to the matrix compared with the single model	The model parameters cannot be adjusted adaptively. It takes more time to stabilize than the single model
Interacting multiple model	It can efficiently adjust the probability of model	It requires a large amount of computation

Given the inertia of moving object, the current position of obstacle is assumed related to its former n positions; this relationship complies with the n -order autoregressive model as follows:

$$p(t) = \sum_{i=1}^n \alpha_i p(t-i) + e(t), \quad (1)$$

where n is the order of the autoregressive model, $e(t)$ is the position prediction error, and α_i is the regression coefficient. The type of regression coefficient depends on the degree of association between two directions of motion target. A scalar α_i enables synchronous alteration between the x and y velocity. A diagonal matrix α_i enables independent alteration between the x and y velocity. If α_i is a two-dimensional matrix, then the x and y velocity are partial interactional.

Considering the motion characteristics of objects at sea, we assume that the acceleration of obstacle changes slowly. This condition can be described using the first-order autoregressive model as follows:

$$a(t) = \beta_i a(t-i) + w(t), \quad (2)$$

where β_i denotes the regression coefficient and $w(t)$ denotes the acceleration prediction error. From the relationship between acceleration and position, we obtain

$$a(t) = p(t) - 2p(t-1) + p(t-2), \quad (3)$$

where $a(t)$ is the acceleration at time t . From Equations (2) and (3), the obstacle position at moment $t+1$ can be expressed as

$$p(t+1) = (2 + \beta_t)p(t) - (2\beta_t + 1)p(t-1) + \beta_t p(t-2) + w(t), \quad (4)$$

During the obstacle avoidance planning of USV, the predictions of target movements in multiple cycles are needed. The obstacle position of step k at moment t is obtained using the mathematical induction method as follows:

$$p(t+k) = p(t) + kv(t) + \left(\sum_{i=1}^k (k+1-i) \prod_{1}^i \beta_{i-1} \right) a(t) \quad (5)$$

where $v(t)$ is the velocity at time t and $v(t) = p(t) - p(t-1)$. To fit the first-order autoregressive model of acceleration by using the least squares method, we assume

$$\beta_i = \left\{ \beta \mid \min \left(\sum_{j=4+i}^{N+j} [a(j) - \beta a(j-1)]^T [a(j) - \beta a(j-1)] \right) \right\} \quad (6)$$

where the function $\min(x)$ is the minimum of x ; N is the number of the foregone motion data, which are used to predict the dynamic positions of obstacle. When the value

of N is large, a large amount of historical data are needed and the effect of pre-movements on the predicted position is significant; this condition is suitable for predicting slow moving objects. When the value of N is small, a small amount of the historical data are needed and the future positions of the obstacle depends mainly on the recent movements of the object; this condition is less constrained by the previous movement and suitable for predicting fast moving objects.

We can find from Equation (5) that, at time t , the predicted difference in positions between two consecutive periods k and $k+1$ is

$$\Delta p(t+k+1) = v(t) + \left(\sum_{i=1}^{k+1} \prod_{1}^i \beta_{i-1} \right) a(t) \quad (7)$$

Equation (7) shows that the difference is closely related to the prediction step k and the acceleration. When the value of k is large, the difference is significant because of the coefficient before $a(t)$. The acceleration of ships at sea often presents a slight change. However, the changes may be significantly magnified with data errors, thereby leading to a remarkable increase in the difference and thus large errors in the multi-step prediction.

A simulation for analyzing the above-mentioned problem is shown in Fig. 1. In the simulation, the obstacle presents an error within the standard range of radar error. The prediction positions are obtained using Equations (5)–(6). The parameters are set as $N=6$ and $k \in [1, 2, 3, 4]$. In particular, no prediction positions are applied at the first six times. Thereafter, six foregone observation positions are needed for prediction, and the first to fourth future positions are forecasted at each moment. The obstacle moves from the left corner. Even in the case of small disturbance of the observed data, the prediction results do not maintain motion inertia but show a great fluctuation. Specifically, when the value of k is large, the difference between the predicted position and the actual position is significant. The effect is highly pronounced when the trajectory changes in a large degree.

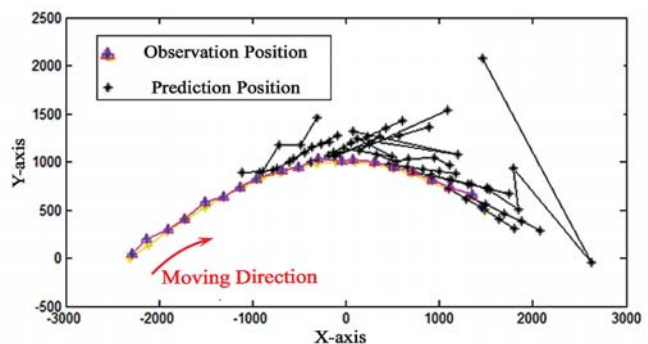


Fig. 1. Obstacle trajectory prediction with observation error

We conclude from the theoretical derivation and simulation results above that, if the observation error of obstacle is ineffectively reduced, then the accuracy of motion prediction cannot be guaranteed and thus the collision avoidance planning of USV may fail. Therefore, the observed

data should be modified to reduce the acceleration change caused by radar errors and obtain a smooth trajectory that is close to the actual one.

ERROR MITIGATION METHOD BASED ON POLYNOMIAL AND PSO

Considering the radar observation error, the obstacle observation position is randomly distributed within the circle with $r_error = 30$, as specified by IMO. We select N sampling coordinates from the obstacle observation data at moment t by a sampling period of $T_p(k)$. The value of $T_p(k)$ is given as follows:

$$T_p(k) = \left\lfloor \frac{R_w}{10 \max(\mathbf{v}_k)} \right\rfloor T \quad (8)$$

where R_w is the radius of the radar observation scope and T is the observation period of the radar. \mathbf{v}_k is the relative velocity set of various periods between the USV and the k th obstacle. In particular, $\mathbf{v}_k = \{\mathbf{v}_{k,1}, \mathbf{v}_{k,2}, \dots, \mathbf{v}_{k,n}\}$. The mathematical symbol $\lfloor x \rfloor$ indicates that the real x is rounded down. Equation (8) shows that $T_p(k)$ is a positive integer multiple of T , and the value of T_p differs with different obstacles. When the radar scanning cycle is short and the relative speed of USV and obstacle is relatively small, the radar observation errors may misalign the observation positions of obstacles in several near scanning cycles T . As a result, the motion of obstacles can be difficult to detect and the errors can be difficult to distinguish and eliminate. Ultimately, the trajectory prediction of obstacles becomes difficult. Thus, the prediction period $T_p(k)$ is adopted for reasonably increasing the data sampling period and improving the accuracy of error elimination.

Given that the polynomial fitting is unidirectional, a local coordinate system $x'Oy'$ is established with N sampling points. The error mitigation is performed in the local coordinate system, and the coordinate conversion is expressed as

$$\begin{bmatrix} x' \\ y' \end{bmatrix} = \begin{bmatrix} \cos(\alpha) & \sin(\alpha) \\ -\sin(\alpha) & \cos(\alpha) \end{bmatrix} \begin{bmatrix} x \\ y \end{bmatrix} \quad (9)$$

where α is the rotation angle between the local coordinate system and global coordinate system.

1. Error mitigation in vertical coordinates with polynomial fitting method.

We fit the sampling points (x', y') with the polynomial as follows:

$$p_n(x'_i) = a_0 + a_1 x'_i + a_2 x'^2_i + \dots + a_k x'^k_i \quad (10)$$

where p_n is the function of the polynomial fitting curve; $a_0, a_1, a_2,$ and a_k are the coefficients of the function. The least squares method is used in the fitting.

The value of the polynomial coefficients can be obtained by solving the extreme of I in the following equation:

$$I = \sum_{i=0}^m [p_n(x'_i) - y'_i]^2 = \sum_{i=0}^m \left[\sum_{k=0}^n a_k x'^k_i - y'_i \right]^2 \quad (11)$$

The points on the curve are fitted using the polynomial method by changing their ordinate values, and the corresponding abscissa values remain unchanged. Thus, the sampling error on y axis only is decreased.

2. Error mitigation in abscissa coordinates with PSO

Sampling data are selected on the fitting curve by using the sampling period of T_p . The early movement of obstacle slightly affects the position prediction. Thus, we set $N=4$ and the sampling positions

$$P_n'' = \{p''(t-3T_p), p''(t-2T_p), p''(t-T_p), p''(t)\},$$

$$p'' = \begin{pmatrix} x' \\ y'' \end{pmatrix}$$

At moment t , we regard the ordinate values of $p''(t-2T_p)$ and $p''(t-T_p)$ as a two-dimensional particle $(x'_{t-2T_p}, y'_{t-2T_p})$ and the corresponding y values $(y'_{t-2T_p}, y'_{t-2T_p})$ are obtained using the polynomial fitting curve function $y'' = p_n(x')$. The distance between the calculated point $(x'_{t-2T_p}, y'_{t-2T_p})$ and the observed position of $p'(t-2T_p)$ is denoted as d_{t-1} , and the distance between the calculated point $(x'_{t-2T_p}, y'_{t-2T_p})$ and the observed position of $p'(t-T_p)$ is denoted as d_{t-2} .

The fitness function in the PSO model to solve the optimal particle $(x'_{t-T_p}, y'_{t-2T_p})$ is as follows:

$$fit() = \begin{cases} \Delta a(t)^2 & \max(\mathbf{H}) = 0 \\ \max(\mathbf{H})^2 & \text{else} \end{cases} \quad (12)$$

where $fit()$ means the function of optimization goal and $\Delta a(t)$ is the acceleration jerk at time t .

$$\mathbf{H} = \{h_{t-1}, h_{t-2}\}, \quad (13)$$

where

$$h_i = \begin{cases} \frac{d_i}{r_error} & d_i > r_error \\ 0 & \text{else} \end{cases} \quad (14)$$

In Equation (14), $i = t-1, t-2$.

Moreover, H is a penalty function and reflects the effect of d_{t-1} and d_{t-2} .

From Equations (12)–(14), we can find that the fitness function aims to obtain a minimal amount of change in

acceleration $\Delta a(t)$ after the correction of the middle two sampling positions. When the fitting point is within the range of the observation error, the penalty function is set as 0; otherwise, a penalty function that is associated with the above-mentioned differences can be added to the fitness function. Fig. 2 shows that, after the best particle $(x'_{t-T_p}, x'_{t-2T_p})$ is obtained, the optimal $p(t-2T_p)$ and $p(t-T_p)$ are obtained from the polynomial fitting curve function.

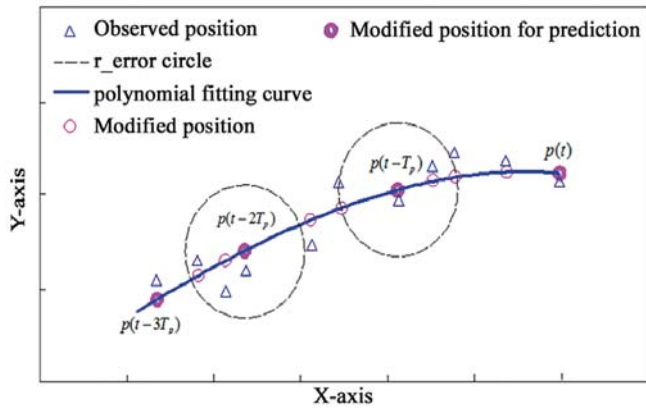


Fig. 2. Error mitigation in x axis with PSO

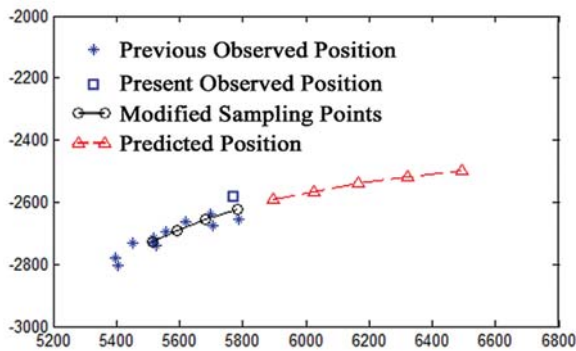
The bidirectional fitting method shows that, after the error mitigation on both axes, all of the modified trajectory points are within the radar accuracy error range with a high possibility and are within the curve by polynomial fitting. As a result, the change in acceleration is decreased and the prediction accuracy of obstacle position is high.

SIMULATION

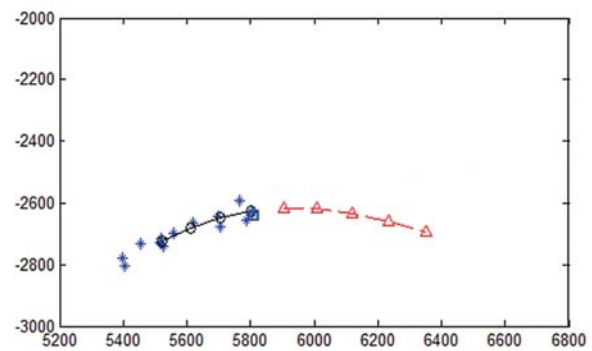
We perform two simulations for predicting the trajectory of obstacle during its slow or fast change in movement by using the proposed method. In each simulation, the prediction is processed in two continuous periods. A new observed point appears in the second period. The calculation parameters are set as $N=4$ and $k=5$. The symbol meanings are presented in Fig. 3(a).

Figs. 3 and 4 show that, regardless of the slow or fast change in movement of obstacle, both trajectories predicted on the basis of the optimized sampling points maintain motion inertia. The results clearly indicate the moving trend of the obstacle and show the effectiveness of the method in error mitigation.

1) Simulation for minor motion change situation



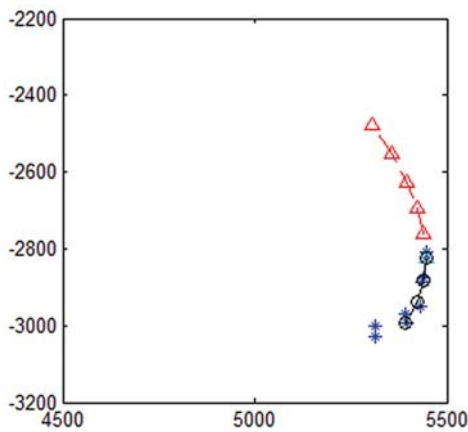
(a) Period 1



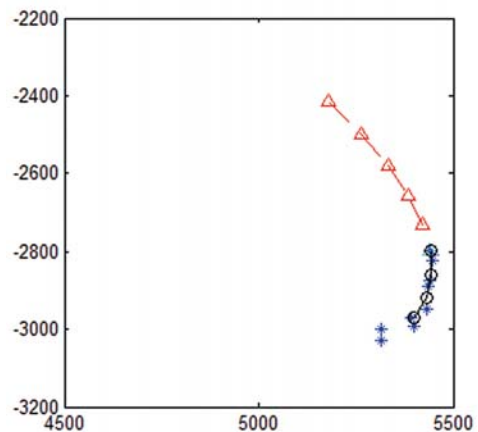
(b) Period 2

Fig. 3. Trajectory prediction during slow change in movement of obstacle

2) Simulation for major motion change situation



(a) Period 1



(b) Period 2

Fig. 4. Trajectory prediction during fast change in movement of obstacle

The prediction is conducted in advance. The errors in prediction are magnified, and the inertia reflected in two periods presents a certain gap. The reason is that the new observed point in the second period provides information that is unavailable in the first period.

3) Simulation of collision avoidance

To test the effect of error mitigation on the avoidance of obstacle, we simulate the collision avoidance of a USV with the Velocity Obstacle (VO) method under MATLAB [23]. In the method, a velocity model between the USV and obstacles is established by the spatial relationship of the position and velocity. The VO method is a collision avoidance algorithm that relies sufficiently on the accuracy of obstacle position and velocity.

In this simulation, the initial position of the USV is (0, 0). The initial position of three obstacles are (1500, -500), (2000, 500), and (6000, -500). The target point is set at (6500, -800). The unit is meter. The obstacles change their speeds and courses randomly. Fig. 5 illustrates the initial headings of four boats. The circles around obstacles indicate the ship domains (the radius of the domain is set to 230 in the simulations), which are used to represent the area of an obstacle that should be avoided.

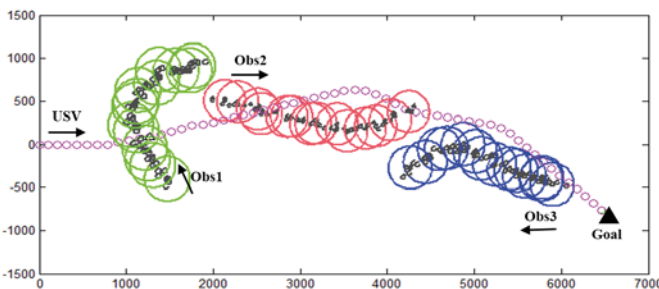


Fig. 5. Simulation of the collision avoidance for unknown dynamic obstacles with error mitigation method

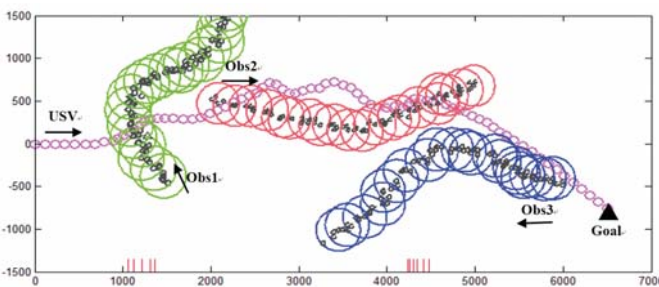


Fig. 6. Simulation of the collision avoidance for unknown dynamic obstacles without error mitigation method

Tab. 2. Correlation data of simulation with and without the error mitigation method

	With the error mitigation method	Without the error mitigation method
Times that the USV enters the domains of obstacles	0	11
Time required to obtain the goal (Unit: period T)	59	85

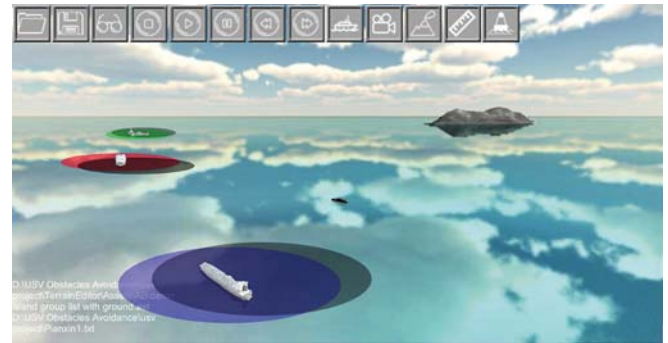


Fig. 7. 3D simulation of the collision avoidance of USV

As shown in Figs. 5 and 6, the observed trajectories of obstacles fluctuate throughout the entire process of collision avoidance, thereby increasing the difficulties in avoidance.

The short red line at the bottom of Fig. 6 shows that, when the USV reaches the abscissa value during the simulation owing to inefficient avoidance, the USV enters into the domain of the obstacle, which is a dangerous situation.

Table 2 shows that no USV enters into the domains of obstacles when the error mitigation method is adopted. By contrast, this situation occurs 11 times when the error mitigation method is not applied, thereby indicating that the avoidance effect is poor.

By comparing the trajectories of the USVs in the two simulations, a frequent fluctuation is observed in the direction and speed of the USV without using the error mitigation method. This finding is due to the unbalanced movement of the obstacles and the existence of observation errors, which may seriously affect the collision avoidance. As shown in Fig. 5, the path of the USV is smooth, because its collision avoidance is based on the modified trajectory of obstacle after error mitigation.

Table 2 also shows the advantage of the error mitigation method in improving collision avoidance efficiency. When using the error mitigation method, the USV takes only 59 cycles to avoid obstacles and reach the goal. On the contrary, the USV without using the error mitigation method requires 85 cycles to complete the same task.

Fig. 7 shows the real-time 3D simulation of collision avoidance with the error mitigation method. In the figure, the obstacle detected is the real position of the obstacle, the gray circle indicates the obstacle domain observed by the radar, and the corresponding colored circle is the obstacle domain after correction. A large deviation exists between the observed and real positions of the obstacle as a result of the existence of radar errors. This deviation may affect the efficiency of collision avoidance of the USV. After adopting the correction algorithm, the domain of the obstacle corresponds to its real position, indicating that the observation errors are effectively eliminated. This simulation can provide a clear insight into the avoidance process of USVs in a real-world environment. The finding indicates the accuracy of the proposed method in predicting obstacle motion.

The trajectory prediction and obstacle avoidance simulations indicate that the bidirectional fitting method

substantially eliminates the observation errors of radar and shows the validity and reliability of the proposed method in obstacle avoidance planning.

CONCLUSION

First, we analyze the motion prediction error caused by observation accuracy by using the autoregressive prediction model. Then, an error mitigation algorithm based on polynomial fitting and PSO is proposed to effectively improve the prediction precision. The polynomial method is used to fit the observed path points for eliminating the longitudinal error, and the PSO algorithm is used to correct the fitting points for eliminating the horizontal error of the observed data. The effectiveness of the bidirectional fitting algorithm in error mitigation is verified by trajectory prediction simulations. Moreover, a simulation on collision avoidance is carried out using the proposed method combined with the VO method. The results show the validity and reliability of the algorithm in collision avoidance.

ACKNOWLEDGMENT

This work is supported by the National Natural Science Foundation of China (Grant No. 51809203 and 51709214) and the Fundamental Research Funds for the Central Universities (WUT: 2017IVA008 and 2017IVA006).

REFERENCES

1. Li W. F., Ma W. Y., *Simulation on Vessel Intelligent Collision Avoidance Based on Artificial Fish Swarm Algorithm*. Polish Maritime Research, 2016, 23:138–143.
2. Campbell S., Naeem W., Irwin G. W., *A review on improving the autonomy of unmanned surface vehicles through intelligent collision avoidance maneuver*. Annual Reviews in Control, 2012, 36(2):267–283.
3. Larson J., Bruch M., Halterman R., Rogers J., Webster R., *Advances in Autonomous Obstacle Avoidance for Unmanned Surface Vehicles*. Space and Naval Warfare Systems Center, San Diego, CA, 2007.
4. U.S. department Homeland Security/U.S. Coast Guard, "Navigation Rules," Paradise Cay Publications, 2010.
5. Kim, H., Park, B., Myung, H., *Curvature path planning with high resolution graph for unmanned surface vehicle*. Robot Intelligence Technology and Applications, 2013, 208:147–154.
6. Riccardo P., Sanjay S., Jian W., Andrew M., Robert S., *Obstacle Avoidance Approaches for Autonomous Navigation of Unmanned Surface Vehicles*. Journal of Navigation, 2017, 71(1): 1–16.
7. Kuwata Y., Wolf M. T., Zarzhitsky D., Huntsberger T. L., *Safe maritime autonomous navigation with COLREGS, using velocity obstacles*, IEEE Journal of Oceanic Engineering, 2014, 39(1):110–119.
8. Zhao Y. X., Wang L., Peng Sh., *A real-time collision avoidance learning system for Unmanned Surface Vessels*. Neurocomputing, 2016, 182:255–266.
9. Park J. H., Kim J. W., Son N. S., *Passive target tracking of marine traffic ships using onboard monocular camera for unmanned surface vessel*. Electronics letters, 2015, 51(31):987–989.
10. Wang H., Mou, X. Zh., Mou W., *Vision based Long Range Object Detection and Tracking for Unmanned Surface Vehicle*. Proceedings of the 2015 7th IEEE International Conference on Cybernetics and Intelligent Systems and Robotics, Automation and Mechatronics, Cambodia, 2015:101–105.
11. Lazarowska A., *Swarm Intelligence Approach to Safe Ship Control*. Polish Maritime Research, 2015, 22(4): 34–40.
12. Zhong K., Lei X., Li SQ., *Wiener filter preprocessing for OFDM systems in the presence of both nonstationary and stationary phase noises*. EURASIP Journal on Advances in Signal Processing, 2013(7):1–9.
13. Widrow B., Hoff M., *Adaptive switch circuits*. IRE Wescom, Conversion Record, Part 4, 1966:96–104.
14. Wang X., Liu J. H., Zhou Q. F., *Real-Time Multi-Target Localization from Unmanned Aerial Vehicles*. Sensors, 2016, 17(1):33–43.
15. Dichev D., Koev H., Bakalova T., *An Algorithm for Improving the Accuracy of Systems Measuring Parameters of Moving Objects*, Metrology and Measurement Systems, 2016, 23(4):555–565.
16. Borodachev S. M., *Recursive Least Squares Method of Regression Coefficients Estimation as a Special Case of Kalman Filter*. International Conference on Numerical Analysis and Applied Mathematics, Rhodes, 2015:23–29.
17. Singer R. A., *Estimating Optimal Tracking Filter Performance for Manned Maneuvering Targets*, IEEE Transaction on Aerospace and Electronic Systems, 1970, 6(4):473–483.
18. Zhou Zh., Liu J. M., Tan X. J., *MCS Model Based on Jerk Input Estimation and Nonlinear Tracking Algorithm*. Journal of Beijing University of Aeronautics and Astronautics, 2013, 39(10): 1397–1402.
19. Zhu W., Wang W., Yuan G., *An Improved Interacting Multiple Model Filtering Algorithm Based on the Cubature Kalman Filter for Maneuvering Target Tracking*. Sensors, 2016, 16(6): 805–815.

20. Afshari H. H., Al-Ani D., Habibi S., *A New Adaptive Control Scheme Based on the Interacting Multiple Model (IMM) Estimation*. Journal of Mechanical Science & Technology, 2016, 30 (6):2759–2767.
21. Jin B., Jiu B., Su T., *Switched Kalman Filter-Interacting Multiple Model Algorithm Based on Optimal Autoregressive Model for Manoeuvring Target Tracking*. IET Radar Sonar and Navigation, 2015, 9(2): 199–209.
22. Yousef, M. T., Ali, H. E. I., Habashy, S. M., *Adaptive Controller based PSO with Virtual Sensor for Obstacle Avoidance in Dynamic Environments*, Radio Science Conference, 2014, 228–235.
23. Liu Y. Ch., Bucknall R., *Path Planning Algorithm for Unmanned Surface Vehicle Formations in a Practical Maritime Environment*, Ocean Engineering, 2015, 97:126–144.

CONTACT WITH THE AUTHOR

Lifei Song

e-mail: songlifei@whut.edu.cn

School of Transportation
Wuhan University of Technology
Heping Avenue No.1178
430063 Wuhan
CHINA

Zhuo Chen

e-mail: 1304972779@qq.com

Key Laboratory of High Performance Ship Technology
Wuhan University of Technology
Ministry of Education
Heping Avenue No.1178
430063 Wuhan
CHINA

Yunsheng Mao

e-mail: ysmao@163.com

Key Laboratory of High Performance Ship Technology
Wuhan University of Technology
Ministry of Education
Heping Avenue No.1178
430063 Wuhan
CHINA

Zaopeng Dong

e-mail: naval_architecture@163.com

Key Laboratory of High Performance Ship Technology
Wuhan University of Technology
Ministry of Education
Heping Avenue No.1178
430063 Wuhan
CHINA

Zuquan Xiang

e-mail: xiangzuquan@whut.edu.cn

Key Laboratory of High Performance Ship Technology
Wuhan University of Technology
Ministry of Education
Heping Avenue No.1178
430063 Wuhan
CHINA

ADAPTIVE SLIDING MODE CONTROL FOR SHIP AUTOPILOT WITH SPEED KEEPING

Zhiquan Liu

Shanghai Maritime University, Shanghai, China

ABSTRACT

The paper addresses an important issue in surface vessel motion control practice that the ship dynamics and sailing performance can be affected by speed loss. The vessel speed is significantly decreased by the added resistance generated by waves. An adaptive sliding mode course keeping control design is proposed which takes into account uncertain ship dynamics caused by forward speed variations, while avoiding performance compromises under changing operating and environmental conditions. The sliding mode control provides robust performance for time-varying wave disturbances and time-varying changes in ship parameters and actuator dynamics. After combining the unknown but bounded system uncertainties, the design of the adaptation law is obtained which is based on the Lyapunov's direct method. Simulations on a ship with two rudders illustrate the effectiveness of the proposed solution.

Keywords: surface vessel; speed loss; adaptive control; course keeping; sliding mode control

INTRODUCTION

When a ship sails in a seaway, its maneuvering characteristics may be strongly affected by the ocean environment (i.e. waves, winds and currents). These environmental disturbances usually affect the ability of the ship to perform its mission, they may also cause cargo damage and produce variations of motion. The marine autopilot system is used to ensure sailing safety and to make the vessel navigate in the path by manipulating the rudder. The first autopilot mechanism was constructed in 1911, and the detailed theoretical analysis of proportional integral derivative (PID) controller for ship steering was presented by Nicholas Minorsky in 1922, when the yaw angle measurement was achieved using a gyrocompass [1]. The PID controller with fixed parameters can reveal good performance in particular operating conditions. However, the vessel dynamics can be affected by sailing conditions and external disturbances, i.e. loading, trim, forward speed and/or course variations, and the change of water depth under keel, which can decrease the quality of control of an autopilot with fixed gain.

Modern steering control systems focus on stability and performance robustness under the condition of uncertainties. The adaptive control probably stays as a good method to deal with this issue. The literature on ship autopilot control using adaptive and robust algorithms is widely surveyed, and a lot of studies have been published. In the area of the surface vessel path tracking control problem, the adaptive and backstepping techniques are combined to deal with unknown parameters and bounded time-varying external disturbances [2]. Zhang et al. [3] developed an adaptive neural network (NN) algorithm to capture system uncertainties and bounded wave disturbances under the condition of the unknown information on hydrodynamic structure. Shojaei [4] proposed a saturated tracking controller with NN and adaptive techniques to take into account unmodeled dynamics and to reduce the risk of actuator saturation. The above three methods are based on the passive bounded stable theory [5]. Peng et al. [6] developed two types of adaptive control methods, employing NNs and the DSC algorithm to track formations of autonomous surface vehicles. For course keeping of surface vessels, Do et al. [7] used the Lipschitz continuous projection

algorithm to estimate uncertainties which allowed to achieve the purpose of adaptive dynamics. Li et al. [8] adopted T-S fuzzy rules to deal with the model uncertainty problem for a nonlinear vehicle system. Kahveci and Ioannou [9] combined the adaptive law and the linear Quadratic (LQ) controller for uncertain ship dynamics with input constraints. The recurrent wavelet NN was employed as adaptive backstepping method to approximate the ideal backstepping law, and then to achieve a robust adaptive marine course changing control system [10]. For underwater vehicles, an adaptive robust controller was proposed for autonomous underwater vehicles (AUV) under changing operating conditions [11]. Do et al. [12] combined the backstepping and parameter projection methods to design a robust adaptive controller for AUV path following. An adaptive fuzzy NN method was introduced for trajectory tracking of an unmanned underwater vehicle (UUV) subject to stochastic bounded disturbances and parameter uncertainties [13].

Ships which advance with certain speed in open sea usually encounter large rate of motions due to ocean disturbances. Consequently, the total water resistance is increased by the added resistance, which may result in speed reduction and energy loss [14]. There is a survey that the magnitude of the added resistance is approximately equal to 10%–30% of the resistance in still water [15]. This added resistance worsens fuel efficiency and energy conservation, which are important issues from the commercial standpoint driven by business requirements in the marine industry [16]. In the area of ship motion control, the related work about the relationship between rolling and added resistance have been done by Liu and Jin [17]. They provided a practical PID method to design an optimal added resistance fin stabilizer controller. Yawing motion also increases the added resistance in waves, like the yawing motion caused by steering in still water [18]. Akinal [19] developed a kind of fuel saving steering control method to minimize propulsion losses. Grimble and Katebi [20] extended the LQG controller to minimize the energy loss caused by the added resistance induced by steering in ship course keeping control. Milon and Pachter [21] considered speed reduction in the collision avoidance control system. Kim et al. [22] studied ship's speed variations under different rudder controllers. The results recorded by them show that the ship speed in regular waves may be improved by decreasing the rudder rotation speed. Liu et al. [23] considered the resistance increase both in waves and in still water, and addressed a rudder roll stabilization (RRS) controller with speed reduction minimization. The control system designs presented in all above works act only under the condition of the ship moving with certain speed and ship dynamics unaffected by speed changes. However in practice, model parameter changes of the ship sailing in open seas are observed due to changes in ship speed. The forward speed is time varying because of the speed loss, which may lead to changes in vessel dynamics and control parameters. This paper aims to develop an adaptive ship autopilot controller with forward speed maintenance, which will consider unknown stochastic wave disturbances and parameter uncertainties caused by ship speed reduction.

The remaining part of the paper is organized as follows. Section 2 introduces the mathematical model, while the control algorithms are presented in Section 3. Simulation results are discussed in Section 4 and conclusions are drawn in Section 5.

Notations. Let \bullet be a scalar, a vector, or a matrix. $\|\bullet\|$ denotes the Euclidean norm when it is a vector or a matrix. $|\bullet|$ denotes the absolute value when it is a scalar.

PROBLEM FORMULATION

MATHEMATICAL MODEL OF SHIP

The model of ship sway-yaw dynamics has been introduced by Perez [25]. The main parameters of the ship are listed in Table 1.

$$m(\dot{v} + ur) + mx_G \dot{r} = Y_{\text{hyd}} + Y_c \quad (1)$$

$$mx_G(\dot{v} + ur) + I_{zz} \dot{r} = N_{\text{hyd}} + N_c \quad (2)$$

where m is the ship mass, I_{zz} is the inertia of the ship along the z-axis, and x_G is the coordinate of the center of gravity with respect to the body fixed frame. Surge and sway velocity components are denoted by u and v , respectively. ψ and r are the yaw angle and the yaw rate, while Y and N are the sway force and the yaw moment, respectively. Subscript hyd and c refer to the hydrodynamic term and to the control force produced by the actuator, respectively.

Tab. 1. Main parameters of the ship

Length (m)	52.50
Breadth (m)	8.80
Draft fore (m)	2.32
Draft aft (m)	2.26
Displacement volume (m ³)	355.88
Keel to transverse metacenter (m)	4.83
Keel to buoyancy (m)	3.34
Rudder area (m ²)	1.50

The hydrodynamic model equations are given as follows:

$$Y_{\text{hyd}} = Y_{\dot{v}} \dot{v} + Y_{\dot{r}} \dot{r} + Y_{|u|v} |u|v + Y_{ur} ur + Y_{v|v|} v|v| + Y_{v|r|} v|r| + Y_{r|v|} r|v| \quad (3)$$

$$N_{\text{hyd}} = N_{\dot{v}} \dot{v} + N_{\dot{r}} \dot{r} + N_{|u|v} |u|v + N_{|u|r|} |u|r + N_{r|r|} r|r| + N_{r|v|} r|v| \quad (4)$$

The rudder is the actuator used for heading control. The corresponding control forces are written as:

$$Y_c = L_r = \frac{1}{2} \rho A_R C_L(\delta) U^2 \quad (5)$$

$$N_c = L_r LCG \quad (6)$$

where ρ is the water density, L_r and A_R are the lift force and the area of the rudder, respectively. $C_L(\bullet)$ denotes the lift coefficient which varies with the rudder angle δ . LCG is the distance from the center of gravity to the rudder stock.

Assumption 1. The position and rate measurements of the sway and yaw motions of the ship are available for feedback.

Assumption 2. The ship parameters and added masses: m , I_z , $Y_{\dot{v}}$, $Y_{\dot{r}}$, $N_{\dot{v}}$, $N_{\dot{r}}$ are known. The nonlinear damping coefficients: $Y_{|u|v}$, Y_{ur} , $Y_{v|r}$, $Y_{v|v}$, $Y_{r|r}$, $N_{|u|v}$, $N_{|u|r}$, $N_{r|r}$, $N_{v|v}$ are also known, but the ship dynamics (damping matrix in the ship state-space model) depend on the ship forward speed.

Assumption 3. The ship control system based on the state-space model starts with the initial value of all parameters equal to zero.

Assumption 4. The surge dynamics is much slower than that in other motions, consequently the variable u is assumed equal to the ship moving speed U and satisfies: $0 < u_{\min} \leq |u(t)| \leq u_{\max}$ and $|\dot{u}(t)| \leq \dot{u}_{\max}$.

Assumption 5. The ship forward speed $U(t) = U_0 + \Delta U$ is time varying, where U_0 is the nominal (design) speed and ΔU is the time-varying speed loss which is unknown but bounded.

Remark 1. Several software packages and identification methods can be used to calculate or estimate ship parameters and added masses. For nonlinear damping terms, Perez [24] has modified the data of the selected vessel to match the load condition and main particulars. The main purpose in this paper is to study the effect of actual speed on ship dynamics and performance. Therefore, Assumption 3 is justified.

Remark 2. Assumption 5 means that the ship forward speed is nonzero and does not change sign.

Remark 3. In this paper, the calculation method presented by Liu et al. [23] is used to calculate the actual forward speed U and the speed loss ΔU .

The ship response to the control action is modelled using the linear model and assuming that $Y_c = Y_\delta \delta$ and $N_c = N_\delta \delta$. Then the model is expressed as:

$$(m - Y_{\dot{v}})\dot{v} + (mx_G - Y_{\dot{r}})\dot{r} = Y_{|u|v} Uv + Y_{ur} Ur - mUr + Y_\delta \delta \quad (7)$$

$$(mx_G - N_{\dot{v}})\dot{v} + (I_{zz} - N_{\dot{r}})\dot{r} = N_{|u|v} Uv + N_{ur} Ur - mx_G Ur + N_\delta \delta \quad (8)$$

Let us define the state-space model describing the ship linear heading control system. The unified model can be written using equations (7) and (8) as

$$\mathbf{M}\dot{\mathbf{v}} = \mathbf{D}(U)\mathbf{v} + \mathbf{H}(U)\delta \quad (9)$$

where the system states can be defined as $\mathbf{v} = [v, r, \psi]^T$, and the other matrices can be further represented as

$$\mathbf{M} = \begin{bmatrix} m - Y_{\dot{v}} & mx_G - Y_{\dot{r}} & 0 \\ mx_G - N_{\dot{v}} & I_z - N_{\dot{r}} & 0 \\ 0 & 0 & 1 \end{bmatrix} \quad (10)$$

$$\mathbf{D}(U) = \begin{bmatrix} Y_{|u|v} U & (Y_{ur} - m)U & 0 \\ N_{|u|v} U & (N_{|u|r} - mx_G)U & 0 \\ 0 & 0 & 1 \end{bmatrix} \quad (11)$$

$$\mathbf{H}(U) = \begin{bmatrix} 1 \\ -LCG \\ 0 \end{bmatrix} \frac{1}{2} \rho A_R U^2 \left. \frac{\partial C_L}{\partial \delta} \right|_{\delta=0} \quad (12)$$

It should be mentioned that the parameters in the damping matrix $\mathbf{D}(U)$ and in the control force matrix $\mathbf{H}(U)$ vary with the forward speed. Consequently, the dynamics of the ship and the actuator will be affected by the speed loss. This problem should be considered in the control system design addressed in the next section.

MATHEMATICAL MODEL OF WAVES

In this study, the long-crest wave spectrum model recommended by ITTC is utilized to simulate the waveforms of random waves. The desired spectrum model is given as:

$$S(\omega_i) = \frac{173H_{1/3}}{T^4 \omega_i^5} \exp\left(-\frac{691}{T^4 \omega_i^4}\right) \quad (13)$$

where $H_{1/3}$ is the significant wave height, T is the wave period, and ω_i is the frequency of the i^{th} regular wave component.

To simulate random waves in the time domain, 60 regular waves were selected to form the irregular wave. The amplitude ζ_i of each regular wave component and the amplitude ζ of the resultant wave used to generate external forces and moments are given by the following expressions:

$$\zeta_i = \sqrt{2S(\omega_i)\Delta\omega} \quad (14)$$

$$\zeta = \sum_{i=1}^{60} \zeta_i \cos(\omega_i t + \varepsilon_i) \quad (15)$$

where ε_i is the random phase angle of the i^{th} regular wave.

Assumption 6. The disturbance signals of sway and yaw motions satisfy $|d_v(t)| \leq d_{v\max}$ and $|d_r(t)| \leq d_{r\max}$, where $d_{v\max}$ and $d_{r\max}$ are unknown positive constants.

ADDED RESISTANCE

The added resistance is independent of the calm water resistance. In this study, the added resistance produced by ship motions both in waves and in still water are considered.

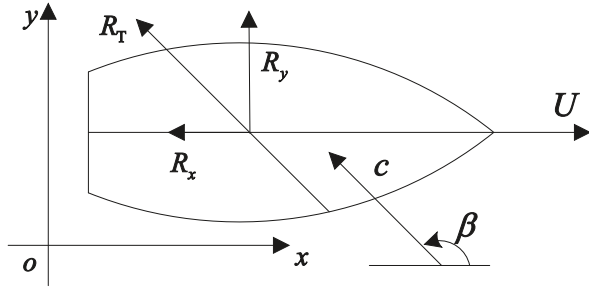


Fig. 1. Definition of added resistance and drift force

The method to calculate the added resistance in oblique waves is the extension of the radiated energy method proposed by Loukakis and Scavounos [25]. In Fig. 1, the ship is moving forward along a fixed direction. The waves are coming with propagation speed c at the encounter angle β . The horizontal force R_T can be resolved into two components: the added resistance R_x and the drift force R_y .

According to the radiated energy theory, the work of the added resistance is assumed to equate the energy of waves radiated away per wave period. With the strip theory approximations, the work of the horizontal force can be equated to the energy radiated away per encounter period. Consequently, the work passed to the fluid is given as follows:

$$P = (-R_T)(-c - U \cos \beta)T_e \quad (16)$$

where T_e is the encounter period.

Since the actuator is the rudder and only horizontal motions are included in this study, then the energy radiated by the horizontal motions are given by the following equations:

$$P_4 = \frac{\pi}{\omega_e} \int_L b_4 |p|^2 dx \quad (17)$$

$$P_{24} = P_{42} = \frac{\pi}{\omega_e} \int_L b_{24} |p U_{RY}| dx \quad (18)$$

$$P_{26} = \frac{\pi}{\omega_e} \int_L b_{26} |U_{RY}|^2 dx \quad (19)$$

where ω_e is the encounter frequency, L is the ship length, b is the motion damping coefficient, and the numerical subscripts represent their corresponding DOFs. U_{RY} is the transverse relative speed. Finally, the added resistance and the drift force in oblique waves can be written as:

$$(-R_T)(-c - U \cos \beta)T_e = P_4 + 2P_{24} + P_{26} \quad (20)$$

$$|R_x| = |R_T \cos \beta| \quad (21)$$

$$|R_y| = |R_T \sin \beta| \quad (22)$$

where P_4 , P_{24} and P_{26} are the energy amounts radiated by roll motion, yaw-roll motion, and sway-yaw motion, respectively, during one encounter period. The roll motion is not included when calculating the added resistance.

When the ship sails in calm water, the yaw angle caused by steering will produce pressure difference between its port and starboard sides. This kind of pressure difference creates extra resistance, referred to as the added resistance in calm water, discussed by Faltinsen [18].

The surge model in the body fixed frame is given as:

$$M(\dot{u} - vr) = X_{\dot{u}}\dot{u} - R_T(u) + (1 - \tau)T(u, n) + X_{vv}v^2 + X_{vr}vr + X_{rr}r^2 + X_{\delta\delta}\delta^2 \quad (23)$$

where $X_{\dot{u}}$, X_{vv} ,... are used to express longitudinal hydrodynamic forces acting on the hull and on the rudder. $R_T(u)$ is the ship calm resistance, τ is the thrust deduction coefficient, and $T(u, n)$ is the propeller revolutions per second.

The main cause of resistance increase is represented by Mvr and $X_{vr}vr$, while $R_T(u)$ and $T(u, n)$ are independent of the turning motion. The values of X_{vv} and X_{rr} are equal to zero when the surface vessel is symmetrical. The term $X_{\delta\delta}\delta^2$ is the extra drag due to rudder angle and can be neglected because of its small value.

Finally, the added resistance caused by yaw motion can be simplified to the form:

$$R_{yaw} = (M + X_{vr})vr \quad (24)$$

where M is the ship mass. This resistance is decided by sway rate and yaw rate.

CONTROL SYSTEM

The total speed loss in the heading control system is determined by the sway rate v and the yaw rate r . In the meanwhile, the heading error must be limited, therefore the three variables v , r , and ψ should be simultaneously constrained. The proposed autopilot system is shown in Fig. 2. Here, ψ_d is the desired heading angle and d is the external disturbance. The other desired values are set equal to zero. The saturation block is adopted to constrain the rudder angle amplitude.

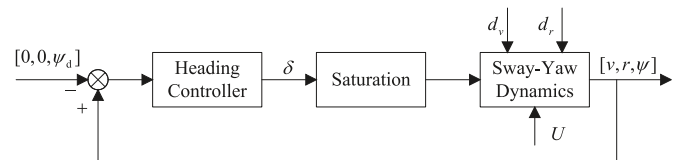


Fig. 2. The autopilot control system

The sliding mode control (SMC) used here can accommodate system parameter uncertainties and reject unknown bounded disturbances, as well as quantify the modeling and performance trade-off. Liu et al. [23] adopted the SMC method to design an RRS control system with forward speed minimization which assumed U as a constant design speed in the ship model. However, the actual forward speed varies in the time domain due to speed losses, which can cause uncertainties in the dynamics of ship and actuator,

and, consequently, decrease the robustness of the SMC. To improve the performance of the controller when the speed is time varying, an adaptive sliding mode control (ASMC) method has been selected. The following sections present the design process of the two controllers.

SLIDING MODE CONTROL DESIGN

In this section, the eigenvalue decomposition method is applied to provide an appropriate scheme to select weighting factors for the sliding surface function [1]. Assuming that the ship dynamics parameters are not affected by speed loss, the value of the parameter U in the ship model is equal to the nominal speed U_0 . After combining the wave disturbance terms, the state-space model (9) is transformed to the form:

$$\dot{\mathbf{x}} = \mathbf{A}\mathbf{x} + \mathbf{b}\delta + \mathbf{d}$$

where \mathbf{d} is bounded as $\|\mathbf{d}\| \leq d_{\max} < \infty$, and the detailed description is regarded as follows:

$$\begin{bmatrix} \dot{v} \\ \dot{r} \\ \dot{\psi} \end{bmatrix} = \begin{bmatrix} a_{11} & a_{12} & 0 \\ a_{21} & a_{22} & 0 \\ 0 & 1 & 0 \end{bmatrix} \begin{bmatrix} v \\ r \\ \psi \end{bmatrix} + \begin{bmatrix} b_1 \\ b_2 \\ 0 \end{bmatrix} \delta + \begin{bmatrix} d_v \\ d_r \\ 0 \end{bmatrix} \quad (25)$$

By choosing a suitable control law, the sliding manifold is used in the state error space to find the relationship for each control element. Let the reference state be $\mathbf{x}_d = [0, 0, \psi_d]^T$, and the sliding surface be defined as:

$$s = \mathbf{h}^T \mathbf{x}_e = \mathbf{h}^T (\mathbf{x} - \mathbf{x}_d) \quad (26)$$

where $\mathbf{h} = [h_1, h_2, h_3]^T$ is the right eigenvector of \mathbf{A}_c (i.e. $\mathbf{A}_c^T \mathbf{h} = \lambda \mathbf{h}$). The weighting vector is selected by computing the characteristic equation $\mathbf{A}_c^T \mathbf{h} = 0$ for $\lambda = 0$.

In the SMC system, the state feedback control law that limits ship motion responses is defined. In this case, the rudder angle command is separated into two parts,

$$\delta = \delta_0 + \delta_s \quad (27)$$

where $\delta_0 = -\mathbf{k}^T \mathbf{x}$ is the state feedback control law, which can also be an equivalent controller.

Substituting the control (27) into the equation (25), we obtain

$$\dot{\mathbf{x}} = \mathbf{A}_c \mathbf{x} - \mathbf{b}\delta_s + \mathbf{d} \quad (28)$$

where the combined state matrix is $\mathbf{A}_c = \mathbf{A} - \mathbf{b}\mathbf{k}^T$. The feedback gain vector is defined as $\mathbf{k} = [k_1, k_2, 0]^T$ to stabilize the sway-yaw dynamics. Here, $k_3 = 0$ due to integration in the yaw channel.

The nonlinear control part δ_s is the switching law which counteracts the destabilizing effects of environmental disturbances. It is written as:

$$\delta_s = -(\mathbf{h}^T \mathbf{b})^{-1} \eta \operatorname{sgn}(s) \quad (29)$$

where the switching gain satisfies $\eta > d_{\max} \|\mathbf{h}\|$.

Differentiating the sliding surface manifold, we arrive at:

$$\begin{aligned} \dot{s} &= \mathbf{h}^T \mathbf{A}_c \mathbf{x} + \mathbf{h}^T \mathbf{b}\delta_s + \mathbf{h}^T \mathbf{d} - \mathbf{h}^T \dot{\mathbf{x}}_d \\ &= \lambda \mathbf{x}^T \mathbf{h} - \eta \operatorname{sgn}(s) + \mathbf{h}^T \mathbf{d} \end{aligned} \quad (30)$$

where $\lambda \mathbf{x}^T \mathbf{h} = 0$ if \mathbf{h} is the right eigenvector, and $\mathbf{h}^T \dot{\mathbf{x}}_d = 0$.

To prove the stability of the closed loop system, the Lyapunov function is selected:

$$V = \frac{1}{2} s^2 \quad (31)$$

The differentiation of Equation (31) can be written as

$$\begin{aligned} \dot{V} &= s\dot{s} = -\eta \operatorname{sgn}(s)s + \mathbf{h}^T \mathbf{d} \\ &= -\eta |s| + \mathbf{h}^T \mathbf{d} \leq 0 \end{aligned} \quad (32)$$

The above equation indicates that the state trajectory can reach the sliding manifold in finite time and decline to zero. Consequently, the control law guarantees the sustainability of the sliding mode.

In order to attenuate the chattering effect, the *tanh* function is used in place of *signum* function. Hence, the total control law of autopilot becomes

$$\delta = -(k_1 v + k_2 r) - (h_1 b_1 + h_2 b_2)^{-1} \eta \tanh(s/\phi) \quad (33)$$

where ϕ is the boundary layer thickness.

ADAPTIVE SLIDING MODE CONTROL DESIGN

In practice, the dynamics of the ship and the actuator are affected by the time-varying speed, which is the source of parameter uncertainties. The upper bounds of disturbance and parameter uncertainties, and the value of η are often difficult to find. The uncertainties in the system are assumed to meet the matching conditions. In this section, the modified control law is presented. The purpose of the adaptive method is to tune the controller gain without the knowledge about the upper bound of system uncertainties.

Considering the speed $U(t) = U_0 + \Delta U$, varying with time due to speed loss, the system state-space model is written as

$$\dot{\mathbf{x}} = \mathbf{A}(U(t))\mathbf{x} + \mathbf{b}(U(t))\delta + \mathbf{d} \quad (34)$$

where the state matrix and the control matrix can be divided into the nominal part and the uncertain part:

$$\mathbf{A}(U(t)) = \mathbf{A} + \Delta \mathbf{A} \quad \text{and} \quad \mathbf{b}(U(t)) = \mathbf{b} + \Delta \mathbf{b}$$

Then we obtain a new equation:

$$\dot{\mathbf{x}} = \mathbf{A}\mathbf{x} + \mathbf{b}\delta + \mathbf{E}(\Delta U, \mathbf{x}, \delta) \quad (35)$$

where $\mathbf{E}(\Delta U, \mathbf{x}, \delta) = \Delta \mathbf{A}\mathbf{x} + \Delta \mathbf{b}\delta + \mathbf{d}$ is the lumped uncertainty.

The modified control law developed here is

$$\delta_a = \delta_{a0} + \delta_{as} \quad (36)$$

where the linear feedback controller δ_{a0} is the same as δ_0 used in the nominal system.

Corresponding to the lumped uncertainty, the robust switching control part is modified as

$$\delta_{as} = -(\mathbf{h}^T \mathbf{b})^{-1} \hat{\eta}_a \operatorname{sgn}(s) \quad (37)$$

where $\hat{\eta}_a$ is the estimate of the adjustable gain. Assuming that there is a positive η_a for which $\delta_{as} = -(\mathbf{h}^T \mathbf{b})^{-1} \eta_a \operatorname{sgn}(s)$ is the terminal solution, the gain η_a must satisfy $\eta_a > \|\mathbf{h}^T\| \cdot \|\mathbf{E}(\Delta U, \mathbf{x}, \delta)\|$.

The adjustable gain can be tuned by the adaptation law defined as

$$\dot{\hat{\eta}}_a = \frac{1}{\alpha} |s| \quad (38)$$

where $\alpha > 0$ is the adaptation gain. Selecting a reasonable adaptation gain can effectively help to avoid high control activity. For simplicity, let it be a positive constant in this control system.

To avoid over increased estimate values of $\hat{\eta}_a$ that may lead to large amplitude control signal, this quantity should be limited in a suitable range. That is why the projection algorithm presented by Do et al. [2] is used to modify the adaptation law into the following

$$\dot{\hat{\eta}}_a = \operatorname{Proj}_{\hat{\eta}_a}(\dot{\hat{\eta}}_a) \quad (39)$$

$$\operatorname{Proj}_{\hat{\eta}_a}(\bullet) = \begin{cases} 0 & \text{if } \hat{\eta}_a \geq \eta_{\max} \text{ and } \bullet > 0 \\ 0 & \text{if } \hat{\eta}_a \leq \eta_{\min} \text{ and } \bullet < 0 \\ \bullet & \text{otherwise} \end{cases} \quad (40)$$

Theorem 1. For the system (26): Given the control law (36) and the eigenvector property in the equation (30), under Assumptions 1-6 the proposed adaptive control strategy can guarantee driving the state trajectories of the system onto the sliding surface in finite time.

Proof: Consider the same sliding surface function as in the above section. Then its differentiation is written as

$$\begin{aligned} \dot{s} &= \mathbf{h}^T \dot{\mathbf{x}}_e = \mathbf{h}^T \dot{\mathbf{x}} = \mathbf{h}^T (\mathbf{A}_c \mathbf{x} + \mathbf{b} \delta_{as} + \mathbf{E}) \\ &= \mathbf{h}^T \mathbf{b} \delta_{as} + \mathbf{h}^T \mathbf{E} \end{aligned} \quad (41)$$

Define the estimate error as $\tilde{\eta}_a = \hat{\eta}_a - \eta_a$, and choose a Lyapunov function candidate as

$$V = \frac{1}{2} s^2 + \frac{1}{2} \alpha \tilde{\eta}_a^2 \quad (42)$$

Multiplying both sides of Equation (41) by the sliding surface, the following equation is obtained

$$s \dot{s} = s(\mathbf{h}^T \mathbf{E} - \hat{\eta}_a \operatorname{sgn}(s)) = s \mathbf{h}^T \mathbf{E} - \hat{\eta}_a |s| \quad (43)$$

In the same way, the corresponding equation for the adaptation error is given as

$$\alpha \tilde{\eta}_a \dot{\tilde{\eta}}_a = \alpha (\hat{\eta}_a - \eta_a) \dot{\hat{\eta}}_a = (\hat{\eta}_a - \eta_a) |s| \quad (44)$$

Applying Equations (43) and (44), and taking the derivative of the Lyapunov function, we get

$$\dot{V} = s \dot{s} + \alpha \tilde{\eta}_a \dot{\tilde{\eta}}_a = s \mathbf{h}^T \mathbf{E} - \eta_a |s| \leq 0 \quad (45)$$

Hence, the convergence of s and $\tilde{\eta}_a$ is proven by the Lyapunov direct method, both s and $\tilde{\eta}_a$ reach zero in finite time. To alleviate the chattering phenomenon, the boundary layer method with *tanh* function can be used to replace *signum*, like in the description in the SMC design section. In the proposed ASMC scheme, the knowledge of the upper bound of system uncertainties is not required.

SIMULATION RESULTS

The simulation of the autopilot control system working on a navy vessel with speed keeping control is demonstrated. The nominal ship speed is 15 knots, the wave height is 3.7 m, and the average period is 7 s. The rudder angle limitation is 35° and two rudders are installed. The desired state trajectory is assumed to be $\mathbf{C}_d = (0, 0, 0)^T$, the initial state vector is $\mathbf{x} = (0, 0, 0)^T$ and the initial guess of η is $\eta = 5$. The adaptation law is set as $\alpha = 0.05$ and $\hat{\eta}_a(0) = 2.5$. The boundary layer is chosen as $\phi = 1$. The other parameters \mathbf{k} and η_{\min}, η_{\max} are set as $[10, 100, 0]^T$ and $(2, 25)$, separately. The ship is sailing with the encounter angle 120°.

Fig. 3 compares autopilot dynamics under the open-loop condition. The solid lines represent the time-histories of ship dynamics which consider the effect of time-varying speed loss, while the dashed lines mean the responses of the nominal ship model. The sway and yaw rate responses are identical for these two models. On the other hand, the yaw angle magnitude is increased under the action of time-varying ship dynamics which may generate ship course changes. The speed response is less declined, as the values of speed loss depend on sway and yaw rates, as presented by Liu et al. [24].

Tab. 2. Cost value of simulation

Controller	Yaw response	Average speed (Kn)	Rudder usage
SMC	1867.09	13.49	48927.57
ASMC	1590.05	13.73	58032.68

The results of ship's performance calculations with the two control methods are presented in Fig. 4. In the first graph, the response of the sway rate is not changed. Actually, the rudder control force for sway motion is *LCG* times smaller than that for yaw motion (compare equations (5) and (6)), therefore we can ignore this control force and assume it as an underactuated surface vessel. The proposed ASMC scheme can give better sailing performance, as the yaw motion and

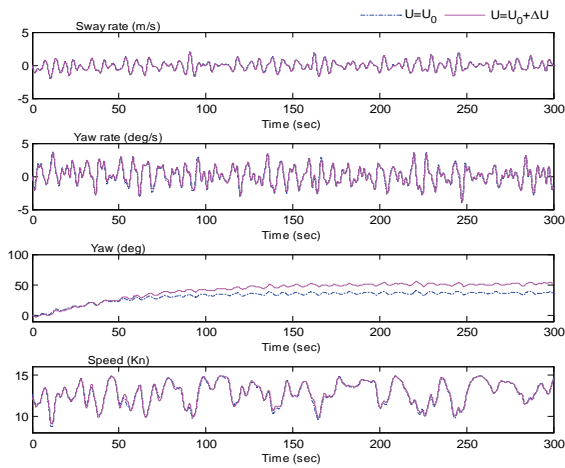


Fig. 3. Responses of the uncontrolled autopilot system

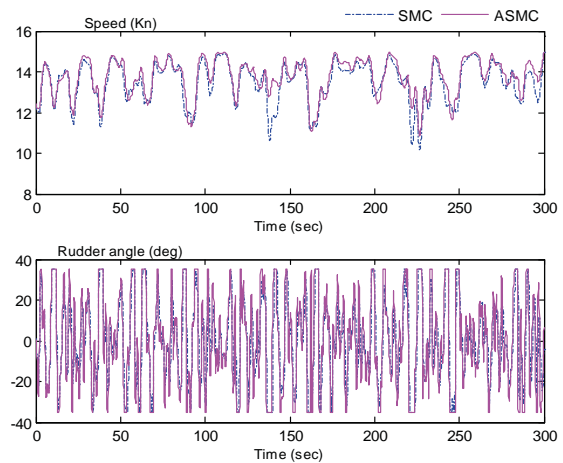


Fig. 5. Comparison of speed and rudder angles

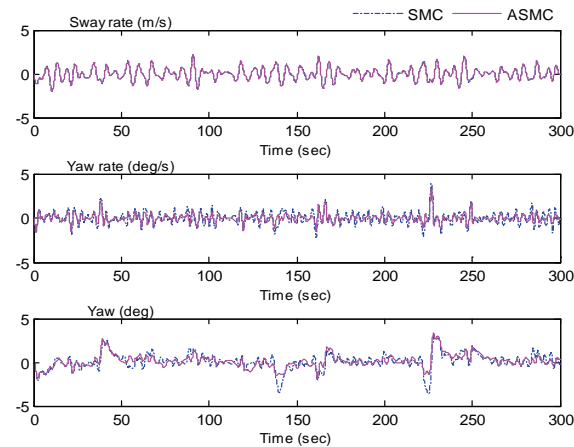


Fig. 4. Simulation results of sway and yaw

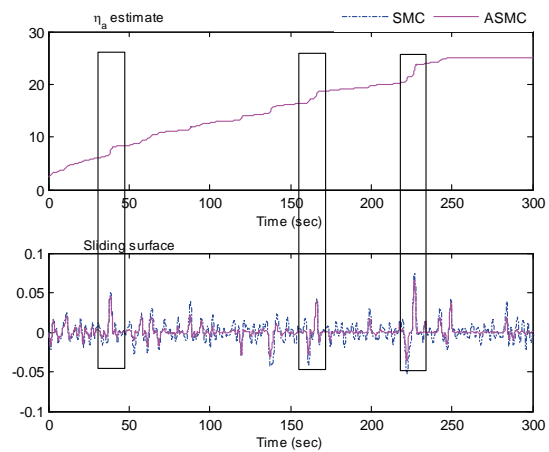


Fig. 6. Simulation results of adaptive trajectory and sliding surface controllers

its rate are both reduced to a greater extent than by the SMC method. That means that the speed loss (i.e. fuel consumption increase) can be reduced more. At the sea state for the case presented in Fig. 5, the reduction of speed loss percentage is 1.54%, which cannot be ignored in the real voyage of a ship. Fig. 5 also compares rudder orders. The adaptive controller may use a little more energy to drive rudders and cause rudder angle saturation. The values calculated from the cost function are listed in Table 2.

Fig. 6 presents the time-histories of the results obtained using the adaptive estimate and sliding surface controllers. The estimate value is continuously increasing, with stepwise increase at each corresponding peak in the sliding surface, marked by three rectangles in Fig. 6. This is because the adaptation law is substantially an integral function of the sliding surface. This is also the reason why the projection algorithm is adopted here to limit this value. This kind of varying estimate value generates more effective rudder control commands to reject system uncertainties due to speed loss and unknown disturbances.

CONCLUSIONS

In the paper, the problem of adaptive sliding mode control design for ship autopilot system with fuel efficiency control is studied. The control problem is formulated in a single-input-multiple-output framework with a time-varying ship model due to speed loss. The adaptation accounts for changes in ship speed to ensure that the appropriate drag forces are minimized. The paper also presents the responses of the rudders to changes in the seaway environment. The variations of parameters in the system and in the external disturbance are both robust, and the tracking capacity is guaranteed. The ASMC method can improve the heading control performance. What is more important, the actual sailing speed of the ship is significantly improved by the control system with respect to sailing energy consumption. Notably, the information on upper bounds of system uncertainties and wave disturbances is not required. When applying this strategy, the initial value set for the adaptation estimate should be smaller than the nominal upper bound. For the sake of safety, the projection

algorithm method is proposed to avoid an unexpected unlimited increase of the adaptation estimate. Simulation results have been provided to illustrate the effectiveness of the proposed approach.

REFERENCES

1. Fossen T.I.: *Handbook of marine craft hydrodynamics and motion control*. Wiley, West Sussex, 2011.
2. Do K.D., Jiang Z.P., Pan J.: *Robust adaptive path following of underactuated ships*. *Automatica*, vol. 40, no. 6, 929, 2004.
3. Zhang G., Zhang X., Zheng Y.: *Adaptive neural path following control for underactuated ships in fields of marine practice*. *Ocean Engineering*, no. 104, 558, 2015.
4. Shojaei K.: *Neural adaptive robust control of underactuated marine surface vehicles with input saturation*. *Applied Ocean Research*, no. 53, 267, 2015.
5. Li J.H., Lee P.M., Jun B.H., Lim Y.K.: *Point to point navigation of underactuated ships*. *Automatica*, vol. 44, no. 12, 3201, 2008.
6. Peng Z., Wang D., Chen Z., Hu X., Lan W.: *Adaptive dynamic surface control for formations of autonomous surface vehicles with uncertain dynamics*. *IEEE Transactions on Control System Technology*, vol.21, no. 2, 513, 2013.
7. Do K.D., Pan J., Jiang Z.P.: *Robust adaptive control of underactuated ships on a linear course with comfort*. *Ocean Engineering*, vol. 30, no. 7, 2201, 2003.
8. Li H., Liu J., Hilton C., Liu H.: *Adaptive sliding mode control for nonlinear active suspension vehicle systems using T-S fuzzy approach*. *IEEE Transactions on Industrial Electronics*, vol. 60, no. 8, 3328, 2013.
9. Kahveci N., Ioannou P.A.: *Adaptive steering control for uncertain ship dynamics and stability analysis*. *Automatica*, vol. 49, no. 3, 685, 2013.
10. Lin C., Hsuen C., Chen C.: *Robust adaptive backstepping control for a class of nonlinear systems using recurrent wavelet neural network [J]*. *Neurocomputing*, no. 142, 372, 2014.
11. Cristi R., Papoulias F.A., Healey A.J.: *Adaptive sliding mode control of autonomous underwater vehicles in the dive plane*. *IEEE Journal of Oceanic Engineering*, vol. 15, no. 3, 152, 1990.
12. Do K.D., Pan J., Jiang Z.P.: *Robust and adaptive path following for underactuated autonomous underwater vehicles*. *Ocean Engineering*, vol. 31, no. 6, 1967, 2004.
13. Liu Y., Liu S., Wang N.: *Fully tuned fuzzy neural network robust adaptive tracking control of unmanned under water vehicle with thruster dynamics*. *Neurocomputing*, no. 196, 1, 2016.
14. Prpic-Orsic J., Faltinsen O.M.: *Estimation of ship speed loss and associated CO2 emissions in a sea way*. *Ocean Engineering*, vol. 44, no. 1, 1, 2012.
15. Arribas F.P.: *Some methods to obtain the added resistance of a ship advancing in waves*. *Ocean Engineering*, vol. 34, no. 7, 946, 2007.
16. Armstrong V.N.: *Vessel optimisation for low carbon shipping*. *Ocean Engineering*, no. 73, 195, 2013.
17. Liu Z., Jin H.: *Extended radiated energy method and its application to a ship roll stabilisation control system*. *Ocean Engineering*, vol. 72, no. 7, 25, 2013.
18. Faltinsen O.M.: *Hydrodynamics of High Speed Vehicles*. Cambridge University Press, Cambridge 2005.
19. Akinsal V.: *Surface ship fuel saving with an optimized autopilot, master dissertation*. Naval Postgraduate School, Monterey, 1985.
20. Grimble M.J., Katabi M.R.: *LQG design of ship steering control systems*. *Signal Processing for Control, Lecture Notes in Control and Information Sciences*, no. 79, 387, 1986.
21. Miloh T., Pachter M.: *Ship collision-avoidance and pursuit-evasion differential games with speed-loss in a turn*. *Computers Mathematics with Application*, vol. 18, no. 1, 77, 1989.
22. Kim S.S., Kim S.D., Kang D., Lee J., Lee S.J., Jung K.H.: *Study on variation in ship's forward speed under regular waves depending on rudder controller*. *International Journal of Naval Architecture and Ocean Engineering*, vol. 7, no. 2, 364, 2015.
23. Liu Z., Jin H., Grimble M.J., Katebi R.: *Ship forward speed loss minimization using nonlinear course keeping and roll motion controllers*. *Ocean Engineering*, no. 113, 201, 2016.
24. Perez T.: *Ship Motion Control: Course Keeping and Roll Reduction Using Rudder and Fins*. Springer, London, 2005.
25. Loukakis T.A., Sclavounos P.: *Some extensions of the classical approach to strip theory of ship motion including the calculation of mean added forces and moments*. *Journal of Ship Research*, vol. 22, no. 1, 1, 1978.

CONTACT WITH THE AUTHOR

Zhiquan Liu

e-mail: liuzhiquan215@sina.com

Shanghai Maritime University

1550 Haigang AVE

201306 Shanghai

CHINA

OPTIMIZATION METHODS IN MARITIME TRANSPORT AND LOGISTICS

Józef Lisowski
Gdynia Maritime University

ABSTRACT

The purpose of the article is to present the goal of optimization of transport and logistics processes, followed by literature review in the field of optimization methods. The optimization methods were categorized and the most commonly used methods were listed. The tasks of static and dynamic optimization were formulated. An example of the single-criterion static and dynamic optimization and multi-criteria game optimization are given.

Keywords: maritime transport, optimization, ship control, computer simulation

DEVELOPMENT OF OPTIMIZATION METHODS - HISTORICAL OUTLINE

The primary goal of optimization is to implement the object control process in the best way. The process may be: physical phenomenon, technological process, technical object, economic system, production and transport planning, etc [1,4]. The mathematical description of the process formulated for the purpose of its optimization is by modelling. The optimization is as good as the mathematical model is adequate [3,9]. Formulating and solving the optimization task can be presented as in Fig. 1.

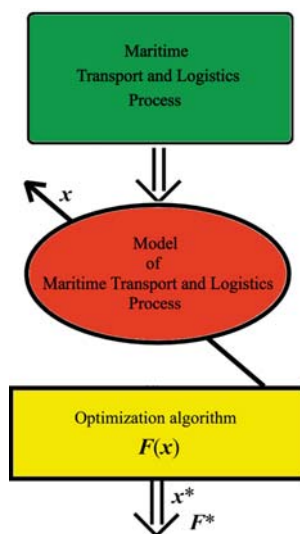


Fig. 1. Stages of formulating and solving the optimization task

The function $F(x)$ means the evaluation of the quality of the object's operation or the course of the control process and assumes the name of the goal control function or control quality index, and x constitutes a set of the decision variables or state variables of the control process [7,10,13].

In many issues of transport and logistics there are many possible and acceptable solutions to the problem, of which only one is the optimal solution under the assumed criterion of the quality of the transport or logistics process [14,15,16].

Both static optimization and dynamic optimization methods are used to solve such issues. Increasingly, the practice of transport and logistics processes must meet both technical and economic criteria. Therefore, apart from the single-criterion optimization, multi-criteria optimization becomes more and more important.

And so, the beginning of the variational calculus is presented in the works of Lagrange (1736-1813), Hamilton (1805-1865), Weierstrass (1815-1897) and Pontriagin (1908-1988).

Modern methods of optimization dated beginning from 1939 are: logistics problems related to planning operations during World War II - linear programming (Dantzig (1914-2005)); integer programming and selection from among a finite number of decisions (Cabot (1922-1984), Balas (1922)); non-linear programming (Kuhn, Tucker and Geoffrion).

The development of methodology of computer calculating has caused interest in numerical algorithms (Powell, Rossen, Fletcher) and dynamic programming (Bellman, Riccati).

Space research has focused on the optimization of rocket constructions and flight control in the stratosphere and space.

Optimization of economic processes includes: problems of production allocation, optimal composition of the investment portfolio, large scale problems and decomposition methods (Lasdon, Findeisen).

The development of methods for solving optimization tasks took place in the following stages:

- analytical classic methods, or methods of “mountain climbing”: models developed by mathematicians of the 17th and 19th centuries, the “unpolluted” world of square functions of the target and ubiquitous derivatives,
- development of computer calculations: modifications of classic methods, algorithmization of calculations enabling application to practical problems of science and technology,
- soft computing, resistant methods: evolutionary, genetic algorithms, neural networks used to optimize complex process models [12].

In transport and logistics, the best possible control of an object is expressed in optimization dealing with how to describe and achieve the best, when we already know how to measure and change good and bad (Beightler, Phillips: *Foundations of Optimization*, 1979).

The general categorization of optimization methods considered the most representative, is shown in Fig. 2.

In practice, the following methods are most commonly used:

- non-gradient static optimization without constraints: golden division, bisection, Gauss-Seidel, division and constraints, division and isolation, Hooke-Jeeves, square interpolation, Nelder-Mead simplex, Rosenbrock, Davies-Swann-Campey;
- gradient static optimization without constraints: simple gradient, the fastest slope, Newton-Raphson, conjugate gradient Hestenes-Stiefel, Levenberg-Marquardt, Powell, Zangwill;
- non-gradient static optimization with constraints: Lagrange, linear programming, Kuhn-Tucker, Schmidt-Fox;
- gradient static optimization with constraints: Zoutendijk, Raster projected gradient;
- heuristics: grouping, Monte Carlo, simulated annealing, genetic algorithms, particle swarm;
- basic direct dynamic optimization: Euler’s calculus, Bellman’s principle of optimality, simple gradient in control space, conjugate gradient in control space, variable metrics, second variation;

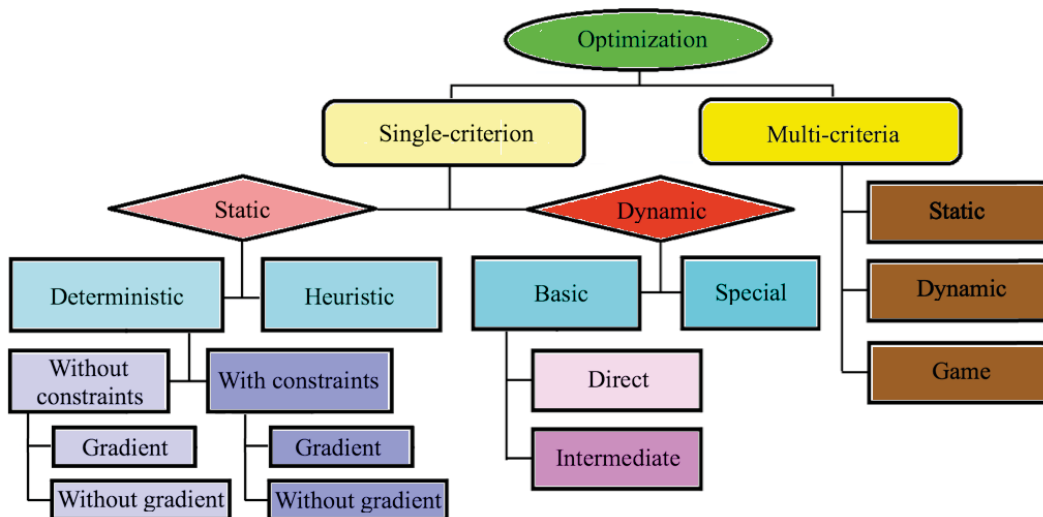


Fig. 2. Categorization of optimization methods

The optimization methods can be divided in respect of:

- object or process properties: into static and dynamic;
- constraints: into without constraints and with constraints;
- way of calculating the optimum: into gradient and non-gradient;
- type of object or process model: into deterministic and stochastic;
- type of calculations: into analytical and numerical;
- form of the goal function: into linear and non-linear;
- complexity of the goal function: into single-criterion and multi-criteria.

- basic intermediate dynamic optimization: maximum principle of Pontriagin, Newton in the state space, Newton-Rapson in the conjugate space;
- special dynamic optimization: time-optimal control of Neustadt, Gilbert, Barr, Balakrishnan punishment function, Findeisen’s two-level optimization;
- static multi-criteria optimization: set of optimal Pareto points in the space of variants, Bentham’s rule of utilitarianism, Rawls principle of justice, Salukvadze reference point, Benson weighted sum method, Haimes ϵ -constraints method, purposeful programming method;
- dynamic multi-criteria optimization: selection of weight coefficients;
- game multi-criteria optimization: multi-stage positional game, multi-step matrix game [9].

PROBLEMS AND METHODS OF OPTIMIZATION IN TRANSPORT AND LOGISTICS

STATIC OPTIMIZATION

The optimization task consists in determining such values of state variables \mathbf{x}^* at which the function of the control goal $F(\mathbf{x})$ reaches its minimum or maximum value.

The values of constituents of the state vector \mathbf{x} cannot be arbitrary and are subject to various constraints. A distinction is made between inequalities:

$$\mathbf{g}_i(\mathbf{x}) \leq 0 \quad \text{for } i=1, 2, \dots, M \quad (1)$$

and equality constraints:

$$\mathbf{h}_p(\mathbf{x}) = 0 \quad \text{for } p=1, 2, \dots, P \quad (2)$$

The introduction of any equality constraint reduces the size of the optimization space by one and may be the reason for the lack of an optimal solution.

SINGLE-CRITERION STATIC OPTIMIZATION

The task of single-criterion static optimization is to search for a minimum or maximum of the objects output or its function:

$$F(\mathbf{x}) = f(\mathbf{x}) \quad \text{for } \mathbf{x} = x_1, x_2, \dots, x_n \quad (3)$$

while meeting the constraints imposed on the variables \mathbf{x} .

Examples of single-criterion static optimization tasks in sea transport and logistics:

- optimization of the product range in the yard of commercial and fishing ships and yachts;
- optimization of rational cutting of sheets in the ship's construction process;
- optimization of transport process of containers, cars, citrus fruits and other loads;
- optimization of logistics of cargo transportation between the port and the recipients;
- optimization of the quantity and type of port equipment for handling ship transshipments;
- investment optimization of the construction or expansion of the port.

MULTI-CRITERIA STATIC OPTIMIZATION

The task of multi-criteria static optimization is determining the optimal decision when there is more than one optimization criterion:

$$F(\mathbf{x}) = \text{for } k=1, 2, \dots, K \quad (4)$$

while meeting the constraints imposed on the variables \mathbf{x} .

Examples of multi-criteria static optimization tasks in sea transport and logistics:

- optimization of transport means works with minimal cost and delivery time;
- maximum use of cargo space with a minimum delivery time.

DYNAMIC OPTIMIZATION

SINGLE-CRITERION DYNAMIC OPTIMIZATION

The task of single-criterion dynamic optimization is to look for the minimum or maximum of a functional as the integral of a function:

$$F(\mathbf{x}) = \int_{t_0}^{t_k} f_0(\mathbf{x}, \mathbf{u}, t) dt \quad (5)$$

where the dynamic properties of the control object are described by the equations of state and output:

$$\dot{\mathbf{x}} = \mathbf{f}(\mathbf{x}, \mathbf{u}, t) \quad (6)$$

$$\mathbf{y} = \mathbf{g}(\mathbf{x}, \mathbf{u}, t) \quad (7)$$

and meeting constraints imposed on the state variables \mathbf{x} and control variables \mathbf{u} .

The task of dynamic optimization can be solved analytically as a task of time-optimal control and minimization of the goal function in a square form, with linear state equations.

Examples of single-criterion dynamic optimization tasks in maritime transport:

- determination of the optimal route of the ship from the initial port to the port of destination, ensuring minimum fuel consumption, including navigational limits and hydro-meteorological forecasts;
- determination of the optimal anti-collision manoeuvre of own ship ensuring minimum risk of collision during passing the encountered ships;
- optimization of the main engine control of the ship, ensuring minimum fuel consumption;
- optimization of ship loading, ensuring maximum ship stability;
- optimization of power distribution between the ship propulsors, ensuring the maximum controllability of the ship;
- optimization of the ship's electrical system, ensuring maximum reliability of power supply for ship's equipment.

MULTI-CRITERIA DYNAMIC OPTIMIZATION

The task of multi-criteria dynamic optimization is to look for the minimum or maximum of a functional as the integral of a function:

$$F(\mathbf{x}) = \int_{t_0}^{t_k} \sum_{k=1}^K f_{0k}(\mathbf{x}, \mathbf{u}, t) dt; \quad \text{for } k=1, 2, \dots, K \quad (8)$$

Examples of multi-criteria dynamic optimization tasks in maritime transport:

- optimization of sea transport process, ensuring maximum profit with a minimum risk;
- optimal control of the ship on a reference course, ensuring maximum control accuracy and minimum fuel consumption;
- safe traffic management ensuring minimum risk of collision and minimum road loss on passing objects.

GAME OPTIMIZATION

The game control of the marine object consists in minimizing goal function given in the form of an integral payment and final payment:

$$F(x) = \int_{t_0}^{t_k} f_o(x, u, t) dt + r_f(t_k) + d_f(t_k) \quad (9)$$

The integral payment of the game determines loss of path of the own object on the passing of cooperating or non-operating objects that were met.

The final payment of the game determines the final risk of collision r_f and the final deviation of own object position d_f from its reference trajectory of movement [2,8,11].

A distinction is made between the following types of game control of a maritime transport object as follows:

- multi-stage positional, non-cooperative or cooperative game;
- multi-step matrix, non-cooperative or cooperative game.

EXAMPLES OF OPTIMIZATION TASKS IN MARITIME TRANSPORT AND LOGISTICS

OPTIMIZATION OF CONTAINER TRANSPORT BY MEANS OF LINEAR PROGRAMMING

The ship owner has five container ships: K1, K2, K3 and K4 with capacity of 2600, 4200, 2100, 1100 TEU containers, respectively. It is necessary to plan the transport of 10 000 containers from Asia to five European ports: P1, P2, P3, P4 and P5 in quantities of 1800, 2100, 3100, 1800, 1100 TEU, respectively, with the lowest total cost of transport from Asia to Europe. Tab. 1 shows the cost of transporting one TEU container.

Tab. 1. Data summary for the task of container transport optimization

Ships					Number of containers expected in port
Ports	K1	K2	K3	K4	
P1 Lisbon	500 USD	450 USD	640 USD	620 USD	1800 TEU
P2 Le Havre	600 USD	540 USD	660 USD	690 USD	2100 TEU

Ships					Number of containers expected in port
Ports	K1	K2	K3	K4	
P3 Bremerhaven	700 USD	610 USD	710 USD	730 USD	3100 TEU
P4 Gdańsk	740 USD	735 USD	870 USD	810 USD	1800 TEU
P5 Sankt Petersburg	900 USD	890 USD	960 USD	930 USD	1200 TEU
Load capacity of ship	2600 TEU	4200 TEU	2100 TEU	1100 TEU	

The standard and simultaneously canonical form of linear programming which it will take, is as follows:

$$F(x) = 500x_{11} + 450x_{12} + 640x_{13} + 620x_{14} + 600x_{21} + 540x_{22} + 660x_{23} + 690x_{24} + 700x_{31} + 610x_{32} + 710x_{33} + 730x_{34} + 740x_{41} + 735x_{42} + 870x_{43} + 810x_{44} + 900x_{51} + 890x_{52} + 960x_{53} + 930x_{54} \rightarrow \min \quad (10)$$

$$x_{11} + x_{12} + x_{13} + x_{14} = 1800$$

$$x_{21} + x_{22} + x_{23} + x_{24} = 2100$$

$$x_{31} + x_{32} + x_{33} + x_{34} = 3100$$

$$x_{41} + x_{42} + x_{43} + x_{44} = 1800$$

$$x_{51} + x_{52} + x_{53} + x_{54} = 1200$$

$$x_{11} + x_{21} + x_{31} + x_{41} + x_{51} = 2600$$

$$x_{12} + x_{22} + x_{32} + x_{42} + x_{52} = 4200$$

$$x_{13} + x_{23} + x_{33} + x_{43} + x_{53} = 2100$$

$$x_{14} + x_{24} + x_{34} + x_{44} + x_{54} = 1100$$

(11)

$$(x_{11}, x_{12}, x_{13}, x_{14}, x_{21}, x_{22}, x_{23}, x_{24}, x_{31}, x_{32}, x_{33}, x_{34}, x_{41}, x_{42}, x_{43}, x_{44}, x_{51}, x_{52}, x_{53}, x_{54}) \geq 0 \quad (12)$$

The *linprog* function from MATLAB software has been used: $[x, fval] = \text{linprog}(f, A, b, Aeq, beq, lb, ub)$, as a result of its operation there will be obtained a vector x with the solution and the containers transporting cost under the variable *fval* (Fig. 3).

The following results of container transport optimization in the MATLAB *linprog* software are obtained:

$$x_{11}^* = 0, x_{12}^* = 0, x_{13}^* = 1800, x_{14}^* = 0$$

$$x_{21}^* = 0, x_{22}^* = 1000, x_{23}^* = 0, x_{24}^* = 1100$$

$$x_{31}^* = 2600, x_{32}^* = 500, x_{33}^* = 0, x_{34}^* = 0$$

$$x_{41}^* = 0, x_{42}^* = 1500, x_{43}^* = 300, x_{44}^* = 0$$

$$x_{51}^* = 0, x_{52}^* = 1200, x_{53}^* = 0, x_{54}^* = 0$$

$$F^*(x) = 7\,007\,500 \text{ USD} \quad (13)$$

Tab. 2 shows the optimal loading of container ships.

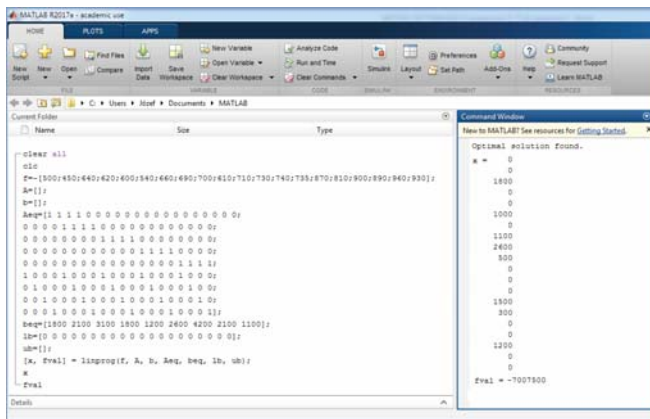


Fig. 3. Results of container transport optimization

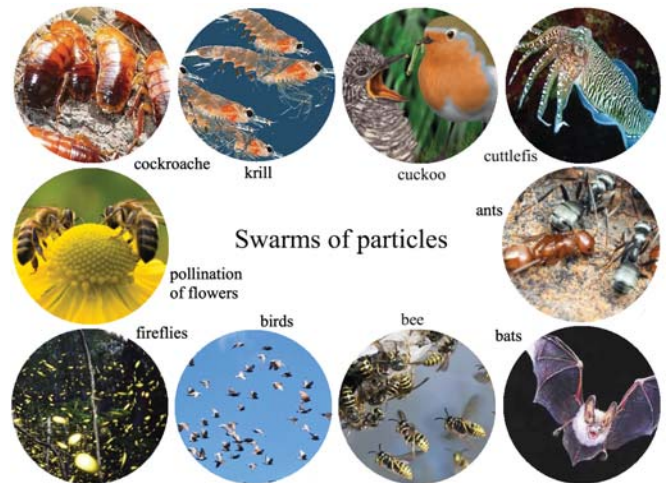


Fig. 4. Examples of individuals forming swarms of particles

Tab. 1. Optimal loading of container ships

Ships					Number of containers delivered in port
Ports	K1	K2	K3	K4	
P1 Lisbon			1800 TEU		1800 TEU
P2 Le Havre		1000 TEU		1100 TEU	2100 TEU
P3 Bremerhaven	2600 TEU	500 TEU			3100 TEU
P4 Gdansk		1500 TEU	300 TEU		1800 TEU
P5 Sankt Petersburg		1200 TEU			1200 TEU
Loading the ship	2600 TEU	4200 TEU	2100 TEU	1100 TEU	

OPTIMIZATION OF SAFE SHIP CONTROL BY MEANS OF SWARM OF PARTICLES

A swarm of particles or a flock is a group of individuals of the same species, rarely different species of animals, insects, birds and fish living in a specific territory, related to each other due to more or less advanced forms of social organization. Mating of individuals into flocks is most often associated with breeding or searching for food.

The Particle Swarm Optimization – PSO was proposed in 1995 by Kennedy and Eberhart. The idea of the algorithm comes from imitating the behaviour of a population of living creatures - birds, ants, bees, fireflies, bats, cockroaches, krill, etc, in which a single individual has a very limited ability to make decisions and mutual communication (Fig. 4).

The whole population, despite the lack of a central control system, demonstrates the features of having intelligence, that is, the responding to changes in the environment and the collective undertaking of related actions.

The numerical model of the behaviour of a group of objects treats the population as a swarm and each individual as a particle. During the next steps of the discretized time, the particles move to new positions, simulating the adoption of the swarm to the environment, i.e. they are looking for the optimum. The algorithm uses to search for the extreme value of the adaptive function as a function of the control target for a population of moving particles that can memorize the point of the best value of the objective function in the search space and transmit this information to whole population or its part.

Bird's algorithm – Particle Swarm Optimization PSO, presented in 1995 by R.C. Eberhart and J. Kennedy, imitates the gregarious behaviour of birds that communicate and observe each other exchanging information among themselves, improving the search of the area as a space for optimal solutions.

Base Bees algorithm – BBA mimics of feeding of honeybee swarms, developed by D.T. Pham in 2005.

Firefly algorithm – FA, developed in 2008 by Prof. Xin-She Yang, is inspired by the social behaviour of skylights, insects from the Lampyridae family, whose phenomenon is bioluminescent communication.

Cuckoo Search – CS algorithm uses cuckoo nesting habits, proposed in 2009 by Xin-She Yang and Suash Deb, mimicking the behaviour of some cuckoo species that use the nest of other birds to hatch eggs and raise their chicks.

Cockroach Swarm Optimization – CSO algorithm uses three cockroach behaviours as insects: swarming, dispersing and absolute behaviour, described by L. Cheng, Z.B. Wang, Y.H. Song and A.H. Guo in 2011.

Flower Pollination – FPA algorithm, inspired by the process of pollination of flowering plants, was developed by Xin-She Yang in 2012.

Cuttlefish algorithm – CFA algorithm, proposed by A.S. Eesa, Z. Orman and A.M.A. Brifcani in 2013, is inspired by the environmental change of cuttlefish skin colour.

Krill Herd – KH algorithm, described in 2012 by A.H. Gandami and A.H. Alavi, is based on the simulation of behaviour of herds of krill individuals.

Ant Colony Optimization – ACO algorithm, proposed in 1999 by Marco Dorigo, is a probabilistic technique for solving problems by looking for good roads in graphs, inspired by the behaviour of ants looking for food for their colony.

The use of ACO algorithm to determine the safe trajectory of a ship in a collision situation has been developed by A. Lazarowska [6].

Calculations of the safe trajectory of the own ship by using the form-based algorithm consist of three main stages which include:

- data initialization;
- constructing solutions;
- updating pheromone traces.

The ship route from the starting point wp_0 to the end point wp_e is divided into k stages. Ships are represented by hexagonal domains, which cannot be crossed by a respective own ship (Fig. 5).

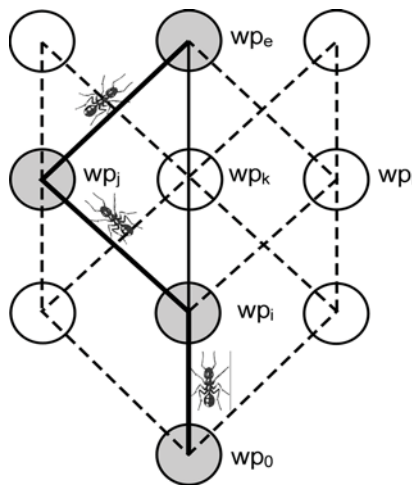


Fig. 5. An example of a route chosen by an ant [35]

The probability of choosing the next top by the ant is:

$$P_{wp_{ij}}(t) = \frac{[\tau_{wp_{ij}}(t)]^\alpha (\eta_{wp_{ij}})^\beta}{\sum_{l \in wp_i} [\tau_{wp_{il}}(t)]^\alpha (\eta_{wp_{il}})^\beta} \quad (14)$$

where:

- $\tau_{wp_{ij}}(t)$ – values of the pheromone trace at the apex j ,
- $\eta_{wp_{ij}}$ – some heuristic information, called visibility, the inverse of the distance between the current vertex i and the neighbouring vertex j ,
- l – ant number,
- α, β – coefficients of algorithm convergence.

Fig.6 shows an example of determining the safe trajectory of an own ship by using a ACO algorithm.

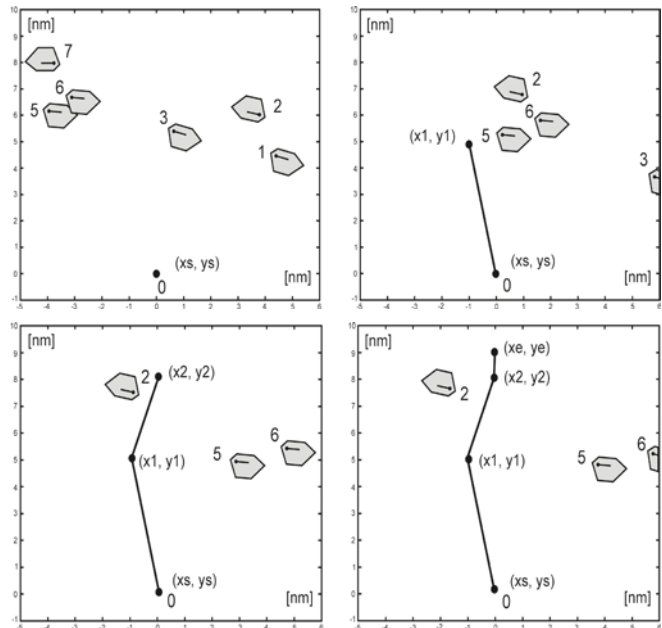


Fig. 6. Solution to the situation of meeting with 7 ships in the Kattegat Strait [35]

OPTIMIZATION OF SAFE SHIP CONTROL BY MEANS OF DYNAMIC PROGRAMMING

Determining the optimal control of the ship in the sense of a fixed control quality indicator can be made by using Bellman's principle of optimality. The principle defines the basic possession of an optimal strategy – regardless of the status and initial decisions, the remaining decisions must form strategies that are optimal from the point of view of the state resulting from the first decision. The principle of optimality is described by the Bellman functional equation:

$$\frac{\partial S}{\partial t} - \min_u \left[f_o(x, u, t) + f(x, u, t) \frac{\partial S}{\partial x} \right] = 0 \quad (15)$$

where: x – state of process, u – control, t – time, f_o – cost function, f – process state function.

Function S is:

$$S(x, t) = \min F = \min \int_0^\infty f_o(x, u, t) dt \quad (16)$$

The optimal time for ship to travel k stages will be:

(17) By going from the first stage to the last one the formula (17) determines the Bellman's functional equation for the process of the ship's control by the alteration of the rudder

$$t_k^* = \min_{u_{1,k-2}, u_{2,k-2}} \left\{ t_{k-1}^* [x_{1,k}, x_{2,k}, x_{3,k-1}, x_{4,k-1}, x_{5,k-1}, x_{6,k-1}] + \Delta t_k [x_{1,k}, x_{2,k}, x_{1,k+1}(x_{1,k}, x_{3,k}(x_{3,k-1}, x_{4,k-1}(x_{4,k-2}, u_{1,k-2}, \Delta t_{k-2}), \Delta t_{k-1}), x_{5,k}(x_{5,k-1}, x_{6,k-1}, (x_{6,k-2}, u_{2,k-2}, \Delta t_{k-2}) \Delta t_{k-1}), x_{2,k+1}(x_{2,k}, x_{3,k}(x_{3,k-1}, x_{4,k-1}(x_{4,k-2}, u_{1,k-2}, \Delta t_{k-2}, \Delta t_{k-1}) x_{5,k}(x_{5,k-1}, x_{6,k-1}(x_{6,k-2}, u_{2,k-2}, \Delta t_{k-2}), \Delta t_{k-1})))] \right\}$$

$k = 3, 4, \dots, K$

where:

- coordinates of ship's position: $x_1=x, x_2=y$;
- ship's course: $x_3=\psi$;
- angular speed of the ship's return: $x_4 = \dot{\psi}$;
- ship's speed: $x_5=V$;
- acceleration of the ship: $x_6 = \dot{V}$;
- time: $x_7=t$;
- relative rudder deflection: $u_1=\alpha/a_m$;
- relative change in rotational speed of the main screw propeller: $u_2=n/n_m$ [5].

By moving from the first to the last stage, the Bellman function equation is obtained for the ship control process by changing the rudder angle and the rotational speed of the propeller.

Including constraints resulting from the safe approach, the right path recommendations consist in checking if the state variables did not exceed the limits in each considered node and reject the nodes in which a violation was detected.

Constraints of state variables and control variables form a separate calculation procedure in the algorithm for determining the dynamic safe trajectory of a ship.

Fig. 7 shows the division of the ship's path into k stages and n nodes.

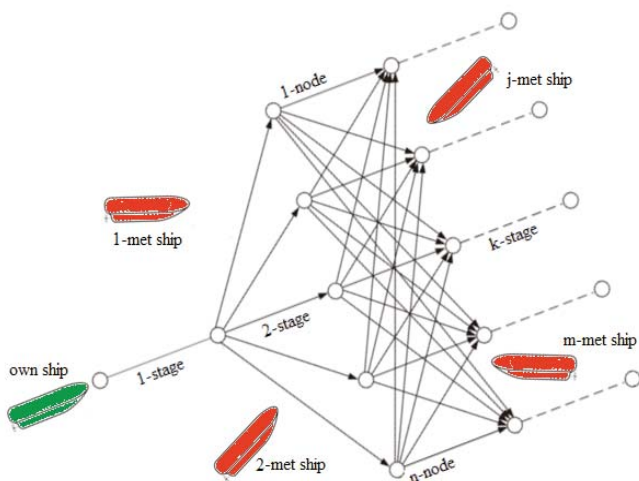


Fig. 7. Determination of the own ship safe and optimal trajectory by means of dynamic programming method

angle and the rotational speed of the propeller. The constraints for the state variables and the control values generate the *Neural Constraints (NC)* procedure in the computer algorithm Dynamic Programming Trajectory - DPT for the determination of the safe ship trajectory.

The consideration of the constraints resulting from maintaining safe approaching distance and the recommendations of the way priority law is performed by checking whether the state variables have not exceeded constraints in each of the considered intersections and by rejecting the intersections in which a violation has been discovered.

The safe trajectories of own ship in the situation of passing by $J=10$ ships met in conditions of good visibility at sea are shown in Fig. 8, and in restricted visibility at sea – in Fig. 9, determined by the DPT algorithm.

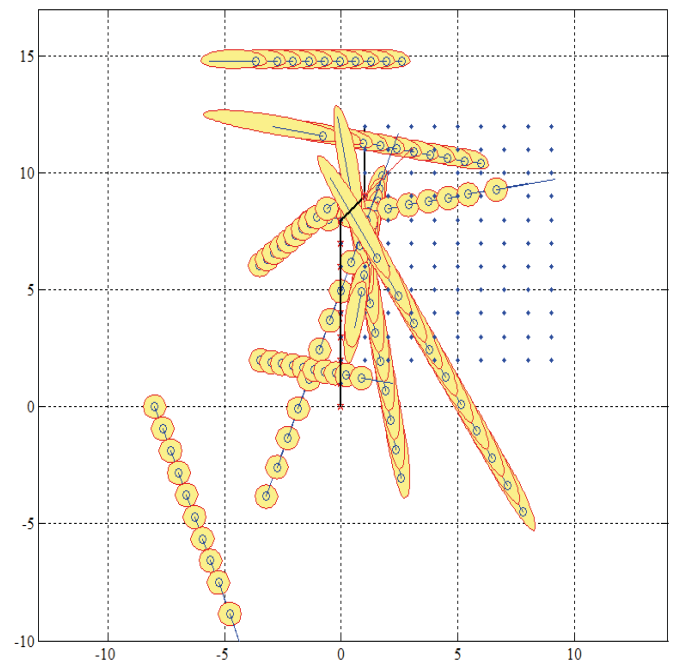


Fig. 8. Optimal and safe trajectory of own ship while passing by $J=10$ ships encountered in conditions of good visibility at sea, $D_s=0.5$ nm, $t_k^*=49.66$ min

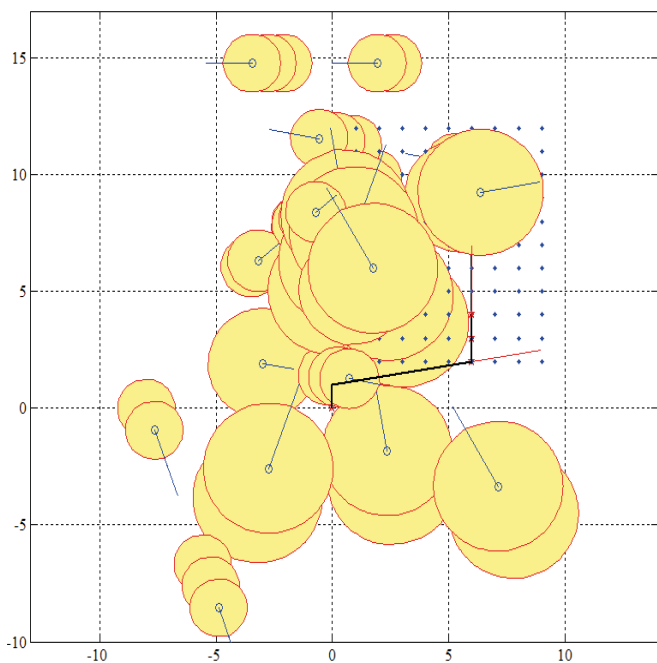


Fig. 9. Optimal and safe trajectory of own ship while passing by $J=10$ ships encountered in conditions of restricted visibility at sea, $D_s=2.0$ nm, $t_k^*=68.33$ min

OPTIMIZATION OF SAFE SHIP CONTROL BY MEANS OF MULTI-CRITERIA GAME CONTROL

In order to ensure the safety of navigation, ships are obliged to respect the legal requirements in the form of COLREGs rules. However, the rules apply only to two ships in terms of good visibility. In the conditions of limited visibility, they only give general recommendations and are not able to take into account all the necessary conditions of the actual process. Thus, the actual process of passing ships occurs under indefinite conditions and conflict with inaccurate cooperation of ships in accordance with the principles of COLREGs.

Therefore, it is expedient to present the process of safe control of the ship as well as development of the appropriate control methods and testing their operation, by using the rules of game theory.

For practical synthesis of control algorithms, positional and matrix game models are used.

The essence of the positional game is the dependence of the own ship's strategy on the ship's position $p(t_k)$ at the current step k .

The optimal control of own ship for non-cooperative game is determined from the following criterion:

$$F(x)_{nc}^* = \min_{u_0 \in U_0} \left\{ \max_{u_{j,0} \in U_{j,0}} \min_{u_{0,j} \in U_{0,j}} S[x_0(t_k)] \right\} \quad (18)$$

$j = 1, 2, \dots, J$

and for cooperative game:

$$F(x)_c^* = \min_{u_0 \in U_0} \left\{ \min_{u_{j,0} \in U_{j,0}} \min_{u_{0,j} \in U_{0,j}} S[x_0(t_k)] \right\} \quad (19)$$

$j = 1, 2, \dots, J$

Trajectories of own ship in the situation of $J=19$ ships encountered in the Kattegat Strait in restricted visibility at sea with $D_s=1.6$ nm, determined according to the non-cooperative positional game algorithm are shown in Fig 10, and for cooperative positional game - in Fig. 11.

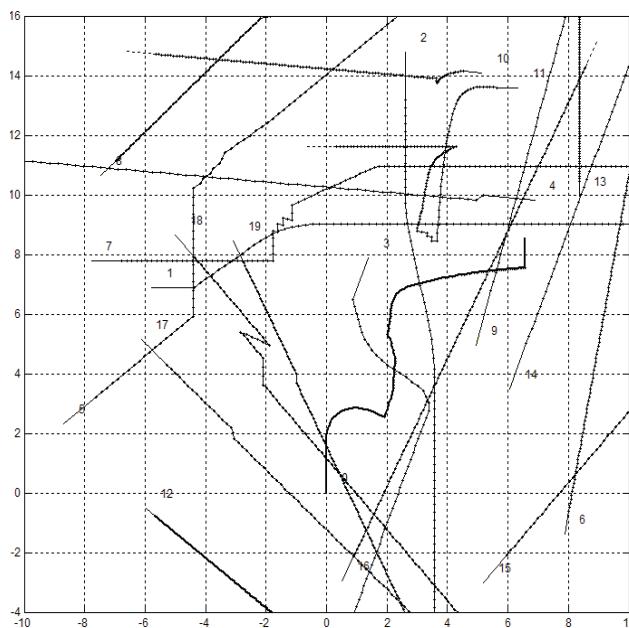


Fig. 10. Computer simulation of multi-stage non-cooperative positional game algorithm for safe own ship control in situation of passing $J=19$ encountered ships in restricted visibility at sea, $D_s=1.4$ nm, $d(t_k)=6.56$ nm

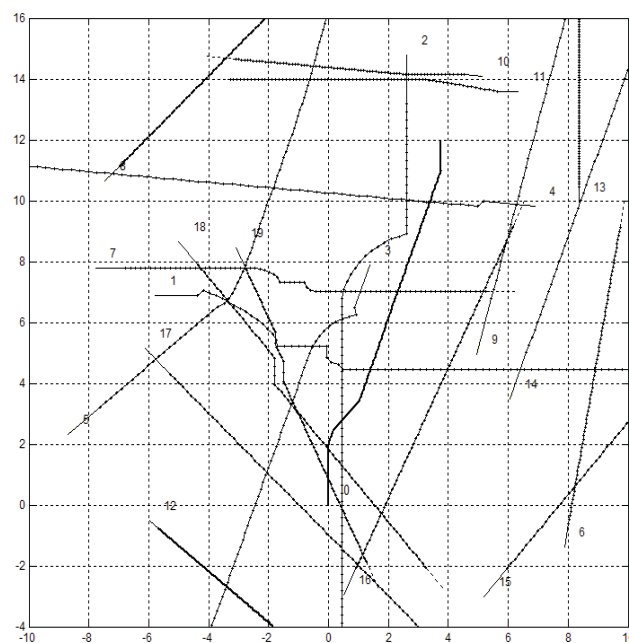


Fig. 11. Computer simulation of multi-stage cooperative positional game algorithm for safe own ship control in situation of passing $J=19$ encountered ships in restricted visibility at sea, $D_s=1.4$ nm, $d(t_k)=3.75$ nm

CONCLUSIONS

In synthesis of the controller or the optimal control algorithm for a given transport or logistic object, both static and dynamic analytical and numerical optimization methods can be used.

However, various optimization tasks in practical applications are most often solved by means of appropriate numerical methods of static and dynamic optimization.

ACKNOWLEDGEMENTS

This research was supported by the Ministry of Science and Higher Education, within the framework of funds for statutory activities No. 446//DS/2018 of the Electrical Engineering Faculty, Gdynia Maritime University, Poland.

BIBLIOGRAPHY

1. Dorf R.C., Bishop R.H.: *Modern control systems*. Addison Wesley Longman, California, 2012.
2. Engwerda J.C.: *LQ dynamic optimization and differential games*. John Wiley & Sons, West Sussex, 2005.
3. Guenin B., Konemann J., Tuncel L.: *A gentle introduction to optimization*. Cambridge University Press, United Kingdom, 2014.
4. King M.: *Process control*. Wiley, West Sussex, 2011.
5. Lazarowska A., Lisowski J.: *The radar data transmission to computer support system of ship safety*. Solid State Phenomena, Vol. 196, 2013, pp. 95-101.
6. Lazarowska A.: *Swarm intelligence approach to safe ship control*. Polish Maritime Research, 2015, Vol. 22, Issue 4, pp. 34-40.
7. Lebkowski A.: *3D navigator decision support system using the smart glasses technology*. Edited by Weintrit A., Neumann T.: Information, communication and environment – marine navigation and safety sea transportation, 2015, pp. 117-122.
8. Lisowski J.: *Game control methods in avoidance of ships collisions*. Polish Maritime Research, 2012, Vol. 19, Special Issue, pp. 3-10.
9. Lisowski J.: *Optimization methods* (in Polish). Wydawnictwo Akademii Morskiej w Gdyni, 2017.
10. Malecki J.: *Fuzzy track-keeping steering design for a precise control of the ship*. Solid State Phenomena, 2013, Vol. 196, pp. 140-147.
11. Nisan N., Roughgarden T., Tardos E., Vazirani V.V.: *Algorithmic game theory*. Cambridge University Press, New York, 2007, pp. 717-733.
12. Speyer J.L., Jacobson D.H.: *Primer on optimal control theory*. SIAM, Toronto, 2010.
13. Szlupczynski R., Smierzchalski R.: *Supporting navigator's decisions by visualizing ship collision risk*. Polish Maritime Research, 2009, Vol. 16, Issue 1, pp. 83-88.
14. Szymak P.: *Comparison of centralized, dispersed and hybrid multi-agent control systems of underwater vehicles team*. Solid State Phenomena, Vol. 180, pp. 114-121.
15. Zak A.: *Controlling a team of unmanned underwater vehicles performing water region search tasks*. Polish Maritime Research, 2013, Vol. 20, Issue 2, pp. 82-89.
16. Zwierzewicz Z.: *On the ship course-keeping control system design by using robust and adaptive control*. Proc. 19th Int. Conf. on Methods and Models in Automation and Robotics, Miedzyzdroje, Poland, 2014, pp. 189-194.

CONTACT WITH THE AUTHOR

Józef Lisowski

e-mail: j.lisowski@we.am.gdynia.pl
Gdynia Maritime University
83 Morska Str.
81-225 Gdynia
POLAND

PATH FOLLOWING CONTROL OF FULLY ACTUATED AUTONOMOUS UNDERWATER VEHICLE BASED ON LADRC

Habib Choukri Lamraoui

Zhu Qidan

Harbin Engineering University, Harbin, China

ABSTRACT

This paper presents an active disturbances rejecter controller (ADRC) for position and path following control of a fully actuated autonomous underwater vehicle (AUV). The unmodeled, undesirable dynamics and disturbances reduce the performances of classical controllers and complicate the design of appropriate and efficient controllers. In the proposed approach, the different modeling complexities; such as uncertain parameters, non-linearities, and external disturbances are considered all as a part of disturbance which is estimated in real-time by the extended state observer ESO, and effectively compensated from the control law. The ESO is also able to estimate the position and velocity of the system in real-time, in case where the full state measurement of the AUV is not possible during experiments. Computer simulations demonstrate the high ability of the AUV tracking control based on ADRC, to follow the desired trajectory in the horizontal plane and space with high precision, and showed high robustness and efficiency in rejecting the external and internal disturbances caused by significant changes in parameters of the system, and the added position disturbances.

Keywords: ADRC, Path following, AUV, uncertain parameters, ESO, Control law.

INTRODUCTION

An autonomous underwater vehicle (AUV) is a type of unmanned underwater vehicles (UUV), operating independently of the human intervention. AUVs have been widely studied and took part in a lot of research and works due to their huge use and domain of application; such as surveillance, reconnaissance [1], anti-submarine warfare, mine countermeasures, mapping of the ocean floor, and pipeline inspection.

The control of AUVs appears imperatively as a pertinent topic of study in order to enable the AUV to execute its task autonomously and reach the desired system behavior. Classical controllers were firstly considered in the AUV's control. A survey of traditional controllers applied to AUV's and their limitations were well addressed in [2]

In order to ameliorate the robustness and accuracy, several control technique and strategies have been proposed such as: proportional-integral-derivative (PID) [3] Integer and

fractional order PID controllers in trajectory tracking [4], robust adaptative control [5–6], robust Fuzzy Logic and PID Control in [7], time delay controller in [8].

More robust controllers have been designed in this area; including a feedback linearization controller for AUV's control [9], self-adaptative fuzzy PID [10], and a combination of different control techniques (adaptative, FLC and Sliding Mode Control (SMC)) in order to reduce the chattering of the SMC to maintain the robustness of the model uncertainties in [11].

In the last decade, the Active Disturbance Rejection Controller (ADRC) introduced by Han in [12], has presented the best immunity to the internal and external disturbances and proved its robustness and independence of mathematical models. Very encouraging results in terms of disturbance rejection have been reported for the ADRC approach, in the control of a cross-coupled highly non-linear aerodynamic system in [13], and in terms of robustness to significant modeling uncertainty in the control of 2-DOF manipulator [14], in the control of mobile robots [15], quadrotors [16]

and manipulators [17]. The results obtained in the works mentioned above encouraged the authors to consider this approach in this work.

The contribution of this paper is the design of an appropriate controller based on ADRC, for position and path following control to force the AUV to track the desired trajectory in the dynamic environment in the presence of disturbances and modeling uncertainties. ADRC contains an extended state observer ESO which is able to estimate in real-time, firstly the position and velocity of the vehicle without the need of using sensors, secondly an extended state variable that represents the value of disturbances, uncertainties and unknown dynamics missed in the modeling, and other undesired dynamics such as the coupling terms. The estimated value of disturbances will be compensated from the control signal which ameliorates the controller's performance and robustness.

For simplicity, the linear version of ADRC called LADRC, and some assumptions were considered in the AUV's modeling and control design. Numerical simulations were run in MATLAB/Simulink, and they illustrate the efficiency of the proposed controller in tracking the desired trajectory and rejecting the different undesired effects. The obtained results are very satisfactory compared to some existing approaches; bio-inspired velocity regulation for three-dimensional trajectory tracking for underactuated AUVs with constant disturbances in [18], and adaptative tracking control for AUV under hydrodynamic parametric uncertainties in [19], nonlinear model predictive control (NMPC) method for the trajectory tracking problem of an autonomous underwater vehicle [20], robust non-linear controller of an autonomous underwater vehicle (AUV) in [21], and L2 Disturbance Attenuation Control for Path Following of AUV in 3D [22].

The paper is organized as follows. Section 2 presents the kinematic and dynamic modeling of the AUV. The design of LADRC based control law for the AUV to track the desired trajectory is developed in Section 3. To verify the efficiency and robustness of the proposed control law, numerical simulations are made. Results discussion is provided in Section 4. Finally, conclusions are presented in Section 5.

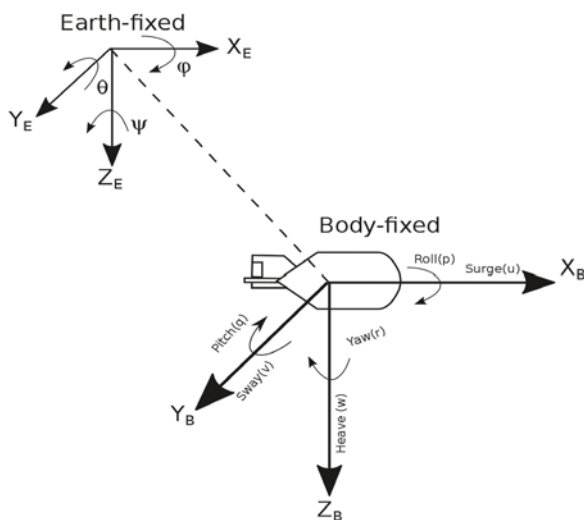


Fig. 1. AUV coordinate system

SYSTEM MODELING

KINEMATICS

The kinematic description represents the motion of the vehicle regardless of the effect of the forces acting on it.

To do this, Earth reference frame {E} and a Body-Fixed reference {B} frame are employed as showed in Fig.1.

The different degrees of freedom of the AUV are detailed in Table.1, and the position and velocity vectors of the AUV defined in the body frame {B} are χ and v respectively as:

$$\chi = [x_B, y_B, z_B, \varphi_B, \theta_B, \psi_B] \quad (1)$$

$$v = [u, v, w, p, q, r] \quad (2)$$

Tab. 1. Degrees of freedom of the AUV

Degree Of Freedom	Positions and Euler angles	Linear and angular velocities
motions in the x-direction (Surge)	x	u
motions in the y-direction (Sway)	y	v
motions in the z-direction (Heave)	z	w
rotation about x-axis (Pitch)	φ	p
rotation about y-axis Roll	θ	q
rotation about z-axis (Yaw)	ψ	r

The motion of the AUV can be described by:

$$\dot{\eta} = R(\eta) * v \quad (3)$$

Where $\dot{\eta}$ is the velocity vector expressed in the earth frame {E}, and R is the transformation matrix between {B} and {E} determined by

$$R(\eta) = \text{diag} \{R1(\varphi, \theta, \psi), R2(\varphi, \theta, \psi)\} \quad (4)$$

$$R1 = \begin{bmatrix} C\theta C\psi & -C\theta S\psi + S\theta S\psi & S\theta S\psi + C\theta C\psi \\ C\theta S\psi & C\theta C\psi + S\theta S\psi & -S\theta C\psi + C\theta S\psi \\ -S\theta & S\theta C\theta & C\theta C\theta \end{bmatrix} \quad (5)$$

$$R2 = \begin{bmatrix} 1 & S\varphi T\theta & C\varphi T\theta \\ 0 & C\varphi & -S\varphi \\ 0 & S\varphi / C\theta & C\varphi / C\theta \end{bmatrix} \quad (6)$$

Where $C.=\cos(\cdot)$, $S.=\sin(\cdot)$, and $T.=\tan(\cdot)$

$R1$ is a derivation of the rotation matrix and $R2$ a derivation of the coordinate transform matrix.

DYNAMICS

The dynamic modeling is a study of the motion of the vehicle taking into consideration the forces affecting it and the physical characteristics of the robot. Since these forces and the AUV's dynamics are highly complex, some assumptions have been considered to simplify the control design task:

- The AUV operates at low speed.
- The AUV is symmetric in the XZ plane and YZ plane.
- Roll and Pitch degrees of freedom are neglected.

Considering these assumptions, several terms can be eliminated from the dynamic model matrices. Any unmodeled dynamics will be considered as a disturbance and, they will be estimated by the LESO, and compensated from the control law.

After considering the previous assumptions, the simplified kinematics are represented by (7)

$$\begin{cases} \dot{x} = u \cos(\psi) - v \sin(\psi) \\ \dot{y} = u \sin(\psi) + v \cos(\psi) \\ \dot{z} = w \\ \dot{\psi} = r \end{cases} \quad (7)$$

$$M\dot{v} + C(v)v + D(v)v + g(\eta) = \tau \quad (8)$$

The terms of the dynamic model defined by (8), can be simplified and presented in the following subsections.

Mass and Inertia Matrix:

The mass and inertia matrix consist of the mass and inertia of the rigid body M_B and the added mass matrix M_A , with

$$M = M_B + M_A \quad (9)$$

$$M_B = \begin{bmatrix} m & 0 & 0 & 0 \\ 0 & m & 0 & 0 \\ 0 & 0 & m & 0 \\ 0 & 0 & 0 & I_{zz} \end{bmatrix} \quad (10)$$

$$M_A = \begin{bmatrix} -X_{\dot{u}} & 0 & 0 & 0 \\ 0 & -Y_{\dot{v}} & 0 & 0 \\ 0 & 0 & -Z_{\dot{w}} & 0 \\ 0 & 0 & 0 & -N_{\dot{r}} \end{bmatrix} \quad (11)$$

Coriolis and Centripetal Matrix

The Coriolis and centripetal matrix consists of the rigid body term C_B and the added mass term C_A with

$$C = C_B + C_A \quad (12)$$

$$C_B(v) = \begin{bmatrix} 0 & 0 & 0 & -mv \\ 0 & 0 & 0 & mu \\ 0 & 0 & 0 & 0 \\ mv & -mu & 0 & 0 \end{bmatrix} \quad (13)$$

$$C_A(v) = \begin{bmatrix} 0 & 0 & 0 & Y_{\dot{v}}v \\ 0 & 0 & 0 & -X_{\dot{u}}u \\ 0 & 0 & 0 & 0 \\ Y_{\dot{v}}v & X_{\dot{u}}u & 0 & 0 \end{bmatrix} \quad (14)$$

Hydrodynamic Damping Matrix

The hydrodynamic damping of AUV is composed of the drag and lift forces since the AUV is assumed to be operating in low speed so the lift force can be neglected, and the drag force consists of two terms; linear D_l and quadratic D_q where

$$D = D_l + D_q \quad (15)$$

and

$$D_l = \begin{bmatrix} -X_u & 0 & 0 & 0 \\ 0 & -Y_v & 0 & 0 \\ 0 & 0 & -Z_\omega & 0 \\ 0 & 0 & 0 & -N_r \end{bmatrix} \quad (16)$$

$$D_q = \begin{bmatrix} -X_{u|u}|u| & 0 & 0 & 0 \\ 0 & -Y_{v|v}|v| & 0 & 0 \\ 0 & 0 & -Z_{\omega|\omega}|\omega| & 0 \\ 0 & 0 & 0 & -N_{r|r}|r| \end{bmatrix} \quad (17)$$

Gravitational and Buoyancy Matrix

$$g(\eta) = \begin{bmatrix} 0 \\ 0 \\ -(W - B) \\ 0 \end{bmatrix} \quad (18)$$

where

$$W = mg \quad \text{and} \quad B = \rho g \nabla \quad (19)$$

The full AUV dynamic model for 4 DOF is

$$\begin{cases} (m - X_{\dot{u}})\dot{u} - (X_u + X_{u|u}|u|)u - (m - Y_{\dot{v}})vr = \tau_x \\ (m - Y_{\dot{v}})\dot{v} - (Y_v + Y_{v|v}|v|)v + (m - X_{\dot{u}})ur = \tau_y \\ (m - Z_{\dot{\omega}})\dot{\omega} - (Y_\omega + Y_{\omega|\omega}|\omega|)\omega = \tau_\omega \\ (m - N_{\dot{r}})\dot{r} - (N_r + N_{r|r}|r|)r + (X_{\dot{u}} + Y_{\dot{v}})uv = \tau_r \end{cases} \quad (20)$$

CONTROL SYSTEM

ADRC

Contrary to traditional approaches dependent on mathematical modeling of the system, and the disturbances acting on it, the ADRC approach is less dependent on mathematical modeling. This control technique presented in [12], has the ability to react in real-time to external and internal disturbances affecting the system, thanks to the ESO which actively estimates the total disturbances, then compensates them from the control signal. Since the unmodeled dynamics and the model uncertainties are considered as a part of the total disturbance, the accurate mathematical models are no more indispensable to accomplish the desired tasks.

APPLICATION OF LADRC TO AUV

Considering the dynamic model of the AUV for 4 DOF, LADRC has been designed for each degree of freedom, the control design for the surge channel illustrated in Fig.2 is presented in this section. The other degrees of freedom are controlled in the same way.

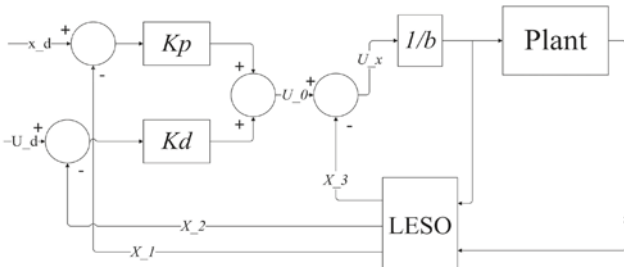


Fig. 2. Surge control loop based on

By considering the assumptions made in the previous section and the full AUV dynamic model for 4 DOF, the one degree of freedom (surge) dynamic equation is:

$$m_{11}\ddot{u} - d_{11}\dot{u} - m_{22}vr = \tau_x \quad (21)$$

where

$$\begin{cases} m_{11} = m - X_{\dot{u}} \\ m_{22} = m - Y_{\dot{v}} \\ d_{11} = X_u + X_{u|u}|u| \end{cases} \quad (22)$$

Equation (21) can be expressed in the Body frame {B} as

$$\ddot{x} = 1/m_{11}(d_{11}\dot{x} + m_{22}\dot{y}\dot{\psi} + \tau_x) + ds \quad (23)$$

d_s is the disturbance term, then the disturbance function f_x is introduced in (24)

$$\ddot{x} = f_x(\dot{x}, \dot{y}, \dot{\psi}, t, ds) + b_x U_x \quad (24)$$

where $b_x = \frac{1}{m_{11}}$ and $U_x = \tau_x$,

The state space form of the system can be written as:

$$\begin{cases} \dot{x}_1 = x_2 \\ \dot{x}_2 = f_x(\dot{x}, \dot{y}, \dot{\psi}, t, ds) + b_x U_x \\ y = x_1 \end{cases} \quad (25)$$

Then, the state space is extended by an additional state variable $x_3 = f_x(\dot{x}, \dot{y}, \dot{\psi}, t, ds)$, which estimates total disturbances, and the extended system state is presented below:

$$\begin{cases} \dot{x}_1 = x_2 \\ \dot{x}_2 = x_3 + b_x U_x \\ \dot{x}_3 = f_x \end{cases} \quad (26)$$

Now, a following third order LESO is designed for the above system:

$$\begin{cases} \dot{\hat{x}}_1 = \hat{x}_2 - \beta_1 \varepsilon_1 \\ \dot{\hat{x}}_2 = \hat{x}_3 - \beta_2 \varepsilon_1 + b_x U_x \\ \dot{\hat{x}}_3 = -\beta_3 \varepsilon_1 \end{cases} \quad (27)$$

The control law of the surge is described by the following equation:

$$U_x = \frac{U_0 - \hat{x}_3}{b_x} \quad (28)$$

$\hat{x} = \hat{f}_x$ and U_0 is a simple PD controller chosen for each LADRC control loop.

$$U_0 = K_p(x_r - \hat{x}_1) + K_d(\dot{x}_r - \dot{\hat{x}}_2) \quad (29)$$

To simplify the tuning of the parameters of the LESO and the controller, they have been set as (30), and the tuning is reduced from 5 to 2 parameters.

$$\begin{cases} \beta_1 = 3\omega_0 \\ \beta_2 = 3\omega_0^2 \\ \beta_3 = \omega_0^3 \\ K_p = \omega_c^2 \\ K_d = 2 * \omega_c \end{cases} \quad (30)$$

where ω_0 is the observer bandwidth and ω_c is the closed loop bandwidth. The LESO and controller gains are set as (30) to ensure the Hurwitz stability [23–24].

By inserting equation (28) in equation (24), one obtains:

$$\begin{cases} \ddot{x} = f_x(\dot{x}, \dot{y}, \dot{\psi}, t, ds) + b_x U_x \\ \ddot{x} = U_0 \end{cases} \quad (31)$$

The system can now be expressed as the following disturbance-free system

$$\begin{cases} \dot{x}_1 = x_2 \\ \dot{x}_2 = U_0 \\ y = x_1 \end{cases} \quad (32)$$

The above model can be rewritten using tracking error:

$$\begin{cases} e_1 = x_d - x_1 \\ \dot{e}_1 = \dot{x}_d - \dot{x}_1 = \dot{x}_d - x_2 \\ \ddot{e}_1 = \ddot{x}_d - \ddot{x}_2 = \ddot{x}_d - U_0 \end{cases} \quad (33)$$

where x_d is the desired value of state x , and U_0 is the feedback controller responsible for minimizing the tracking error:

$$U_0 = \ddot{x}_d + K_p(x_r - \hat{x}_1) + K_d(\dot{x}_r - \hat{x}_2) \quad (34)$$

By applying (34) to the last term of (33), the error dynamic equation is obtained as

$$\ddot{e}_1 + K_d \dot{e}_1 + K_p e_1 = 0 \quad (35)$$

According to (35), by setting the controller gains, the exponential convergence of the tracking error to zero for any initial condition will be obtained.

The 4D control loop based on LADRC is presented in Fig. 3

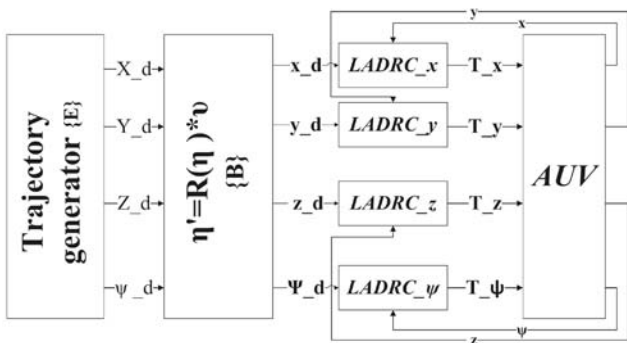


Fig. 3. Control structure of LADRC scheme

SIMULATION AND RESULTS

In order to verify the efficacy of the proposed path following control law, computer simulations are carried out considering different desired trajectories.

The parameters of the AUV used in the numerical simulations are listed in table 2

Tab. 2. AUV's parameters used in simulation

mass (kg)	Damping coefficients (Ns/m)
$m_{11} = 215$	$d_{11} = 70 + 100 u $
$m_{22} = 265$	$d_{22} = 100 + 200 v $
$m_{33} = 265$	$d_{33} = 100 + 200 \omega $
$m_{44} = 80$	$d_{44} = 50 + 100 r $

2D PATH

The AUV is set to track a desired 2D curvy trajectory (red dashed line) in the XY plane as shown in the figure below.

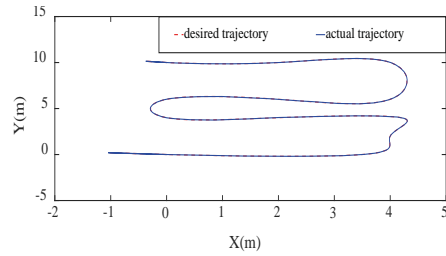


Fig. 4. AUV 2D path following

Fig. 4 shows the matching between the desired and the actual trajectory, which means that a precise tracking was assured by the proposed controller.

Positions and velocities are represented in Fig. 5 and Fig. 6.

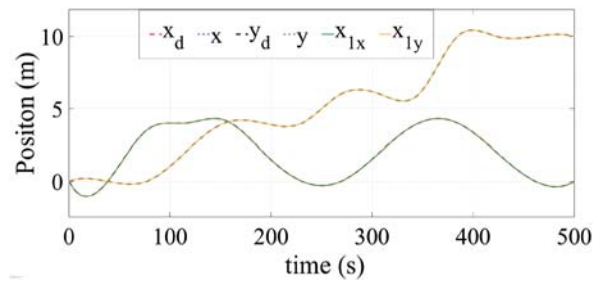


Fig. 5. Actual, estimated and desired positions

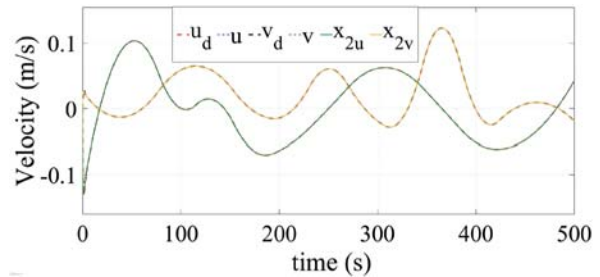


Fig. 6. Actual, estimated and desired velocities

Fig. 5 and Fig. 6 show the match between the estimated, the actual and the desired positions and velocities, respectively, which proves the efficiency of the LESO in estimating the full state of the AUV during the tracking task, and the satisfactory tracking accuracy presented by the proposed controllers.

Positions and velocities errors are represented in Fig. 7 and Fig. 8.

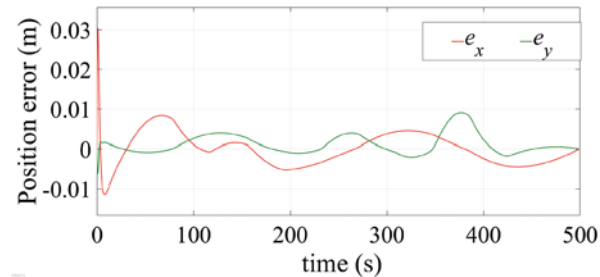


Fig. 7. Position errors

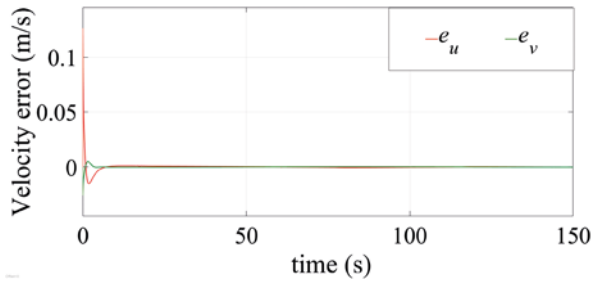


Fig. 8. Velocity errors

Fig. 7 and Fig. 8 show the positions and velocities errors. From these figures, it is observed that the errors converge to zero in less than 5s and the error is acceptable considering the changes due to the turns in the desired trajectory.

Fig. 9 shows the real-time estimation of the disturbances during the tracking.

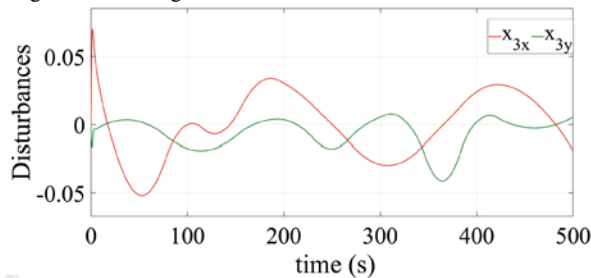


Fig. 9. Disturbances estimator

The torques or control inputs are represented in Fig.10.

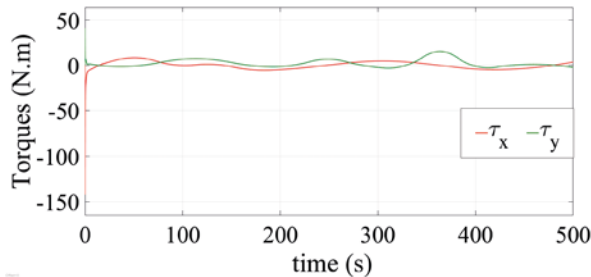


Fig. 10. Torques

Fig. 10 represents the torques or control signals applied to the AUV. It shows that in the first 5 seconds of motion, the torques have high values due to the AUV's trend to catch the desired positions and velocities, which introduce considerable acceleration that will decrease when the trajectory is smooth, and increase a bit when there are sudden changes in the curve.

Fig. 11 represent the trajectory tracking for different initial conditions ($x_0 = -1, y_0 = -1$), so initial errors are ($x_e = -1, y_e = -1$). From this figure, the fast convergence of the AUV to the desired trajectory is observed with a small initial overshoot.

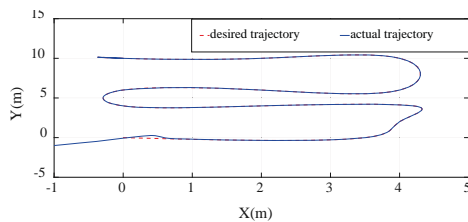


Fig. 11. 2D path following with different initial positions

3D PATH FOLLOWING: SPIRAL PATH

The referenced path presented in Fig.11 is a spiral path in space defined as:

$$\begin{cases} x_d = 10 \sin(0.01t) \\ y_d = 10 \cos(0.01t) \\ z_d = t \\ \psi_d = \pi/3 \end{cases} \quad (36)$$

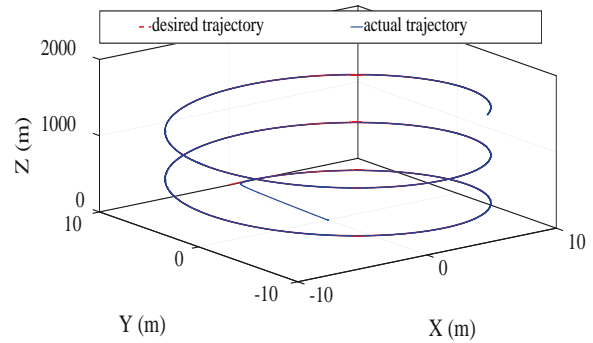


Fig. 12. AUV spiral path following

The XY plane projection of the desired path is illustrated in Fig. 12.

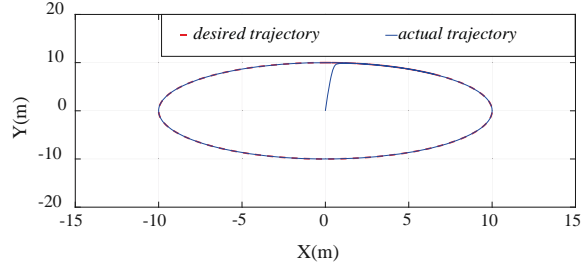


Fig. 13. XY plane projection

Fig. 12 and Fig. 13 illustrate the desired and tracked spiral paths followed by the AUV in the space and the XY plane. From these figures, it is clear that the proposed control law assured a precise tracking of the path.

Fig. 14 and Fig. 15 show the desired and actual positions and velocities. From these figures, the match between the desired and actual positions and velocities of the AUV are well observed which proves good tracking performance of the controller.

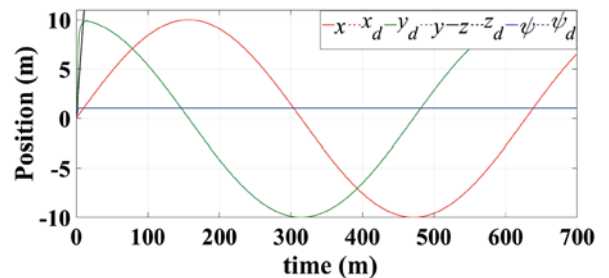


Fig. 14. Actual and desired positions

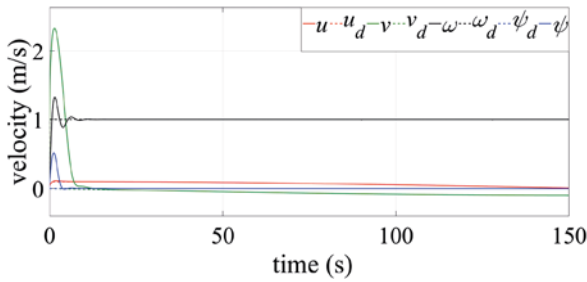


Fig. 15. Actual and desired velocities

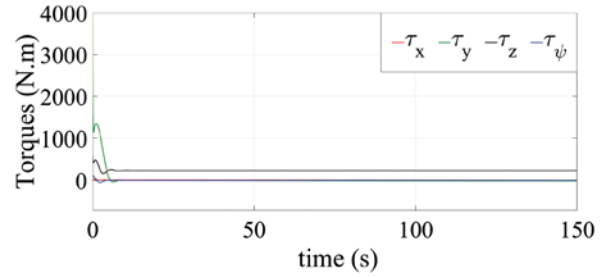


Fig. 19. Torques

Fig. 16 and Fig. 17 show the positions and velocities errors. From these figures, it is observed that the errors in the surge, heave, and yaw converge to zero in 5s and the error in the sway after 10s from the beginning.

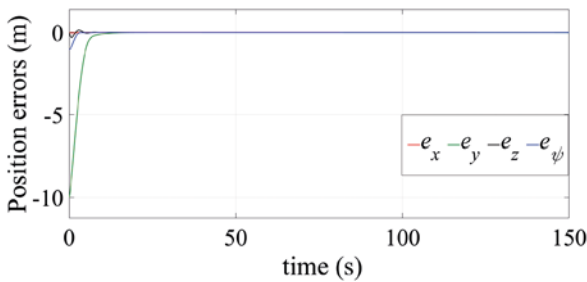


Fig. 16. Position errors

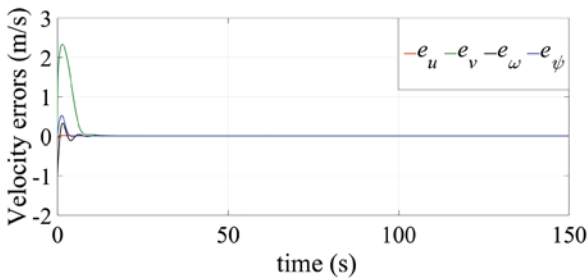


Fig. 17. Velocity errors

Fig. 18 represents the estimated value of the different external and internal disturbances during the tracking time.

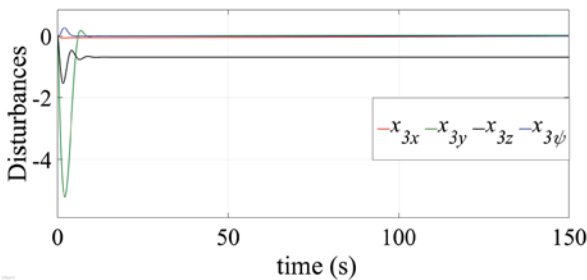


Fig. 18. Disturbances estimator

Fig. 19 illustrates the torques or control signals applied to the AUV. It shows that in the beginning stage of motion torques had peak values due to the AUV's trend to catch the desired positions which provoke a considerable acceleration that will gradually tend to a constant value (zero in the case of z and psi).

SPIRAL PATH FOLLOWING UNDER UNCERTAINTIES AND DISTURBANCES EFFECTS

In order to evaluate the proposed LADRC-based control under parameter uncertainties and external disturbances, the tracking controllers are tested under a perturbed parameters situation as in (36) and (37), and added disturbances to the surge position signal as white noise, and to the heave position signal as a step signal, as detailed in table 3.

Tab. 3. Disturbances

Perturbation signal	Time	Value
Step	300 s	15 m
White noise	500 s	0.02 m

$$\begin{cases} m_{11} = m_{11} + 20\%m_{11} \\ m_{33} = m_{33} + 20\%m_{33} \end{cases} \quad (37)$$

And

$$\begin{cases} d_{11} = d_{11} + 20\%d_{11} \\ d_{33} = d_{33} + 20\%d_{33} \end{cases} \quad (38)$$

The path tracking under disturbances and uncertain parameters and disturbances is shown with the disturbance-free path, and the desired path in Fig. 20 and the XZ plane projection in Fig. 21.

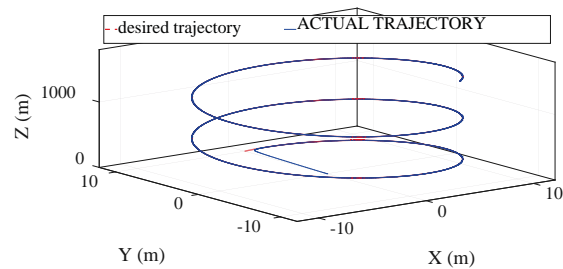


Fig. 20. AUV spiral path following with disturbances and uncertain parameters

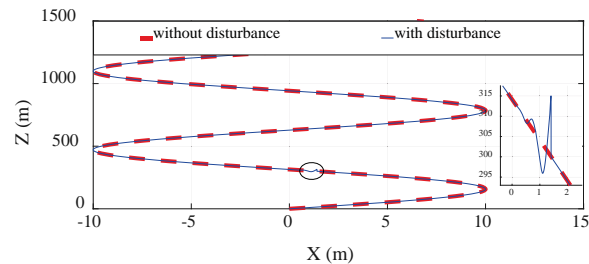


Fig. 21. XZ plane projection

As shown by the figures above, the tracking performances were slightly affected by the uncertainties in parameters values and the added position disturbances.

The LADRC has a strong ability to reject disturbance in a short time and re-join the zero-error steady state, thanks to the compensation of the disturbances values estimated by x_3 as shown in Fig. 22.

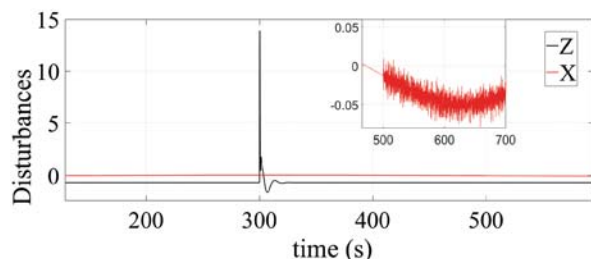


Fig. 22. Disturbances estimator

CONCLUSION

In this paper, the path following control of autonomous underwater vehicles has been carried out. First, a simplified model of the AUV has been established. Then, a LADRC based controller has been designed for each degree of freedom in order to track the desired positions.

The designed extended state observer (ESO) has effectively estimated the full state of the system, which is extremely useful and practical in the case of unmeasured states due to inaccessibility to sensors information during the experiments. The extended state variable has estimated the total disturbances value that were canceled out from the control signal.

The path following control for AUV based on LADRC showed good tracking performance when it is moving in the plane and space, with a satisfactory accuracy that can be concluded by comparing the actual and desired positions and velocities, and the convergence of related errors to zero.

To evaluate the robustness of the proposed controller, the system has been tested under model uncertainties and added disturbances. The obtained results confirm the ability of the LADRC based controllers to reject the different disturbances, and its immunity to the modeling uncertainties.

By analysing the obtained simulation results on the background of some related works [18, 22], the following points has been concluded:

- Comparing to [18, 19]; in the tracking of 3D spiral path, the authors proposed approach presented faster path convergence speed, and better tracking performance in term of tracking errors, overshoot and response time of the system.
- Comparing to [20]; in the tracking of a circular path in the plane, the proposed approach has presented more accurate trajectory tracking.
- Comparing to [21], better tracking performance and robustness has been reported for the authors proposed approach in the tracking of a 2D curved trajectory.

- Comparing to a closer approach which has been presented in [22], basing on disturbances attenuation control, better tracking accuracy, and robustness is also reported.

In the future works, the authors consider the frequency domain study and stability analysis of the proposed system, and validating it with an experimental study.

CONFLICT OF INTEREST

The authors declare that there is no conflict of interest regarding the publication of this paper.

REFERENCES

1. S.Karthik, *Underwater vehicle for surveillance with navigation and swarm network communication*, in Indian Journal of Science and Technology, October 2014, Vol 7(S6), pp. 22–31.
2. S. Zhao, *Advanced control for autonomous underwater vehicles*, Ph.D. dissertation, Dept. Mech. Eng., The University of Hawai'i, Aug. 2004, pp 9–17.
3. Duo Qi, Jinfu Feng, An Liu, Junhua Hu, Hu Xu, Yongli Li, Muhammad Aqeel Ashraf, *Stability control of propeller autonomous underwater vehicle based on combined sections method*, POLISH MARITIME RESEARCH, Volume 22, Issue s1 (Sep 2015), pp. 157–162.
4. S. D. Joshi and D. B. Talange, *Integer & fractional order PID Controller for fractional order subsystems of AUV*, 2013 IEEE Symposium on Industrial Electronics & Applications, Kuching, 2013, pp. 21–26.
5. S. Pezeshki, A. R. Ghiasi, M. A. Badamchizadeh, K. Sabahi, *Adaptive Robust Control of Autonomous Underwater Vehicle*, Journal of Control, Automation and Electrical Systems, June 2016, Volume 27, Issue 3, pp 250–262.
6. Ji-Hong Li, Pan-Mook Lee, *Design of an adaptive nonlinear controller for depth control of an autonomous underwater vehicle*, Ocean Engineering, Volume 32, Issues 17–18, 2005, pp. 2165–2181.
7. M. A. Salim, A. Noordin and A. N. Jahari, *A Robust of Fuzzy Logic and Proportional Derivative Control System for Monitoring Underwater Vehicles*, 2010 Second International Conference on Computer Research and Development, Kuala Lumpur, 2010, pp. 849–853.
8. J. Kim, H. Joe, S. c. Yu, J. S. Lee and M. Kim, *Time-Delay Controller Design for Position Control of Autonomous Underwater Vehicle Under Disturbances*, in IEEE Transactions on Industrial Electronics, vol. 63, no. 2, Feb. 2016, pp. 1052–1061.

9. G. Evers et al., *Modeling and simulated control of an under actuated autonomous underwater vehicle*, 2009 IEEE International Conference on Control and Automation, Christchurch, 2009, pp. 343–348.
10. MH Khodayari, S Balochian, *Modeling and control of autonomous underwater vehicle (AUV) in heading and depth attitude via self-adaptive fuzzy PID controller*, Journal of Marine Science & Technology, September 2015, Volume 20, Issue 3, pp. 559–578.
11. Wei Zhang, Zhicheng Liang, Yi Guo, Detao Meng, Jiajia Zhou and Yunfeng Han, *Fuzzy adaptive sliding mode controller for path following of an autonomous underwater vehicle*, OCEANS 2015 – MTS/IEEE Washington, Washington, DC, pp. 1–6.
12. J. Han, *From PID to Active Disturbance Rejection Control*, in IEEE Transactions on Industrial Electronics 2009, vol. 56, no. 3, pp. 900–906.
13. R. Madoński and P. Herman, *An experimental verification of ADRC robustness on a cross-coupled Aerodynamical System*, Industrial Electronics (ISIE), 2011 IEEE International Symposium Gdansk, pp. 859–863.
14. M. Przybyła, M. Kordasz, R. Madoński, P. Herman, and P. Sauer, *Active Disturbance Rejection Control of a 2DOF manipulator with significant modeling uncertainty*, in The Journal of Polish Academy of Sciences, volume 60, issue 3 December 2012.
15. H. C. Lamraoui and Z. Qidan, *Speed tracking control of unicycle type mobile robot based on LADRC*, 2017 3rd IEEE International Conference on Control Science and Systems Engineering (ICCSSE), Beijing, 2017, pp. 200–204.
16. T. Niu, H. Xiong and S. Zhao, *Based on ADRC UAV longitudinal pitching Angle control research*, 2016 IEEE Information Technology, Networking, Electronic and Automation Control Conference, Chongqing, 2016, pp. 21–25.
17. Y. Zhao, Z. Zhao, B. Zhao and W. Li, *Active Disturbance Rejection Control for Manipulator Flexible Joint with Dynamic Friction and Uncertainties Compensation*, 2011 Fourth International Symposium on Computational Intelligence and Design, Hangzhou, 2011, pp. 248–251.
18. J. Zhou, D. Ye, D. He and D. Xu, *Three-dimensional trajectory tracking of an underactuated UAV by backstepping control and bio-inspired models*, 2017 36th Chinese Control Conference (CCC), Dalian, 2017, pp. 966–972.
19. Basant Kumar Sahu, Bidyadhar Subudhi *Adaptive Tracking Control of an Autonomous Underwater Vehicle*, International Journal of Automation and Computing, vol. 11, no. 3, pp. 299–307, jun. 2014.
20. Chao Shen, Brad Buckham, Yang Shi, *Modified C/GMRES Algorithm for Fast Nonlinear Model Predictive Tracking Control of AUVs*, IEEE Transactions on Control Systems Technology (Volume: 25, Issue: 5, Sept. 2017), pp. 1896–1904.
21. L. Lapierre and B. Jouvencel, *Robust Nonlinear Path-Following Control of an AUV*, in IEEE Journal of Oceanic Engineering, April 2008, vol. 33, no. 2, pp. 89–102.
22. L. Wang, H. M. Jia, L. J. Zhang, L. X. Yang and H. B. Wang, *L2 disturbance attenuation control for path following of AUV in 3D*, 2011 IEEE 3rd International Conference on Communication Software and Networks (ICCSN), Xi'an, 2011, pp. 126–129.
23. Q. Zheng, L. Gao, and Z. Gao, *On stability analysis of active disturbance rejection control for nonlinear time-varying plants with unknown dynamics*, 46th IEEE Conference on Decision and Control 2007, pp. 3501–3506.
24. Y. Zhou, R. Li, D. Zhao and Q. Wu, *Ship heading control using LESO with wave disturbance*, 2016 IEEE International Conference on Robotics and Biomimetics (ROBIO), Qingdao, 2016, pp. 2081–2086.

CONTACT WITH THE AUTHOR

Habib Choukri Lamraoui

e-mail: habib_choukri@yahoo.com

Automation Colleg, Harbin Engineering University

Nantong Str. Nangang Dist.

150001 Harbin

CHINA

Zhu Qidan

e-mail: zhuqidan@hrbeu.edu.cn

Automation College, Harbin Engineering University

Nantong Str. Nangang Dist.

150001 Harbin

CHINA

MAPPING MARINE TRAFFIC DENSITY BY USING AIS DATA: AN APPLICATION IN THE NORTHERN AEGEAN SEA

Burak Kundakçı

Selçuk Nas

Dokuz Eylul University Maritime Faculty, Buca, 35160 Izmir, Turkey

ABSTRACT

Automatic Identification System (AIS) data is used for monitoring the movements of vessels live movements through instant transmission of vessel information while, at the same time, historical AIS data is used for marine traffic analysis by researchers. There are several methods and computer programs developed for the analysis of marine traffic by the use of AIS data.

Combining the intersection algorithm proposed by Antonio (1992) and distance calculation method, this study develops a method to analyse vessel distribution on a selected cross sectional line (SCS) in the Northern Aegean Sea. As a complementary to the new methods proposed, a desktop application is developed in C# programming language to visualize the vessel distribution on the SCS line. SQL server is used for AIS data storage and analysis. The study is conducted over 7-day AIS data, specifically 2.382.469 rows and 42.884.442 data in total, belonging to the Northern Aegean Sea marine traffic. As a result, the mapping of the movements of different types of vessels in the Northern Aegean Sea is effectively performed and Frequency-Distance, Draught-Distance, SOG-Distance, SOG-COG distributions on the SCS line are successfully analysed by the new method introduced.

Keywords: Automatic Identification System; Marine Traffic; Marine Traffic Analysis

INTRODUCTION

The AIS is developed as a tool that allows for the instant monitoring of ships, as well as the analysis of marine traffic by using historical data gathered through these devices. It is possible to map the marine traffic density [26,19,27], calculate the probability of collision and/or grounding [10,6,18,14], carry out the analysis of marine traffic and reveal the intense areas [13,17,1,12] by means of the AIS data.

The AIS devices operate as demonstrated in Figure 1. These devices transmit and receive data through Very High Frequency (VHF) radio frequency and their range varies according to the shape of the earth, the islands and mountains in the vicinity and wave propagation [5,23]. The exchange of data can be ship-to-ship, ship-to-shore station and shore station-to-ship. Such data exchange allows for the monitoring and control of the marine traffic [22] which consequently enhances the safety of navigation.

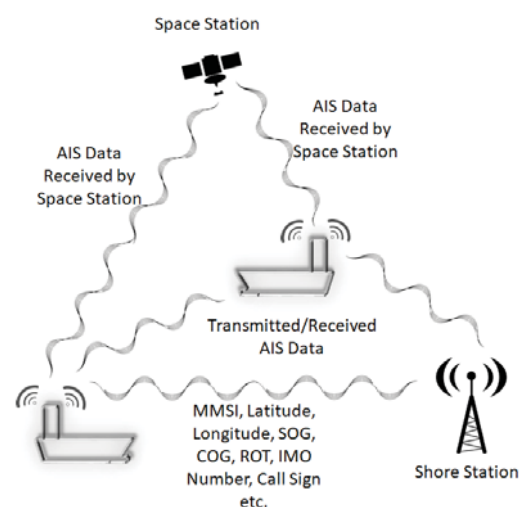


Fig. 1. The Working Principle of the AIS (Developed from [25])

There are basically two types of AIS devices on vessels which are Class A and Class B [23]. Class A AIS devices are used on all ships over 300 GRT engaged on international voyage and passenger ships irrespective of size, while Class B AIS devices are used on small ships such as the ones that operate in the fishing industry and pleasure crafts [15,16]. AIS devices can also be used as an aid to navigation on buoys, lighthouses and additionally it is exploited as a virtual navigation aid, to mark dangerous navigation zones such as shipwrecks and shallow waters [20].

AIS devices transmit static, dynamic and navigation data appropriately [9] and use time division multiple access (TDMA) which eliminates the risk of overlapping of signals transmitted [4]. There are also Self-Organizing (SOTDMA), Random Access (RATDMA), Incremental (ITDMA) and Fixed Access (FATDMA) protocols for the proper operation of the system. Thus, a random time slot is allocated to the AIS device at the beginning, and the next signal transmission time slot is determined by ITDMA while FATDMA is reserved for shore stations [8].

Time slots and the ITDMA working principle are shown in Figure 2 below. According to Figure 2, the AIS device broadcasts the information of the ship in a time slot to the receivers and then reserves another time slot for the next broadcast. This system prevents multiple transmissions or transmission overlap from different devices in a single time slot.

The data, both instant and historical, sent by AIS devices are of great value for researchers and analysts since they provide critical information, with regard to marine traffic, by locating the current and past positioning of ships [11,21]. There is multiple studies in literature on the investigation and analysis of marine traffic by the use AIS data. While some studies have focused on the mapping and analysis of the regional or global marine traffic [15,16,19,27] some others have concentrated on the analysis of the probability of the collision and/or grounding accidents [10,6,14]. Aimed at analysis in marine traffic, a study by Xiao et al. (2015) [28] compared the differences in the movements of vessels in a narrow channel in the Netherlands with a larger channel in China. The study examined the distribution of vessels passing across presumed cross sectional lines through the channels with regard to the variables such as speed and ship type. In another study, Altan and Otay (2017) [1] analysed vessel navigation patterns and the distribution of vessels in the İstanbul Strait according to their sectors of operation.

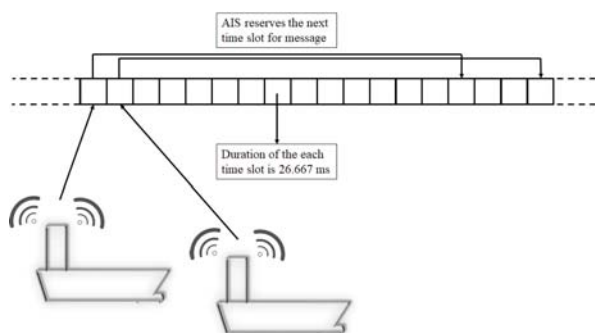


Fig. 2. AIS ITDMA Working Principle (Adapted from [8])

In this study, a desktop application is developed by using intersection algorithm and distance calculations for analysing the distribution of the vessels on a selected cross sectional (SCS) line similar with the Xiao et al. (2015) [28].

METHODS

The AIS data comes in sequence and appear as a point on the map that shown in Figure 3. In order to reveal ship distributions on a selected cross sectional (SCS) line, it is necessary to demonstrate that the SCS line is intersected by two consecutive points of a vessel.

There are various intersection algorithm such as line, polygon etc. It was found out that the line intersection algorithm is more suitable than the others in our study. Intersection of those lines in Figure 3 can be a trivial question to answer for most people but to get the same answer from a computer is not an easy process [29]. For a computer, there are 4 different points, 8 coordinates (X, Y) that represents the start and end points of the lines. The computer need to calculate those lines (4 points) whether they intersect or not. There are different algorithms to calculate this intersection [29, 30] but line intersection method proposed by Antonio (1992) [2] was most suitable, efficient and easy to use for this study.

In this study the authors propose a method in which the line intersection algorithm proposed by Antonio (1992) [2] and distance calculation method are used together to analyse vessel distribution on a SCS line. A desktop application is developed accordingly in C# programming language to visualize vessel distributions on the SCS line and an SQL server is used for AIS data storage and analysis. For the purpose of this research, the intersection algorithm is employed to calculate the passage of vessels across the SCS line taken for the study. The AIS data of the intersected vessels are gathered in a table in the SQL server. Distance calculations method is used to measure the distances on the map.

INTERSECTION OF TWO LINES.

As the AIS data come in sequence, vessel positioning information transmitted from the vessel is as shown in Figure 3. The dots marked by the numbers from 1 to 7 show any ship pattern on the map. Intersection between SCS line and the ship pattern line is calculated by means of the intersection algorithm, which is a practical way of calculation, within the framework of the study to analyse ship distribution on that pattern.

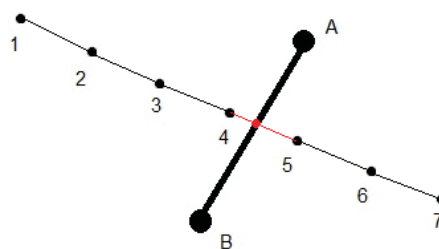


Fig. 3. Symbolic View of the AIS Data and SCS Line.

The intersection algorithm calculates the intersection of two lines and the intersection points. The lines are presented in Figure 4 below.

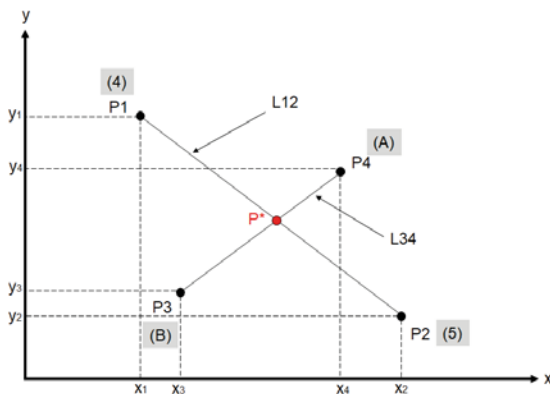


Fig. 4. Line Intersection in 2D Space (Adapted from [2])

Formulas 1, 2, and 3 below are used for the computation of the intersection of the two lines, namely L12 and L34. In Figure 4, P3 and P4 points represent the selected points, L34 shows the SCS line, P1 and P2 represent the vessel position, L12 shows the ship pattern.

$$A = P2 - P1$$

$$B = P3 - P4 \quad (1)$$

$$C = P1 - P3$$

$$\alpha = \frac{B_y C_x - B_x C_y}{A_y B_x - A_x B_y} \quad (2)$$

$$\beta = \frac{A_x C_y - A_y C_x}{A_y B_x - A_x B_y} \quad (3)$$

With formula 1, X and Y coordinates of the points can be calculated. After that, formula 2 and 3 can be calculated. For example, to calculate the value B_y in formula 2, Y value of the P4 should be subtracted from the Y value of the P3. This process should be done for all values in formula 2 and 3. In this study, X and Y values represent the Latitude and Longitude values of the vessels and SCS lines.

After the calculations, if α and β take any value between [0, 1], this means that L12 and L34 intersect. Once the values for α and β are calculated, the formulas 4a and 4b below are applied to compute the intersection point P^* on Figure 4.

$$P^* = P1 + \alpha(P2 - P1) \quad (4a)$$

$$P^* = P3 + \beta(P4 - P3) \quad (4b)$$

To calculate the intersection point P^* , X and Y coordinates should be calculated separately by using the formula 4a or 4b. Both formulas give the same values. For example, to calculate the X coordinates of the intersection point, $P1_x + \alpha(P2_x - P1_x)$ should be calculated. In this study, X and Y values of the intersection points represent Latitude and Longitude of the intersection point.

DISTANCE CALCULATION

The distance of the SCS line and the distance of the intersection point to the selected points can be found by means of distance calculation. ‘Departure’ and ‘Distance’ calculations are required to find the distance between two latitude and longitude points that are given. The required values for these calculations are [3]:

- ‘Dlat’ is the difference between two latitudes.
- ‘Mlat’ is the mid latitude. For the position on the same hemisphere, it can be computed by the sum of the two latitudes divided by 2.
- ‘Dlong’ is the difference between two longitudes.
- ‘Departure’ is the distance between two longitudes and generally defined in nautical miles (NM).
- ‘Distance’ is the distance of the line between two positions. This line makes the same angle with all meridians.

Distance between two given points of latitude and longitude is shown in Figure 5.

There are different sailing types and distance calculations according to those sailings. “Middle-latitude sailing is a method of converting departure into difference of longitude, or vice versa, by assuming that such a course is steered at the middle or mean latitude; if the course is 090° or 270° true, it is called parallel sailing... Meridian sailing is used when the course is 000° or 180° true.” [3]. For this study, because of the different latitude and longitude of the points, distance can be calculated according to the middle latitude sailing calculations.

In the next step, the formulas 5, 6, 7 and 8 below are used to find the distance between the two given points of latitude and longitude. Specifically, the difference value between the latitudes is calculated through formula 5 while the difference value between longitudes through formula 6, and the departure value is calculated by formula 7 while the distance value by formula 8.

THE MODEL OF THE STUDY

There is an incessant transfer of versatile data from AIS stations. This data transfer occurs in the directions of ship-to-ship or ship-to-shore and vice versa and the transferred data can be stored. The scope of this study begins with the receipt of the AIS data from Turkey’s Directorate General of Coastal Safety. The AIS data analysed for the purpose of this study encapsulate seven (7) days in September 2014 and covers the latitude between $38^\circ 18,0' N - 38^\circ 58,0' N$ and the longitudes between $026^\circ 21,0' E - 027^\circ 12,0' E$ longitudes. There are 2.382.469 rows and totally 42.884.442

(2.382.469*18=42.884.442) AIS database. Visualisation of the vessel movements and ship distribution on SCS line is analysed in the following step. Figure 6 depicts the model of the study.

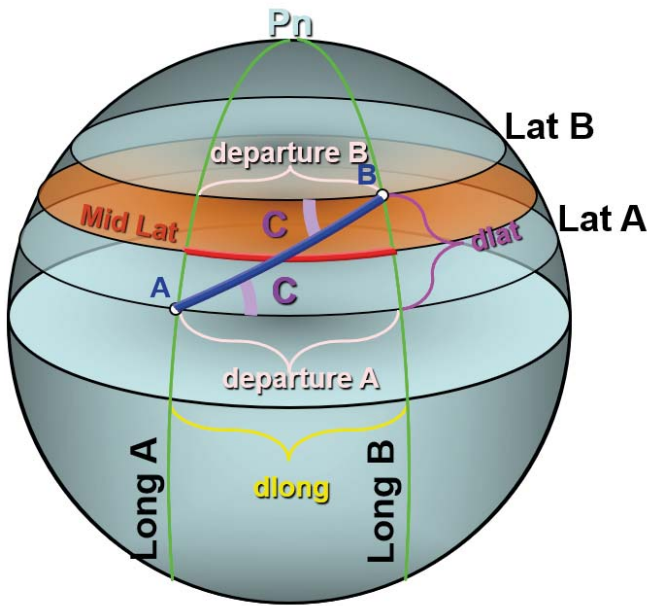


Fig. 5. Distance between Two Given Points of Latitude and Longitude [25]

$$Dlat = Lat A - Lat B \quad (5)$$

$$Dlong = Long A - Long B = Departure / \cos(Mlat) \quad (6)$$

$$Departure = Dlong * \cos(Mlat) \quad (7)$$

$$Distance = Dlat / \sin(C^\circ) = Departure / \cos(C^\circ) \quad (8)$$

Visual Studio Community 2017 software is used along with the C# programming language for the visualization of the vessel movements and distributions. Furthermore, the dataset was added to the MSSQL Server 2016 database to enable quick data processing and to ensure data security. Table 1 below exhibits an example of the tabulated dataset in the MSSQL server. The AIS data is stored in different columns in the tables according to the data type as shown in Table 1.

Tab. 1. Data Type in the Database

Column Name	Data Type	Column Name	Data Type
MMSI	int	CallSign	nvarchar(50)
Lon	float	ShipandCargo	int
Lat	float	Draught	float
Report Date	nvarchar(50)	Type	int
SOG	float	NavigationalStatus	int
COG	float	DimA	float
HDG	float	DimB	float
ROT	float	DimC	float
IMO	int	DimD	float

Mapping of ship movements is performed according to ship types and the type of a ship can be identified by the 'ShipandCargo' column. The ship and cargo codes are grouped according to the ship types as listed in Table 2 below.

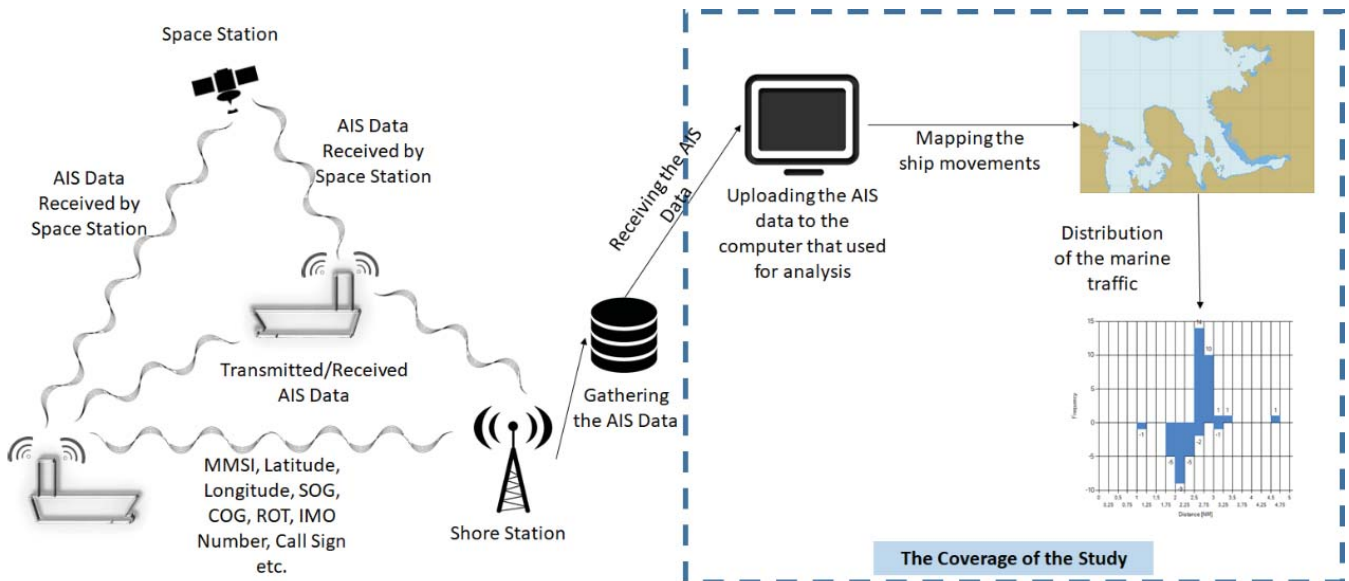


Fig. 6. The Model of the Study

Tab. 2. Ship Types and Ship and Cargo Codes

Ship Types	Ship and Cargo Code
Cargo Vessels	70, 71, 72, 73, 74, 75, 76, 77, 78, 79
Tankers	80, 81, 82, 83, 84, 85, 86, 87, 88, 89
Passenger Vessels	60, 61, 62, 63, 64, 65, 66, 67, 68, 69
High Speed Crafts	40, 41, 42, 43, 44, 45, 46, 47, 48, 49
Tug / Towing	31, 32, 52
Special Crafts	33, 34, 35, 36, 38, 39, 50, 51, 53, 54, 55, 56, 57, 58, 59
Fishing Vessels	30
Pleasure Crafts	37
Other types of Ships	20, 21, 22, 23, 24, 25, 26, 27, 28, 29, 90, 91, 92, 93, 94, 95, 96, 97, 98, 99
Unspecified	0, 10, 11, 12, 13, 14, 15, 16, 17, 18, 19
All types of Ships	

MAPPING OF THE NORTHERN AEGEAN SEA MARINE TRAFFIC DENSITY

In the first step, for the purpose of mapping, the map of the Northern Aegean Sea, which covers 38,3° N – 39,0° N latitudes and 026,0° E – 027,3° E longitudes, exhibited in the Figure 7 is picked. Every row in the database is equalised to 1 pixel on the map in order to demonstrate the ship pattern in the Northern Aegean Sea.



Fig. 7. Application Area of the Research (The Part of the Northern Aegean Sea)

In the Mercator projection, distance scale is changing considering the latitude. In this study, only the middle

latitude of the application area chart is taken as a reference for the distance scale. This creates a scale error of no more than 0.6 NM between the north and south latitudes of the application chart. This scale error is caused by the Mercator projection. When comparing the size of the field with the analysed area this error was insignificant and not taken into account and the map is taken as a proper rectangular area. Different types of vessels are symbolised by different colours on the map. The ship-colour matching is demonstrated in Figure 8 below.



Fig. 8. The Colour Code according to the Ship Type

DISTRIBUTION OF THE MARINE TRAFFIC

In the second step of the analysis, two random points are selected on the map and the distribution on the SCS line is shown on the screen. The computer application has calculated the intersection of the AIS dots and the SCS line for every AIS data respectively and updated the Intersection_Table in the database by data relating to intersection position, draught, speed over ground (SOG), course over ground (COG) as well as other related data. Distance-Frequency, Distance-Draught, Distance-SOG and COG-SOG distributions have become visible at this phase. The interval of the Distance-Frequency distribution could optionally take 0,25, 0,5 or 1,0 NM values. The screen interface of the application is shown in Figure 9.

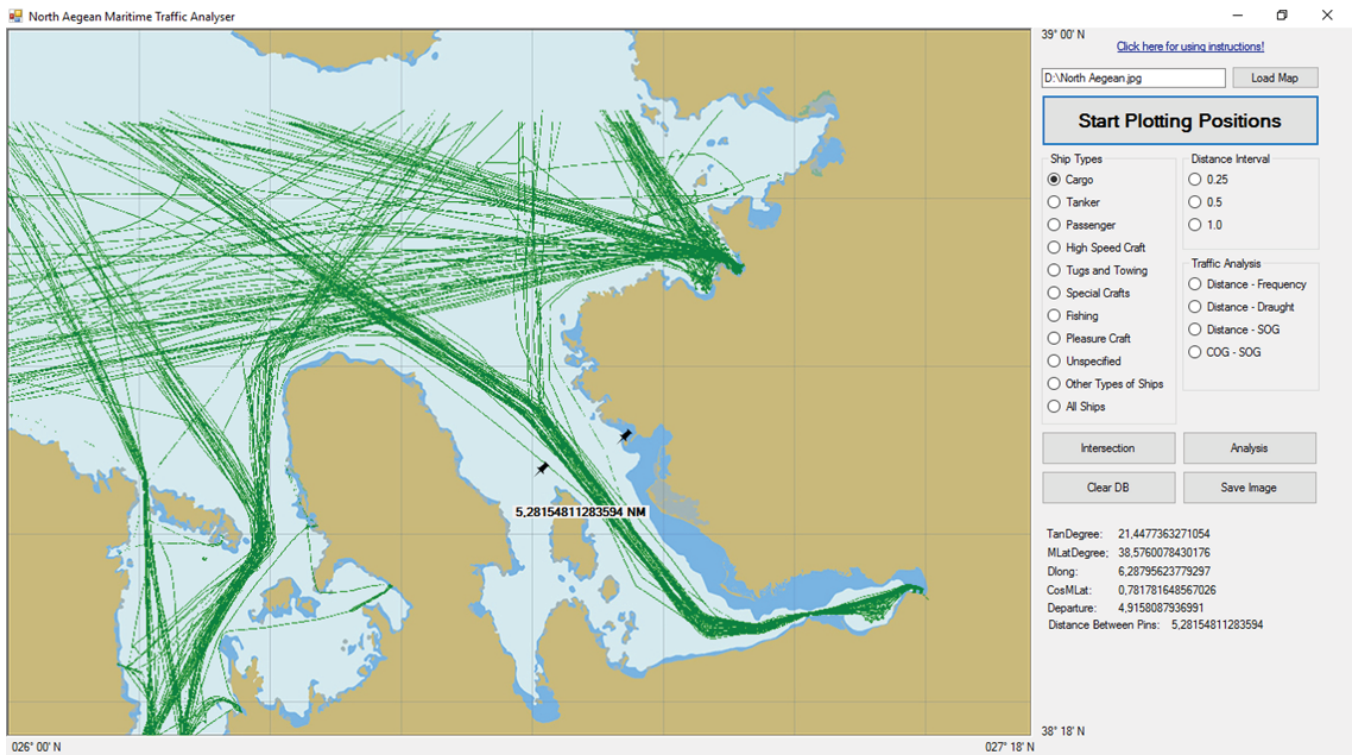


Fig. 9. Screen Interface of the Application

RESULTS

The statistical results of the analysis of the seven-day AIS data belonging to the Northern Aegean Sea are shown in Table 3 below. The dataset revealed in Table 3 consists of 2.382.469 rows of data belonging to 723 vessels.

Tab. 3. General Information Related to the Researched Area

Average SOG of the vessels	6,56 knots
Average draught of the vessels	2,87 meter
Average LOA of the vessels	67,78 meter
Cargo Vessels	
Ship count	304
Average SOG	8,00 knots
Average LOA	124,70 meter
Average draught	5,47 meter
Passenger Vessels	
Ship count	83
Average SOG	5,18 knots
Average LOA	60,55 meter
Average draught	1,79 meter
Tankers	
Ship count	57
Average SOG	6,54 knots
Average LOA	114,23 meter
Average draught	5,67 meter
Fishing Vessels	
Ship count	108
Average SOG	3,37 knots
Average LOA	24,66 meter
Average draught	0,62 meter

Tug / Towing	
Ship count	29
Average SOG	0,66 knots
Average LOA	22,46 meter
Average draught	2,28 meter
Special Crafts	
Ship count	60
Average SOG	31,05 knots
Average LOA	20,86 meter
Average draught	0,70 meter
Pleasure Crafts	
Ship count	55
Average SOG	2,29 knots
Average LOA	20,91 meter
Average draught	0,46 meter
High Speed Crafts	
Ship count	1
Average SOG	5,01 knots
Average LOA	70 meter
Average draught	2 meter
Other Types of Ships	
Ship count	10
Average SOG	2,92 knots
Average LOA	25,33 meter
Average draught	0,01 meter
Unspecified	
Ship count	16
Average SOG	2,44 knots
Average LOA	14,75 meter
Average draught	0,38 meter
Total Number of Ships	723

The ship distribution according to the length over all (LOA) is as shown in Figure 10.

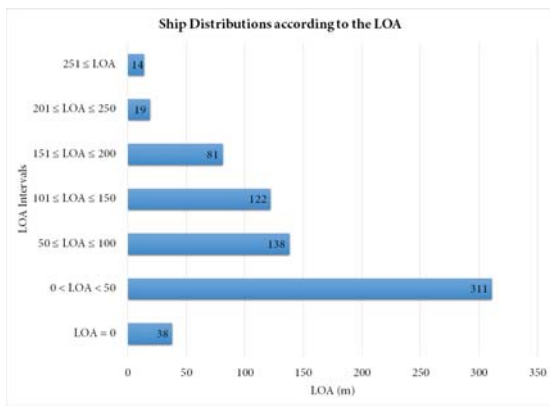


Fig. 10. Ship Distributions according to the LOA

The marine traffic map according to the ship types is as shown in Figure 11.

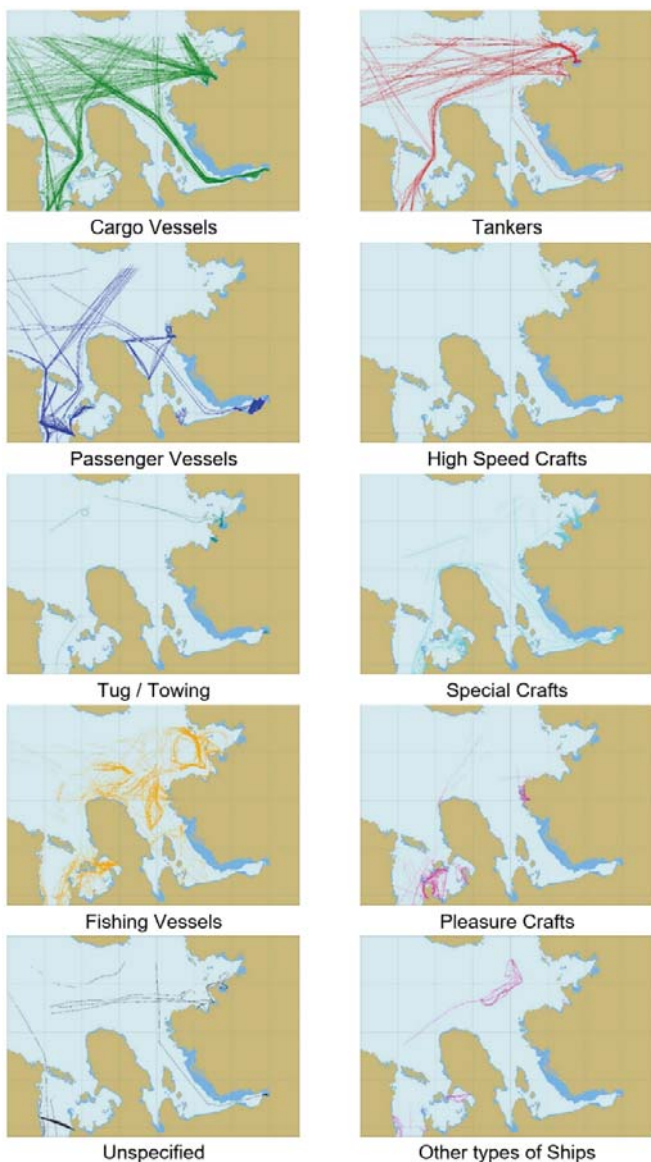


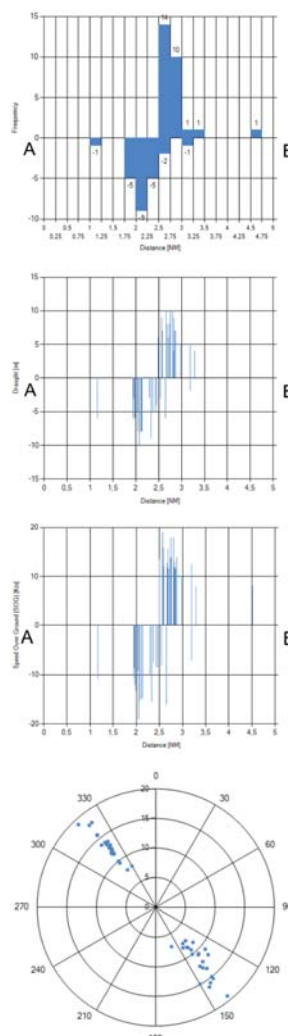
Fig. 11. The Marine Traffic Map according to the Ship Type

The marine traffic of the cargo ships and points A and B that are randomly selected are shown on the in Figure 12.

Whereas the calculation of intersection may vary according to the size of the data, the process lasted about 25-30 seconds in this example. The distribution of cargo vessels on the SCS line is as shown in Figure 13.



Fig. 12. The Marine Traffic Map of the Cargo Ships and the Selected Two Points



Frequency – Distance Distribution
It can be seen from the Figure 13 that 3 ships inside the red circle used the same line with NW'ly navigated vessels.

Draught – Distance Distribution
Draughts of the vessels and the using line can be seen from the Figure 13.

SOG – Distance Distribution
SOG of the vessels and the line used can be seen from the figure.

COG – SOG Distribution
General Distribution of the COG and SOG can be seen from the figure.

Fig. 13. The Distribution of the Cargo Vessel on the Selected Cross Sectional Line (Cont')

DISCUSSION AND CONCLUSION

The quest in the scholarly circles for enhanced marine traffic safety has always been vivid. Researchers have been exploiting historical AIS data in the examination of traffic distributions on Selected Cross-sectional (SCS) lines and density of marine traffic for risk evaluation, for example through the detection of high risk areas, and accident prevention purposes. Notwithstanding of many studies in the literature, the authors study is the first one that employed the intersection algorithm proposed by Antonio (1992) [2] and the method of distance calculation for the analysis of vessel distribution statistically. The analysis in this study can be used as in the study done by Xiao et al. (2015) [28]. Xiao et al. (2015) [28] investigated the ship distributions in a narrow and wide channel. Some cross sections were taken from the channel and the passages of the vessels were investigated. It is possible to investigate the ship distributions by taking similar SCS lines in the same way by using the methods mentioned in this study. Some of the similar analysis can also be done as in the study done by Altan and Otay (2017) [1]. SOG, COG or draught distribution on a SCS lines can be analysed by using the methods mentioned above.

Using seven-day period data, this study has analysed, mapped and visualised the 723 ships on the Northern Aegean Sea with regard to variables such as the number of ships, SOG, COG and draught. Visualisation included, but was not limited to, the mapping according to ship types and Frequency-Distance, Draught-Distance, SOG-Distance and COG-SOG distributions. The study exhibited that AIS data are rich and practical data sources for researchers and research that focus on marine traffic.

The model and the method developed here in this study can be exploited to investigate ship distributions in sections of a target area. The revealed vessel distributions can be used for the calculation of the probability of grounding or collision in further studies. For example with regard to grounding accidents, variables such as passage distance of vessels to shallow water, draught or SOG of the vessel can be analysed and risk assessments can be carried out. Similarly, SOG, COG or draught distributions on a selected cross sectional line can be analysed by using the methods mentioned above, which then may help the advancement of measures for waterway traffic safety. Similar analyses can be performed in traffic separation schemes to find routes and distributions of vessels navigating on the opposite side of the line or in the mid-line and take precautions accordingly. Hence, the model, method and the desktop application developed in the authors study can be used by decision-makers as a decision support system and by the researchers working in the region.

The desktop application developed within the framework of this study enables visualisation of vessel movements. It helps to map the ship movements according to vessel types and enables analysts to evaluate waterway traffic density in the target area. For example, one can view the activities of any type of vessel in a target zone, such as fishing or cargo vessel activities. The desktop application can further be developed

for detailed analysis for different purposes such as economic and environmental needs.

Researchers should be aware of any missing values in the AIS datasets, as experienced in the existing study, and should bear in mind the possibility of wrongly added data as reported by Harati-Mokhtar et al. (2007) [7].

This study covered a limited (seven day) time period AIS data belonging to a specific region, the Northern Aegean Sea. Future studies may target a wider time period and use dynamic global maps for the global mapping of marine traffic and analysis.

ACKNOWLEDGEMENTS

The AIS data used in the study is provided by Turkey's Directorate General of Coastal Safety. The authors acknowledge the contributions of Turkey's Directorate General of Coastal Safety's to the study and thoroughly thank to the distinguished officials of this institution.

BIBLIOGRAPHY

1. Altan, Y., & Otay, E. (2017). Maritime Traffic Analysis of the Strait of Istanbul based on AIS data. *Journal of Navigation*, 70(6), 1367-1382. doi:10.1017/S0373463317000431
2. Antonio, F. (1992). Faster Line Segment Intersection. In D. Kirk (Ed.), *Graphics Gems III* (1st ed., pp. 199-202). Academic Press, Inc.
3. Bowditch, N. (2002). *The American Practical Navigator*. Bethesda, Maryland: National Imagery and Mapping Agency.
4. Eriksen, T., Høy, G., Narheim, B., and Meland, B. J. (2006). Maritime Traffic Monitoring Using a Space-Based AIS Receiver. *Acta Astronautica*. 58 (2006), 537-549. <https://doi.org/10.1016/j.actaastro.2005.12.016>
5. Greidanus, H., Alvarez, M., Eriksen, T. and Gammieri, V. (2016). Completeness and Accuracy of a Wide-Area Maritime Situational Picture Based on Automatic Ship Reporting Systems. *The Journal of Navigation*. 69, 156-168. <https://doi.org/10.1017/S0373463315000582>
6. Hanninen, M. and Kujala, P. (2010). The Effects of Causation Probability on the Ship Collision Statistics in the Gulf of Finland. *International Journal on Marine Navigation and Safety of Sea Transportation*. 4(1), 79-84.
7. Harati-Mokhtari, A., Wall, A., Brooks, P. and Wang, J. (2007). Automatic Identification System (AIS): Data Reliability and Human Error Implications. *The Journal of Navigation*. 60, 373-389. <https://doi.org/10.1017/S0373463307004298>

8. IALA-AISM. (2003). *IALA Guidelines on the Universal Automatic Identification System (AIS)*. Volume 1, Part I – Operational Issues. Edition 1.1.
9. ITU-R. (2014). *Technical Characteristics for an Automatic Identification System Using Time Division Multiple Access in the VHF Maritime Mobile Frequency Band*. Recommendation ITU-R M.1371-5. Geneva: Electronic Publication.
10. Kujala, P., Hänninen, M., Arola, T. and Ylitalo, J. (2009). Analysis of the Marine Traffic Safety in the Gulf of Finland. *Reliability Engineering and System Safety*. 94, 1349–1357. <https://doi.org/10.1016/j.ress.2009.02.028>
11. Lei, P-R., Tsai, T-H. and Peng, W-C. (2016). Discovering Maritime Traffic Route from AIS Network. *The 18th Asia-Pacific Network Operations and Management Symposium (APNOMS)*. <https://doi.org/10.1109/APNOMS.2016.7737223>
12. Li, L., Lu, W., Niu, J., Liu, J., & Liu, D. (2017). AIS Data-based Decision Model for Navigation Risk in Sea Areas. *Journal of Navigation*, 1-15. doi:10.1017/S0373463317000807
13. Mazaheri, A., Montewka, J. and Kujala, P. (2013). Correlation between the Ship Grounding Accident and the Ship Traffic – A Case Study Based on the Statistics of the Gulf of Finland. *International Journal on Marine Navigation and Safety of Sea Transportation*. 7(1), 119–124.
14. Mehta, A. L. (2016). *Analysis of Waterway Transportation in Southeast Texas Waterway Based on AIS Data*. Texas: Lamar University.
15. Marine Management Organisation (MMO) (2014). *Mapping UK Shipping Density and Routes Technical Annex*. A report produced for the Marine Management Organisation, pp 52. MMO Project No: 1066. ISBN: 978-1-909452-26-8
16. Mustafa, M., Ahmat, N. H. and Ahmad, S. (2015). Mapping Vessel Path of Marine Traffic Density of Port Klang , Malaysia Using Automatic Identification System (AIS) Data. *International Journal of Science and Research (IJSR)*. 4(11), 245–248.
17. Mustafa, M., Abas, M., Ahmad, S., Aini, N. A., Abbas, W. F., Abdullah, S. A. C., Razak, N. I. A., Darus, M. Y. (2016). Marine Traffic Density Over Port Klang, Malaysia Using Statistical Analysis of AIS Data: A Preliminary Study. *Journal of ETA Maritime Science*. 4(4), 333-341. <https://dx.doi.org/10.5505/jems.2016.60352>
18. Nas, S. (2014). Deniz Trafiğinde Çatışma Tehlikesi Olasılığının Analizi: Marmara Denizi Uygulaması. *I. Ulusal Gemi Trafik Hizmetleri Kongresi*. 08-09 Aralık. İstanbul.
19. Natale, F., Gibin, M., Alessandrini, A., Vespe, M. and Paulrud, A. (2015). Mapping Fishing Effort through AIS Data. *PLOS ONE*. 10(6). <https://doi.org/10.1371/journal.pone.0130746>
20. PIANC (2014). *Harbour Approach Channels Desing Guidelines*.
21. Seta, T., Matsukura, H., Aratani, T. and Tamura, K. (2016). An Estimation Method of Message Receiving Probability for a Satellite Automatic Identification System Using a Binomial Distribution Model. *Scientific Journals of the Maritime University of Szczecin*. 46 (118), 101–107. <http://dx.doi.org/10.17402/125>
22. Skauen, A. N. (2016). Quantifying the Tracking Capability of Space-Based AIS Systems. *Advances in Space Research*. 57, 527–542. <https://doi.org/10.1016/j.asr.2015.11.028>
23. UNCTAD (2016). *Review of Maritime Transport 2016*. United Nations Publication.
24. International Maritime Organization. *Automatic Identification Systems (AIS)*. <http://www.imo.org/en/OurWork/safety/navigation/pages/ais.aspx>, Accessed 01 June 2017.
25. Selçuk NAS, <http://www.nasmaritime.com/PRESENTATIONS/SN-DEPARTURE.ppt>, Accessed 02 April 2017.
26. Willems, N., Wetering, H. V. D. and Wijk, J. J. V. (2009). Visualization of Vessel Movements. *Eurographics/ IEEE-VGTC Symposium on Visualization 2009*. 28(3), 959–966.
27. Wu, L., Xu, Y., Wang, Q., Wang, F., and Xu, Z. (2017). Mapping Global Shipping Density from AIS Data. *The Journal of Navigation*, 70(1), 67-81. <https://doi.org/10.1017/S0373463316000345>
28. Xiao, F., Ligteringen, H., Gulijk, C. V. and Ale, B. (2015). Comparison Study on AIS Data of Ship Traffic Behavior. *Ocean Engineering*. 95, 84–93. <https://doi.org/10.1016/j.oceaneng.2014.11.020>
29. Wise, S. (2014). *GIS basics*. Taylor & Francis.
30. Wolfram Mathworld, *Line-Line Intersection*, <http://mathworld.wolfram.com/Line-LineIntersection.html>, Accessed 25 May 2018.

CONTACT WITH THE AUTHORS

Burak Kundakçi

e-mail: bkkundakci@gmail.com

Dokuz Eylul University

Maritime Faculty, Buca

35160 Izmir

TURKEY

Selçuk Nas

e-mail: snas@deu.edu.tr

Dokuz Eylul University

Maritime Faculty, Buca

35160 Izmir

TURKEY

MEMS TECHNOLOGY QUALITY REQUIREMENTS AS APPLIED TO MULTIBEAM ECHOSOUNDER

Krzysztof Bikonis

Jerzy Demkowicz

Gdansk university of Technology, Poland

ABSTRACT

Small, lightweight, power-efficient and low-cost microelectromechanical system (MEMS) inertial sensors and microcontrollers available in the market today help reduce the instability of Multibeam Sonars. Current MEMS inertial measurement units (IMUs) come in many shapes, sizes, and costs — depending on the application and performance required. Although MEMS inertial sensors offer affordable and appropriately scaled units, they are not currently capable of meeting all requirements for accurate and precise attitudes, due to their inherent measurement noise. The article presents the comparison of different MEMS technologies and their parameters regarding to the main application, namely Multibeam Echo Sounders (MBES). The quality of MEMS parameters is crucial for further MBES record-processing. The article presents the results of undertaken researches in that area, and these results are relatively positive for low-cost MEMS. The paper undertakes some vital aspect of using MEMS in the attitude and heading reference system (AHRS) context. The article presents a few aspects of MEMS gyro errors and their estimation process in the context of INS processing flow, as well as points out the main difficulties behind the INS when using a few top MEMS technologies.

Keywords: Inertial Measurements Unit, Multibeam Echo Sounder, Attitude and Heading Reference System, Motion Reference Unit

INTRODUCTION

The main target of the paper is evaluating a low-cost microelectromechanical system (MEMS) in a very demanding application context, i.e. Multibeam Echo Sounders, using a Kalman estimator. Low-cost MEMS inertial sensors and microcontrollers available in the market today help reduce the instability of Multibeam Sonar measurements. Over the past decades, MEMS researchers have demonstrated a number of microsensors for almost every possible sensing modality, including attitudes. Today, MEMS-based gyros challenge the 'prone to wear' mechanical gyro solutions, as well as gyros based on fibre optic (FOG) technology. MEMS sensors have proved and demonstrated performances exceeding those

of their macroscale counterpart sensors [9]. Obviously, the quality of MEMS parameters is crucial for further MBES record-processing, especially in the context of attitudes, which is the main motivation for the author to present the results of researches undertaken in that area.

The measurement methodology follows the Seatex MRU Calibration Certificate methodology applied for vessels equipped with MBES and operating at sea, at highly challenging activity, by its very nature. So the methodology of roll and pitch accuracy tests carried out during the research consist of static accuracy and dynamic accuracy tests [17], and is compared to the available Kongsberg Motion Rotation Unit (MRU) which obtained the certificate. The static accuracy is measured by sampling at 4 Hz for 30 minutes, when the IMU

is stationary. The dynamic accuracy is measured in a rate table test with simultaneous sinusoidal excitation in two axes for 10 minutes. The standard uncertainty error of static roll and pitch test requirements is expected to be less than 0.10 deg. The standard uncertainty error dynamic requirement should be less than 0.15 deg [17].

The rate gyro accuracy test consists in measuring the angular rate sensor noise level and the rate gyro scale factor error. The angular rate sensor noise level is measured by sampling at 4 Hz for 30 minutes when the IMU is stationary. The rate gyro scale factor error is tested by single-axis rotation on a rate table at ± 30 deg/s and at ± 50 deg/s.

The accelerometer accuracy test consists in measuring the acceleration sensor noise level and the accelerometer scale factor. The accelerometer sensor noise level is measured by sampling at 4 Hz for 30 minutes when the IMU is stationary, while the accelerometer scale factor is measured by tilting the IMU in steps of 90 deg around a circle [17].

HIGH PRECISION IMU REQUIREMENTS

High precision IMU requirements, as applied to MBES, are very demanding. Fig. 1a presents the MBES scanning acquisition process, and 3D data visualization of 0.1 m resolution (Fig. 1b). High resolution accuracy depends on IMU resolution and stability. At 10 meters of depth, the angular error of 0.1 degree results in a near 0.02 m linear horizontal error at the bottom; and of course, at 100 meters of depth, that error gives a 0.2 m error, which is unacceptable in many current applications [18].

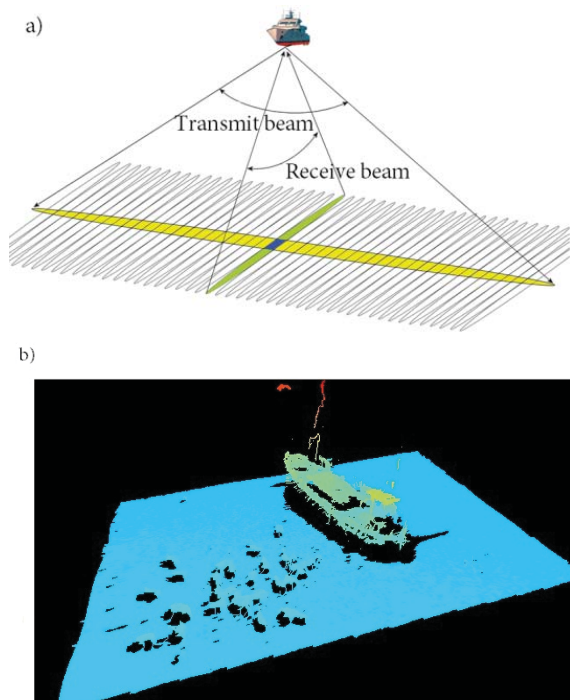


Fig. 1. Multibeam sonar system a) data acquisition b) data visualization

Fig. 2 presents the overall context of IMU applications. The most important are accelerometer and gyroscope sensors. In a wider perspective, Inertial Navigational Systems utilize them, and it is well-known what a challenge it is [7, 8]. But even in this narrowed IMU context, these sensor errors are still a serious issue, see Tab. 1 as a reference where the bias error possesses the most important impact. A motion reference unit (MRU) from Kongsberg was chosen for the experiment, along with IMU systems with parameters similar to those of the MRU. The most important parameters in the context of attitudes of selected systems are shown in Tab. 2, where g is the acceleration due to gravity (assumed to be $9,80665 \text{ m/s}^2$). Tab. 1 and Tab. 2 can be treated as the budget error calculation start point of the tested MEMS unit.

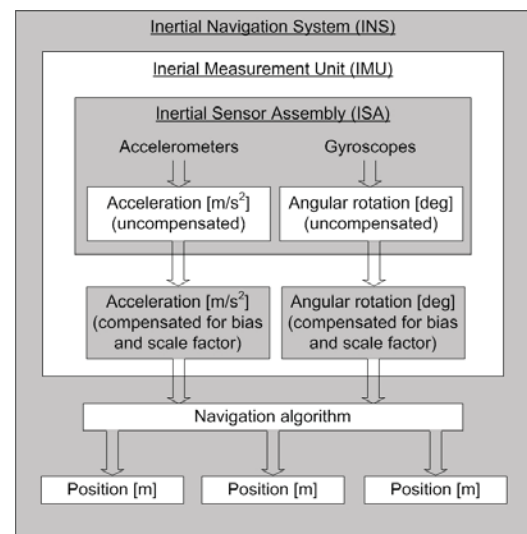


Fig. 2. Classification of inertial systems

To mitigate the accuracy problem, the Kalman estimator usually reads in the sensor data, and in turn outputs the Euler angles and the bias of the gyros as presented in Fig. 3.

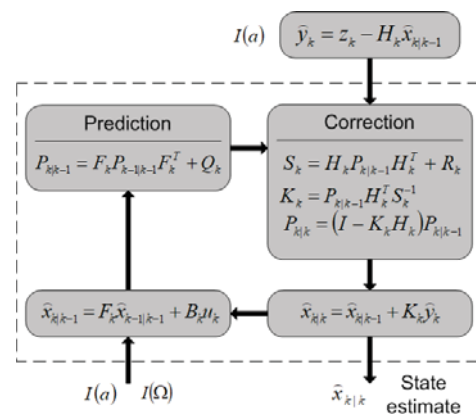


Fig. 3. Kalman filtering algorithm

The Kalman filter uses the knowledge of deterministic and statistical properties of system parameters and measurements to obtain estimates which are optimal. It is an example of

the Bayesian estimation technique. The estimation process is supplied with initial estimates, usually a one-dimensional matrix, and then operates recursively updating the working estimates with the optimal weighted average of their previous values and new values derived from the innovation measurement. In Fig. 3, \hat{x}_k stands for matrix state estimation, which consists of linear acceleration from accelerometers $I(a)$, angular velocities from gyroscopes $I(\Omega)$, and attitudes. P_k stands for process covariance, y_k – innovation, z_k – current measurement, K_k – Kalman gain, H_k – measurement matrix, R_k – measurement error variance, Q_k – model variance, and F_k – stands for process model. B_k may be interpreted as the control matrix; however, it was not used in the model.

Tab. 1. Gyroscope error sources

Error type	Description	Results of integration
Bias	Constant bias ϵ	Steadily growing angular error $\theta(t) = \epsilon \cdot t$
White noise	White noise with some standard deviation σ	Angular random walk, whose standard deviation $\sigma_\theta(t) = \sigma \cdot \sqrt{\delta t \cdot t}$ grows with the square root of time
Temperature effects	Temperature dependent residual bias	Any residual bias is integrated into the orientation, causing an orientation error which grows linearly with time
Calibrations	Deterministic errors in scale factors, alignments and gyro linearity	Orientation drift proportional to the rate and duration of motion
Bias instability	Bias fluctuations, usually modeled as a bias random walk	Second-order random walk

Tab. 2. Comparison of selected IMU parameters

	MRU EM3002	3DM-GX3-25	MTi-G700	MTi-G
Static accuracy				
Roll and Pitch	0.04 deg	0.5 deg	0.2 deg	0.5 deg
Dynamic accuracy				
Roll and Pitch	0.05 deg	2 deg	0.3 deg	1 deg
Gyroscope				
Full scale	±100 deg	±300 deg	±450 deg	±300 deg
Bias	0.1 deg/s	0.25 deg/s	0.2 deg/s	1 deg/s
In-run bias stability	–	18 deg/h	10 deg/h	20 deg/h
Non-linearity (% of full scale)	0.2	0.1	0.01	0.1
Accelerometer				
Full scale	±3 g	±5 g	±5 g	±5 g
Bias	0.001 g	0.002 g	0.003 g	0.01 g
In-run bias stability	0.2 mg	0.04mg	0.04 mg	2 mg
Non-linearity (% of full scale)	0.02	0.03	0.03	0.2

CURRENT MEMS GYRO CAPABILITIES. OPERATIONAL TESTS AND RESULTS

Operational measurements for the following IMU devices were carried out simultaneously, as presented in Fig. 4. The MRU from Kongsberg is specially designed for high precision motion measurements in marine applications, and for users requiring high accuracy roll, pitch, and heave measurements. The MRU provides high performance motion data for various marine applications, ranging from small underwater vehicles to large ship motion control systems. Very high reliability is achieved by using solid state sensors, with no moving parts and with proven MRU electrical and mechanical construction.

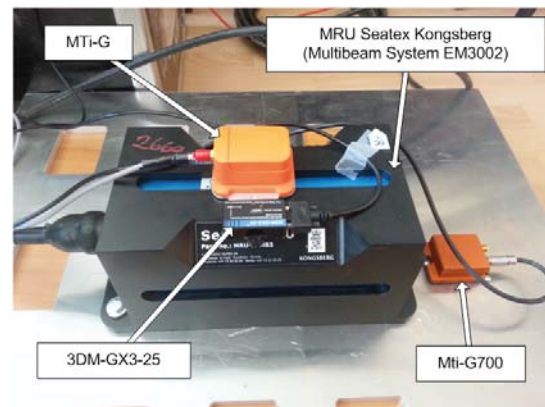


Fig. 4. Operational measurements carried out simultaneously for various devices

3DM-GX3-25 is a high-performance, miniature Attitude Heading Reference System (AHRS), utilizing MEMS sensor technology. It combines a triaxial accelerometer, triaxial gyro, triaxial magnetometer, temperature sensors, and an on-board processor running a Kalman sensor fusion algorithm to provide static and dynamic orientation and inertial measurements.

MTi-G is an integrated GPS and MEMS Inertial Measurement Unit with a Navigation and Attitude and Heading Reference System processor. The internal low-power signal processor runs a real time Xsens Kalman Filter (XKF), providing inertial enhanced 3D position and velocity estimates. The MTi-G also provides drift-free and GPS enhanced 3D orientation estimates, as well as calibrated data of 3D acceleration, 3D rate of turn, 3D earth - magnetic field, and static pressure (barometer). In theory, the MTi-G is a measurement unit for navigation and control of vehicles and other objects.

Results of static tests are presented in Fig. 5, for static Roll measurements. These measurements were also performed for Roll at other attitudes and for various IMU units, but the recorded results were similar and are omitted in the article. Fig. 6 summarizes some of the obtained results.

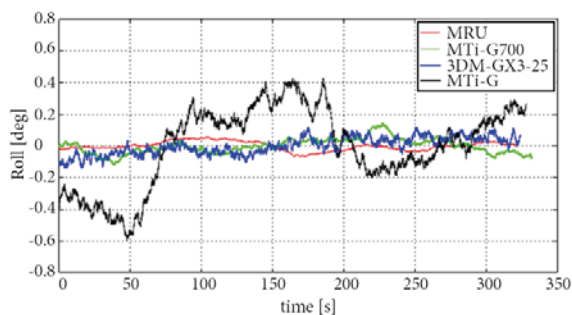


Fig. 5. Measurement results for static Roll tests

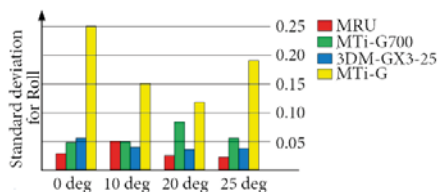


Fig. 6. Standard deviation for static Roll measurements

It can be seen clearly from Fig. 6 that the MRU is distinctly the best IMU. However, the results of dynamic tests reveal a rather opposite tendency in some situations. In the latter case, significant differences can be observed between new generation MTi-G700, 3DM-GX3-25, and MTi-G, but the MTi-G satisfies the requirements. That all is true for dynamic measurement frequencies under 1Hz see Fig. 7.

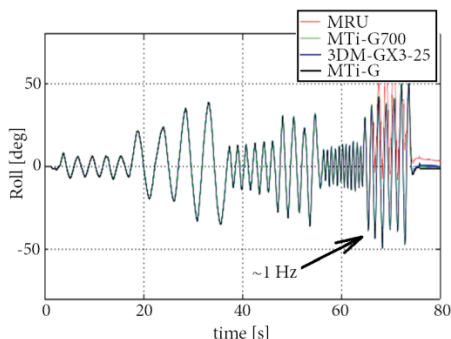


Fig. 7. Dynamic IMU tests for all IMU units

For frequencies close to 1 Hz and higher, the MRU is very unstable and returns to a stable state after over 16 minutes. The records for MTi-G700, 3DM-GX3-25, and MTi-G are much better, and the stable state return period lasts only over 10 seconds. Figs. 8 and 9 present some details of dynamic IMU tests carried for all devices out simultaneously. The highest precision MRU features very long time constant and low sampling time (see Fig. 9).

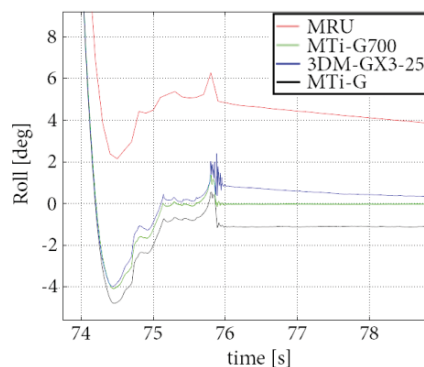


Fig. 8. Dynamic IMU measurements, enlarged for some seconds

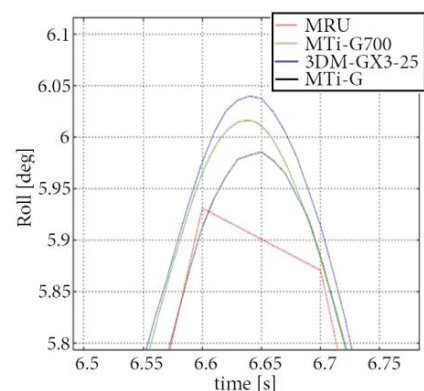


Fig. 9. Dynamic IMU tests for all IMU units, enlarged for some seconds

It should be mentioned that IMU gyros are typically of higher quality, but burden with a bias, as integrating over the time yields a drift. The drift over time results in unreliable input for further processing in the INS system and some compensation is required. So another sensor is used to provide a second tilt or orientation measurement to remove the drift and improve real orientation of the system. Here, an accelerometer or magnetic sensor is a typical choice. However, the magnetic sensor is subject to the influence of physical environment and cannot measure a pitch, but only roll and yaw, and is not always reliable again, therefore the accelerometer sensor is the only choice in practice.

Figs. 7,8,9 present the results of AR integration for the examined IMU technologies, after bias removal. These figures prove high quality of the MEMS gyro and present real roll as a result of the Kalman fusion algorithm process. The AR integration of the gyros as presented in the figures proves their high quality, because the obtained results are comparable to those recorded for the tested Kongsberg MRU device (see Fig. 5). E.g. the standard deviation equals 0.022579 for MRU, 0.076428 for MTi-G700, 0.034849 for 3DM-GX3-25, and 0.15256 for MTi-G. The standard deviation and the variance error obtained from operational tests as presented in Fig. 6.

SUMMARY

The paper presents a unique opportunity of performance comparison of the Seatex MRU Calibration Certificated device to other low cost IMUs. The Seatex MRU is used in high end MBES EM3000. Different MEMS technologies were presented above in very demanding context, where the 10cm resolution required at 100m proofs that even in the narrowed AHRS (Attitude and Heading Reference System) applications, the presented sensor's errors are still a serious problem.

Operational tests were carried out for Kongsberg MRU-M-MB3 – certified device, Xsens MTi-G700, Xsens MTi-G-28A53G3, and MicroStrain 3DM-GX3-25. The tests carried out according to [17] consisted of static operational test comparisons, and dynamic tests for frequencies < 1Hz and higher. They have proved that dynamic tests above 1Hz are a very demanding case for all tested IMUs, but especially for the Kongsberg MRU. In that last case, the test procedure was carried out very carefully and repeated. The results of the dynamic tests above 1Hz resemble a low pass filter answer with long time constant, and that is the case of the Kongsberg MRU.

Other MEMS inertial sensors, which are not certified (see Fig.4), offer affordable and appropriately scaled units that are currently capable of meeting all requirements for accurate and precise attitude evaluation. While the MRU offers the best standard variance of 0.01 deg for the Roll and Pitch, the new generation MTi-G700 offers comparable performance with low noise.

The last question is if these technologies can be used in INS. In author's opinion, they can, perhaps in non-shocking, close to stable conditions. Low cost MEMS gyros are still proving their high quality, but they are not as perfect as other sensors and introduce small errors in each measurement. The gyro sensors currently present quite good quality only for AVHR applications, and progress in this area is still observed.

It is noteworthy that the results of the researches presented in the paper, namely comparative researches and especially the Kalman fusion algorithm, are important issues of marine drone vertical stability estimation. Marine drones possess distinctive dynamic parameters, and that area of investigation has been undertaken as a continuation of current author's investigations.

BIBLIOGRAPHY

1. Anderson B. D. O., Moore J. B.: *Optimal Filtering (Dover Books on Electrical Engineering)*. Paperback – January 5, 2005.
2. Craig J. B., Blondel Ph.: *Developments in the application of multibeam sonar backscatter for seafloor habitat mapping*, Applied Acoustics, 2008
3. Li W., Wang J.: *Effective Adaptive Kalman Filter for MEMS-IMU/Magnetometers Integrated Attitude and Heading Reference Systems*, The Journal of Navigation, 2012
4. Arshad A., Rizal M.: *Recent advancement in sensor technology for underwater applications*, Indian Journal OF Geo Marine Science 2009.
5. Prandi L., Caminada C., Coronato L.: *A low-power 3-axis digital-output MEMS gyroscope with single drive and multiplexed angular rate readout*- Solid-State Circuits , 2011, ieeexplore
6. Zhu R., Sun D., Zhou Z., Wang D.: *A linear fusion algorithm for attitude determination using low cost MEMS-based sensors* - Measurement, 2007 - Elsevier
7. Luczak S., Oleksiuk W., Bodnicki M.: *Sensing tilt with MEMS accelerometers*- IEEE Sensors Journal, 2006
8. Wang M., Yang Y., Hatch R. R.: *Adaptive filter for a miniature MEMS based attitude and heading reference system* - Position Location, 2004
9. Blondel P.: *The Handbook of Sidescan Sonar*, Springer 2018
10. Demkowicz J.: *Submerged objects modeling and storing in a global reference context using multiresolution spline technique*. HYDROACOUSTICS ANNUAL JOURNAL pp. 47-52, vol. 18, 2015.
11. Demkowicz J.: *Multibeam Sonar Records Data Decimation Using Hierarchical Spline Interpolation*. HYDROACOUSTICS 2013 , Vol. 16, pp. 41-46, 2013.
12. Demkowicz J.: *Submerged objects modeling and storing in a global reference context using multiresolution spline technique*. HYDROACOUSTICS ANNUAL JOURNAL pp. 47-52, vol. 18, 2015
13. Bikonis K., Demkowicz J.: *Data Integration from GPS and Inertial Navigation Systems for Pedestrians in Urban Area*. TransNav – International Journal on Marine Navigation and Safety of Sea Transportation 2013, vol. 7, No. 3, pp. 401-406.
14. *L-3 Communications SeaBeam Instruments, Multibeam Sonar Theory of Operation*. 2000.
15. Demkowicz J.: *Particle Filter Modification using Kalman Optimal Filtering Method as Applied to Road Detection from Satellite Images*. MIKON 2014, 20th International Conference on Microwaves, Radar and Wireless Communications.
16. *Analog Devices Technical Articles*. (source: www.analog.com).
17. *Seatex MRU Calibration Certificate*, Kongsberg Gruppen

18. Seube N., Levilly S., de Jong K.: *Automatic Estimation of Boresight Angles Between IMU and Multi-Beam Echo Sounder Systems*, Quantitative Monitoring of the Underwater Environment, Springer, 2016, pp. 13-23

CONTACT WITH THE AUTHORS

Krzysztof Bikonis

e-mail: binio@eti.pg.edu.pl

Gdansk University of Technology

Narutowicza 11/12

80-233 Gdansk

POLAND

IJerzy Demkowicz

e-mail: demjot@eti.pg.edu.pl

Gdansk University of Technology

Narutowicza 11/12

80-233 Gdansk

POLAND

ESTIMATION OF HYDRODYNAMIC COEFFICIENTS FROM RESULTS OF REAL SHIP SEA TRIALS

Daewon Kim

University of Rostock, Rostock, Germany

ABSTRACT

This paper suggests an estimation method for ship's hydrodynamic coefficients, which is based on the system identification method that calculates an optimum value in a mathematical way. For the purpose of modelling existing ships, this study collects real ship sea trial data as benchmarks. Prior to the optimization, a sensitivity analysis is carried out for easy and effective optimization. The simulation results using optimized coefficients agree well with corresponding benchmarks. Following this, with various trim and draught conditions, this study suggests new estimation formulas that concern all trim and draught conditions. Simulation results applying the estimation formulas are satisfactory in regard to a corresponding benchmark, compared to a result obtained by using an existing regression formula.

Keywords: ship manoeuvrability, system identification method, hydrodynamic coefficients, sea trial, mathematical optimization

INTRODUCTION

Modelling is an important way to predict ship's manoeuvrability, and the need for it is continuously growing with the development of marine information technology. The forces and moments acting especially on a submerged part of the hull can be described by hydrodynamic coefficients. International Towing Tank Conference (ITTC) summarized various methods for estimating hydrodynamic coefficients for a ship's manoeuvrability [6].

Fig. 1 and 2 show an overview of all methods and their accuracy with respect to effort/cost characteristics [6]. In the design stage, the captive model test and the Computational Fluid Dynamics (CFD) are common because there is no real ship yet and those are the most reliable sources of hydrodynamic coefficients in the environment [12, 15]. For existing ships, the full-scale trial is the most reliable, but it is not preferred due to its relatively high cost [5, 18]. Thus, a combination of empirical methods and tuning is widely used to model a ship.

This paper suggests an estimation method based on the system identification method that calculates an optimum

value in a mathematical way. This method estimates the hydrodynamic coefficients in a ship's mathematical model by a mathematical optimization algorithm that runs a manoeuvre simulation and compares it with benchmark data at every iteration. Finally, it provides optimized hydrodynamic coefficients.

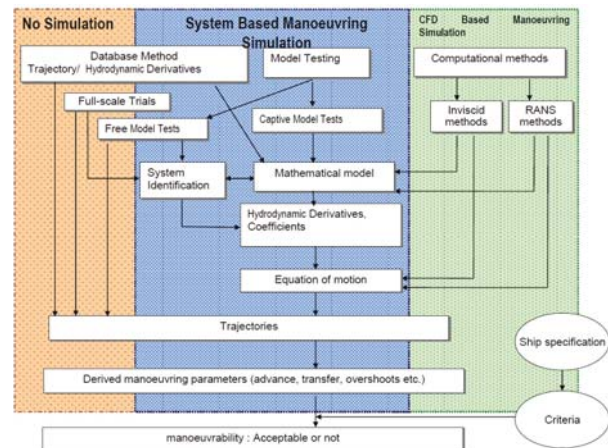


Fig. 1. Overview for prediction methods

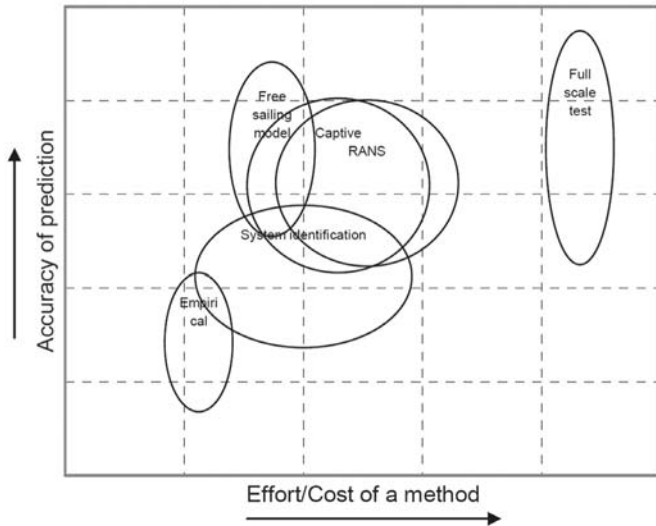


Fig. 2. Accuracy of prediction methods with respect to effort/cost ratio

The system identification method has been studied with various ideas. Abkowitz was the first to apply the Extended Kalman Filter (EKF) to full-scale sea trial data. Rhee and Zhang conducted system-based (SB) free running tests with the EKF algorithm [1, 3, 13, 19]. Tran introduced Sequential Quadratic Programming (SQP) and Broyden-Fletcher-Goldfarb-Shanno (BFGS) algorithms for an optimization process [14, 16]. Kim optimized hydrodynamic coefficients with an interior point algorithm using simulation results as benchmark data [4].

Change of trim and draught has a significant impact on ship's manoeuvrability. This leads to a change in corresponding ship's conditions, such as displacement, location of the centre-of-pressure for the sway force, rudder inflow angle and so on. Much of the previous studies on changing manoeuvrability with various loading conditions have focused on the corresponding changes of displacement, stern shape and rudder area. Kijima and Kose studied influence and importance of trim and draught conditions on a ship's manoeuvrability. In order to estimate ship's manoeuvrability in different trim and draught conditions, they performed captive model tests with multiple ships in four trim and draught conditions: fully loaded, half loaded, ballast with even keel and ballast aft trim conditions [7, 8, 9]. The prediction results based on the estimation agreed well with the measured results of free running model tests. Yasukawa et al. investigated influence of the load condition on the effect of rudder force [17].

Based on previous studies, this paper estimates hydrodynamic coefficients in a mathematical way. A set of results from real ship sea trials in various trim and draught conditions is the benchmark data in an optimization process, and a regression formula is suggested to estimate hydrodynamic coefficients for all trim and draught conditions.

MODELLING AND BENCHMARK DATA

MATHEMATICAL MODEL

Three degrees of freedom (3DOF) ship- and earth-fixed coordinate systems are applied to the modelling for the optimization process. Both coordinate planes are placed on the undisturbed free surface. In the mathematical model, a ship is considered a massive and rigid body. Forces and moment acting on the hull are described as follows.

$$\begin{aligned} X &= m(\dot{u} - vr - x_g r^2) \\ Y &= m(\dot{v} + ur - x_g \dot{r}) \\ N &= I_z \dot{r} + m x_g (\dot{v} + ur) \end{aligned} \quad (1)$$

To each force and moment the modular structure composed by hull, propeller, rudder and other external forces or moments, is applied as follows:

$$\begin{aligned} X &= X_H + X_P + X_R \\ Y &= Y_H + Y_P + Y_R \\ N &= N_H + N_P + N_R \end{aligned} \quad (2)$$

The hydrodynamic forces and moments acting on the ship's hull are comprised of several velocity and acceleration elements. The basic empirical regression formulas for the initial values of the optimization process are taken from Norrbin and Clarke [2, 11]. Each hydrodynamic coefficient can be expressed by a function of ship's main dimensions, such as length, beam, draught, its trim and displacement. The nonlinear components Y_{non} and N_{non} are influenced by the position of the ship's turning point.

$$\begin{aligned} X'_H &= X'_{up} \dot{u} + X'_{vr} vr + X'_{uu} |u| \\ &+ X'_{u^4} u^3 |u| + X'_{uvv} uv^2 |v| \end{aligned} \quad (3)$$

$$\begin{aligned} Y'_H &= Y'_{up} \dot{v} + Y'_{rp} \dot{r} + Y'_{ur} ur + Y'_{uv} |u|v + Y'_{non} \\ N'_H &= N'_{rp} \dot{r} + N'_{vp} \dot{v} + N'_{ur} |u|r + N'_{uv} uv + N'_{non} \\ \{Y'_{uv}, Y'_{ur}, N'_{uv}, N'_{ur}, Y'_{non}, N'_{non}\} &= \\ &f(L, B, T, \Delta) \end{aligned} \quad (4)$$

BENCHMARK DATA

Benchmark data for the optimization are recorded on a 4,500 TEU class container carrier. Five zigzag manoeuvres with three trim and draught conditions were performed for this study. Tab. 1 shows details of the vessel, and Tab. 2 shows manoeuvre conditions of each trial.

where,

- x is/are variable(s) to be optimized;
- f is an objective function that returns minimum or maximum scalar; and
- c_i s are constraints, both equality and inequality conditions, in which variable(s) x must follow the whole optimization process.

Tab. 3 presents an example of the optimization conditions. According to the result of sensitivity analysis, stepwise optimization is applied to the process. Initial values that are essential for the mathematical optimization are calculated by the empirical formulas of Clarke and Norrbín. Objective functions for both steps calculate the sum of X- and Y-coordinate differences between the benchmark data and an optimization result at each iteration.

Optimizations are carried out only for the Data 2 to 4, which have different trim and draught conditions. Remaining measurement data are used for the first validation of optimization results.

Tab. 3. Optimization conditions for Data 3

	Step 1		Step 2	
Solver	fmincon			
Algorithm	interior-point			
Initial values	Xuu	-0.0373	Yuv	-1.3811
	Xu4	-0.4534	Yur	0.3820
			Nuv	-0.4401
			Nur	-0.2348
Lower bounds	Xuu	-0.3700	Yuv	-13.811
	Xu4	-4.5000	Yur	0.0001
			Nuv	-4.4019
			Nur	-2.3480
Upper bounds	Xuu	-0.0001	Yuv	-0.0001
	Xu4	-0.0001	Yur	3.8201
			Nuv	-0.0001
			Nur	-0.0001
Objective function	Track difference			
	Straight motion		Zigzag 10 degrees	
Constraints	None		None	

VALIDATION OF OPTIMIZED COEFFICIENTS

OPTIMIZATION RESULTS

Tab. 4 presents Clarke estimation coefficients and optimization results, and Tab. 5 compares manoeuvre characteristics with corresponding benchmark data. The results show that a simulation result obtained by using finally optimized coefficients is relatively more close to the corresponding benchmark data than a result by using Clarke estimation coefficients.

Tab. 4. Optimization results for hydrodynamic coefficients

		Xuu	Xu4	Yuv	Yur	Nuv	Nur
Data 2	C	-0.0280	-0.3405	-1.5857	0.4281	-0.5625	-0.2675
	S1	-0.0250	-0.2865				
	S2			-1.9472	0.3426	-1.2354	-0.2783
Data 3	C	-0.0373	-0.4534	-1.3811	0.3820	-0.4401	-0.2348
	S1	-0.0515	-0.5873				
	S2			-2.2214	0.4827	-3.4181	-0.6116
Data 4	C	-0.0407	-0.4948	-1.3947	0.3934	-0.3965	-0.2339
	S1	-0.0665	-0.4536				
	S2			-2.2611	0.3919	-0.9541	-0.2335
Remarks	C: Clarke estimation S1: Step 1 (Straight motion) S2: Step 2 (Zigzag manoeuvre)						

Tab. 5. Optimization results for manoeuvre characteristics

		Way/Lpp	Init.	Yaw	Ovst1	Ovst2
Data 2	Clarke	3.33	82	266	1.87	2.73
	Step 1	3.52	79	319	1.99	2.55
	Step 2	3.52	69	378	5.31	9.66
	Bench	3.53	58	370	6.70	11.80
Data 3	Clarke	5.58	57	272	1.87	2.51
	Step 1	5.22	64	286	1.68	2.42
	Step 2	5.22	38	265	3.63	7.13
	Bench	5.22	47	279	4.80	7.40
Data 4	Clarke	3.89	89	414	1.71	1.79
	Step 1	3.50	93	438	1.53	1.72
	Step 2	3.51	87	423	2.98	3.90
	Bench	3.52	78	398	3.20	4.60
Remarks	Bench: Benchmark data (Measured data) Way/Lpp: Distance from start point/Lpp Init.: Initial turning time (s) Yaw: Yaw checking time (s) Ovst1: First overshoot angle (°) Ovst2: Second overshoot angle (°)					

Fig. 5 and 6 show comparisons for track coordinates and heading angle of the measurement Data 3, respectively.

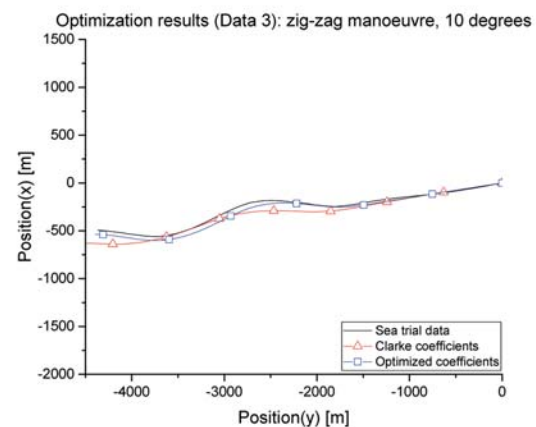


Fig. 5. Trajectory comparison for Data 2

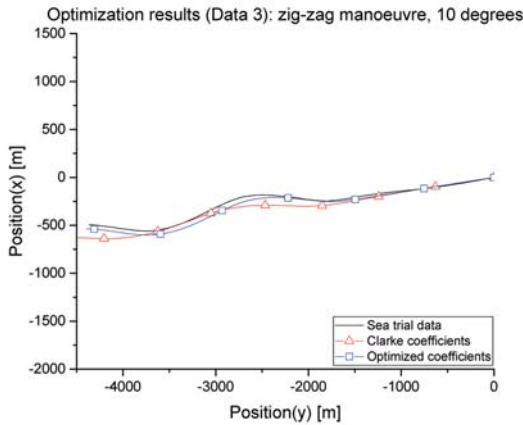


Fig. 6. Heading comparison for Data 2

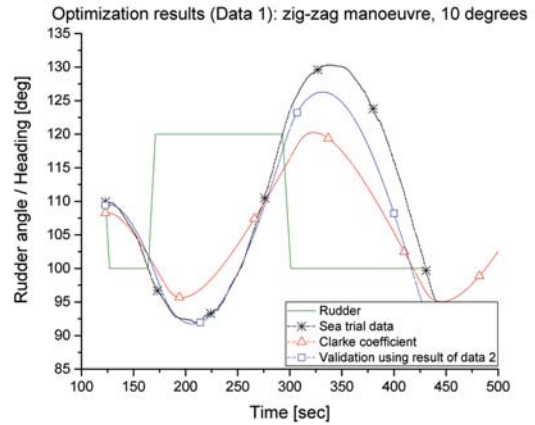


Fig. 8. Heading comparison for Data 1

VALIDATION WITH OTHER BENCHMARKS

Benchmark Data 1 and 5 are compared with simulation results that use optimized coefficients of Data 2 and 4, respectively. Tab. 6 compares the benchmark data and the simulation results.

Tab. 6. Validation with additional benchmarks

		Way/Lpp	Init.	Yaw	Ovst1	Ovst2
Data 1	Clarke	4.7	76	267	2.34	2.26
	Val.	4.8	51	278	6.27	8.28
	Bench	4.42	46	293	6.00	12.30
Data 5	Clarke	2.15	93	441	3.21	3.25
	Val.	1.93	84	436	5.59	6.26
	Bench	1.96	81	405	5.60	6.10
Remarks		Val.: Validation of hydrodynamic coefficients using optimization results of Data 2 and Data 4, respectively Bench: Benchmark data (Measured data)				

Fig. 7 to 10 compare benchmark data and corresponding simulation results. In the case of Data 1, it is supposed that difference in a second overshoot angle and an item Way/Lpp is caused by difference in trajectories of the benchmark and the simulation result.

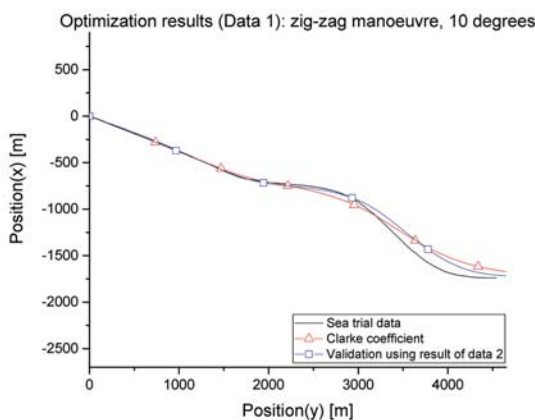


Fig. 7. Trajectory comparison for Data 1

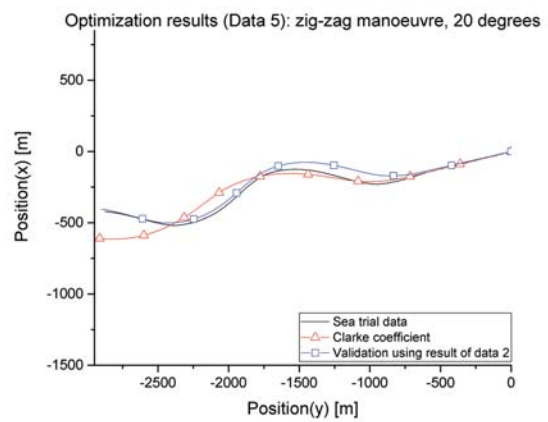


Fig. 9. Trajectory comparison for Data 5

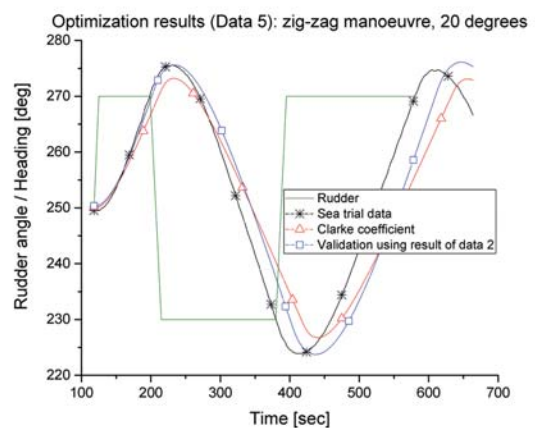


Fig. 10. Heading comparison for Data 5

SUGGESTION ON NEW ESTIMATION FORMULAS

Based on the results of the optimization and the Clarke estimation, a new estimation formula is suggested regarding all trim and draught conditions. A set of optimized coefficients under certain trim and draught condition is set to a default condition, and differences of trim and draught are calculated to other optimized coefficients. Details of the estimation formula are as follows.

$$\begin{aligned}
& \text{Coeff.new} \\
& = OT.Coeff.standard.trim\&draught \\
& + (Corr.draught*CE.Diff.draught \\
& + Corr.trim*CE.Diff.trim)
\end{aligned}
\tag{6}$$

$$\begin{aligned}
& CE.Diff.draught \\
& = CE.Coeff.standard.trim\&draught \\
& - CE.Coeff.target.draught\&standard.trim
\end{aligned}$$

$$\begin{aligned}
& CE.Diff.trim \\
& = CE.Coeff.standard.trim\&draught \\
& - CE.Coeff.target.trim\&standard.draught
\end{aligned}$$

where,

- *Coeff.new* is an estimated coefficient;
- *OT.Coeff.standard.trim&draught* is a coefficient that has been optimized (Own Tuned) under the standard trim and draught condition;
- *Corr.xxx* is a correlation value that is calculated by all of the optimized coefficients;
- *CE.Diff.xxx* is the difference between standard trim and draught Clarke estimation coefficient and target trim and draught Clarke estimation coefficient; and
- *CE.Coeff.xxx* is a Clarke estimation coefficient.

A standard condition for this study is set to be : 10m draught and even keel. Tab. 7 shows results of Clarke estimation and the new estimation method.

Tab. 7. Estimation results: hydrodynamic coefficients

Tm=11.85m t=-0.1m	Clarke	Estimated
	76	267
Xuu	-0.0304	-0.0260
Xu4	-0.3699	-0.5263
Yuv	-1.4991	-2.3778
Yur	0.4056	0.5005
Nuv	-0.5144	-3.0489
Nur	-0.2527	-0.5670

To validate the estimated result, Tab. 8 compares characteristics of a zigzag manoeuvre with 20 deg rudder angle inclination. A benchmark is taken from the official manoeuvring booklet of the vessel. Since there is no trajectory data in the booklet, only the numeric values and a heading angle graph are applied to the validation. As Fig. 11 shows, the

simulation result using coefficient with the new estimation method is relatively closer to the benchmark data than that obtained by using Clarke estimation.

Tab. 8. Validation of estimation formulas

Tm=11.85m t=-0.1m	Way/Lpp	Init.	Yaw	Ovst1	Ovst2
Clarke	28.5491	56	285	3.4	6.8
Val.	28.5608	48	275	7.7	11.9
Bench	-	53	278	8.8	13.7
Remarks	Val.: Validation of hydrodynamic coefficients using estimation formulas Bench: Benchmark data (Measured data)				

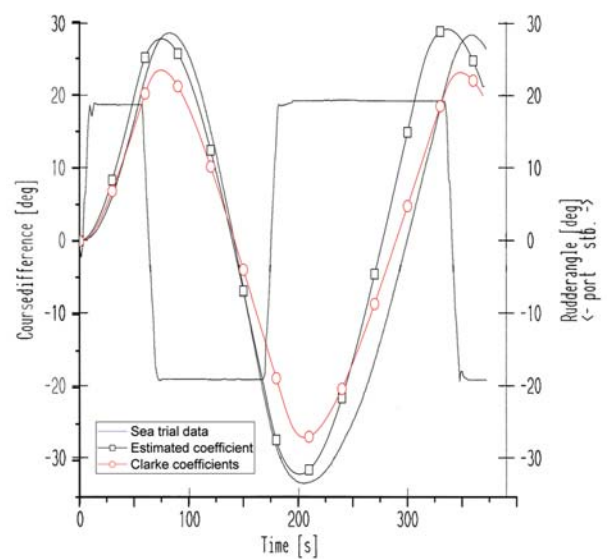


Fig. 11. Heading comparison with the use of manoeuvring booklet (sea trial data)

CONCLUSION

This paper presents a study on estimating hydrodynamic coefficients by using real ship sea trial data, especially for all trim and draught conditions. A mathematical optimization, a part of system identification, is used to calculate optimum hydrodynamic coefficients. Benchmarks are taken from the sea trial of a container carrier. Results of this study can be summarized as follows.

Simulation results that use optimized hydrodynamic coefficients are closer to the corresponding benchmarks than those obtained from Clarke estimation.

The benchmarks Data 1 and 5 which are not used to optimize hydrodynamic coefficients, and their corresponding simulation results using optimized coefficients are similar to each other, compared with simulation results using Clarke estimation coefficients.

Hydrodynamic coefficients, estimated by using the suggested formulas, are satisfactory for simulation running, compared to a corresponding benchmark from a manoeuvring booklet (sea trial data).

This summary shows that the proposed estimation formulas can complement the existing Clarke formulas. However, five measurement data are not enough to attribute a high reliability to the proposed estimation method. In addition, various manoeuvres such as turning and other emergency manoeuvres should be included in the optimization process. These issues should be considered in future studies.

REFERENCES

1. Abkowitz, M. A.: *Measurement of Hydrodynamic Characteristics from Ship Manoeuvring Trials by System Identification*, SNAME Transactions, Vol. 88 (1980), pp. 283–318.
2. Clarke, D., P. Gedling, G. Hine: *The Application of Manoeuvring Criteria in Hull Design Using Linear Theory*, Transactions of the RINA, London (1983), pp. 45–68.
3. Hwang, W. Y.: *Application of System Identification to Ship Manoeuvring*, PhD thesis, MIT (1980).
4. Kim, D. W., K. Benedict, M. Paschen: *Estimation of Hydrodynamic Coefficients from Sea Trials Using a System Identification Method*, Journal of the Korean Society of Marine Environment & Safety, Vol. 23, No. 3 (2017), pp. 258–265.
5. Im, N., S. Kweon, S. Kim: *The Study on the Effect of Loading Condition on Ship Manoeuvrability*, Journal of the Society of Naval Architects of Korea, Vol. 42, No. 2 (2005), pp. 105–112.
6. ITTC: *The Manoeuvring Committee – Final Report and Recommendations to the 25th ITTC*, Proceedings of 25th ITTC, Vol. 1 (2008), pp. 145–152.
7. Kijima, K., T. Katsuno, Y. Nakiri, Y. Furukawa: *On the manoeuvring Performance of a Ship with the Parameter of Loading Condition*, Journal of the Japan Society of Naval Architects and Ocean Engineers, No. 168 (1990), pp. 141–148.
8. Kijima, K., Y. Nakiri, Y. Furukawa: *On the Prediction Method for Ship Manoeuvrability*, Proceedings of the Internal Workshop on Ship Manoeuvrability, Hamburg Ship Model Basin, No. 7 (2000).
9. Kose, K.: *Studies on the Effect of Loading Condition on the Maneuverability of Ships*, Journal of the Japan Society of Naval Architects and Ocean Engineers, No. 82 (1991), pp. 155–165.
10. Nocedal, J., Wright S. J.: *Numerical Optimization – second edition*, Springer (2006).
11. Norrbin, N. H.: *Theory and Observations on the Use of a Mathematical Model for Ship Manoeuvring in Deep and Confined Waters*, SSPA Publication, No. 68, Gothenburg (1971).
12. Oltmann, P.: *Identification of Hydrodynamic Damping Derivatives – A Pragmatic Approach*, International Conference on Marine Simulation and Ship Manoeuvrability, Vol. 3, Paper 3 (2003), pp. 1–9.
13. Rhee, K. P., K. Kim: *A New Sea Trial Method for Estimating Hydrodynamic Derivatives*, Journal of Ship and Ocean Technology, Vol. 3, No. 3 (1999), pp. 25–44.
14. Saha, G. K., A. K. Sarker: *Optimization of Ship Hull Parameter of Inland Vessel with Respect to Regression Based Resistance Analysis*, Proceedings of MARTEC – The International Conference of Marine Technology (2010).
15. Seils, J.: *Die Identifikation der hydrodynamischen Parameter eines mathematischen Modells für die gesteuerte Schiffsbewegung mit Verfahren der nichtlinearen Optimierung* (in German), Doktorarbeit der Hochschule für Seefahrt Warnemünde-Wustrow (1990).
16. Tran, K. T., A. Ouahsine, F. Hissel, P. Sergent: *Identification of Hydrodynamic Coefficients from Sea Trials for Ship Manoeuvring Simulation*, Transport Research Arena, Paris (2014).
17. Yasukawa, H., Y. Yoshimura, K. Nakatake: *Hydrodynamic Forces on a Ship Moving with Constant Rudder Angle: A Theoretical Treatment of Rudder Angle Test*, Proceeding of MARSIM 1996 (1996), pp. 435–448.
18. Yoon, S., D. Kim, S. Kim: *A Study on the Manoeuvring Hydrodynamic Derivatives Estimation Applied the Stern Shape of a Vessel*, Journal of the Society of Naval Architecture of Korea, Vol. 53, No. 1 (2016), pp. 76–83.
19. Zhang, X., Z. Zou: *Identification of Abkowitz Model for Ship Manoeuvring Motion Using Support Vector Regression*, Journal of Hydrodynamics, Vol. 23, No. 3 (2011), pp. 353–360.

CONTACT WITH THE AUTHOR

Daewon Kim

e-mail: kim.daewon@hotmail.com

University of Rostock
Albert-Einstein-Strasse 2
18059 Rostock
GERMANY

SIMPLE COMPUTATIONAL METHODS IN PREDICTING LIMIT LOAD OF HIGH-STRENGTH COLD-FORMED SECTIONS DUE TO LOCAL BUCKLING: A CASE STUDY

Paweł Bielski

Leszek Samson

Gdansk University of Technology, Faculty of Ocean Engineering and Ship Technology, Poland

Oskar Wysocki

Jacek Czyżewicz

Gdansk University of Technology, Faculty of Mechanical Engineering, Poland

ABSTRACT

Cold-formed thin-walled sections are prone to local buckling caused by residual stresses, geometrical imperfections and inconsistency of material properties. We present a real case of buckling failure and conduct a numerical and experimental study aimed to identify methods capable of predicting such failures. It is important because designers of structures are getting more FEA-oriented and tend to avoid lengthy procedures of cold-formed structures design. Currently adopted methods are complicated and require patience and caution from a designer which is reasonable in case of the most important structural members but not necessarily so in ordinary design. Since it is important, we offer an insight into several FEA and manual methods which were sufficient to predict the failure while remaining fairly simple. Using a non-uniform partial safety factor was still necessary. We hope that this paper will be of interest for people performing a lot of routine analyses and worrying about reliability of their computations.

Keywords: high-strength steel structures; cold-formed thin-walled sections; local buckling; stability of structures; Eurocode 3 safety factor

INTRODUCTION

The paper addresses the problem of local stability of cold-formed high-strength steel members in the context of industrial design. We examined a real case of buckling failure and performed several relatively effortless computational steps which would have been enough to predict and prevent this failure. It is an important issue, since most currently available procedures are either complicated or demand non-obvious informations on residual stresses, field of imperfections, changes in ductility, etc. Cold-formed steel members are equally popular in coastal and offshore engineering (eg. [9]), machine industry, civil engineering and any branch of industry relying on steel structures. With the

growing popularity of FEA software in average design offices, the design practices are shifting more towards numerical analyses of individual cases. As long as no extraordinary structural members of great importance are concerned, it is easier and faster to perform simple FEM calculations than to apply complicated procedures. Of course, if complicated structures requiring special care are involved or a specialised research study is executed, geometrical imperfections are measured or assumed in order to get more correct results (eg. [9]). In contrast, performing such precise computations in regular design practice is considered too costly. As a result, according to our own experience and observations, local stability is often overlooked or overly simplified in the design phase, since the available methods are beyond the reach of

an average engineer or are too time-consuming. What is needed is a feasible method for quick and reliable calculation of ultimate load of such structures. Since it is important, we try to identify the main neglects on the stage of design which led to this particular failure. In the same time we try to suggest some alternative methods which might be sufficient while remaining relatively simple and straightforward to execute by any structural engineer.

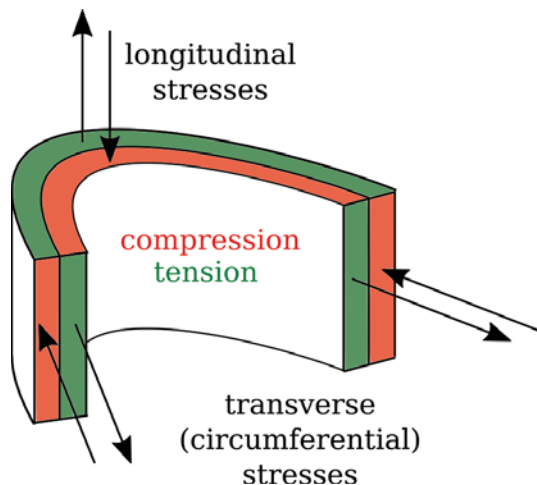


Fig. 1. Simplified visualisation of the final residual stresses in a corner after the “spring-back” phase of cold-forming according to Quach [11]; note that in reality the stress distribution especially in the transverse direction is considerably more complex than in the figure

Although many recommendations for calculating the cold-formed sections load capacity already exist (notably AISI [3] and Eurocode 3 [5]), a universal and simple method of safe design is yet to be developed. In 1975 Ingvarsson came up with a theoretical analysis which proved the existence of residual stresses not only in the circumferential direction of a profile (perpendicular to the bending axis), but also in the longitudinal direction [6]. Magnitude of this stress component varies depending on the cold-forming conditions. This finding was of much importance for understanding the cold-formed section strength, since longitudinal stresses directly affect the overall bending load capacity. In 1981 Crisfield developed a numerical method allowing to compute non-monotonous equilibrium paths and thus enabled to predict post-buckling behaviour [4]. In 1990 Weng and Pekoz exhibited that cold-forming induces a field of residual stresses which is different from that of hot-rolling, regardless of the fact that at the time AISI did not distinguish between these two technologies in terms of calculating the load capacity [18]. In the following years a series of numerical, analytical and empirical methods were developed to deal with the problem. Schafer and Pekoz insisted on including both residual stresses and imperfections as initial conditions in numerical modelling and proposed to employ at least 2 different states of geometrical imperfection based on eigenmodes along with flexural residual stresses in all elements [13]. Since residual stresses in the cold-formed corners can reach even up to 50% of the initial yield

stress, membrane stresses should also be assumed in corner areas of such models. The same authors popularised usage of the Direct Strength Method in engineering practice as an alternative to the commonly acknowledged Effective Width Method [3] due to the excessive complexity of the latter [14]. Yu and Schafer executed some experimental studies on local buckling behaviour of cold-formed members [21] and discussed usability of cumulative distribution function in adopting the magnitude of initial imperfections [22]. Quach wrote a massive PhD dissertation on multiple aspects of modelling the development of the cold-forming stresses [11] and together with Qiu they exhibited that in the process of cold-forming not only residual stresses are established, but also modifications of the yield stress value are applied (generally increase of this value) and even more importantly the ductility of material is changed, which causes the corner cracking during local buckling [12]. Laim et al. compared empirical and numerical methods for predicting the cold-formed sections buckling behaviour and coupled the study with the experimental work on real specimens. Usability of Eurocode 3 methods was confirmed, however only medium strength (up to 460 MPa) steel was tested and still a need for “new design guidelines” was stated [7]. Abambres and Quach explicitly stated that “One of the most challenging aspects in FEA aimed to simulate the real behaviour of steel member, is the modelling of residual stresses” [1]. Szymczak and Kujawa [15] and Lu [8] provided additional analytical solutions to predict the buckling behaviour of cold formed-members based on eigenmodes, however these methods are not always suitable to applications where a very local form of stability loss is expected (such as development of individual wrinkles [20]). Wang et al. conducted experimental and numerical tests again in terms of Eurocode 3 efficiency, however this time a high strength S700MC steel was involved. The standard procedure was found to be insufficient to assure safety of cold-formed structures, stating that the “Partial safety factor γ_{m0} greater than the currently adopted value of unity is required for high-strength steels” [17]. To date there is no reliable and fast method liberating a designer from identifying or assuming complex imperfection and stress fields in the process of cold-formed members design.

In the paper we present a real case of failure of a cold-formed high-strength steel member along with description of the overly simplified design methods which might have led to over-estimation of the structure load capacity. Later we describe a little more complex, however still relatively simple numerical methods (without introducing random or measured imperfection field, residual stresses or changes in material properties other than plasticity), which were used in the following investigation of the failure. Lastly we present a controlled destructive test carried out on another specimen of the discussed beam type and we conclude on usability and safety of the executed computational methods in this particular case. Some conclusions regarding Eurocode 3 procedures are then drawn. It should be noted that the work featured in the paper is an extension and development of the study presented earlier at a conference [2].

MATERIALS AND METHODS

OBJECT OF THE STUDY

The discussed beams are structural members of a refuse collection vehicle more commonly known as garbage truck. Refuse Collection Vehicle (RCV) consists of a container body, a tailgate and a lifter. Its main function is collection, compaction and transportation of waste. The mechanism is powered by a hydraulic system supplied by the pump mounted on the truck's engine. A greater part of RCV is a welded steel structure designed to withstand a cyclic load produced by high pressure in hydraulic cylinders. Many of the load bearing elements are thin-walled structures, since mass reduction is an important factor of RCV development. Lighter vehicles can carry larger waste cargo due to legal limitations of total unit mass.

The examined beams were designed to resist the ejector plate during compaction of waste and discharging of the RCV. They were made of a high strength S700MC steel and consisted mainly of 3 to 5 mm thick steel sheets. The beams were manufactured using cold-forming (4 mm bending radius) and welding (backplate / reinforcing elements).

INITIAL FAILURE

We will use the term "beam A" to refer to the first failure. The beam was re-designed in the office as a part of mass reduction program. Originally only linear FEM calculations were performed in Autodesk Inventor and a generic, industry-ready solid geometry was used for this purpose. A screenshot of the analysis and its complex geometry is shown in Fig. 2. The structure was considered safe.

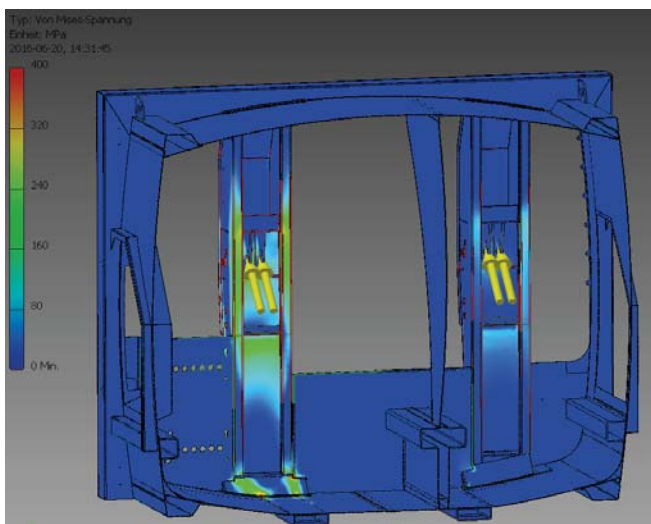


Fig. 2. Stresses obtained during the initial linear FEM calculations performed by designers beforehand; the stresses are evenly distributed along the beam length and generally do not exceed 400 MPa

What happened later was a buckling failure of the newly designed member during fatigue stress tests. The following investigation has been described in detail in the previous paper [2]. Here we will focus only on the essential part of the study.

According to the Eurocode 3 EN 1993-1-1 [5] recommendations, thin-walled steel sections can fall under one out of four categories. This classification is based on slenderness of the cross-section wall and describes section's local stability in plastic, elasto-plastic and elastic ranges. The class 1 and 2 sections are able to reach full plasticity without losing local stability. The class 3 sections are prone to buckling in an elasto-plastic state, after reaching yield stress partially but before entering plastic limit state. The class 4 sections lose stability in the elastic state, so full material strength can not be utilised (Fig. 3). The examined section was classified as a Class 3 element, which means that the elastic limit state should be reached before buckling.

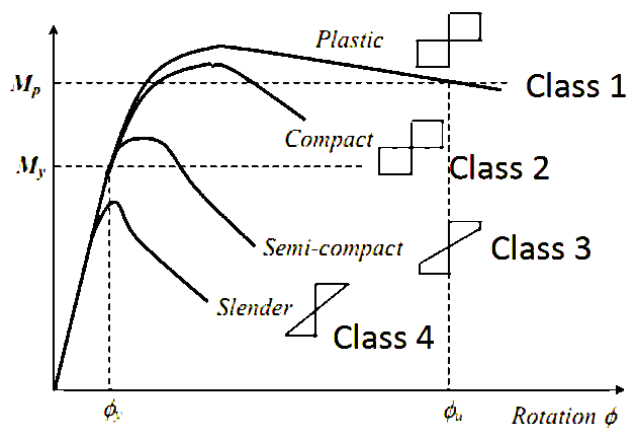


Fig. 3. M_y (elastic) and M_p (plastic) moment acting as an envelope for the real limit state moment for the Class 3 sections based on Eurocode 3 [5]

The rest of the study was conducted in Abaqus FEA software. The geometry was simplified and reduced to a mid-surface model (Fig. 4) with shell elements, since it is more appropriate for modelling bending of thin-walled structures and avoiding volumetric locking of solid elements [10]. Symmetry conditions were applied and several support conditions were assumed to create an envelope of possible solutions. It was later inspected in the following experimental work that the boundary conditions are actually simple pinned supports.

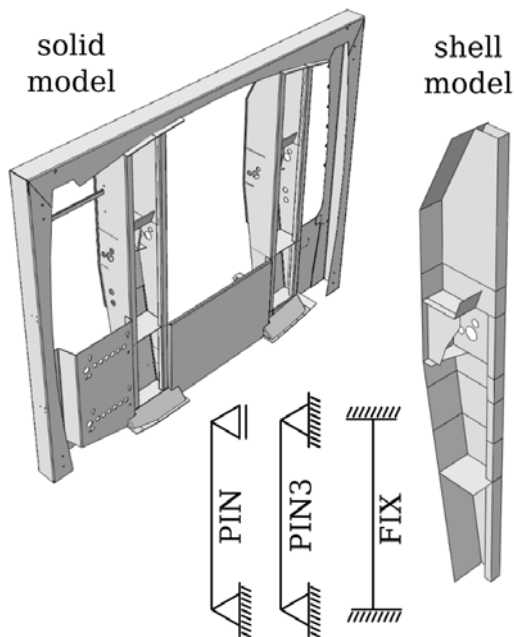


Fig. 4. Full geometrical model and its simplified representation as shell model with symmetry conditions and pinned / fixed support schemes

The real ultimate load was 280 kN and the one predicted by geometrical and material non-linear analysis was 320 kN, which equals about 15% of dangerous over-estimation. These results differ slightly from the ones obtained in the current study, because beams A and B had different spans (beam A 1880 mm, beam B 1780 mm) due to asymmetric layout of the RCV container body.

CONTROLLED FAILURE

An experimental study on beam B was conducted to further investigate the issue. The study was designed in a way to closely reflect the first case of failure. Simultaneous measurements of strains, load and displacement were performed. Preliminary measurements were executed to identify the real boundary conditions (supports) of the beam before destruction. As a result, we managed to reproduce the initial failure mechanism (deformation) while collecting additional information concerning what is happening within the structure.

Response of the system was recorded by means of strain and displacement measurements. Displacement was measured only in a single representative spot using a traditional dial distance indicator. This single displacement value was later used to identify the supports. Additionally, two cameras were used to record the experiment in two perpendicular directions. Strains were recorded using strain gauges placed in 10 different spots, however only 6 of them were active during destruction (limitations of the 6-channel recording device). The remaining gauges were used to identify stiffness of the supports. The spots were selected so that the following regions were covered:

- two boundary areas near the supports;

- a single representative cross-section without stiffeners, including areas of tension and compression;
- locations of the predicted local buckling, based on the observations from the initial failure and the coupled numerical study.

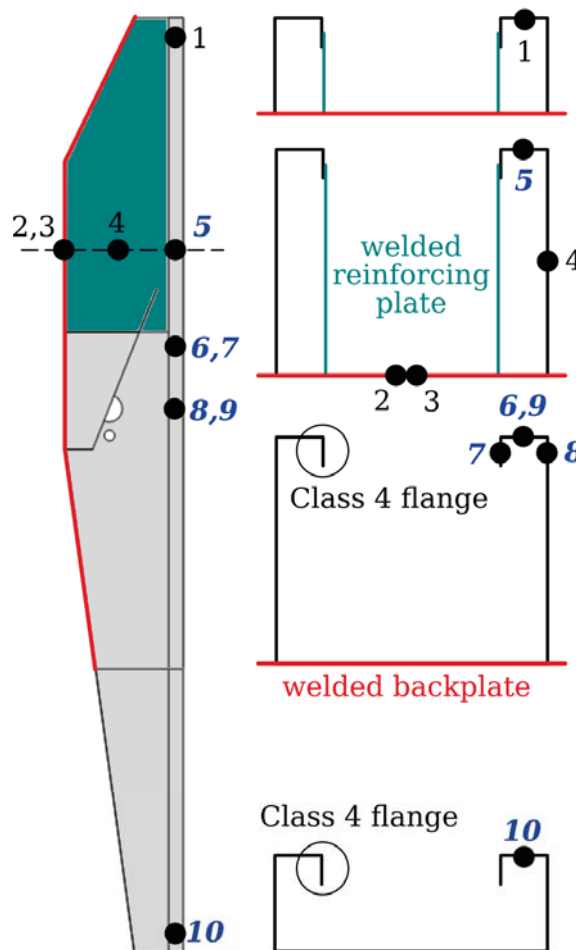


Fig. 5. Scheme of the examined beam with locations and numbers of strain gauges marked; the strain gauges active during the destructive test are indicated; note the differences in cross-section along the height of the beam

All of the strain gauges were oriented in a way to measure the longitudinal strains and not the circumferential strains. The equipment used to capture strains was composed of the following elements:

- bonded resistance strain gauges of 350 Ohm resistance and a gauge factor of 2.15;
- the strain gauge was arranged as a quarter Wheatstone bridge circuit;
- the bridge was connected via an instrumentation amplifier to one of the six 24-bit ADC channels;
- the converted signal from ADC was transferred to PC using a microcontroller;
- the *pySerial* Python library was used to register digital signals as text files;
- the data collected from the test was illustrated by Python scripts using *Numpy* package and *Matplotlib* plotting library.



Fig. 6. Location of a dial distance indicator used to measure displacement; the same spot is used as reference displacement to compute ultimate load in the numerical analysis

The test stand varied slightly from the one used for the initial experiment. The load was applied by a 120 mm diameter cylinder at 15 degree angle relatively to horizontal direction. Maximum pressure of 270 bar (305 kN) was gradually achieved as a result of beam resistance to cylinder extension in approximately 1 mm/s. Inner resistance of the cylinder sealing was experimentally tested by means of repeated loading and taken into account in the final force calculation as 5 kN according to the hysteresis graphs. Measurement accuracy of pressure gauge was +3 bar (3.5 kN).



Fig. 7. Location of the strain gauges on the real structure

Preliminary loading was conducted in a linear range to identify the stiffness of the beam. It was measured that the average displacement measured by the dial indicator is 1 mm per 37 kN of force, which corresponds to the simple support conditions assumed in the numerical model. Additionally, strain gauges 1 and 10 (boundary sections) and 2–5 (control sections) were used to measure strains, which were consistent with the simple support predictions (Fig. 10). Thus the boundary conditions provided by the frame were considered identified as near-zero rotational stiffness (Fig. 8)

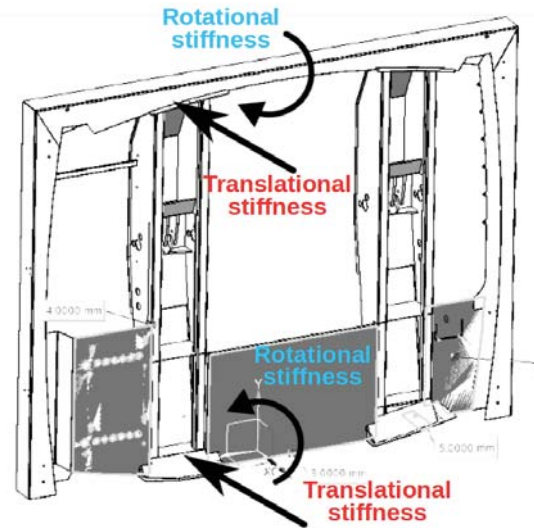


Fig. 8. Interpretation of the boundary conditions with regard to the stiffness of support provided by frame

After the initial failure several steel samples were cut from the original beam and from raw material as reference and tested for their mechanical properties (external analysis and expert opinion). The test focused on determining the chemical composition and tensile strength of specimens. It was confirmed that the steel used for production was actually S700MC in terms of chemical compounds. However, tensile tests exhibited reduced yield stress, averaging around 630 MPa for all samples. It was concluded that the reduced properties of the steel was faulty from the beginning. Nevertheless the 630 MPa value of yield stress was taken into consideration in the following numerical analyses. In general, three material variants were assumed: b700 (700 MPa yield with no hardening), b630 (630 MPa with no hardening), r700 (real strain-stress curve to examine the dangerous optimistic area near the yield stress shown in Fig. 9).

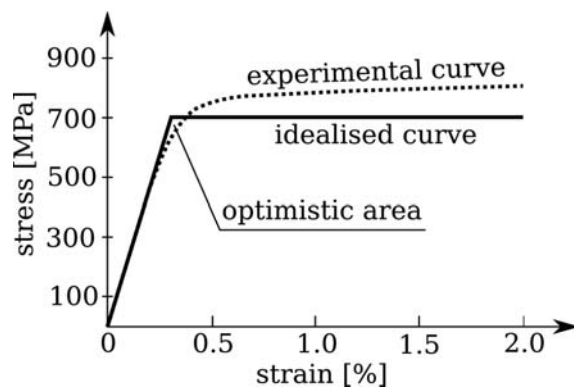


Fig. 9. Experimental (obtained by Winful et al. [16]) and idealised stress-strain relation of S700MC steel; note the optimistic area where the idealised curve delivers more stiffness than the experimental one

Numerical investigations covered LBA (linear buckling analysis), GMNA (geometric and material non-linear analysis) and linear static analysis. Imperfections were assumed basing on the LBA deformation and real deformation of beam A.

Manual calculations were performed too to provide an overview of possible results.

RESULTS

Results of the manual calculations performed on the simplified geometry are presented in Fig. 10. The elastic and plastic limit states form a boundary for the real ultimate load of a Class 3 section [5]. From these calculations we can conclude that a failure should occur somewhere between the 330 kN and 478 kN values of concentrated force on a hydraulic cylinder. It is important to note that since the cross-sections vary between the loaded and control sections, the 0.46 ratio of maximum stresses were calculated taking both the different locations and sections into account.

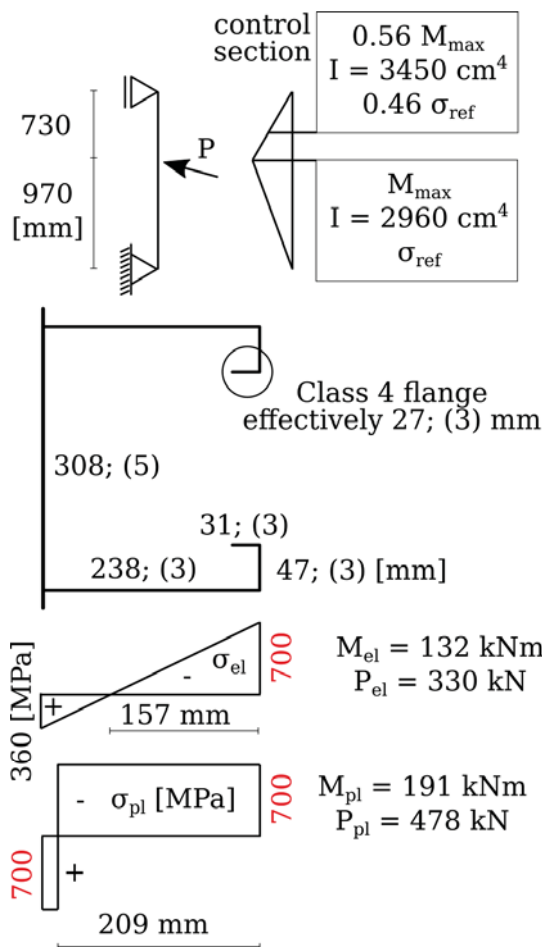


Fig. 10. Top: simplified diagram of the beam and its basic characteristic values; Bottom: Simplified cross-section of the beam ([length]; ([thickness]) of each element) and distribution of stresses in elastic and plastic limit states; M_{el} – extreme elastic moment, M_{pl} – extreme plastic moment, P_{el} and P_{pl} – forces corresponding to the moments

The post-buckling deformations of the A beam (initial failure) and B beam (controlled failure) are presented in Fig. 11. The large bulge on the side is located around the holes in both cases. This feature will be used to evaluate the deformations obtained from the numerical analyses.

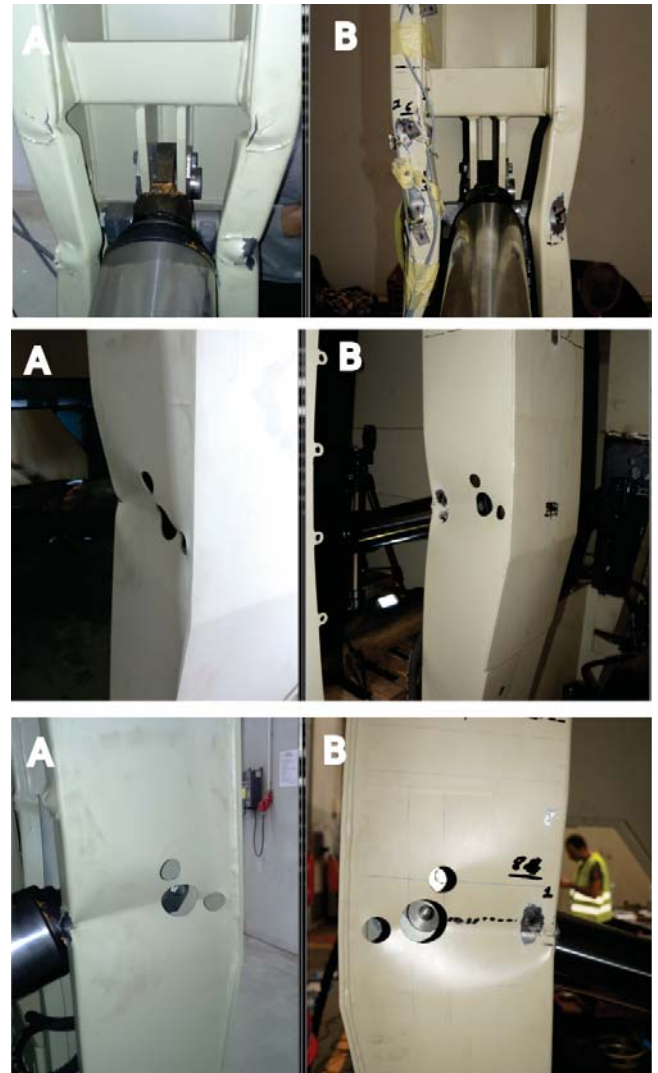


Fig. 11. Various views of the A (initial failure) and B (controlled failure) beams after buckling; the deformations are essentially the same

Results of the experimental loading are presented in Fig. 12 (direct values from strain gauges) and Fig. 13 (calculated stresses). The first thing worth noting is the ratio of stresses between 5 (control section) and 6+9 (loaded sections) strain gauges, which equals the predicted 0.46 and justifies the boundary conditions assumed in the numerical model. The next thing are the strain gauges 7 curves, which indicate the largest values of stress and strain in the whole structure. The stresses are actually elevated in this location due to stress concentration, which was also exhibited in a simple linear numerical analysis (Fig. 14) The last thing to notice in the graph is development of the small bulge (Fig. 15) around the 220 kN force in the strain gauge 7 area.

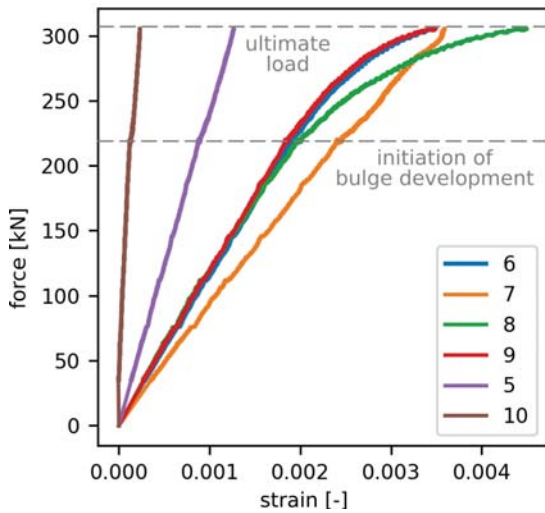


Fig. 12. Experimental strain-force curves obtained directly from the strain gauges during the destructive test; strain gauge numbers in the legend



Fig. 15. Deformation of the strain gauge 7 location due to local buckling; note the bulge developing straight at the center of the strain gauge

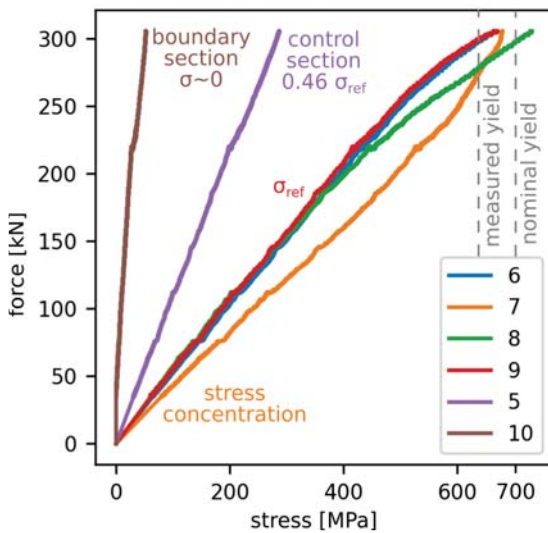


Fig. 13. Experimental stress-force curves computed from the strain curves using the strain-stress relationship by Winful et al. [16]

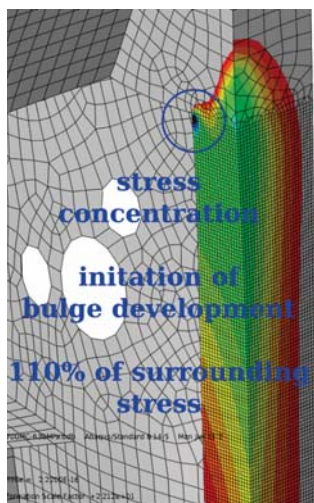


Fig. 14. Numerical representation of the local concentration of stresses around the strain gauge 7 area

The first buckling mode obtained by means of LBA is presented in Fig. 16. The shape of deformation was always the same regardless of the type of imperfection applied, however the buckling factor varied accordingly. It was the highest (360 kN) for no imperfections and the lowest (325 kN) for both imperfections in the same time. Applying individual imperfections resulted in values lying between these two. Locations of the load imperfections were chosen basing on the shape of buckling mode.

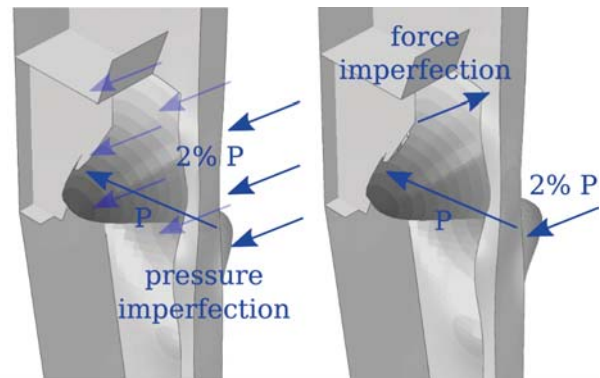


Fig. 16. The first buckling mode obtained via linear buckling analysis and the two types of imperfections applied during all analyses

Force-displacement equilibrium paths obtained from GNMA are presented in Fig. 17. Note that the curves are nearly linear up to the limit load, which means that no bulges are developed earlier. The 630 MPa with force imperfection and 630 MPa with pressure imperfection variants result in the same 322 kN limit load. However it is extremely important to notice that the post-buckling curves and deformations (Fig. 18) vary greatly and the one resulting from the pressure imperfection is far closer to the experimental one (Fig. 11) than the force imperfection variant.

DISCUSSION

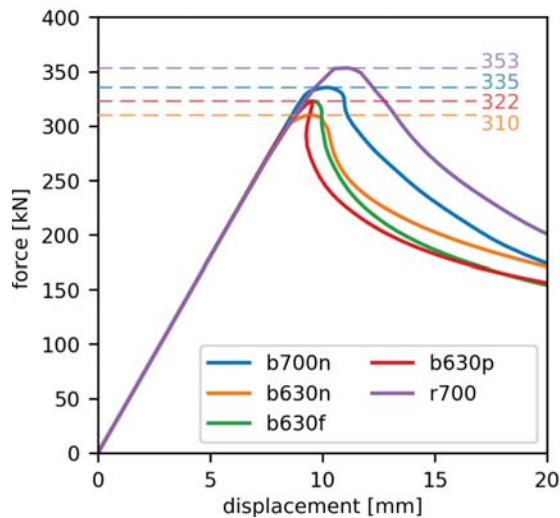


Fig. 17. Numerical displacement-force curves used to predict the ultimate load values; b – bilinear, r – real, 700 / 630 yield stress, n – no imperfection, f – force imperfection, p – pressure imperfection

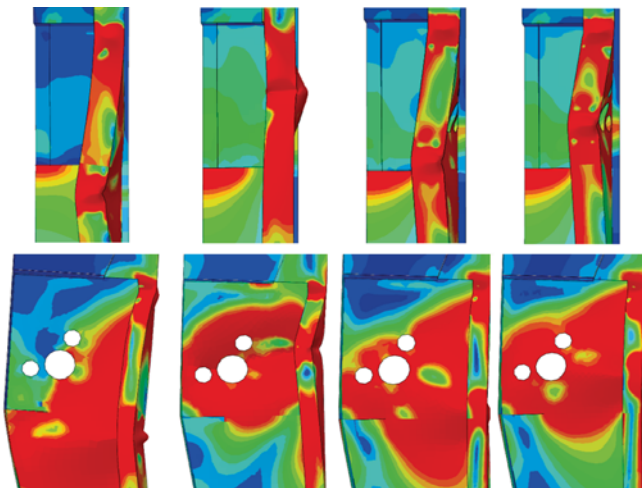


Fig. 18. Results of the numerical GNMA analyses, from left to right: 700 MPa yield stress w/o imperfections, 630 w/o imperfections, 630 with force imperfection, 630 with pressure imperfection; note the different height of the lower bulge in each case

All of the numerical and manual results of limit load prediction are presented in Tab. 1 along with relative deviations from the experimental value.

Tab. 1. Ultimate loads obtained by various computational methods, the three LBA values stand for no imperfection, pressure imperfection and force imperfection; the two linear static values stand for the actual maximum moment section and the strain gauge 7 concentration region; the three GMNA values stand for 630 MPa with no imperfections, 630 MPa with load imperfections and 700 MPa with no imperfections

Source	Force [kN]	Difference [%]
Simplified plastic moment	478	56.7
Linear buckling analysis	360 / 344 / 338	18.0 / 12.8 / 10.8
Simplified elastic moment	330	8.2
Linear static analysis	315 / 362	3.3 / 18.7
Geometric and material non-linear analysis	310 / 322 / 335	1.6 / 5.6 / 9.8
Experimental measurements	305	0.0

All predictions failed to meet the real value of the limit force, however they varied greatly among themselves. The manual calculations resulted in an envelope exceeding the real value by over 8% on the lower boundary, indicating that the Eurocode 3 predictions regarding the Class 3 section behaviour were not right in this case. The analysed beam had a non-uniform cross-section along its height and despite the fact that the weakest cross-section was taken under consideration, the real failure started in a different place—at the stress concentration region caused by the rapid cross-section change. This is an important observation which suggests that the Eurocode 3 regulations regarding thin-walled sections made of high-strength steel might not be always appropriate in case of partially reinforced members with changing cross-section.

All of the numerical equilibrium paths are nearly linear up to the limit load, while the experimental ones are slightly disturbed around the 220 kN mark due to the local buckling initiating around the strain gauge 7 area. This small bulge caused the overall stiffness of the whole beam to decrease, which can be deduced from the reduced slope angle of all curves over the 220 kN mark. This phenomenon is absent in the numerical analysis.

What happens with the strain gauge 7 location is essential for understanding the failure mechanism. From the very beginning the stresses and strains there are greater than in other parts of the structure, even though it is not a section of maximum bending moment. It is caused by the stress concentration in this region, which results in an early development of the out-of-plane bulge in this area. The same shape of deformation was achieved only in a load case with pressure imperfection and reduced 630 MPa yield stress (the last one in Fig. 18). Even though the GMNA limit load is not the lowest in this case (322 kN in contrast to 310 kN with no imperfections), the actual behaviour of a real structure was captured. It was not achieved in any 700 MPa yield stress variants with imperfections (not shown in the figures)—in each of these cases the lower bulge developed way too low. It implies that lowering the plastic yield stress by a safety factor might be more appropriate than lowering the overall limit load, since it may partially compensate for not involving residual stresses in the computations.

CONCLUSIONS

- Existing methods of analytical/empirical calculation or computer-aided simulation of cold-formed members with regard to local stability are complicated and demand specialised or unavailable knowledge from the designer (e.g. measured or assumed imperfections, implementation of residual stresses and modifications to mechanical properties of steel at heavily deformed areas);
- Basing on our professional experience and familiarity with the industrial environment, we can state that the

aforementioned methods are not very popular among designers due to their excessive difficulty, low cost-effectiveness or lack of an uniform, universal procedure; as a result, they are often omitted or simplified in the process of design;

- It is necessary to develop a relatively simple method capable of providing safety and reliability of design even at cost of over-estimation and excessive safety factor;
- Numerical approach consisting of LBA and GNMA analyses with perfect geometry and no initial stresses managed to estimate the real ultimate load capacity, however the achieved results were too optimistic and should be treated with a reasonable safety factor; the factor is best applied to the yield stress value in GMNA analysis and even a 15% reduction might give reasonable results;
- By no means should thin-walled structures be computed using a single solid element per wall thickness; regretfully it is not uncommon among designers to do so, because solid geometrical models of a given structure are often readily available in the design office; these models should be transformed to shell models because of the well-known issues with volumetric locking and excessive bending stiffness;
- We suggest that the γ_{m0} safety factor applicable to the class 3 and 4 cross-sections in Eurocode 3 should not be considered 1.0 in case of high-strength steel, since at the present form it puts the designed structures on the verge of safety; this statement is in line with that of other researchers [17]; we suggest that the plastic yield stress value should be reduced by a factor of at least 0.85;
- Elastic-perfect plastic material model produced safer (lower) ultimate load values than the real experimental strain-stress relation despite the possibly dangerous over-estimation of Young's modulus near the yield stress value;
- The study was limited by not including residual stresses and geometrical imperfections in the numerical computations; it was however the aim of the study to evaluate methods lacking in these features to reflect simple design conditions.

ACKNOWLEDGEMENTS

The experimental research was carried out with support from and in cooperation with the RCV manufacturing company ZOELLER TECH Sp. z o.o. The FEM calculations presented in the paper were carried out at the TASK Academic Computer Center in Gdansk, Poland.

REFERENCES

1. Abambres M, Quach W-M. Residual stresses in steel members: a review of available analytical expressions. *International Journal of Structural Integrity*. Emerald; 2016 Feb;7(1):70–94.
2. Bielski P, Wysocki O, Czyżewicz J. Failure of cold-formed beam: How does residual stress affect stability? *Shell Structures: Theory and Applications*. 2017;4:529-32. CRC Press / Balkema.
3. Cold-Formed Steel Design Manual, American Iron and Steel Institute, 2013
4. Crisfield MA. A fast incremental/iterative solution procedure that handles “snap-through.” *Computational Methods in Nonlinear Structural and Solid Mechanics*. Elsevier; 1981;55–62.
5. Eurocode 3: Design of Steel Structures, Parts 1-1, 1-3 and 1-5, European Committee for Standardization, 2004.
6. Ingvarsson L. Cold-forming residual stresses effect on buckling. University of Missouri-Rolla. 1975.
7. Laím L, Rodrigues JPC, Silva LS da. Experimental and numerical analysis on the structural behaviour of cold-formed steel beams. *Thin-Walled Structures*. Elsevier BV; 2013 Nov;72:1–13.
8. Lu Y, Li W, Zhou T, Wu H. Novel local buckling formulae for cold-formed C-section columns considering end condition effect. *Thin-Walled Structures*. Elsevier BV; 2017 Jul;116:265–76.
9. Niklas K. Strength analysis of a large-size supporting structure for an offshore wind turbine. *Polish Maritime Research*. 2017 Apr 25;24(s1):156-65.
10. Olovsson L, Simonsson K, Unosson M. Shear locking reduction in eight-noded tri-linear solid finite elements. *Computers & structures*. 2006 Feb 1;84(7):476-84.
11. Quach WM. Residual stresses in cold-formed steel sections and their effect on column behaviour (Doctoral dissertation, The Hong Kong Polytechnic University). 2005.
12. Quach WM, Qiu P. Strength and ductility of corner materials in cold-formed stainless steel sections. *Thin-Walled Structures*. Elsevier BV; 2014 Oct;83:28–42.
13. Schafer B., Peköz T. Computational modeling of cold-formed steel: characterizing geometric imperfections and residual stresses. *Journal of Constructional Steel Research*. Elsevier BV; 1998 Sep;47(3):193–210.
14. Schafer BW, Pekoz T. Direct strength prediction of cold-formed steel members using numerical elastic buckling solutions. 14th International Specialty Conference on Cold-Formed Steel Structures. 1998;69-76.
15. Szymczak C, Kujawa M. On local buckling of cold-formed channel members. *Thin-Walled Structures*. Elsevier BV; 2016 Sep;106:93–101.

16. Winful D, Cashell KA, Afshan S, Barnes AM, Pargeter RJ. Elevated temperature material behaviour of high-strength steel. Proceedings of the Institution of Civil Engineers - Structures and Buildings. Thomas Telford Ltd.; 2017 Nov;170(11):777–87.
17. Wang J, Afshan S, Schillo N, Theofanous M, Feldmann M, Gardner L. Material properties and compressive local buckling response of high strength steel square and rectangular hollow sections. Engineering Structures. Elsevier BV; 2017 Jan;130:297–315.
18. Weng CC, Pekoz T. Residual Stresses in Cold-Formed Steel Members. Journal of Structural Engineering. American Society of Civil Engineers (ASCE); 1990 Jun;116(6):1611–25.
19. Woloszyk K, Kahsin M, Garbatov Y. Numerical assessment of ultimate strength of severe corroded stiffened plates. Engineering Structures. Elsevier BV; 2018 Aug;168:346–54.
20. Wong YW. Analysis of wrinkle patterns in prestressed membrane structures. PhD Thesis, University of Cambridge, Department of Engineering, August. 2000 Aug.
21. Yu C, Schafer BW. Local Buckling Tests on Cold-Formed Steel Beams. Journal of Structural Engineering. American Society of Civil Engineers (ASCE); 2003 Dec;129(12):1596–606.
22. Yu C, Schafer BW. Simulation of cold-formed steel beams in local and distortional buckling with applications to the direct strength method. Journal of Constructional Steel Research. Elsevier BV; 2007 May;63(5):581–90.

CONTACT WITH THE AUTHORS

Paweł Bielski

e-mail: pawbiels@pg.edu.pl
 Gdansk University of Technology
 Narutowicza 11/12
 80-233 Gdansk
POLAND

Leszek Samson

e-mail: lessamso@pg.edu.pl
 Gdansk University of Technology
 Narutowicza 11/12
 80-233 Gdansk
POLAND

Oskar Wysocki

e-mail: oskwys@gmail.com
 Gdansk University of Technology
 Narutowicza 11/12
 80-233 Gdansk
POLAND

Jacek Czyżewicz

e-mail: jacczyze@pg.edu.pl
 Gdansk University of Technology
 Narutowicza 11/12
 80-233 Gdansk
POLAND

DYNAMIC ANALYSIS OF EMBEDDED CHAINS IN MOORING LINE FOR FISH CAGE SYSTEM

Hui-Min Hou
Guo-Hai Dong
Tiao-Jian Xu
Yun-Peng Zhao
Chun-Wei Bi

State Key Laboratory of Coastal and Offshore Engineering, Dalian University of Technology, China

ABSTRACT

Investigation of the embedded chains in soil starts to play an important role in understanding the structural performance of mooring system, when the embedded anchors will be employed to sustain large loads with the gradually growth of installation depth of offshore aquaculture farm. The aim of this study is to investigate the dynamic response of mooring line considering the influence of embedded chains in clay soil for net cage system. Lumped-mass method is used to establish the numerical model for evaluating the performance of mooring line with embedded chains. To validate the numerical model, comparisons of numerical results with the analytical formulas and the experimental data are conducted. A good agreement of the profile and the tension response is obtained. Then, the effect of embedded chains on the static and dynamic response of mooring line is evaluated, and the dynamic behavior of mooring system considering embedded chains for net cage system is investigated. The results indicate that the soil resistance on embedded chains should be included to predict the mooring line development and the load on the embedded anchors in the numerical simulations. An appropriate safety factor should be included if employing the simplified model Case C at the initial design phase. And the effect of embedded chains on the holding capacity of embedded anchors in single-point mooring system for single net cage cannot be negligible during the design and operation phases. Consequently, it is profound to take into account the interaction of embedded chains and soil for accurately predicting the reliability of mooring system for fish cage.

Keywords: embedded chains, soil resistance, parameter sensitivity, dynamic analysis

INTRODUCTION

According to Kapetsky et al. 2013, the potential of the offshore aquaculture is large due to the inshore space competition, wave quality problems, food security concern and environmental and aesthetic impacts. For the fish farm installed in the open sea, the mooring system should be re-designed since the load is more severe than that for the inshore fish farm. Similar to the offshore drilling platform, suction anchors may be employed in mooring system of offshore fish farm due to the advantage of simple design, high resistance against vertical loading, simple and fast installation (Cheng et al. 2014). Generally, the attachment point of suction anchors is below the seabed level and the chains are employed to avoid the abrasion and wear when

the interaction between mooring line and the seabed occurs. Thus, it is essential to consider the interaction of embedded chains and soil to analyze the structural performance of mooring system for fish farm.

Numerous existing researches on the hydrodynamic behavior of mooring system for fish cage were conducted involving physical experiments and numerical models, assuming that the anchor point was fixed at the seabed. Huang et al. 2010 recorded mooring line tension of a single-point-mooring cage system by a full-scale physical model, where a concrete block was used as an anchor. Tang et al. 2011 investigated the dynamic properties of a dual pontoon floating cage structure by physical model, which is moored to the load cells by a symmetric coil spring connected by

rollers fixed to the seabed. Xu et al. 2013 measured the tension forces on the mooring line in submerged mooring grid system of a scaled fish cage model. Zhao et al. 2015 conducted a series of physical model experiments to measure the mooring line tension for multiple net cages in steady current. DeCew et al. 2010 employed a finite element analysis program to predict the tension response of a single-point mooring system under a variety of currents. Shainee et al. 2013 numerically investigated the submergence characteristics of a single-point-mooring fish cage system, considering the mooring line anchored to the seabed directly. Kim et al. 2014 modeled the hydrodynamic response of the moored containment structure using the finite element model. Huang et al. 2016 developed a finite element model to investigate the elastic deformations and mooring line tension of floating collar in waves.

Provided that the embedded anchors would be utilized to sustain larger loads than the dead weight anchors, the mooring system including the chains embedded in soil is becoming more popular when the environmental loading is extremely severe in the open sea. Some researches considering mooring chains embedded in soil have been conducted by laboratory tests and numerical simulations. Choi et al. 2014 conducted the lab-scale model tests to obtain the pullout capacity of embedded chains. O'Loughlin et al. 2015 observed the chain-soil interaction during physical model tests and estimated the capacity of the mooring chain both on and within the seabed. Rocha et al. 2016 performed the physical experiment to investigate the static load attenuation from the soil frictional forces for embedded chains, and then the relationship between mean ratio of the frictional to transversal force and the undrained soil shear strength was studied. Wang et al. 2010a proposed a two-dimensional static model and a three-dimensional quasi-static model to predict the mooring cable behavior considering the currents, soil resistance and cable elasticity during pretensioning and in service. Wang et al. 2010b adopted the three-dimensional numerical model for embedded chains to obtain the chain profiles and tension distributions under different pretension levels. Guo et al. 2016 employed a two-dimensional quasi-static model to predict the response of mooring lines comprising multiple types of mooring lines or chains. Xiong et al. 2016 investigated the influence of embedded chains on the response of mooring line considering the interaction of soil and chains.

However, the understanding of the dynamic response of mooring line considering the effect of embedded chains is still not comprehensive. And with the enormous potential application of the embedded anchors in the open ocean aquaculture industry, the interaction of embedded chains and soil for offshore aquaculture farm needs to make a quantitative estimation. In addition, the safety of the embedded anchors will be of vital importance for the entire system of aquaculture farm since the cost of mooring system with the embedded anchors is high and the installation and maintenance cost increases significantly with the growth of water depth. And in the design of net cage system in the open sea, it is a challenging problem to obtain the most optimized balance between the cost and the safety of embedded anchors

including the interaction of embedded chains and soil. Therefore, the importance in modeling embedded chains of mooring line and the parameter sensitivity should be investigated to better understand the structural response of mooring line with embedded chains. And the influence of embedded chains on the dynamic response of offshore fish farm should be evaluated to provide a basis for the design of embedded anchors. In this study, the performance of mooring line including embedded chains is predicted using the lumped-mass method. The effect of embedded chains on the structural response of mooring line is quantified by the proposed numerical model. And the sensitivity of the response of mooring line with embedded chains to the variation of parameters, including initial pretension level of mooring line, soil shear strength gradient and the multipliers in soil resistance, is conducted in static and dynamic analysis. Furthermore, the dynamic response of mooring system for net cage system is investigated considering the effect of embedded chains.

NUMERICAL SIMULATION

To provide a better understanding of the performance of embedded chains in mooring system and help improve the future prediction for the structural response of open sea fish farm, a numerical model for mooring line including embedded chains (as depicted in Fig. 1) is developed based on the lumped mass method in this study.

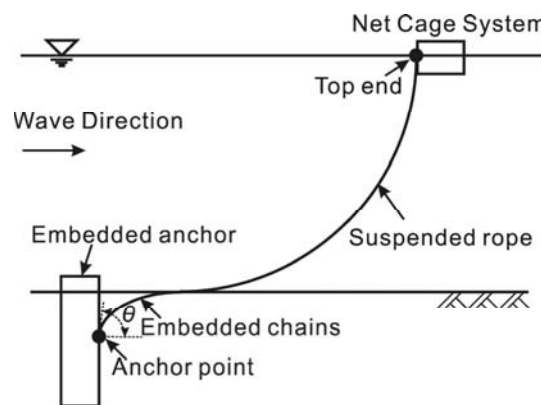


Fig. 1 Definition of the mooring line considering embedded chains

LUMPED MASS MODEL

The lumped mass method is used to model the structural behavior of mooring line with embedded chains. And only tension effect of mooring line is considered ignoring bend and torsion effects and the mooring line is assumed to be anchored to the fixed embedded anchors.

In the proposed numerical model, the entire mooring line is divided into numerous elements to calculate the dynamic behavior of mooring system, as depicted in Fig. 2. An element is composed of two end nodes and a mass-less spring. Mass of each element is concentrated at the end nodes and the mass

nodes are connected by the elastic spring without mass. The tension force at the two ends of each element becomes the concentrated load acting on the corresponding end nodes. And the external forces on each element are calculated first and then evenly distributed to the corresponding end nodes. More details about the lumped mass method can refer to many references, e.g. Huang et al. 2006, Surendran and Goutam 2009, Masciola et al. 2011 and Hall and Goupee 2015).

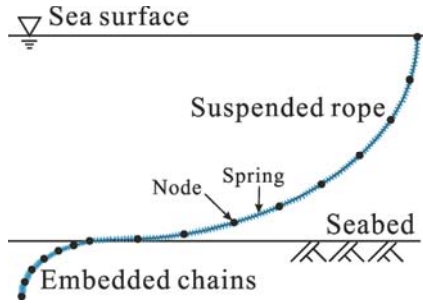


Fig. 2 Schematic of mass-spring model for mooring line

HYDRODYNAMIC LOADS ON MOORING LINE

A local coordinate system ($o'-\tau-\eta-\xi$) (see Fig. 3) is defined to describe the direction of the hydrodynamic forces acting on elements. Concerning the local coordinate system $o'-\tau-\eta-\xi$, the η -axis lies on the plane that includes the τ -axis and V , and the velocity vector of the water particle at the mid-point of the element can be divided into τ (tangential) and η (normal) components. The scattering effect of the net twine on the flow field can be neglected because the diameter of net twine is relatively small compared with the characteristic wave length.

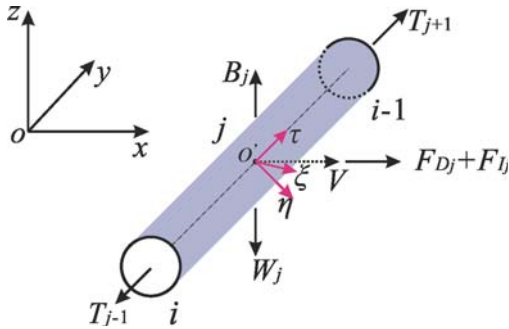


Fig. 3 Schematic of the local coordinate system for an element j of suspended rope

Thus, it is appropriate to calculate the wave loads on the net using the modified Morison equation considering the relative motion between net element and flow field,

$$\begin{cases} F_\tau = \frac{1}{2} C_{D\tau} \rho A_\tau |u_\tau - \dot{R}_\tau| \cdot (u_\tau - \dot{R}_\tau) + \rho V_0 a_\tau + C_{m\tau} \rho V_0 |a_\tau - \ddot{R}_\tau| \\ F_\eta = \frac{1}{2} C_{D\eta} \rho A_\eta |u_\eta - \dot{R}_\eta| \cdot (u_\eta - \dot{R}_\eta) + \rho V_0 a_\eta + C_{m\eta} \rho V_0 |a_\eta - \ddot{R}_\eta| \\ F_\xi = \frac{1}{2} C_{D\xi} \rho A_\xi |u_\xi - \dot{R}_\xi| \cdot (u_\xi - \dot{R}_\xi) + \rho V_0 a_\xi + C_{m\xi} \rho V_0 |a_\xi - \ddot{R}_\xi| \end{cases} \quad (1)$$

where F_η and F_ξ are the normal components of external forces on the net twine, and F_τ is the tangential component

of external forces on the net twine; $\bar{u} = (u_\tau, u_\eta, u_\xi)$ is the fluid particle velocity vector at the element center; $\bar{R} = (\dot{R}_\tau, \dot{R}_\eta, \dot{R}_\xi)$ is the central velocity vector of element; $\bar{\dot{u}} = (\dot{u}_\tau, \dot{u}_\eta, \dot{u}_\xi)$ is the fluid particle acceleration vector at the element center; $\bar{\ddot{R}} = (\ddot{R}_\tau, \ddot{R}_\eta, \ddot{R}_\xi)$ is the central acceleration vector of element; ρ is the density of water; V_0 is the water displaced volume of an element; A_τ, A_η and A_ξ are the effective projected areas of an element in the direction of the τ, η and ξ components, respectively; $C_{D\tau}, C_{D\eta}$ and $C_{D\xi}$ are the drag coefficients in the direction of the τ, η and ξ components, respectively; $C_{m\tau}, C_{m\eta}$ and $C_{m\xi}$ are the added mass coefficients in the direction of the τ, η and ξ components, respectively.

For the suspended-part of mooring line in water, the hydrodynamic coefficients are calculated using a method described by Choo and Casarella 1971:

$$C_\eta = \begin{cases} 8\pi / (\text{Re}_\eta \cdot s) \cdot (1 - 0.87s^{-2}) & (0 < \text{Re}_\eta \leq 1) \\ 1.45 + 8.55\text{Re}_\eta^{-0.90} & (1 < \text{Re}_\eta \leq 30) \\ 1.1 + 4\text{Re}_\eta^{-0.50} & (30 < \text{Re}_\eta \leq 10^5) \end{cases} \quad (2)$$

$$C_\tau = \pi \cdot \mu \cdot (0.55\text{Re}_\eta^{1/2} + 0.084\text{Re}_\eta^{2/3}) \quad (3)$$

where $\text{Re}_\eta = \rho V_{R\eta} D / \mu$; $s = -0.077215665 + \ln(8/\text{Re}_\eta)$; μ is the viscosity of water; C_η and C_τ are the normal and tangential drag coefficients for mesh bar; $V_{R\eta}$ is the normal component of the fluid velocity relative to the bar; ρ is the density of water and is assumed as 1000 kg/m^3 .

SOIL RESISTANCE ON EMBEDDED CHAINS

A segment for embedded chains in clay soil is presented in Fig. 4. The soil resistance consists of two components: the normal resistance Q and the tangential resistance F .

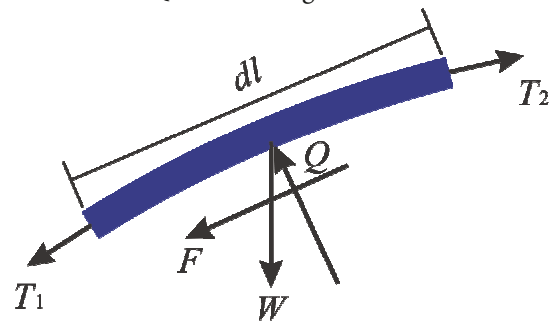


Fig. 4 Force sketch of embedded chains in soil

According to Skempton 1951 and Gault and Cox 1974, the soil resistance per unit length of embedded chains for clay soils can be expressed as,

$$\begin{aligned} Q &= E_n \cdot d \cdot N_c \cdot s_u \\ F &= E_\tau \cdot d \cdot s_u \end{aligned} \quad (4)$$

where E_n and E_τ are the multipliers for the effective width in the normal and tangential directions; d is the nominal

diameter of embedded chains; s_u is the undrained shear strength of soil (Yen and Tofani 1984); N_c is a bearing capacity factor and set as 7.6 for simplicity (Skempton 1951, Degenkamp and Dutta 1989). Degenkamp and Dutta 1989 recommended the values of E_n and E_c for the chains as 2.5 and 8.0, respectively. The undrained soil shear strength is proportional to the embedded depth,

$$s_u = s_{u0} - k \cdot z \quad (5)$$

where s_{u0} is the soil shear strength at the seabed level; k is the soil shear strength gradient; z is the depth measured from the seabed level downwards. In this study, $s_{u0} = 0.0$ kPa (Neubecker and Randolph 1995, Liu et al. 2014, Xiong et al. 2016, Racha et al. 2016) and $k = 1.45$ kPa/m (Andersen et al. 2005).

TENSION ON MOORING LINE

The mooring line usually consists of fiber rope and embedded chains. The embedded chain located at the lower part of mooring line is linked to the embedded anchors to avoid the decrease in the strength due to excessive friction with the sea floor. The material of fiber rope is polypropylene (PP) and the material of mooring chains is steel. The elasticity relationship of fiber rope is $T=3.52(\Delta S/S)^{1.132}$, where T is the tension on fiber rope with the unit of MN; ΔS is the elongation of fiber rope; S is the initial length of fiber rope (referring to Xu 2014). The tension on mooring chains can be calculated through $T=284.2(\Delta l/l)$, where T is the tension on chains with the unit of MN; Δl is the elongation of chains; l is the initial length of chains.

MOTION EQUATION

The forces on the element are distributed to the end nodes evenly after calculating the hydrodynamic loads, soil resistance and tension force on each element in the local coordinate system, and then the force on the nodes in the local coordinate system are transformed into the global coordinate system. According to the Newton's second law, the motion equation for the lumped mass point is given as

$$M\vec{R} = \vec{T} + \vec{W} + \vec{F}_{envir} \quad (6)$$

where M is the mass of the lumped mass point; \vec{R} is the acceleration vector of the mass center of the lumped mass point; \vec{T} is the elastic tension vector between the lumped mass points; \vec{W} is the gravity force on the lumped mass point; \vec{F}_{envir} is the environmental force acting on the lumped mass point. The environmental force on suspended fiber rope is composed of the drag force, inertia force and buoyant force in water, while the environmental force on embedded chains consists of the soil resistance and the buoyancy force in soil (Degenkamp and Dutta 1989). Runge-Kutta-Verner fifth-order and sixth-order method is adopted to solve the equations. More details

about the motion equation of lumped mass points can refer to Xu et al. 2013.

VALIDATION OF THE NUMERICAL MODEL

In order to validate the proposed numerical model, the analytical solutions and the experimental results for investigating the structural response of mooring line from previous researches are compared with the numerical results in static analysis and dynamic analysis, respectively.

STATIC ANALYSIS

The validations are performed for the static response of embedded chains and suspended rope. Referring to Neubecker and Randolph 1995, the analytical form for the profile of embedded chains is written as Eq. (A.3) shown in Appendix A. Fig. 5 presents the profiles of embedded chains for different chain angles θ_0 at the seabed obtained from the numerical model and the analytical formulation, where the non-dimensional tension at the anchor point is $T^*=4$ and $T^*=20$. A good agreement is obtained, and thus the proposed model is reasonable to calculate the profile and static tension response of embedded chains.

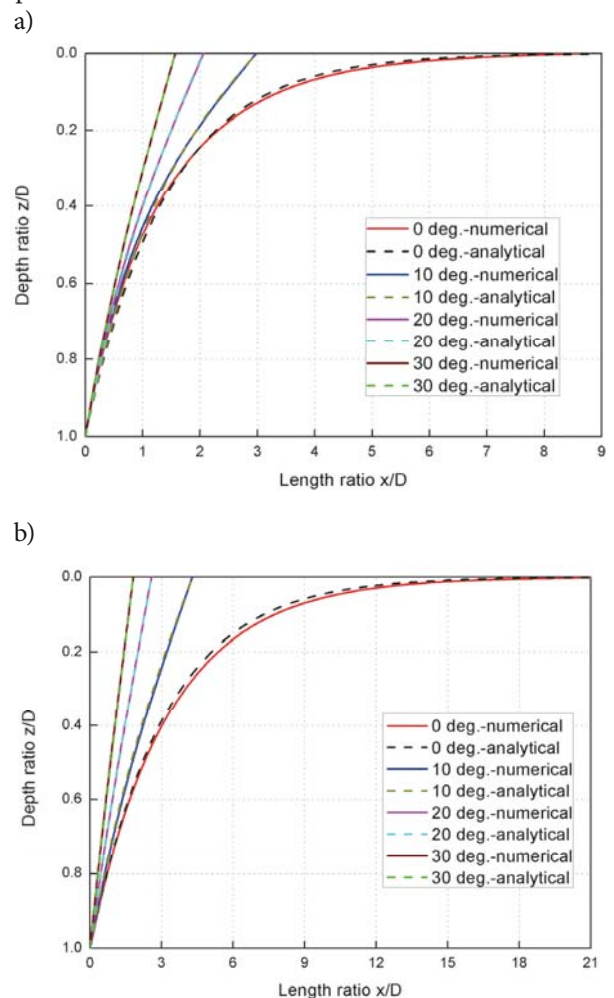
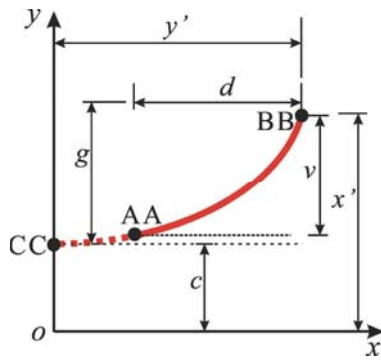


Fig. 5 Profiles of embedded chains for different chain angles at seabed: (a) $T^*=4$; (b) $T^*=20$

In addition, the static response of suspended rope is validated by catenary equation when the elongation is insignificant. The sketch of and the force acting on catenary curve is shown in Fig. 6. According to Cella 1999, the analytical form for the static response of catenary curve is listed in Appendix B. The configuration of fiber rope suspended in water can be calculated by Eq. (B.4) and the tension at the top end is obtained by Eq. (B.6). Here, the length of fiber rope is 80.0 m and the wet weight per unit length is 9.1 N/m.

a)



b)

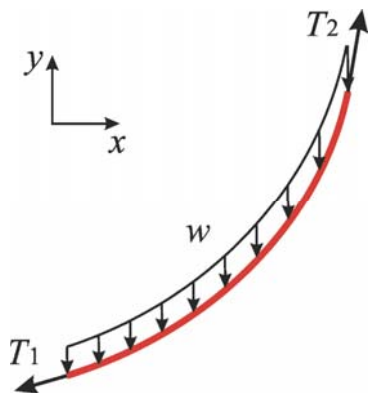


Fig. 6 Catenary curve: (a) the sketch; (b) the forces

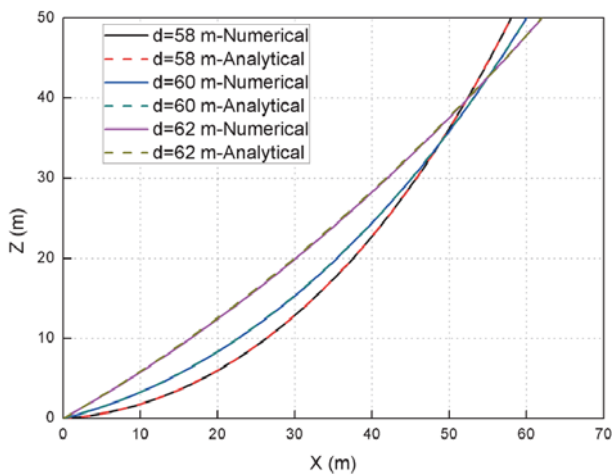


Fig. 7 Comparison of fiber rope profiles between the numerical simulations and analytical results

Fig. 7 shows the profiles of fiber rope with the variation of the horizontal distance d , which are calculated from the numerical simulations and analytical method. The results show a good agreement of the profile of fiber rope is achieved for different horizontal distances. In addition, the tension at the top end of fiber rope is listed in Table 1. It reveals that the static tension on suspended rope could be estimated accurately through the numerical simulations. Therefore, our proposed numerical model is available and appropriate to predict the configuration and static tension response of suspended rope.

Tab. 1 Top end tension on fiber rope for different horizontal distances

Horizontal distance (m)	Method	Tension (N)			Error (%)
		Horizontal	Vertical	Total	
58.0	Numerical	386.7	748.1	842.2	0.89
	Analytical	393.6	753.0	849.2	
60.0	Numerical	552.9	854.6	1017.8	0.86
	Analytical	555.2	863.6	1026.7	
62.0	Numerical	1296.3	1430.9	1930.7	3.47
	Analytical	1354.1	1472.0	2000.1	

DYNAMIC ANALYSIS

The dynamic behavior of suspended mooring line is validated by the experimental results by Chen et al. 2001 through the forced oscillation tests in this context. The mooring line is anchored at the bottom and a prescribed unidirectional harmonic motion is excited on the top end. The brief description of the process is given below.

The mooring line is composed of mooring chains with a spring inserted in the middle position. The water depth of 223.5 m was applied in tests and the main physical properties of mooring line are given in Table 2. And the in-plane regular oscillations at the top end with the amplitudes and periods listed in Table 3 were conducted in the numerical model. The amplitude ratio is defined as the ratio of the average of peak-to-peak line tension to the average of peak-to-peak top-end motion. Comparisons of the amplitude ratios with the variation of the frequency between the numerical simulations and experimental results in Chen et al. 2001 are shown in Fig. 8. It demonstrates that the numerical results are in a good agreement with the experimental results in the entire frequency range included in Table 3. This indicates that the

present numerical model is quite reasonable to predict the dynamic tension response of mooring line.

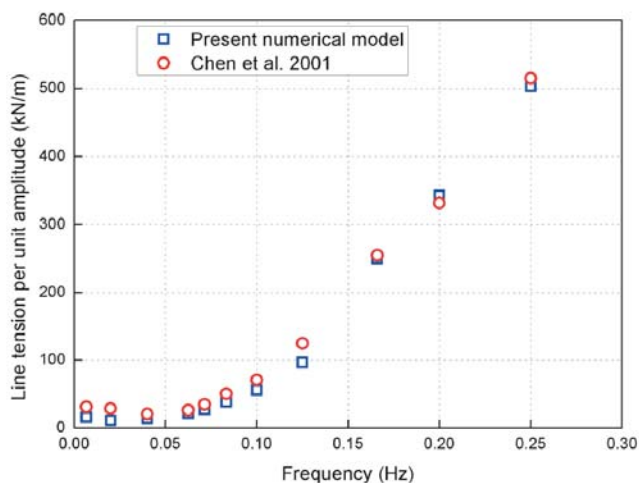


Fig. 8 Line tension per unit amplitude with the variation of the frequency in oscillation tests

Tab. 2 Properties of mooring line in physical tests (Chen et al. 2001)

Component	Item	Value
Chain	Nominal diameter (m)	0.2
	Chain length (m)	635
	Mass per unit length (kg/m)	834.1
	Elastic stiffness (kN)	2.98×10^7
	Hydrodynamic coefficient C_{Dt}	0.6
	Hydrodynamic coefficient C_{Dn}	3.2
	Hydrodynamic coefficient C_{Mt}	0.6
Inserted spring	Hydrodynamic coefficient C_{Mn}	2.8
	Position of the spring	In the middle
	Unstretched length (m)	48.8
	Elasticity (kN/m)	56.5
	Mass per unit length (kg/m)	1185.6
	Pretension (kN)	4453.7

Tab. 3 Harmonic oscillation parameters in physical tests (Chen et al. 2001)

No. of test	Amplitude (m)	Period (s)
1	0.9144	4.0
2	0.9144	5.0
3	0.9144	6.0
4	4.572	8.0
5	6.096	10.0
6	9.144	12.0
7	9.144	14.0
8	9.144	16.0
9	9.144	25.0
10	36.576	50.0
11	36.576	150.0

RESULTS AND DISCUSSION

Numerical simulations are conducted to investigate the structural response of mooring line with embedded chains: first, the effect of embedded chains on the response of mooring line is investigated by the proposed numerical model; second, the parameter sensitivity for mooring line with embedded chains is calculated in static and dynamic analysis; finally, the dynamic response of net cage system including the soil resistance is adopted to evaluate how much influence of embedded chains.

The mooring line is installed in 50 m water depth. In the numerical model, the mooring line is discretized into 50 elements and half of them are allocated to chains. And most of chains are assumed to be buried in soil. The wet unit weight of soil is 18.80 kN/m^3 to obtain the effective chain weight in soil (Degenkamp and Dutta 1989). The parameters of mooring line in the numerical simulations are tabulated in Table 4. The top end of mooring line is located at a depth of 5 m below the water surface level to be consistent with the parameters of anchor line for net cage system.

Tab. 4 Parameters of mooring line in the numerical simulations

Component	Parameter	Value
Suspended rope	Diameter (m)	0.091
	Density (kg/m^3)	953
	Material	PP
	Rope length (m)	57.6
	Elastic coefficient (MN)	3.52
	Initial pretension (kN)	138.1
Embedded chains	Diameter (m)	0.030
	Density (kg/m^3)	7850
	Material	Steel
	Chain length (m)	6.4
	Elastic coefficient (MN)	284.2
	Initial pretension (kN)	0.0

THE INFLUENCE OF EMBEDDED CHAINS ON THE RESPONSE OF MOORING LINE

Five cases are investigated to quantify the influence of embedded chains on the response of hybrid mooring line in static and dynamic analysis in this section. Fig. 9 shows the schematic diagram of Case 0, Case A, Case B, Case C and Case D. The reference case considering the effect of embedded chains is denoted as Case 0 and the anchor point is located at the point C in Fig. 9. And Case A, Case B, Case C and Case D represent different simplified positions (points A, B, C and D in Fig. 9 correspondingly) for the anchor point around the seabed level ignoring the impact of the soil resistance, where the lengths of mooring line are always 64.0 m. The effect of

embedded chains on static and dynamic response of mooring line is discussed as follows.

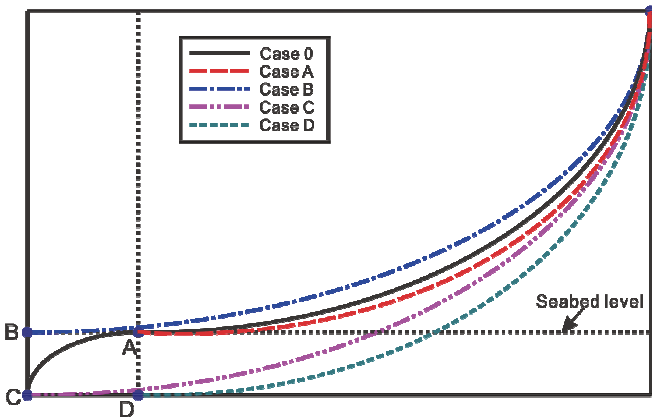


Fig. 9 Schematic diagram of Case 0, Case A, Case B, Case C and Case D

Static analysis

Tab. 5 Parameters of simplified fish cage system

Component	Parameter	Value
Outer circle	General diameter (m)	42.3
	Pipe diameter (m)	0.625
	Thickness (m)	0.0325
	Density (kg/m)	71.0
Inner circle	Material	HDPE
	General diameter (m)	39.8
	Pipe inner diameter (m)	0.625
	Thickness (m)	0.0325
Bottom ring	Density (kg/m)	71.0
	Material	HDPE
	Diameter (m)	39.8
	Pipe diameter (m)	0.15
Sinkers	Density (kg/m)	25.3125
	Material	HDPE
	Diameter (m)	0.075
	Mass of each sinker (kg)	228.125
Rigid frame	Number	10
	Diameter (m)	0.625
	Thickness (m)	0.042
	Width (m)	29.0
	Height (m)	25.0
Mooring line	Density (kg/m)	71.0
	Anchor line length (m)	64.0
	Bridle line length (m)	20.5
	Buoy line length (m)	5.0

Figs. 10 and 11 show the profiles and static tension response of mooring line calculated from the numerical model in Case 0, Case A, Case B, Case C and Case D.

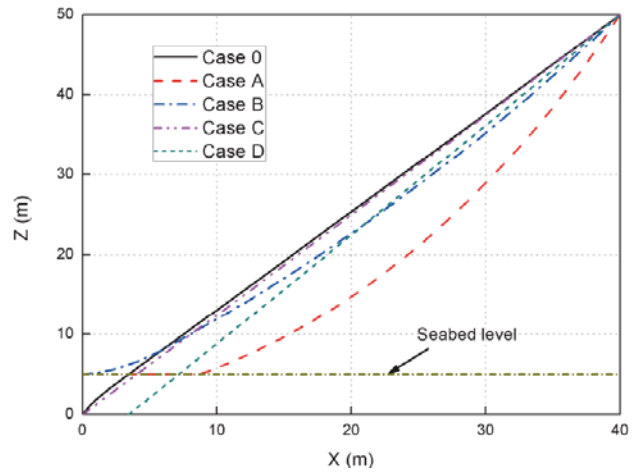


Fig. 10 Profiles of hybrid mooring line in five cases

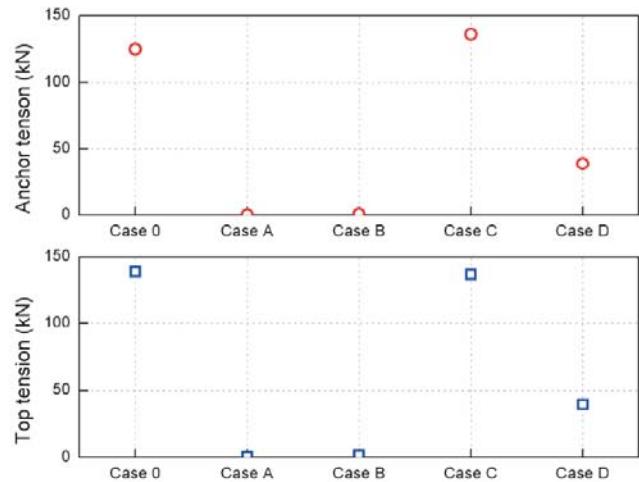


Fig. 11 Static tension force at the anchor point and the top end of mooring line

Obviously, the mooring line remains slack in Case A and Case B, and this leads to a small magnitude of tension force at both the anchor point and the top end. And the tension force at the anchor point and the top end of mooring line in Case D is significantly less than that in Case 0. Provided that the load acting on embedded anchors and offshore structures is equivalent to the tension force at the anchor point and the top end of mooring line, it is not reasonable by simplifying the mooring line as Case A, Case B and Case D to obtain the corresponding response of embedded anchors and offshore structures. Although the profile and the static tension in Case C are the nearest to those in Case 0, the difference of the tension at the anchor point between Case 0 and Case C could be up to 9.14%. This indicates that the load on embedded anchors predicted in Case C will be overestimated if neglecting embedded chains. It is noted that Case A, Case B, Case C and Case D fail to provide an acceptable result of the static response of mooring line regardless of the soil resistance.

Thus, the simulation of embedded chains in soil is beneficial to estimate the load on embedded anchors more accurately in design for practical engineering. If the static tension on the anchor point is estimated by Case C at the initial design phase, the safety factor of 1.09 should be included.

Dynamic analysis

The time history of dynamic tension response for hybrid mooring line is shown in Fig. 12, when the amplitude and period in harmonic oscillation are 4.0 m and 4.5 s.

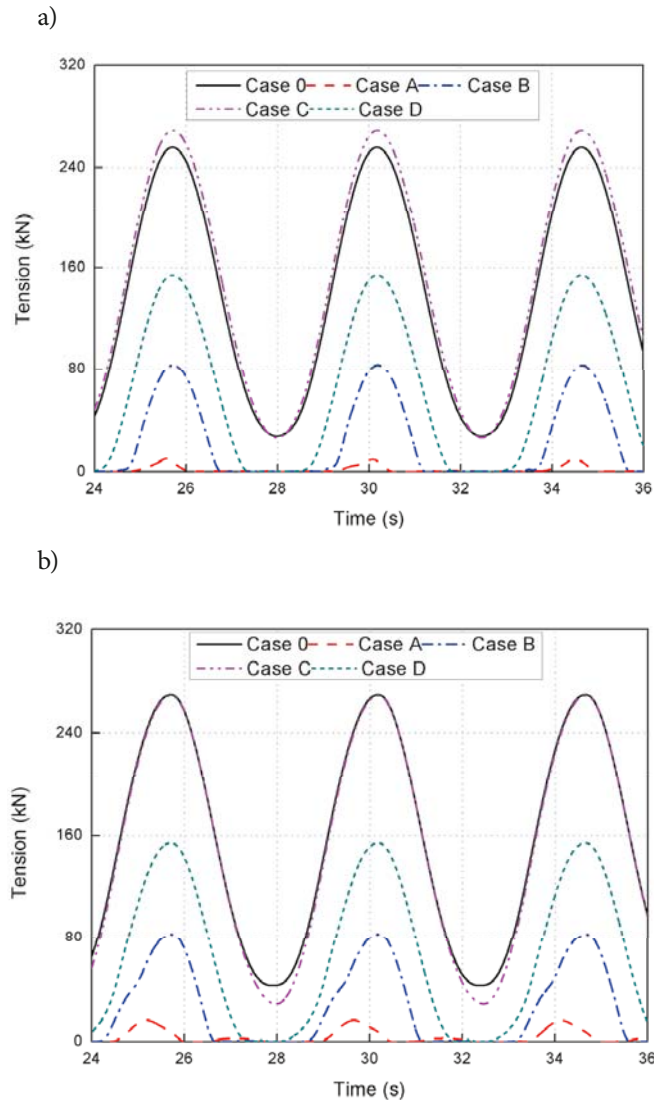


Fig. 12 Tension histories of mooring line at: (a) anchor point; (b) top end

The results reveal that the maximum tension at the top end of mooring line in Case 0 and Case C has little difference, whereas the maximum tension at the anchor point in Case C is overestimated. For Case A, Case B and Case D, it may be too dangerous to obtain the load acting on embedded anchors ignoring the effect of embedded chains. And the crest and trough of the tension history of mooring line in Case A, Case B and Case D is extremely asymmetrical. This indicates the slack of mooring line in Case A, Case B and

Case D could induce the nonlinearity of tension response of mooring line. It can be concluded that Case A, Case B, Case C and Case D may result in an un-reasonable evaluation for the dynamic response of mooring line and embedded anchors. Therefore, the soil resistance on embedded chains is critical to the dynamic tension on mooring line and should be comprehensively investigated for the design of embedded anchors. At the initial design phase, the safety factor of 1.05 should be included to evaluate the maximum tension on the anchor point by Case C.

PARAMETER STUDY

In this section, the configuration and the tension response of mooring line with embedded chains are investigated to evaluate the effect of the variation of parameters, including initial pretension level of mooring line, soil shear strength gradient and the multipliers in soil resistance. The amplitude and period of harmonic oscillation in dynamic analysis are 4.0 m and 4.5 s.

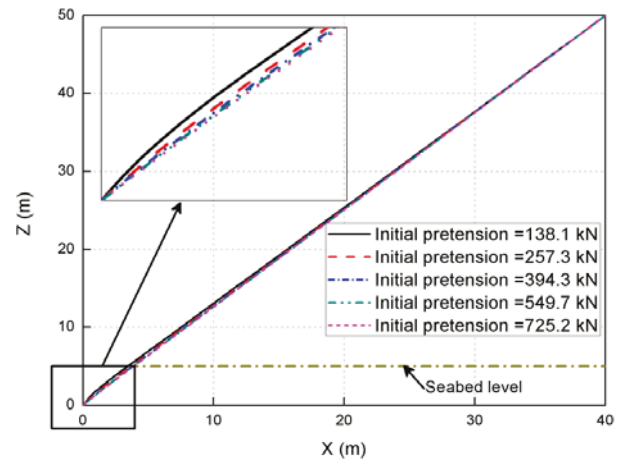


Fig. 13 Profiles of mooring line for different initial pretension levels

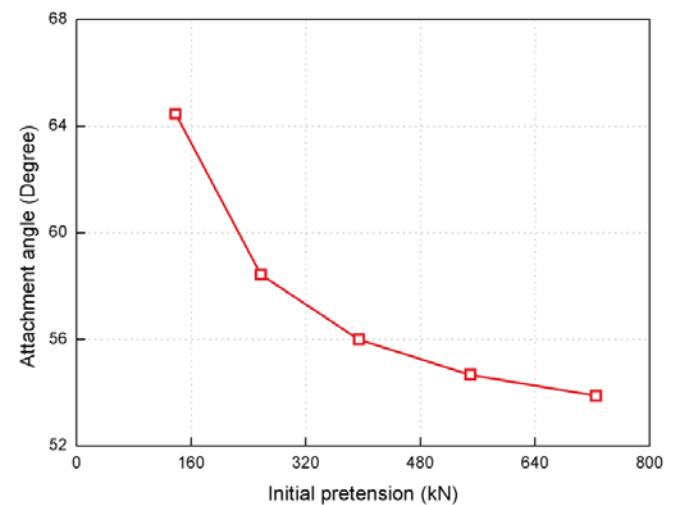


Fig. 14 Attachment angle of embedded chains with the variation of the initial pretension

Initial pretension level

The initial pretension level may affect the structural behavior of mooring line with embedded chains in static and dynamic analysis. The initial pretension investigated in this section involves the values of 138.1 kN, 257.3 kN, 394.3 kN, 549.7 kN and 725.2 kN for suspended rope. And the attachment angle θ (shown in Fig. 1) is defined as the angle of inclination of embedded chains at the anchor point, which is of vital importance to determine the mode failure and the embedded performance of embedded anchors. Fig. 13 shows the static configurations of mooring line and Fig. 14 presents the corresponding attachment angles of embedded chains with the variation of the initial pretension level. It can be inferred that the larger initial pretension of mooring line makes embedded chains tauter. As described in Fig. 14, the increase of initial pretension of mooring line results in the sharp decrease of the attachment angle of embedded chains substantially. This demonstrates that the initial pretension of mooring line may have a non-negligible influence on the attachment angle of embedded chains and may lead to a significant variation of the vertical tension on embedded anchors.

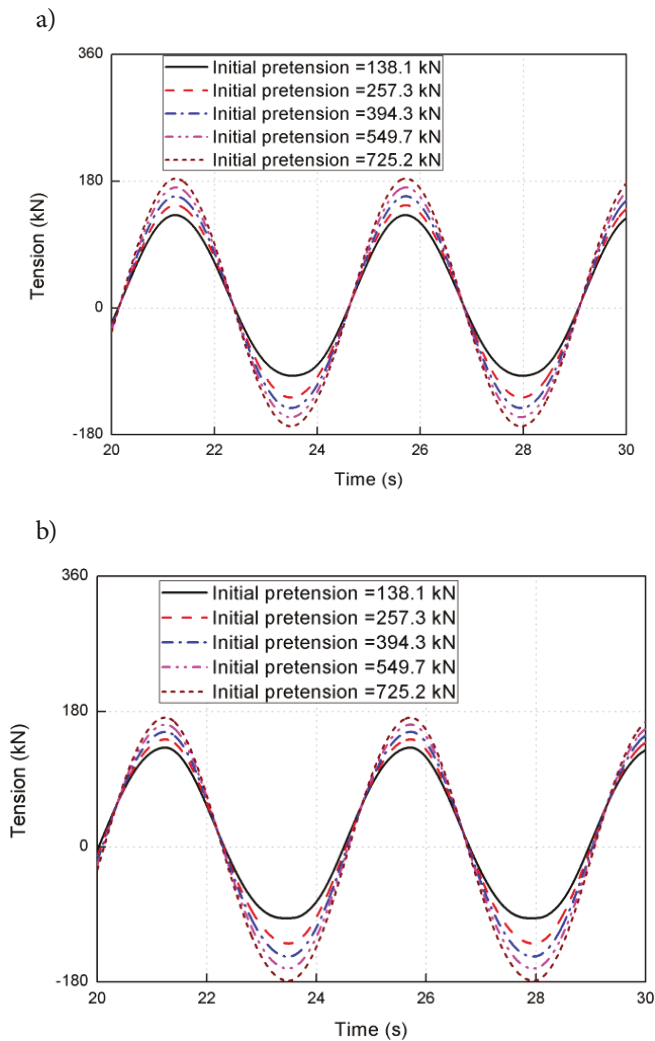


Fig. 15 Time history of mooring line tension at: (a) anchor point; (b) top end

Fig. 15 presents the time history of tension force on mooring line for different initial pretension levels, where the static tension at the anchor point and top end is subtracted correspondingly. The crest and trough of the tension history of mooring line becomes gradually symmetrical with the increase of the initial pretension. This indicates that the nonlinear effect of tension history of mooring line becomes weaker with a larger initial pretension due to the tauter embedded chains (shown in Fig. 13). And the tauter embedded chains the larger tension at the anchor point of mooring line. In addition, when the initial pretension of mooring line increases, the maximum tension force at the anchor point of mooring line has almost a linearly upward trend as seen from Fig. 15. Therefore, the initial pretension of mooring line is beneficial to make embedded chains tauter, and thus the mean offset of fish cage system could be limited in an acceptable range to meet the design requirement of mooring system. However, the load capacity of embedded anchors would increase and enhance the cost of embedded anchors. Thus it is crucial to select an appropriate value of initial pretension of mooring line to achieve a balance between the safety of net cage and the economic cost of embedded anchors in context of the safety of the offshore net cage system.

Soil shear strength gradient

Since the soil resistance in Eq. (4) is proportional to the soil shear strength in Eq. (5), it is of great importance to investigate the sensitivity of the structural response of mooring line in static and dynamic analysis with respect to the soil shear strength gradient. In this section, soil shear strength at the seabed level $s_{u0} = 0.0$ kPa is always used, whereas the soil shear strength gradient k changes with different hypothetical cases.

The soil shear strength gradient varies from 0.725 kPa/m to 3.625 kPa/m with a constant increment of 0.725 kPa/m, and the corresponding static and dynamic results of mooring line are shown in Fig. 16. The results indicate the profile and maximum tension force at the anchor point of mooring line is significantly sensitive to the variation of the soil shear strength gradient. With the decrease of the soil shear strength gradient, the embedded chains become gradually tightened. And the attachment angles of embedded chains are 57.8°, 64.5°, 70.6°, 76.5° and 82.4° for soil shear strength gradient from 0.725 kPa/m to 3.625 kPa/m. It is demonstrated that the mooring line development has great sensitivity to the soil shear strength gradient. Fig. 16b illustrates that the maximum tension at the top end of mooring line is more significant than that at the anchor point, especially for a large soil shear strength gradient. This may be a consequence of being the embedded part of mooring line supported by soil, while the un-embedded part is kept taut under a large tension. When the soil shear strength gradient increases, the maximum tension force at the anchor point of mooring line has a significant downward trend, while the maximum tension force at the top end has a slight upward trend. Different from a larger tension on the tauter embedded chains as mentioned above, the increase of the soil resistance results in the decrease of the tension at the anchor point of embedded chains on the basis

of the principle of the equilibrium of internal and external forces. The relative difference of the maximum tension at the anchor point of mooring line for the soil shear strength gradient between 0.725 kPa/m and 3.625 kPa/m could be up to 10.44%. This indicates that the soil shear strength gradient is dominant for the load carrying capacity of embedded anchors in the design. Thus the soil shear strength gradient should be determined carefully through the geological survey before the design of the fish farm for predicting the tensile capacity of embedded anchors and the mooring performance accurately.

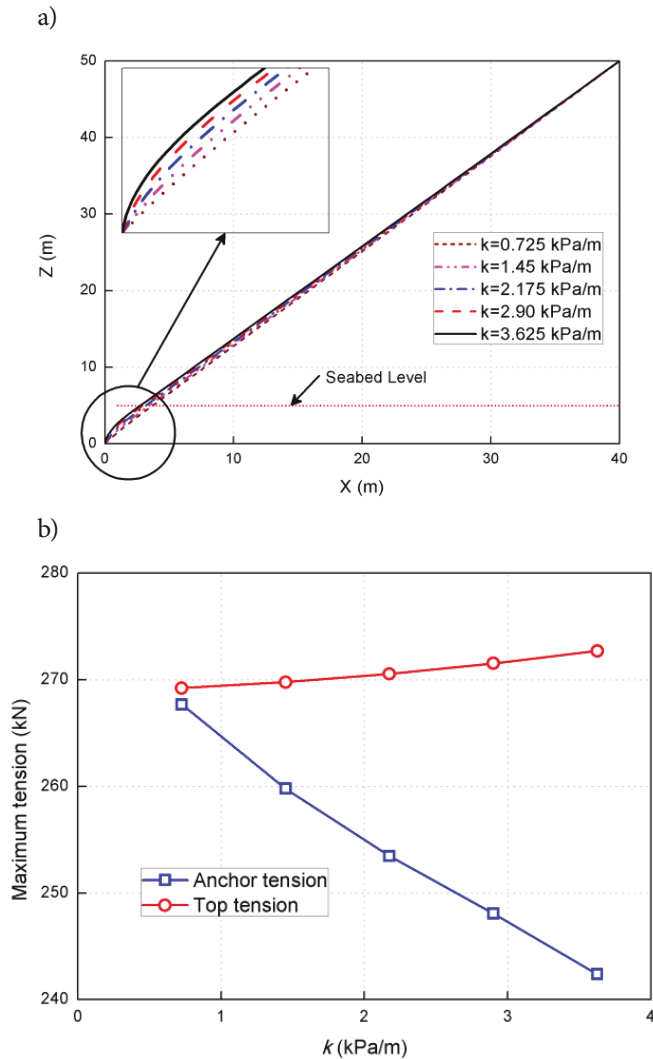


Fig. 16 Response results of mooring line: (a) profiles; (b) maximum tension force

Multipliers in soil resistance

Based on the principle of the equilibrium of internal and external forces, the variation of normal soil resistance for different multipliers may affect the mooring line development and the tension response of mooring line. The value of E_n is recommended as 1.0 and 2.5 for cables and chains, and the value of N_c rises from 5.1 at the seabed to 7.6 at a chain depth of 6d (d is the nominal diameter of embedded chains) (Degenkamp and Dutta 1989). In this section, the sensitivity of the static and dynamic response of mooring line to the

variation of the product of $E_n \cdot N_c$ is investigated to evaluate the effect of normal soil resistance.

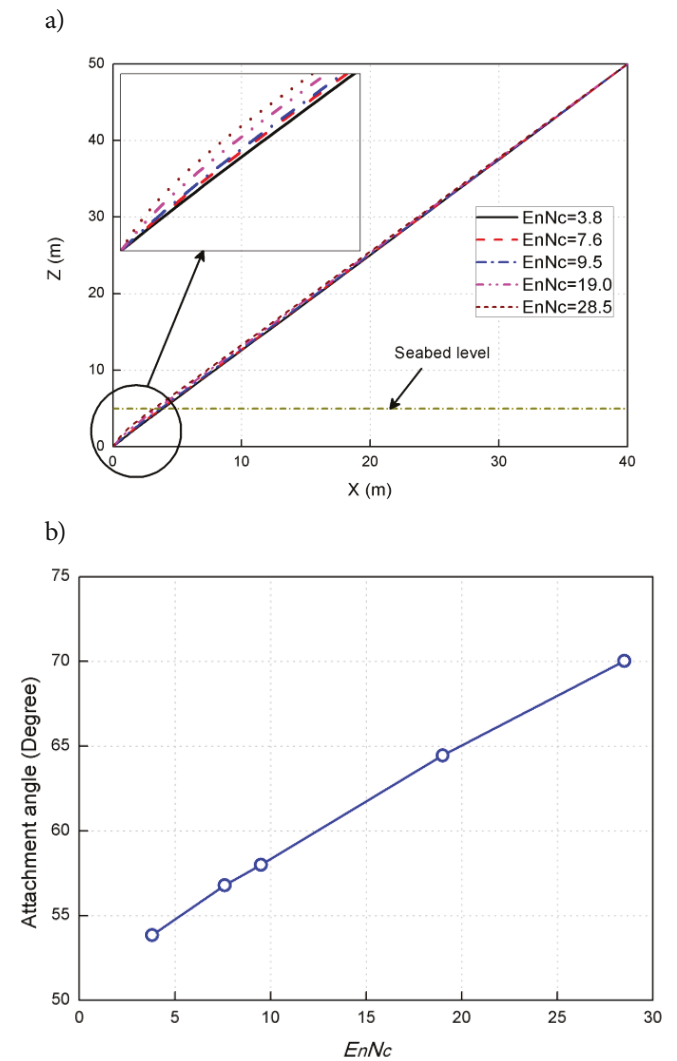


Fig. 17 Sensitivity to the value of $E_n \cdot N_c$: (a) mooring line profile; (b) attachment angle

Fig. 17 shows the configuration and the corresponding attachment angle of mooring line with the variation of the value of $E_n \cdot N_c$. The results demonstrate that the embedded chains supported by soil become slack apparently and the attachment angle of embedded chains increases approximately linearly with the increase of the value of $E_n \cdot N_c$. And Fig. 18 presents the tension response of mooring line for different values of $E_n \cdot N_c$. This indicates that there is no significant difference between the tension at both the anchor point and top end of mooring line for different normal soil resistance. However, the vertical component of the tension on embedded anchors may reach the allowable maximum, due to the large inclination angle at the anchor point of mooring line with increasing value of $E_n \cdot N_c$. This indicates that it is conservative to consider the effect of embedded chains with the large value of $E_n \cdot N_c$ to obtain the vertical component of the tension on embedded anchors. Thus, the impact of normal soil resistance is significant on the mooring line development and the

vertical component of the tension on embedded anchors and should be included during the design phase of mooring system.

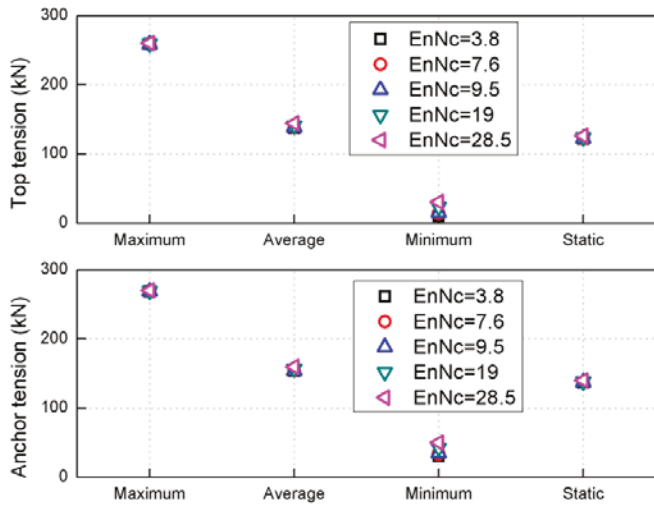


Fig. 18 Sensitivity of the tension on mooring line to the value of $E_n \cdot N_c$

DYNAMIC ANALYSIS OF NET CAGE SYSTEM WITH EMBEDDED CHAINS

In this section, a full dynamic analysis of mooring system for net cage in the open sea is conducted and the moored fish cage system was installed in 50 m water depth. Following previous works (Xu et al. 2014), this study adopted the self-developed numerical model based on the lumped-mass method and rigid body kinematics principle to obtain the dynamic response of net cage and mooring system. The net cage and mooring system is composed of a gravity cage and a single-point mooring system with a frontal rigid frame, as shown in Fig. 19. The fish cage consists of float collar, net pen, bottom ring and sinkers. The cage net is made of PE with a mass density of 953 kg/m^3 . There are 90 meshes in the circumferential direction and 12 meshes in the depth direction. The net is knotless, with a mesh size of 29.25 mm and a twine thickness of 1.80 mm. When mounted as diamond meshes, the net forms an open vertical cylinder with a diameter of 39.8 m and a height of 22.5 m. The anchor line is composed of embedded chains and fiber rope and the main properties have been listed in Table 4. The detailed parameters of fish cage and mooring system are given in Table 5.

In this section, Case 0 and Case C mentioned in Section 4.1 are adopted as the anchor line of net cage system (see Fig. 19b) and the cases are correspondingly denoted as Case S0 and Case SC to evaluate the effect of embedded chains. Here the wave-frequency excitation with the wave height of 4.0 m and period of 4.5 s is employed for a certain probability of occurrence at Bohai bay area in one year according to Global Wave Statistics Online (www.globalwavestatistics.com). Fig.20 provides the maximum tension force on mooring system in single-cage system in Case S0 and Case SC, including bridle

lines, anchor lines and buoy line. Anchor-1 and Anchor-2 are described as the pad-eye point and the top end of anchor line.

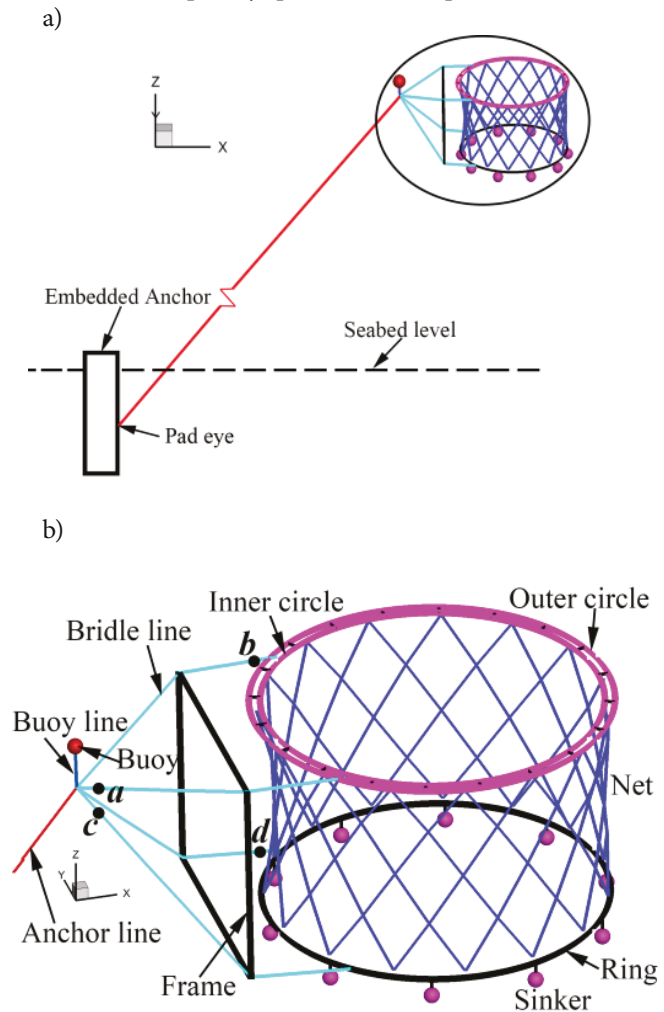


Fig. 19 Schematic of: (a) open sea fish farm system; (b) net cage system

As shown in Fig. 20, the soil resistance on embedded chains has a negligible effect on the maximum tension on bridle lines and buoy line. And for net cage, the maximum volume reduction factor in Case S0 and Case SC are 7.15% and 7.14%. The insignificant difference of the dynamic response of net cage between considering and neglecting the effect of embedded chains may be attributed to the insignificant variation of the tension response at the top end of anchor line (see Fig. 20). Due to the insignificant force transmission from the anchor line, the dynamic response of the upper structure is almost uninfluenced by embedded chains. However, the difference of maximum tension at the pad-eye point of anchor line between Case S0 and Case SC is 8.19%. And the tension response at the pad-eye point in Case S0 is significantly less than that in Case SC, consistent with the results in Section 4.1. The results indicate that the existence of soil resistance should not be neglected for estimating the load acting on embedded anchors precisely.

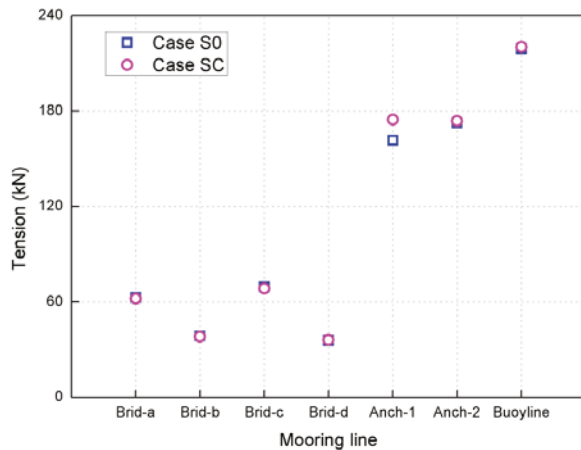
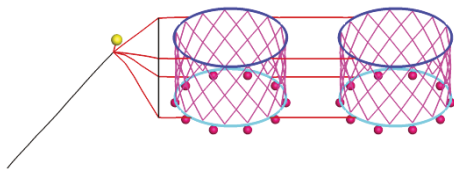


Fig. 20 Maximum tension on mooring system of Case S0 and Case SC

In addition, the dynamic response at the pad-eye point of anchor line for multi-cage system is investigated considering the anchor line with and without embedded chains as Case 0 and Case C. And the cases for the double-cage system and four-cage system (shown in Fig. 21) with anchor line in Case 0 and Case C are denoted as Case D0, Case DC and Case F0, Case FC, respectively.

a)



b)

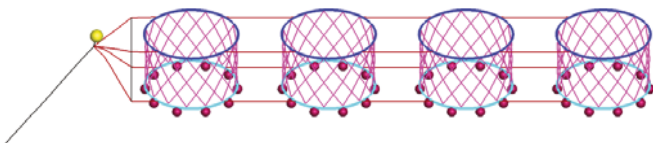


Fig. 21 Schematic of: (a) double-cage system; (b) four-cage system

Fig. 22 shows the tension histories at the pad-eye point of anchor line in Case S0, Case SC, Case D0, Case DC, Case F0 and Case FC. The maximum tension on anchor line for multi-cage system is more remarkable than that for single-cage system. The relative difference of the maximum tension on anchor line between Case D0 and Case DC is 5.62%, while the relative difference of the maximum tension between Case F0 and Case FC is 4.02%. The decrease of the relative difference of tension response may be attributed to the decreasing

proportion of the soil resistance to the external load with the growth of the scale of net cage system. And the interaction of soil and embedded anchors would be dominant for the safety of embedded anchors and the large-scale system in service.

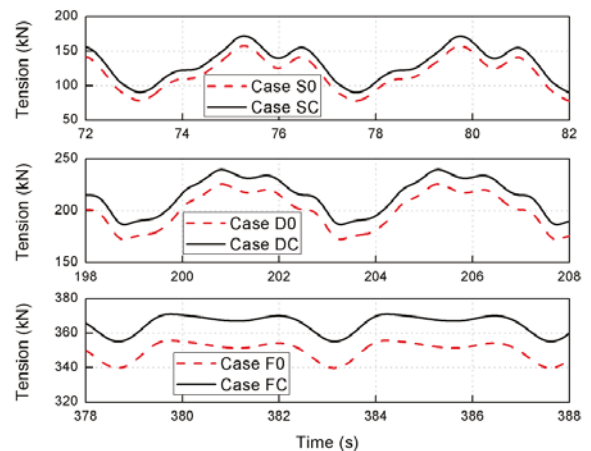


Fig. 22 Tension histories of anchor line at the anchor point

While the mooring line undergoes cyclic environmental loads in service, the embedded chains will have a cyclic motion due to the top end motion and cause the degradation of the soil shear strength around embedded anchors. And the embedded chains and seabed interaction will induce the soil trenching near embedded anchors as the soil experiences the cycles of loading and unloading. However, it can be seen from Fig. 22 that the load on embedded anchors would be more significant after the trenching phenomenon appears. Meanwhile, the surrounding soil of embedded anchors will be remolded and may decrease the holding capacity of embedded anchors. As a consequence, the embedded anchors would move and may be even pulled out, which is undesirable during the operation of offshore structures. Thus it is essential to include embedded chains into anchor line and propose a full coupled model to estimate the interaction among mooring system, embedded anchors, soil and offshore net cage system in the future work.

CONCLUSIONS

A numerical model for hybrid mooring line considering embedded chains in soil is developed. The proposed numerical model was validated by analytical formulations in static analysis and experimental results in dynamic analysis, respectively. The results indicate that our numerical model is available to predict the structural response of mooring line with embedded chains. Several conclusions can be drawn as follows:

The simplified cases of mooring line ignoring the effect of embedded chains, including Case A, Case B, Case C and Case D, would result in an un-reasonable evaluation for the static and dynamic response of mooring line and embedded anchors, and it is essential to select an appropriate safety

factor using the simplified model at the initial design stage. In parameter sensitivity study, initial pretension of suspended rope and the soil shear strength gradient have a significant effect on mooring line development and the load acting on embedded anchors. For single-cage system, the difference of the maximum tension at the pad-eye point of anchor line between Case S0 and Case SC could be up to 8.19%. And the corresponding difference for double-cage and four-cage system is 5.62% and 4.02%. The reduction of the impact of embedded chains may be attributed to the smaller proportion of the soil resistance to the external load for the larger-scale net cage system. However, the interaction of soil and embedded anchors for the multi-cage system may increase, and the trenching phenomenon may appear resulting in the decrease of the soil shear strength and capacity of embedded anchors. In the future work, the interaction with embedded chains, soil and embedded anchors for net cage system in the open sea and how to improve the safety condition deserves to be further studied.

ACKNOWLEDGEMENTS

This work was financially supported by National Key R&D Program of China (2017YFC1404200), the National Natural Science Foundation (NSFC) Projects No. 51409037, and the Fundamental Research Funds for the Central Universities No. DUT18LK41.

APPENDIX A ANALYTICAL FORM FOR STATIC RESPONSE OF EMBEDDED CHAINS

According to Vivatrat et al. 1982, the differential equations of embedded chains are

$$\begin{aligned} \frac{dT}{dl} &= F + W \cdot \sin \theta \\ T \cdot \frac{d\theta}{dl} &= -Q + W \cdot \cos \theta \end{aligned} \quad (\text{A. 1})$$

where W is the wet weight per unit length of chains; θ is the angle from the chains to the horizontal axis; T is the chain tension; l is the distance along the chains, starting at the anchor point; F and Q are the normal and tangential components of soil resistance on chains, respectively. Considering the small attachment angle assumption and ignoring the chain weight (referring to Neubecker and Randolph 1995), the analytical expression of the profile for embedded chains can be written as,

$$dx^* = -\frac{dz^*}{\sqrt{\theta_0^2 + \frac{2}{T^*} \cdot (z^*)^2}} \quad (\text{A. 2})$$

where x^* and z^* are the horizontal and vertical coordinates normalized by the attachment depth D ; θ_0 is the chain angle at the seabed; T^* is the non-dimensional tension at the attachment point, $T^* = \frac{T_a}{DQ}$. Thus the profile can be expressed as,

$$\sqrt{2/T^*} \cdot x^* = \ln \left[\frac{(1 + \sqrt{1 + T^* \cdot \theta_0^2 / 2}) / (z^* + \sqrt{(z^*)^2 + T^* \cdot \theta_0^2 / 2})}{(1 + \sqrt{1 + T^* \cdot \theta_0^2 / 2})} \right] \quad (\text{A. 3})$$

APPENDIX B ANALYTICAL FORM FOR STATIC RESPONSE OF CATENARY CURVE

The global coordinate system and the sketch of catenary curve are shown in Fig. 6a. Points AA, BB and CC represent the anchor point, the top end and the virtual sag point, respectively. According to the derivation in Cella 1999, the formulas are shown as follows,

$$l = c \cdot \left(\sinh \left(\operatorname{atanh} \left(\frac{v}{l} \right) + \frac{d}{2c} \right) - \sinh \left(\operatorname{atanh} \left(\frac{v}{l} \right) - \frac{d}{2c} \right) \right) \quad (\text{B. 1})$$

$$\frac{x'}{c} = \operatorname{atanh} \left(\frac{v}{l} \right) + \frac{d}{2c} \quad (\text{B. 2})$$

$$y' = c + g = c \cdot \cosh \left(\frac{x'}{c} \right) \quad (\text{B. 3})$$

where d is the horizontal distance between the top end and the anchor point; v is the vertical distance between the top end and the anchor point; l is the length of catenary curve; g is the distance between the top end and the virtual sag point of catenary curve; x' is the abscissa value of the top end in the global coordinate system; y' is the ordinate value of the top end in the global coordinate system; c is the ordinate value of the virtual sag point of catenary curve in the global coordinate system; $\sinh(\cdot)$ and $\cosh(\cdot)$ are the hyperbolic sine and cosine functions; $\operatorname{atanh}(\cdot)$ is the arc-hyperbolic tangent function.

In this study, the variables v , d and l in Fig. 6a are known a priori. From Eq. (B. 1), the parameter c can be obtained by Newton-Raphson method. Subtracting c into Eq. (B. 2), the x' is calculated. Then the variable g is yielded by Eq. (B. 3). Therefore, the profile of the catenary curve can be calculated by,

$$y = c \cdot \cosh \left(\frac{x+x'-d}{c} \right) - (c + g - v) \quad (\text{B. 4})$$

where x and y is the abscissa and ordinate values of the top end in the local coordinate system, respectively. The origin of the local coordinate system is located at the anchor point. The horizontal and the vertical components of the tension on catenary curve at the top end are

$$\begin{aligned} T_x &= w \cdot c \\ T_y &= w \cdot c \cdot \sinh \left(\frac{x'}{c} \right) \end{aligned} \quad (\text{B. 5})$$

where w is the wet weight per unit length of catenary curve. Thus the total tension on catenary curve at the top end is

$$T = w \cdot c \cdot \cosh \left(\frac{x'}{c} \right) \quad (\text{B. 6})$$

REFERENCES

- Andersen, K.H., Murff, J.D., Randolph, M., Clukey, E.C., Erbrich, C.T., Jostad, H.P., Hansen, B., Aubeny, C.P., Sharma, P., Supachawarote, C., 2005. Suction anchors for deepwater applications. In: Proceedings of the International Symposium on Frontiers in Offshore Geotechnics, 3-30.
- Cella, P., 1999. Methodology for exact solution of catenary. *Journal of Structural Engineering*, 125(12): 1451-1453.
- Chen, X.H., Zhang, J., Johnson, P., Irani, M., 2001. Dynamic analysis of mooring lines with inserted springs. *Applied Ocean Research* 23, 277-284.
- Cheng, M.Y., Cao, M.T., Tran, D.H., 2014. A hybrid fuzzy inference model based on RBFNN and artificial bee colony for predicting the uplift capacity of suction caissons. *Automation in Construction* 41, 60-69.
- Choi, Y., Kim, B., Kwon, O., Youn, H., 2014. Horizontal pullout capacity of steel chain embedded in sand. *Advances in Soil Dynamics and Foundation Engineering GSP*, 240, 500-508.
- Choo, Y.I., Casarella, M.J., 1971. Hydrodynamic resistance of towed cables. *Journal of Hydronautics*, 126-131.
- DeCew, J., Tsukrov, I., Risso, A., Swift, M.R., Celikkol, B., 2010. Modeling of dynamic behavior of a single-point moored submersible fish cage under currents. *Aquacultural Engineering* 43(2), 38-45.
- Degenkamp, G., Dutta, A., 1989. Soil resistances to embedded anchor chain in soft clay. *Journal of Geotechnical Engineering* 115(10), 1420-1438.
- Gault, J.A., Cox, W.R., 1974. Method for predicting geometry and load distribution in an anchor chain from a single point mooring buoy to a buried anchorage. In: Proceedings of 6th Annual Offshore Technology Conference. Houston, Texas, USA, 309-318.
- Guo, Z., Wang, L.Z., Yuan, F., 2016. Quasi-static analysis of the multi-component mooring line for deeply embedded anchors. *Journal of Offshore Mechanics and Arctic Engineering*, 138(1), paper No: OMAE-11-1097.
- Hall, M., Goupee, A., 2015. Validation of a lumped-mass mooring line model with DeepCwind semisubmersible model test data. *Ocean Engineering* 104, 590-603.
- Huang, X.H., Guo, G.X., Tao, Q.Y., Hu, Y., Liu, H.Y., Wang, S.M., Hao, S.H., 2016. Numerical simulation of deformations and forces of a floating fish cage collar in waves. *Aquacultural Engineering* 74, 111-119.
- Huang, C.C., Tang, H.H., Liu, J.Y., 2006. Dynamic analysis of net cage structures for marine aquaculture: Numerical simulation and model testing. *Aquacultural Engineering* 35(3), 258-270.
- Huang, C.C., Tang, H.J., Wang, B.S., 2010. Numerical modeling for an In Situ single-point-mooring cage system. *IEEE Journal of Oceanic Engineering* 35(3), 565-573.
- Kapetsky, J.M., Aguilar-Manjarrez, J., Jenness, J., 2013. A global assessment of potential for offshore mariculture development from a spatial perspective. *FAO Fisheries and Aquaculture Technical Paper No. 549*. Rome, FAO. 181 pp.
- Kim, T., Lee, J., Fredriksson, D.W., DeCew, J., Drach, A., Moon, K., 2014. Engineering analysis of a submersible abalone aquaculture cage system for deployment in exposed marine environments. *Aquacultural Engineering* 63, 72-88.
- Liu, H.X., Liu, C.L., Zhao, Y.B., Wang, C., 2014. Comparative study of reverse catenary properties of the installation line for drag anchors. *Applied Ocean Research* 48, 42-54.
- Masciola, M.D., Nahon, M., Driscoll, F.R., 2011. Static analysis of the lumped mass cable model using a shooting algorithm. *ASCE Journal of Waterway, Port, Coastal, and Ocean Engineering*
- Neubecker, S.R., Randolph, M.F., 1995. Profile and frictional capacity of embedded anchor chains. *Journal of Geotechnical Engineering* 121(11), 797-803.
- O'Loughlin, C., White, D., Stanier, S., 2015. Novel anchoring solutions for FLNG-Opportunities driven by scale. In: Proceedings of the 47th Annual Offshore Technology Conference, Houston, Texas, USA, OTC-26032-MS.
- Rocha, M., Schnaid, F., Rocha, C., Amaral, C., 2016. Inverse catenary load attenuation along embedded ground chain of mooring lines. *Ocean Engineering* 122, 215-226.
- Shainee, M., DeCew, J., Leira, B.J., Ellingsen, H., Fredheim, A., 2013. Numerical simulation of a self-submersible SPM cage system in regular waves with following currents. *Aquacultural Engineering* 54, 29-37.
- Skempton, A.W., 1951. The bearing capacity of clays. *Building Research Congress, Division 1, Part 3*, London, 180-189.
- Surendran, S., Goutam, M., 2009. Reduction in the dynamic amplitudes of moored cable systems. *Ships and Offshore Structures* 4(2), 145-163.
- Tang, H.J., Huang, C.C., Chen, W.M., 2011. Dynamics of dual pontoon floating structure for cage aquaculture in a two-dimensional numerical wave tank. *Journal of Fluids*

and Structures 27, 918-936.

26. Vivatrat, V., Valent, P.J., Ponterio, A.A., 1982. The influence of chain friction on anchor pile design. In: Proceedings of the 14th Annual Offshore Technology Conference, Houston, Texas, USA, 153-163.
27. Wang, L.Z., Guo, Z., Yuan, F., 2010a. Quasi-static three dimensional analysis of suction anchor mooring system. *Ocean Engineering* 37, 1127-1138.
28. Wang, L.Z., Guo, Z., Yuan, F., 2010b. Three-dimensional interaction between anchor chain and seabed. *Applied Ocean Research* 32, 404-413.
29. Xiong, L.Z., Yang, J.M., Zhao, W.H., 2016. Dynamic of a taut mooring line accounting for the embedded anchor chains. *Ocean Engineering* 121, 403-413.
30. Xu, T.J., 2014. Hydrodynamics of net cage group in the open sea. Doctoral Thesis. Dalian University of Technology.
31. Xu, T.J., Dong, G.H., Li, Y.C., Guo, W.J., 2014. Numerical study of a self-submersible single-point mooring gravity cage in combined wave-current flow. *Applied Ocean Research* 48, 66-79.
32. Xu, T.J., Zhao, Y.P., Dong, G.H., Gui, F.K., 2013. Analysis of hydrodynamic behavior of a submersible net cage and mooring system in waves and current. *Applied Ocean Research* 42, 155-167.
33. Yen, B.C., Tofani, G.D., 1984. Soil resistance to stud link chain. In: Proceedings of 16th Annual Offshore Technology Conference, Houston, Texas, USA, OTC 4769, 1-10.
34. Zhao, Y.P., Bi, C.W., Chen, C.P., Li, Y.C., Dong, G.H., 2015. Experimental study on flow velocity and mooring loads for multiple net cages in steady current. *Aquacultural Engineering* 67, 24-31.

CONTACT WITH THE AUTHORS

Tiao-Jian Xu

e-mail: 1533191728@qq.com

State Key Laboratory of Coastal and Offshore
Engineering
Dalian University of Technology
No.2 Linggong Road
116024 Dalian City
CHINA

ESTIMATION OF BUCKLING RESPONSE OF THE DECK PANEL IN AXIAL COMPRESSION

Ozgur Ozguc, Ph.D.

Department of Naval Architecture and Ocean Engineering, Istanbul Technical University, Istanbul, Turkey

ABSTRACT

In this work, buckling strength assessment of a deck of a double hull oil tanker is carried out using the non-linear finite element code ADVANCE ABAQUS. The comparisons are performed with the Det Norske Veritas (DNV-GL) PULS (Panel Ultimate Limit State) buckling code for the stiffened panels, DNV-GL Classification Notes (CN) No.30.1 and the DNV-GL Ship Rules.

The case studied corresponds to axial compression. Two levels of imperfection tolerances are analyzed, in accordance with the specifications in the DNV-GL Instruction to Surveyors (IS) and the DNV-GL Classification Notes No. 30.1. Both “as built” and DNV-GL Rule “net” dimensions are analyzed.

The strength values from ADVANCE ABAQUS and PULS are very close. DNV-GL CN 30.1 is in conservative side, but the strength differences between the “as built” and “net” dimension cases are consistent with the finite element analysis results.

This paper gives a brief description of the background for the stiffened panel models used in PULS, and comparison against non-linear FE analysis, and DNV-GL Classification Society Rules. The finite element code ADVANCE ABAQUS is employed in a non-linear buckling analysis of a stiffened deck panel on a double skin tanker that is subjected to a Condition Assessment Program (CAP) hull survey. The aim of the analyses has been to validate and compare the buckling capacity estimates obtained from PULS, DNV-GL Classification Notes No.30.1 (CN 30.1) and the DNV-GL Ship Rules.

Keywords: buckling failure; non-linear finite element analysis; deck panel; initial imperfection; collapse mechanism

INTRODUCTION

Ship and offshore structures are basically an assembly of plate elements and estimation load-carrying capacity or the ultimate strength is one of the most important criterion for estimated safety assessment and rational design on the ship structure. In addition, structural elements making up ship-plated structures do not work individually under external load. One of the critical collapse events of a ship structure is the occurrence of overall buckling and plastic collapse of deck structure subjected to longitudinal bending. Hence, the deck plates are reinforced by a number of longitudinal stiffeners to increase their strength and load-carrying capacity. For a rational design avoiding such a sudden collapse, it is very

important to know the buckling response and collapse pattern of the stiffened plate subjected to axial compression.

Stiffened panels' structural response under compressive loading is a topic of significant practical interest in ship design. This applies for the detail design phase as well as for ships in the service phase for which a trustworthy strength and safety margin assessment are of paramount importance. It is well known that post buckling and ultimate strength limits only can be treated in a consistent manner using non-linear plate theory. This fact has for many decades been an obstacle for practising engineers and designers since resort to advanced and time consuming non-linear finite element programs and expert judgements were a prerequisite for assessing the strength of critical elements. However, with

the recent development of computers, it has become feasible to make use of buckling models based on non-linear plate theory. By introducing semi-analytical computerized ultimate strength models into ship and offshore rules and standards, engineers and designers will improve their understanding of non-linear structural response. The result will be more optimal and robust design solutions with more effective use of the material and improved control of the actual safety margins against failure. Corrosion margins and minimum thickness requirements for ships in service can be prescribed with larger confidence than hitherto possible with simpler and more traditional curve fitting methods.

Ko et al. [1] performed a series of FEM elastoplastic large deflection analyses on a stiffened plate with flat-bar, angle-bar and tee-bar stiffeners to examine numerically characteristics of buckling and ultimate strength behavior according to the analysis method of ship's stiffened plate subject to axial loading.

Ozguç et al. [2] developed the new simple design equations for predicting the ultimate compressive strength of stiffened plates with initial imperfections in the form of welding-induced residual stresses and geometric deflections were developed in the study. To perform ANSYS elastic-plastic buckling analyses, a non-linear finite element method was employed, where a wide range of typical ship panel geometries such as 60 different models was accounted for. Reduction factors of the ultimate strength were produced from the results of 60 ANSYS inelastic finite element analyses. The accuracy of the proposed equations was validated by the experimental results. Comparisons indicated that the adopted method had sufficient accuracy for practical applications in ship design.

Paik et al. [3] concentrated on methods for the ultimate limit state assessment of stiffened plate structures under combined biaxial compression and lateral pressure actions considering the bottom part of an AFRAMAX-class hypothetical double-hull oil tanker structure. Three methods, namely ANSYS nonlinear finite element method, DNV-GL PULS method, and ALPS/ULSAP method were used.

Chaithanya et al. [4] evaluated the behavior of stiffened plates with different distortion levels in order to address a rational structural design procedure, as pre-existing and fabrication-related initial geometrical distortion from a structural design point of view. Non-linear finite element (FE) analysis using ABAQUS was carried out under axial loading condition to predict the behaviour and the buckling strength.

Xu and Soares [5] simulated numerically the behaviour of stiffened panels under uniaxial compression until collapse and beyond, and then compared with tests made to investigate the influence of the stiffener's geometry and the boundary conditions. The stiffened panel models have three longitudinal bays to produce reasonable boundary conditions in the longitudinal direction. The material and geometric nonlinearities were accounted for in the FE analyses. The initial geometric imperfections, which affect significantly the collapse behaviour of stiffened panels, were assumed to have the shape of the linear buckling mode. Four types of stiffeners

were made of mild or high tensile steel for bar stiffeners and mild steel for 'L' and 'U' stiffeners to investigate different material and geometry configurations, and four boundary conditions were analyzed.

Tekgoz et al. [6] analyzed the effect of different finite element models on the ultimate strength assessment of stiffened plates, where the effect of element size, and type, boundary conditions, shape of initial imperfection, thickness and net sectional configurations were accounted for. Four different finite element models and different structural configurations were compared to the solution described by the Common Structural Rules (CSR).

Cho et al. [7] proposed ultimate strength formulation for stiffened plates. The formulation was developed by a regression study using the parametric study results. The accuracy and reliability of the proposed formulation were compared with those of commercial packages, such as ABAQUS and DNV-GL PULS, and experimental results.

Zhang [8] presented a review and study on ultimate strength analysis methods for steel plates and stiffened panels in axial compression. Buckling and collapsing mechanisms of steel plates and stiffened panels were described. A study and further validation on the authors developed formula for ultimate strength of stiffened panels using a comprehensive non-linear finite element analysis, 110 models in total, and a wide range of model test results, 70 models in total, were carried out. Finally, applications of the developed formula to existing oil tankers and bulk carriers were presented.

Zhang et al. [9] investigated pitting corrosion effect on the ultimate strength of hull structural stiffened plates under uniaxial compression. In the dedicated analyses, the relative parameters such as sizes of panels, size and shape of pits, initial imperfections, boundary condition, and number of stiffeners were accounted for. The ultimate strength reduction formula of pitted stiffened plates based on corroded volume loss were obtained by the data analysis from lots of non-linear finite element analyses.

Ozdemir et al. [10] proposed a new approximate method based on analytical formulas to estimate the ultimate strength of stiffened panels, where a series of detailed elastoplastic large deflection FEA was carried out. The initial deflections were accounted for in the form of thin-horse mode plus overall buckling mode for the plates, and flexural buckling mode plus tripping mode for the stiffeners. A good agreement was obtained within all collapse scenarios studied.

Shi et al. [11] investigated the collapse mechanics of pitted stiffened plates using numerical approach and compared with the tests. A series of FEAs were performed to address the influence of pit damage. Pits can eventually induce the buckling and reduction of the ultimate strength capacity of stiffened panel. A formula was introduced with regards to the reduction of the plate slenderness ratio and column slenderness induced by pits.

In this study, buckling strength assessment of a deck of a double hull oil tanker is carried out using the non-linear finite element code ADVANCE ABAQUS [12, 13]. The comparisons are being performed with the DNV-GL

PULS [14] buckling code for stiffened panels, DNV-GL Classification Notes No.30.1 [15] and the DNV-GL Ship Rules [16]. The results and insights developed from the present study are summarized in terms of ultimate strength characteristics of deck stiffened plate structures.

THE MODEL FOR ANALYSIS

A Condition Assessment Program (CAP) strength check of a double hull oil tanker revealed a potential buckling strength problem in its deck structure. The DNV-GL Ship Rules, the DNV-GL Classification Notes No. 30.1 (CN 30.1) and the PULS buckling acceptance criteria indicated insufficient buckling strength.

The PULS buckling code is developed by DNV-GL for direct computational assessment of buckling limits and ultimate strength limits of stiffened panels based on non-linear large deflection plate theory. The idea is to combine a user friendly and easy to understand user interface, with advanced but still efficient direct calculations. The numerical algorithms included in the buckling code provide results for a given case in the order of a second on a standard modern personal computer [14, 18].

In principle, the PULS buckling models can be classified as semianalytical in the sense that they are based on the recognized plate theory of Marguerre [17] in combination with numerical techniques for solution of the governing equations. Using non-linear plate theory, second order membrane strains are accounted for, and the postbuckling response may be traced. The principle of minimum potential energy is used, together with Fourier series expansion of the displacements. The non-linear elastic equilibrium equations are solved, and the load-deflection path traced, using the perturbation technique in an incremental scheme with arc length control. Using arc length incrementation, complex response histories may be solved, including snap-through problems [18].

The deck structure is without intermediate longitudinal girders between the two longitudinal bulkheads, and has flat-bar stiffeners. Previous experience indicates that the acceptance criteria tend to underestimate the ultimate strength of this type of panel. On the other hand, the higher strength has been associated with a violently unstable collapse. A more accurate analysis of the deck panels was judged interesting both as a verification of the simplified buckling strength formulations as well as providing decision support in the CAP rating. A non-linear finite element buckling analysis of the deck panel using the ADVANCE ABAQUS program has therefore been undertaken.

The deck panel has been analyzed for both gross (“as built”) and DNV-GL Ship Rule net scantlings ($t-t_k$) [16]. The dimensions for these two cases are given below Table 1 and Table 2 (measured between girders).

Tab. 1. Gross scantling for studied deck panel

Stiffener length	3770 mm
Stiffener spacing	735 mm
Number of stiffeners	13
Plate thickness	13.5 mm
Stiffener height	283 mm
Web thickness	18 mm
Profile type	Flat bar

Tab. 2. Net scantling for studied deck panel

Stiffener length	3770 mm
Stiffener spacing	735 mm
Number of stiffeners	13
Plate thickness	11.5 mm
Stiffener height	283 mm
Web thickness	15 mm
Profile type	Flat bar

It is noted that the panel is loaded in purely axial compression.

FINITE ELEMENT MODEL (FEM)

The high number of stiffeners justifies the use of a single stiffener (column) model to analyse this case. If this at all has any impact on the strength, this will be to the conservative side.

To reduce the uncertainties introduced through boundary conditions the finite element model extends over three frame spaces ($1/2+1+1/2$). The model is illustrated in Fig.1. It has six elements between stiffeners, twenty-eight elements between transverse frames and three elements across the stiffener height.

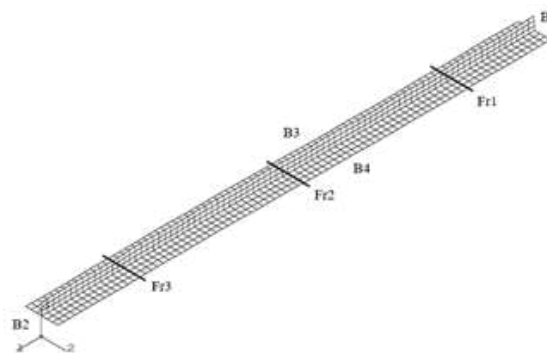


Fig.1. The finite element model with labelled boundaries

Strain hardening effect together with a bi-linear strain-stress curve as shown in Fig.2. The Cowper-Symonds rate enhancement formula is used to consider the effect of strain rate on material properties as given Eq.3, Eq.4 and Eq.5 that are shown in Fig.2. and Fig.3. The material parameters are shown in Table 3.

Tab. 3. The material properties

Young's modulus, E [N/mm ²]	206 000
Poisson ratio, ν	0.30
Material yield stress [N/mm ²]	235
Strain hardening parameter, ET [N/mm ²]	1000
Strain rate (C)	40.4
Strain rate (P)	5.0

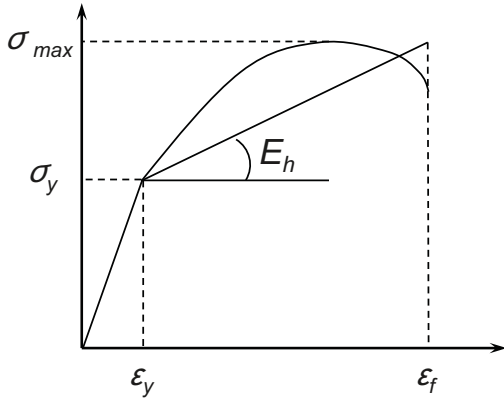


Fig.2. Stress-strain curve for bi-linear material

$$\sigma_p = \sigma_y + \frac{EE_h}{E - E_h} \epsilon_p \quad (3)$$

$$E_h = \frac{\sigma_{max} - \sigma_y}{\epsilon_f - \epsilon_y} \quad (4)$$

- σ_y = Yield stress
- E_h = Hardening modulus
- σ_p, ϵ_p = Plastic stress & Plastic strain
- E = Young's modulus

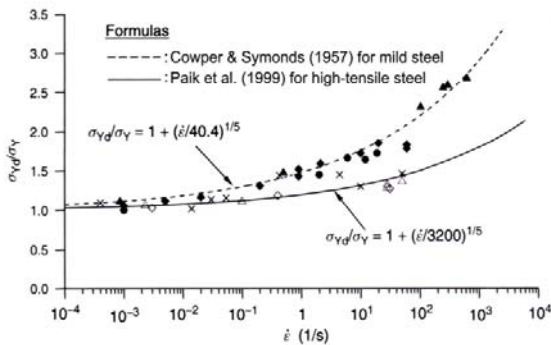


Fig.3. Strain rate effect

$$\frac{\sigma_{yd}}{\sigma_y} = 1 + \left\{ \frac{\epsilon}{D} \right\}^{1/q} \quad (5)$$

It is noted that for mild steel grade D = 40.4 and q = 5 are used.

Boundary conditions are imposed on the edges and lines indicated in Fig.1.

T [1, 2, 3] indicate translation constraints and on R [1, 2, 3] indicate rotational constraints about the 1, 2 and 3 coordinates as shown in Fig.1. Boundary conditions are imposed on the edges and lines indicated in Fig.1. In other words, free meaning no constraint and fix meaning is fully constrained.

- Symmetry conditions are given on edges B1 and B2. Namely, T [fix, free, free] and R [free, fix, fix].

This might represent a constraint on the deformation of the plate and on the web and flange of the stiffener, but the experience from other similar analyses [9, 10] indicates that this has small impact on the results. Edge B2 is fixed in the 1-direction.

- On edges B3 and B4 the rotation about the 2-axis is fixed (symmetry). Namely, T [free, fix, free] and R [fix, free, fix].

Edge B4 is fixed in the 2-direction, while edge B3 is free to translate in this direction but the edge constrained to remaining straight.

Lines labelled Fr1, Fr2 and Fr3 correspond to the positions of transverse frame. At these locations, the panel is fixed in the lateral direction. Furthermore, the stiffener is constrained to remain vertical in order to simulate presence of frames.

INITIAL IMPERFECTIONS

Imperfections in a buckling strength context usually refer to geometric imperfections (plate out-of-flatness, stiffener out-of-straightness, misalignments) and residual stresses. Both are a result of welding or plastic forming during manufacture. The presence of residual stresses has been disregarded in this study.

Two levels of tolerances on the geometric imperfections have been analysed, consistent with the specifications in the DNV-GL Instruction to Surveyors [19] (DNV-GL IS) and DNV-GL Classification Notes No.30.1. The relevant values of plate out-of-flatness and stiffener out-of-straightness specified in these documents are given in Table 4.

Tab. 4. Tolerances on plate out-of-flatness and stiffener out-of-straightness specified in the DNV-GL IS and in CN 30.1. See Fig.4 for a definition of the imperfection parameters.

	DNV IS	CN 30.1
$\delta_{p0} = 0.01s$	0.01s (7.35mm)	6mm
$\delta_{s0} = 0.0015L$	0.0015L (5.655mm)	13mm
$\delta_{T0} = 0.0015L$	0.0015L (5.655mm)	13mm

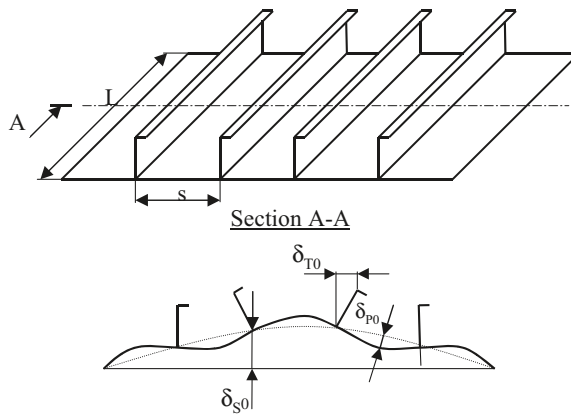


Fig.4. The imperfection parameters used in this study

The shape of the imperfections is generally composed of a local component (plate out of flatness and stiffener flange out of straightness) and a global component (stiffener out of straightness) as shown in Fig.4. The local component is itself composed from a subset of the elastic buckling modes for the panel for the specific load combination at hand. In this case, a weighed combination of the ten first buckling modes is used. This procedure requires that the deformation pattern in the buckling modes exclude lateral deflection of the stiffeners, a requirement that is met in this case. Global stiffener imperfections are specified in a half sine wave pattern along the stiffener length, and with a constant value across the column cross-section. A magnified illustration of the resulting imperfection shape is shown in Fig.5.

LOAD APPLICATION

All analyses are being performed in displacement control, i.e. the non-linear solution is found by incrementing the magnitude of a specified edge displacement. This approach is selected because it eliminates that the need to apply the modified Riks algorithm [12, 13] in the solution. The Riks method is generally used to predict unstable, geometrically nonlinear collapse of a structure that can include nonlinear materials and boundary conditions. It often follows an eigenvalue buckling analysis to provide complete information about a structure's collapse; and can be used to speed convergence of ill-conditioned or snap-through problems that do not exhibit instability.

The Riks algorithm failed for some of the cases, by "backtracking" along the elastic unloading equilibrium path. Displacement control and load control are equivalent for axial load cases.

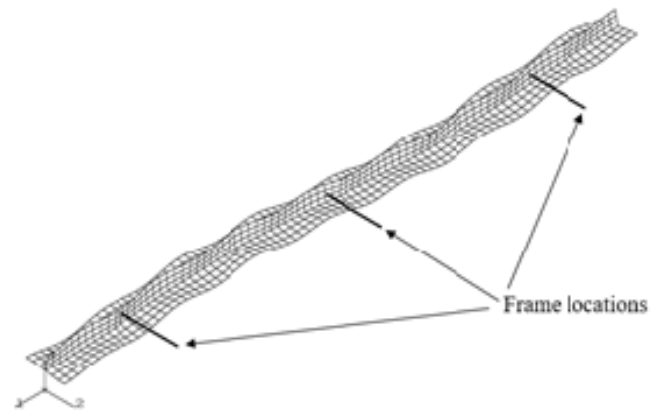


Fig. 5. Illustration of the imperfection shape used in the analyses

FINITE ELEMENT ANALYSIS RESULTS

The results from the finite element analysis will firstly be presented as equilibrium curves in a diagram spanned by a scaled nominal strain on the first axis (ϵ/ϵ_f) and a scaled nominal stress (σ/σ_f) on the second axis, where σ_f is defined as material yield strength and ϵ_f is yield strain. This will illustrate both the ultimate strength of the panel and its pre- and post-buckling response. The finite element results are being compared with PULS, CN30.1 and the DNV-GL Ship Rules.

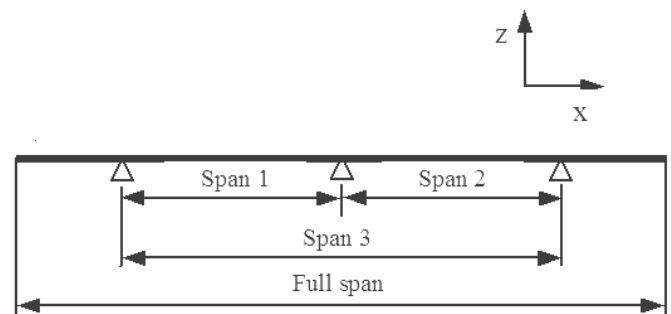


Fig. 6. Identification of the four mechanical systems selected for response visualisation

For a multi-span model, the load-displacement response will depend on what part of the system one considers. To illustrate this difference, the load displacement response is presented in Figs. 7-10 for the four mechanical systems identified in Fig.6.

Collapse of the panel is in all cases initiated and progresses in "Span 1" of the model, in the form of stiffener tripping close to the centre of the span. The tripping in turn reduces the out of-plane bending stiffness of the panel, leading to failure in lateral buckling.

Figs.7 and 12 illustrates the collapse modes for the DNV-GL IS Gross and the CN 30.1 Gross cases respectively. The two cases based on net dimensions show similar collapse modes as their gross dimension counterparts. Observe that the tripping failure differs in the two cases, an effect that most likely is the

reason for difference in response between the cases based on the CN 30.1 imperfection tolerance level and the DNV-GL IS imperfection tolerance level. No attempt is performed to explain this difference in tripping behaviour, but it is noted that the difference must be related to the magnitude of the imperfections. In particular, it is the magnitude of the global stiffener imperfection that constitutes the difference between the models.

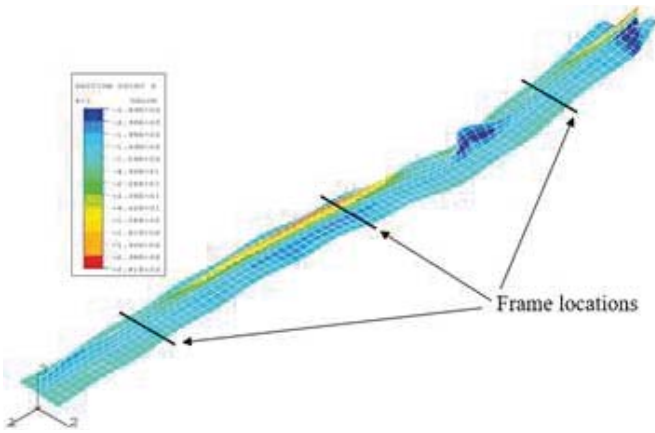


Fig. 7. Axial stress and displacement plot for the "DNV IS Gross" case. Note that displacements are magnified by five times

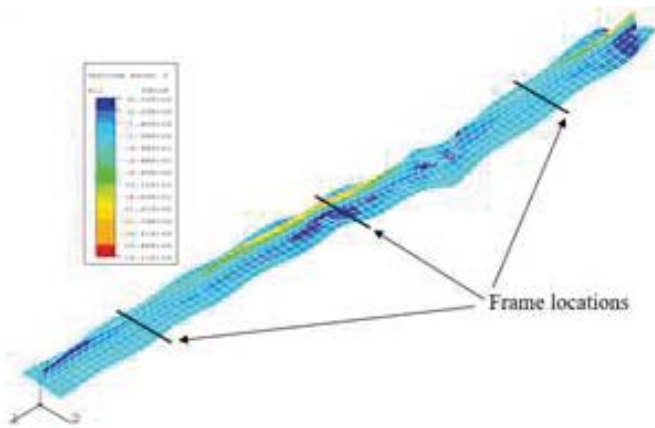


Fig. 8. Axial stress and displacement plot for the "CN 30.1 Gross" case. Note that displacements are magnified by five times

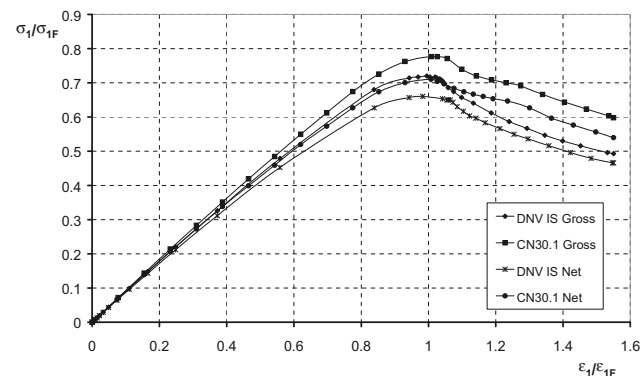


Fig. 9. Axial load vs. axial displacement response for the full model system

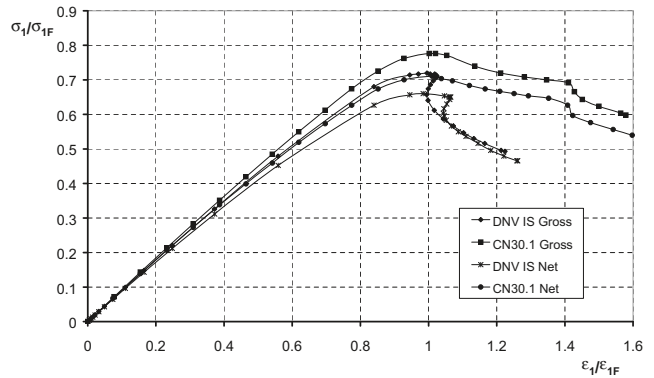


Fig. 10. Axial load vs. axial displacement response for the "Span 3" system

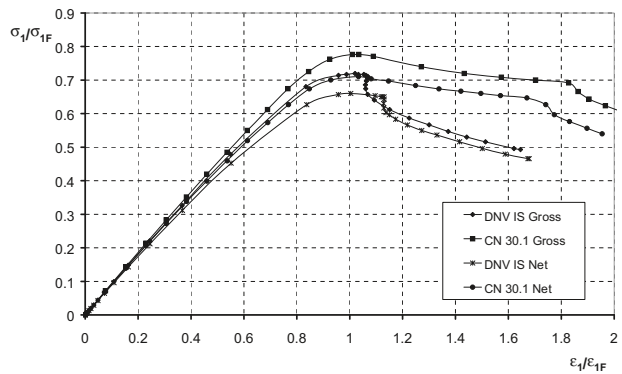


Fig. 11. Axial load vs. axial displacement response for the "Span 1" system

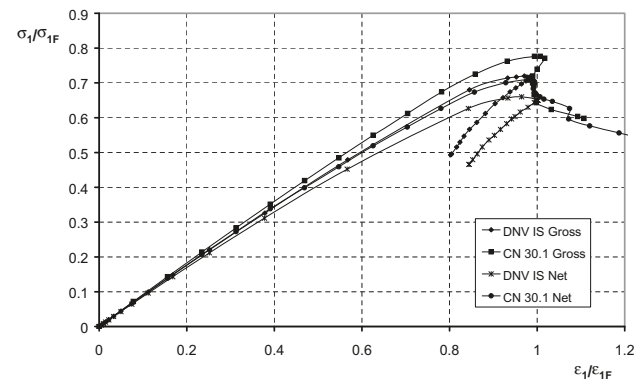


Fig. 12. Axial load vs. axial displacement response for the "Span 2" system

In "Span 2", the two analyse based on the DNV-GL IS imperfection tolerance level show an extreme "snap back" behaviour, whereas the remaining two cases show a smoother response. The response indicates that "Span 2" is unloading mainly elastically for the two cases based on DNV-GL IS tolerances. In the two cases based on CN 30.1 tolerances, a failure mode seems to be developing in "Span 2" allowing for an increase in axial displacement despite the decrease in load.

Clearly, the response of the full model is smoother than the response of the individual spans. This happens because a localised plate buckling deformation progresses at one of the panel ends, thus compensating for the decreasing displacement in "Span 2".

COMPARISON WITH SIMPLIFIED CALCULATION METHODS

None that the simplified strength formulations allow for a specification of an imperfection tolerance level. Strictly speaking, the DNV-GL Ship Rule and the PULS results should therefore be compared to the ADVANCE ABAQUS results relevant for DNV IS tolerance level, whereas the CN 30.1 results should be compared to the ADVANCE ABAQUS results relevant for the tolerance level specified in CN 30.1. On the other hand, the uncertainties related to the magnitude of the geometric imperfections is large, and there is no evidence that the imperfections are larger in ship than in offshore structures. An alternative approach is to interpret the results based on the CN 30.1 tolerance level and the DNV-GL IS tolerance level as lower and upper bound strength values, respectively, valid for typical stiffened panels in ship and offshore structures.

A summary of the strength values obtained from ADVANCE ABAQUS and the three simplified buckling strength formulations are provided in Tab.5. Clearly, the PULS strength results is in excellent agreement with the ADVANCE ABAQUS results based on the DNV-GL IS tolerance level. CN 30.1 appears to be conservative, in particular in comparison to the ADVANCE results relevant for the CN 30.1 imperfection tolerance level.

The DNV-GL Ship Rule strength estimate are higher than both the PULS and the CN 30.1 strength estimates, but still below the ADVANCE ABAQUS results relevant for the CN 30.1 tolerance level. Relative to the ADVANCE ABAQUS results, the Ship Rule strength estimates are higher for the gross dimensions than the net dimensions indicating that the Ship Rules do not exhibit the same qualitative trend as the ADVANCE ABAQUS analyses. Some lack of physical consistency must be anticipated since the DNV-GL Ship Rule strength estimates are governed by the plate-buckling criterion, whereas the collapse is governed by stiffener tripping. Both PULS and CN 30.1 indicate stiffener-induced failure mode.

Tab. 5 Comparison of panel buckling strengths for different analysis methods.

Analysis Id.	Buckling strength in gross dimensions [MPa]	Buckling strength in net dimensions [MPa]	Ratio Gross/Net
Abaqus with DNV IS Tol.	169	155	1.090
Abaqus with CN 30.1 Tol.	182	167	1.089
PULS	165	155	1.064
DNV-GL CN 30.1	148	135	1.096
DNV-GL Ship Rules	180 (plate)	159 (plate)	1.132

CONCLUDING REMARKS

Direct application of geometrical non-linear plate theory is the main concept in the new Panel Ultimate Limit State (PULS) stiffened panel models recently recognized by DNV-GL as part of the new rules and standards for ships and offshore constructions. The focus is on assessment of the ultimate capacity limit, rather than the more traditional elastic buckling limit. The method is streamlined for rules based on modern ultimate limit state design principles. The models are validated against non-linear FE analyses. Comparison against existing codes used by DNV-GL Classification Society are also included.

The finite element code ADVANCE ABAQUS has been used in a non-linear buckling analysis of a stiffened deck panel on a single skin tanker that has recently been subjected to a Condition Assessment Program (CAP) hull survey. Further, CAP is a specialized survey program which offers owners a detailed assessment of a ship's actual condition, based on strength evaluation, and fatigue strength analysis as well as a detailed on site systematic inspection of the hull, machinery and cargo systems. With the CAP, owners can be confident that they have an accurate assessment of the ships actual condition, especially as far as the condition compares with the normal Class requirements. The CAP applies, in principle, to oil tankers, chemical carriers and bulk carriers, though other types of ships may be covered, provided that the CAP is properly modified. The CAP consists of two major parts. CAP-MACHINERY/CARGO SYSTEM can be applied in addition to CAP-HULL upon request.

The aim of the analyses has been to validate and compare the capacity estimates obtained from PULS, DNV-GL Classification Notes No.30.1 and the DNV-GL Ship Rules, which all indicated insufficient buckling strength in the deck. Analyses are carried out for both "as built" and DNV-GL Rule net dimensions.

One single uniaxial load case has been investigated. The imperfection tolerances given in the DNV-GL Instruction to Surveyors (DNV-GL IS) and the CN 30.1 have been used as basis for the analyses. For this case the main difference in imperfection tolerances is in the stiffener out-of-straightness, which is over twice as large in the DNV-GL IS as in the CN 30.1 tolerances.

The results show that the PULS code produce capacity estimates in very good agreement with the finite element analysis results based on the tolerance level specified in the DNV IS. It is slightly conservative compared to the finite element analysis results based on the CN 30.1 tolerance level. CN 30.1 buckling strength estimates are conservative compared to the finite element results for both tolerance levels.

Further, as presented in Table 5 the buckling strength in accordance with DNV-GL Ship Rules based on DNV-GL IS initial deflection tolerances gives higher value than ABAQUS finite element analysis. In other words, the buckling strength with DNV-GL Ship Rules based on CN 30.1 initial deflection tolerances gives lower value than ABAQUS finite element analysis.

However, the qualitative impact of the change from “as built” to net dimensions do not comply as well with the finite element analysis results as is the case for the two other formulations.

REFERENCES

1. Ko JY, Oh YC, Park JS.: Estimation of buckling and plastic behaviour according to the analysis model of the stiffened plate. *Journal of Navigation and Port Research*, Vol.31, Issue 3, 2007, pp.271-279.
2. Ozguc O, Das PK, Barltrop N.: The new simple design equations for the ultimate compressive strength of imperfect stiffened plates. *Ocean Engineering*, Vol. 34, Issue 7, 2007, pp. 970–986.
3. Paik JK, Kim BJ, Seo JK.: Methods for ultimate limit state assessment of ships and ship-shaped offshore structures: Part II stiffened panels. *Ocean Engineering*, Volume 35, Issue 2, 2008, pp. 271–280.
4. Chaithanya PP, Das PK, Crow A, Hunt S.: The effect of distortion on the buckling strength of stiffened panels, *Ships and Offshore Structures*, Vol.5, 2010.
5. Xu MC and Soares CG.: Numerical assessment of experiments on the ultimate strength of stiffened panels, *Engineering Structures*, Vol.45, 2012, pp. 460–471.
6. Tekgoz M, Garbatov Y, Soares CG.: Ultimate strength assessment for the effect of finite element modelling, *Maritime Engineering and Technology*, 2012.
7. Cho SR, Kim HS, Doh HM, Chon YK.: Ultimate strength formulation for stiffened plates subjected to combined axial compression, transverse compression, shear force and lateral pressure loadings. *Ships and Offshore Structures*, Vol.8, 2013.
8. Zhang S.: A review and study on ultimate strength of steel plates and stiffened panels in axial compression. *Ships and Offshore Structures*, Vol.11, 2016.
9. Zhang Y, Huang Y, Meng F.: Ultimate strength of hull structural stiffened plate with pitting corrosion damage under uniaxial compression, *Marine Structures*, Volume 56, November 2017, pp. 117-136.
10. Ozdemir M, Ergin A, Yanagihara D, Tanaka S, Yao T.: A new method to estimate ultimate strength of stiffened panels under longitudinal thrust based on analytical formulas. *Marine Structures*, Vol. 59, 2018, pp. 510-535.
11. Shi XH, Zhang J, Soares CG.: Numerical assessment of experiments on the ultimate strength of stiffened panels with pitting corrosion under compression, *Thin-Walled Structures*, Vol. 133, 2018, pp. 52-70.
12. ABAQUS Analysis User’s Guide.: Unstable collapse and post-buckling analysis, 2017.
13. Hibbit Karlson and Sorensen Inc.: ABAQUS/Standard User’s Manual, 2012.
14. Steen E, Byklum E and Vilming KG.: PULS verification manual - PULS Version 2.0, May 2010.
15. DNV GL Classification Notes.: Buckling strength analyses, CN 30.1, 2017.
16. DNV GL Rules for Classification.: Hull structural design ships with length 100 metres and above, Part 3 Chapter 1, 2018.
17. Marguerre K.: Zur theorie der gekrümmten platte grosser formeändrug”, *Proceedings of the 5th international congress for applied mechanics*, p. 93101, 1938.
18. Byklum E, Steen E, and Amdahl J.: A semianalytical model for global buckling and postbuckling analysis of stiffened panels”. *Thin Walled structures*, Vol. 42 (5), pp 701-7171, 2004.
19. DNV GL.: Hull survey – Workmanship standard, DNV Instructions to Surveyors No. I-B3.3, 2015.

CONTACT WITH THE AUTHOR

Ozgur Ozguc

e-mail: ozguco@yahoo.com.sg

Istanbul Technical University

Dept. of Naval Architecture and Ocean Eng.

Maslak, 34469 Istanbul

TURKEY

ELASTIC-PLASTIC ANALYSIS FOR CIRCUMFERENTIAL THROUGH CRACK AT BOUNDARY OF SEMI'S BRACE UNDER BEAM WAVE

Fei Wang¹
Xiong Deng¹
Yuqiong Li²

¹ Southwest Petroleum University, Chengdu, China

² School of Materials Science and Engineering, Southwest Petroleum University, Chengdu, China

ABSTRACT

In order to ensure the safety and reliability of the horizontal brace of semi-submersible platform (SEMI) which functions as the supporting structure in SEMI, this article presents an elastic-plastic method to analyze the variations of the crack tip opening displacement, elastic zone and plastic zone of the cracked section of the horizontal brace under beam wave. The brace of the SEMI was assumed to be located a circumferential through crack at its boundary in this article. In addition, the cracked section of the brace has been divided into crack zone, tensile plastic zone, elastic zone and compressive plastic zone in the presented theoretical model. Moreover, the closed form of the solution has been found in this article which is especially suitable solving complicated problems in practical engineering application. Also, a typical new-generation SEMI that is in practical use was selected to analyze the variation tendency of the cracked brace's parameters using the proposed model which could give good suggestion to semi-submersible platform designers and managers.

Keywords: theoretical model, crack damaged brace, semi-submersible platform, beam wave

INTRODUCTION

Semi-submersible platform (SEMI), one of the most widely used reusable exploitation platform due to their mobility and ability to operate in deep-water, have gained popularity in recent decades with on-going development of deep-water oil and gas exploitation. Although the safety design standards for this kind of structures are quite strict, cracks inescapably initiated during their service life [1]. According to the destruction accident happened before, engineers found that the cracks often occur at the horizontal brace which functions as the supporting structures in SEMI and bear complex loads [2–3]. The presence of such cracks at critical locations can compromise the safety of the braces and then cause serious disaster eventually. Take the accident of *Alexander Keilland* platform as an example, the loads were transferred to the other braces and led them break because of the overload due to the initial fracture of a horizontal brace [4].

As the semi-submersible platform would encounter very harsh marine environment during its service life, it is necessary to analyze the variation tendencies of the crack-damaged brace to ensure the safety and reliability of the SEMI. A number of researchers has investigated such problems [5–7]. In additionally, the crack has been assumed to be on the surface of the brace or lies far away from the boundary section of the brace. However, according to the evaluation of the effects of hydrodynamic loads on the strength of the SEMI's horizontal braces, the high stress almost concentrates on the connection between the horizontal brace and the column of the platform [8]. Moreover, the crack-induced accidents of the SEMIs of *Sedco*, *Alexander Keilland* and *Ocean Ranger* indicate that a circumferential through crack usually lies at the boundaries. Therefore, it is crucial to analyze the mechanical characteristics of these cracks at critical locations that could easily compromise the safety of the semi-submersible platform. Many researchers using finite element method whose effectiveness has been accepted by the engineering

community to analyze these crack damaged brace [9–10]. Nevertheless, by using the finite element method, calculations need to be carried out for every specific case and there would be only one calculation for each case. Moreover, the nonlinear calculations will be inefficient and spend significant resources for a structure system with some local defective elements. In this sense, the theoretical analysis on these cracked brace is still necessary.

The present article is aimed to investigate a theoretical analysis method to analyze the variations of the crack tip opening displacement, elastic zone and plastic zone of the cracked section of the horizontal brace under beam wave, which significantly affects the safety and reliability of the brace.

GOVERNING EQUATIONS

A typical new-generation semi-submersible platform is selected to analyze the cracked damaged brace. As can be seen from Fig. 1, the selected platform is mainly composed of the main deck, four columns, two parallel pontoons and the horizontal braces connected to the columns. In this research, the circumferential through crack is assumed to be located at the boundary of the brace. Moreover, the brace of the SEMI mainly subjected to splitting force under beam wave, shown as in Fig. 1 where the coordinate system and direction of the load have been shown.

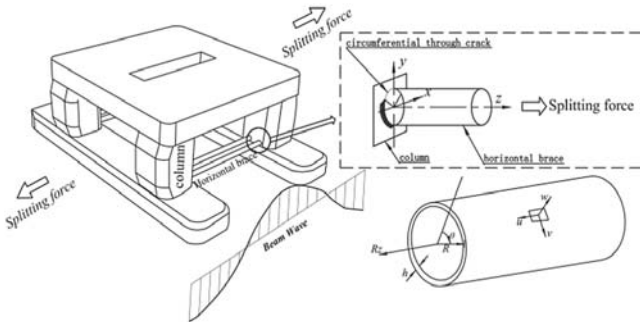


Fig. 1. Beam wave loaded on the brace of the semi-submersible platform

According to the historical records [11–13], the characteristic functions of the cracked damaged brace varies slowly in the z direction but not too rapidly in the θ direction. In the disastrous even of the *Alexander Kielland*, the circumferential through crack at the boundary of brace propagated to almost 67% of circumferential length of the brace before fracture [14]. Additionally, the brace of SEMI belong to the mid-long cylindrical shell category from the viewpoint of the shell theory. Then, the governing equation of the brace can be expressed under a semi-membrane state [5] with the complex-valued variable $\Omega = w + i\zeta$ as follow,

$$\frac{\partial^2}{\partial \theta^2} \left(\frac{\partial^2 \Omega}{\partial \theta^2} + \Omega \right) - i \varepsilon^{-2} \frac{\partial^2 \Omega}{\partial z^2} = 0 \quad (1)$$

The complex characteristic functions Φ and φ both satisfy Eq. (1) here and can be related to each other by

$$\frac{\partial^2 \Phi}{\partial z^2} = \varepsilon^2 \varphi \quad (2)$$

Here, ε is a small parameter given by $\varepsilon^2 = (h/R)[12(1 - \nu^2)]^{-1/2}$, where h and R is the thickness and radius of the horizontal brace, ν is Poisson's ratio. Then, the expression of dimensionless complex displacements u, v , and w , stress functions χ_z, χ_θ , and ζ can be given in terms of Φ and φ by

$$\begin{cases} \varepsilon^2 u = \frac{\partial}{\partial z} \left(\frac{\partial^2 \Phi}{\partial \theta^2} \right) & \varepsilon^2 v = -\frac{\partial^3 \Phi}{\partial \theta^3} & w = -\frac{\partial^2 \Phi}{\partial \theta^2} + i\varphi \\ \varepsilon^2 \chi_z = -i \frac{\partial}{\partial z} \left(\frac{\partial^2 \Phi}{\partial \theta^2} \right) & \varepsilon^2 \chi_\theta = -i \frac{\partial^3 \Phi}{\partial \theta^3} & \zeta = -i \frac{\partial^2 \Phi}{\partial \theta^2} + \varphi \end{cases} \quad (3)$$

Moreover, the dimensionless load parameter corresponding to tension load T can be defined as $\sigma_T = T / (2\pi R h \sigma_F)$ and the dimensionless characteristic functions mentioned above are given as follows,

$$\begin{cases} (\bar{u}, \bar{v}, \bar{w}) = \frac{\sigma_F R}{E} (u, v, \varepsilon^{-2} w) \\ (\bar{\chi}_z, \bar{\chi}_\theta, \bar{\zeta}) = \sigma_F R^2 h^2 \varepsilon^2 (\chi_z, \chi_\theta, \varepsilon^{-2} \zeta) \end{cases} \quad (4)$$

Here, E is Young's modulus, σ_F is yield stress of the material and parameters with an overbar denotes dimensional quantity.

According to the research done by Nicholson [15], the complete solution of cracked cylindrical shell composed by the elementary solutions and the solution, Φ_c , incurred by the existence of the crack. Then, the complete solution Φ_c to the problem of brace with a circumferential through crack at the boundary presented in this research can be obtained as

$$\Phi_c = \Phi_b + \Phi_s \quad (5)$$

Here, Φ_b refers to the elementary solutions and Φ_s refers to the solution incurred by the existence of the crack. Here, the elementary solutions to the proposed model in this research can include the splitting force solution, rigid-body motion (for which stresses disappear) solution and null solution (for which displacements disappear). Then, the elementary solution can be expressed as

$$\frac{\partial^2 \Phi_b}{\partial \theta^2} = \left\{ 0.5i \left[1 + i\varepsilon^2 (2 + \mu) \right] \theta^2 + (1 + i\varepsilon^2 \mu) (0.5\varepsilon^2 z^2 - i) \right\} \sigma_T + ia - \varepsilon b z + i c c \cos \theta + \varepsilon d z \cos \theta \quad (6)$$

Here, a, b, c, d are unknown constants.

In order to simplify the treatment of the governing equations of the proposed theoretical model, expressions for the values of the stress functions in terms of prescribed edge load T_z, T_θ, V and M_n acting on the edge $z = 0$ can be obtained by Eq. (7) for there is a static-geometric analogy between displacements and stress functions.

$$\begin{cases} \varepsilon^2 \chi_z = \sin \theta \int_0^\theta (T_\theta \sin \eta + \varepsilon^2 V \cos \eta) d\eta + \cos \theta \int_0^\theta (T_\theta \cos \eta - \varepsilon^2 V \sin \eta) d\eta - \int_0^\theta T_z d\eta \\ \varepsilon^2 \chi_\theta = \sin \theta \int_0^\theta (T_z + \varepsilon^2 M_n) \sin \eta d\eta + \cos \theta \int_0^\theta (T_z + \varepsilon^2 M_n) \cos \eta d\eta - \int_0^\theta T_z d\eta \end{cases} \quad (7)$$

Here, η refers to the infinitesimal angle of the cracked section. As the circumferential through crack is assumed located at the boundary of the brace, the cross section $z = 0$ is the border form the condition of symmetry. Shown as in Fig. 2, the cracked section has been divided into circumferential through crack zone, tensile plastic zone, elastic zone and compressive plastic zone in this research.

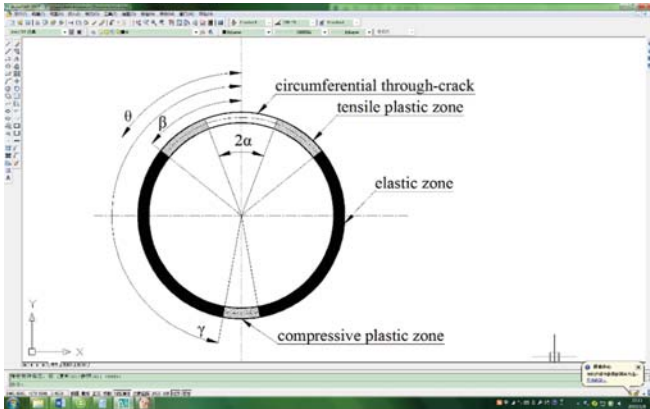


Fig. 2. Cracked section of the brace of SEMI

Here on the cracked section, opening angle of the circumferential through-crack equals to 2α , the tensile zone equals to $\beta-\alpha$, the elastic zone equals to $\gamma-\beta$, and the compressive plastic zone equals to $\pi-\gamma$. The boundary conditions can be obtained by means of methods given by Sanders [17]. Those and the displacement conditions are given as follows,

$$\begin{cases} T_z = T_\theta = V = M_n = 0 & (0 \leq \theta < \alpha) \\ v = V = M_n = 0; T_z = 1 & (\alpha \leq \theta < \beta) \\ u = v = w = \frac{\partial w}{\partial z} = 0 & (\beta \leq \theta < \gamma) \\ v = V = M_n = 0; T_z = -1 & (\gamma \leq \theta \leq \pi) \end{cases} \quad (8)$$

Then, by inputting the Eq. (3) and Eq. (7) into the boundary conditions mentioned above, the governing equations can be obtained in terms of the characteristic function Φ and φ as

$$\begin{cases} R \left\{ i \frac{\partial}{\partial z} \left(\frac{\partial^2 \Phi_c}{\partial \theta^2} \right) \right\} = 0 \\ R \left\{ i \frac{\partial^2 \Phi_c}{\partial \theta^2} \right\} = 0 \end{cases} \quad (0 \leq \theta < \alpha) \quad (9)$$

$$\begin{cases} R \left\{ \frac{\partial^2 \Phi_c}{\partial \theta^2} \right\} = 0 \\ R \left\{ i \frac{\partial^2 \Phi_c}{\partial \theta^2} \right\} = -\cos(\theta - \alpha) - 0.5(\theta - \alpha)^2 + 1 \end{cases} \quad (\alpha \leq \theta < \beta) \quad (10)$$

$$\begin{cases} R \left\{ \frac{\partial}{\partial z} \left(\frac{\partial^2 \Phi_c}{\partial \theta^2} \right) \right\} = 0 \\ R \left\{ \frac{\partial^2 \Phi_c}{\partial \theta^2} \right\} = 0 \end{cases} \quad (\beta \leq \theta < \gamma) \quad (11)$$

$$\begin{cases} R \left\{ \frac{\partial^2 \Phi_c}{\partial \theta^2} \right\} = 0 \\ R \left\{ i \frac{\partial^2 \Phi_c}{\partial \theta^2} \right\} = -\pi \sigma_T \theta - \cos \theta - G_1 \cos \theta + 0.5(\pi - \theta)^2 - 1 + G_2 \end{cases} \quad (\gamma \leq \theta \leq \pi) \quad (12)$$

The symbol $R\{\}$ denotes the real part of the expression in brackets and the subscript c means that the expression are in terms of the complete characteristic functions.

With Eq. (5-6) and Eq. (9-12), the particular integral Φ_s at the boundary incurred by the existence of the crack turns into

$$\begin{cases} R \left\{ i \frac{\partial}{\partial z} \left(\frac{\partial^2 \Phi_s}{\partial \theta^2} \right) \right\} = -\varepsilon b_l + \varepsilon d_l \cos \theta \\ R \left\{ i \frac{\partial^2 \Phi_s}{\partial \theta^2} \right\} = a_R + c_R \cos \theta + (1 - 0.5\theta^2) \sigma_T \end{cases} \quad (0 \leq \theta < \alpha) \quad (13)$$

$$\begin{cases} R \left\{ \frac{\partial^2 \Phi_s}{\partial \theta^2} \right\} = a_l + c_l \cos \theta \\ R \left\{ i \frac{\partial^2 \Phi_s}{\partial \theta^2} \right\} = a_R + c_R \cos \theta + (1 - 0.5\theta^2) \sigma_T - \cos(\theta - \alpha) - 0.5(\theta - \alpha)^2 + 1 \end{cases} \quad (\alpha \leq \theta < \beta) \quad (14)$$

$$\begin{cases} R \left\{ \frac{\partial^2 \Phi_s}{\partial \theta^2} \right\} = a_l + c_l \cos \theta \\ R \left\{ \frac{\partial}{\partial z} \left(\frac{\partial^2 \Phi_s}{\partial \theta^2} \right) \right\} = \varepsilon b_R - \varepsilon d_R \cos \theta \end{cases} \quad (\beta \leq \theta < \gamma) \quad (15)$$

$$\begin{cases} R \left\{ \frac{\partial^2 \Phi_s}{\partial \theta^2} \right\} = a_l + c_l \cos \theta \\ R \left\{ i \frac{\partial^2 \Phi_s}{\partial \theta^2} \right\} = a_R + (c_R - G_1) \cos \theta - \cos \theta + 0.5(\pi - \theta)^2 (\gamma \leq \theta \leq \pi) \\ + [\pi(\pi - \theta) + (0.5\theta^2 - 1)] \sigma_T + G_2 - 1 \end{cases} \quad (16)$$

Here, the subscripts R and I refer to the real and imaginary parts of these constants. Furthermore, any solution to the Eq. (1) satisfy the conditions [10]

$$\int_0^\pi \frac{\partial^2 \Phi_s}{\partial \theta^2} \Big|_{z=0} d\theta = \int_0^\pi \frac{\partial^2 \Phi_s}{\partial \theta^2} \Big|_{z=0} \cos \theta d\theta = 0 \quad (17)$$

$$\frac{\partial}{\partial z} \left(\frac{\partial^2 \Phi_s}{\partial \theta^2} \right) = -i^{\frac{3}{2}} \varepsilon \frac{\partial^2}{\partial \theta^2} \left(\frac{\partial^2 \Phi_s}{\partial \theta^2} + \frac{1}{2} \Phi_s \right) \quad (18)$$

Now put

$$\frac{\partial^2 \Phi_s}{\partial \theta^2} \Big|_{z=0} = F(\theta) \quad (19)$$

And following the Eq. (17) and Eq. (18) to get

$$\int_0^\pi (F'' + F) d\theta = \int_0^\pi F'' \cos \theta d\theta = 0 \quad (20)$$

$$\frac{\partial}{\partial z} \left(\frac{\partial^2 \Phi_s}{\partial \theta^2} \right) \Big|_{z=0} = -i^{\frac{3}{2}} \varepsilon \left(F'' + \frac{1}{2} F \right) \quad (21)$$

Additionally, by using Eq. (20) and Eq. (21), the Eq. (13-16) can be expressed in the equivalent form as follows,

$$\begin{cases} F_R = -(a_R + 2\sqrt{2}b_l) - (c_R + 2\sqrt{2}d_l) \cos \theta \\ + S \cos \frac{\theta}{\sqrt{2}} - (0.5\theta^2 - 1) \sigma_T \quad (0 \leq \theta < \alpha) \\ F_I = -(a_R + c_R \cos \theta) - (0.5\theta^2 - 1) \sigma_T \end{cases} \quad (22)$$

$$\begin{cases} F_R = a_I + c_I \cos \theta \\ F_I = -(a_R + c_R \cos \theta) - (0.5\theta^2 - 1)\sigma_T \quad (\alpha \leq \theta < \beta) \\ \quad + \cos(\theta - \alpha) + 0.5(\theta - \alpha)^2 - 1 \end{cases} \quad (23)$$

$$\begin{cases} F_R = a_I + c_I \cos \theta \\ F_I = 2\sqrt{2}b_R - a_I + (2\sqrt{2}b_R - c_I) \cos \theta \quad (\beta \leq \theta < \gamma) \\ \quad + 2\sqrt{2}P \cos \frac{\theta - \beta}{\sqrt{2}} + 2\sqrt{2}Q \cos \frac{\theta - \beta}{\sqrt{2}} \end{cases} \quad (24)$$

$$\begin{cases} F_R = a_I + c_I \cos \theta \\ F_I = -a_R - (c_R - G_1) \cos \theta - [\pi(\pi - \theta) + (0.5\theta^2 - 1)]\sigma_T \quad (\gamma \leq \theta \leq \pi) \\ \quad + \cos \theta - 0.5(\pi - \theta)^2 - G_2 + 1 \end{cases} \quad (25)$$

Then, the governing equations mentioned above got 15 unknown constants including the five real constants of integration of S , P , Q , G_1 and G_2 , the two undetermined parameters of the cracked section of brace β and γ , and eight real and imaginary parts of the constants a_R , b_R , c_R , d_R , a_I , b_I , c_I , d_I . Additionally, the continuity of the displacements and stress functions at the cracked section implies that F_R , F_R' , F_R'' , at α and F_I , F_I' , F_I'' , F_I''' at β and γ should be continuous (F_I , F_I' , F_I'' at α are continuous from simply checking), from which eleven equations can be got. Moreover, four more equations can be found for the real parts and the imaginary parts equal to zero in Eq. (20). There are thus 15 conditions to determine the 15 constants and all the constants can be finally determined by means of algebraic methods. And results for the 15 constants follow from

$$a_I = \frac{1}{\pi} \left[S \left(\frac{\alpha}{2} \cos \frac{\alpha}{\sqrt{2}} - \frac{\sqrt{2}}{2} \sin \frac{\alpha}{\sqrt{2}} \right) - \frac{1}{3} \alpha^3 \sigma_T \right]$$

$$b_I = \frac{1}{2\sqrt{2}} \left[-a_R - a_I + 0.5S \cos \frac{\alpha}{\sqrt{2}} - 0.5\alpha^3 \sigma_T \right]$$

$$c_I = \frac{1}{2\pi \cos \alpha} \left[S \cos \frac{\alpha}{\sqrt{2}} (\alpha - \sin \alpha \cos \alpha) - 2(2\alpha \cos^2 \alpha - \alpha - \sin \alpha \cos \alpha) \sigma_T \right]$$

$$d_I = \frac{1}{2\sqrt{2} \cos \alpha} \left(-c_R \cos \alpha - c_I \cos \alpha + 0.5S \cos \frac{\alpha}{\sqrt{2}} + \sigma_T \right)$$

$$a_R = \frac{(\pi - \beta)A}{\pi} + \frac{P}{\pi} \left[2 \sin \frac{\gamma - \beta}{\sqrt{2}} + \sqrt{2}(\pi - \gamma) \right] + \frac{2Q}{\pi} \left(1 - \cos \frac{\gamma - \beta}{\sqrt{2}} \right) + \frac{\sigma_T}{\pi} \left[\frac{1}{6} (2\pi^3 - 2\gamma^3 - \beta^3) - \pi\gamma(\pi - \gamma) \right] + \frac{1}{6\pi} \left[(\beta - \alpha)^3 + 2(\pi - \gamma)^3 \right]$$

$$b_R = \frac{\sqrt{2}}{4} (A - a_R + a_I)$$

$$c_R = -(\beta - \gamma + \sin \beta \cos \beta - \sin \gamma \cos \gamma) \frac{C}{\pi} + (\pi - \gamma - \sin \gamma \cos \gamma) \frac{G_1}{\pi} + \left(\sqrt{2} \sin \gamma - \sqrt{2} \sin \beta \cos \frac{\gamma - \beta}{\sqrt{2}} - \cos \beta \sin \frac{\gamma - \beta}{\sqrt{2}} \right) \frac{4P}{\pi} + \frac{2}{\pi} (\sin \alpha - \sin \beta - \sin \gamma) - \left(\sin \gamma + \sqrt{2} \sin \beta \sin \frac{\gamma - \beta}{\sqrt{2}} - \cos \beta \cos \frac{\gamma - \beta}{\sqrt{2}} \right) \frac{4Q}{\pi} - (\sin \gamma - \sin \beta) \frac{2\sigma_T}{\pi} + \frac{(\beta - \alpha) \cos \alpha + \cos \beta \sin(\beta - \alpha) - \sin \gamma \cos \gamma - \gamma}{\pi} + 1$$

$$d_R = \frac{\sqrt{2}}{4} (C - c_R + c_I)$$

$$A = -\sqrt{2} \left(P \cos \frac{\gamma - \beta}{\sqrt{2}} + Q \sin \frac{\gamma - \beta}{\sqrt{2}} \right) - 0.5\beta^2 \sigma_T + 0.5(\beta - \alpha)^2$$

$$C = \frac{-\beta \sigma_T + \sin(\beta - \alpha) + \beta - \alpha}{\sin \beta}$$

$$G_1 = \frac{C \cos \gamma + \sqrt{2}P - \sigma_T - \cos \gamma - 1}{\cos \gamma}$$

$$G_2 = -A - \sqrt{2}P - [\pi(\pi - \gamma) + 0.5\gamma^2] \sigma_T - (\pi - \gamma)^2$$

$$P = Q \cot \frac{\gamma - \beta}{\sqrt{2}} - \frac{\beta \sigma_T + \beta - \alpha}{\sin \frac{\gamma - \beta}{\sqrt{2}}}$$

$$Q = -(\pi - \gamma) \sigma_T - \pi + \gamma$$

$$S = \frac{2(\sin \alpha - \alpha \cos \alpha) \sigma_T}{\sqrt{2} \cos \alpha \sin \frac{\alpha}{\sqrt{2}} - \sin \alpha \cos \frac{\alpha}{\sqrt{2}}}$$

In order to obtain the unknown parameters of the cracked section β and γ which can the tensile plastic zone, elastic zone and compressive plastic zone of the cracked section with given α and σ_T , the following simultaneous transcendental equations should be used.

$$\begin{cases} B_1 \sigma_T - N_1 = 0 \\ B_2 \sigma_T - N_2 = 0 \end{cases} \quad (26)$$

Where

$$B_1 = (\sin \beta + \beta \cos \beta) \sin \frac{\gamma - \beta}{\sqrt{2}} + \sqrt{2} \left(\pi - \gamma + \beta \cos \beta \cos \frac{\gamma - \beta}{\sqrt{2}} \right) \sin \beta$$

$$B_2 = [(\pi - \gamma) \cos \gamma - \sin \gamma] \sin \frac{\gamma - \beta}{\sqrt{2}} - \sqrt{2} \left[(\pi - \gamma) \cos \frac{\gamma - \beta}{\sqrt{2}} + \beta \right] \sin \gamma$$

$$N_1 = [\sin \beta - \sin \alpha + (\beta - \alpha) \cos \beta] \sin \frac{\gamma - \beta}{\sqrt{2}} - \sqrt{2} \left[\pi - \gamma - (\beta - \alpha) \cos \frac{\gamma - \beta}{\sqrt{2}} \right] \sin \beta$$

$$N_2 = [\sin \gamma - (\pi - \gamma) \cos \gamma] \sin \frac{\gamma - \beta}{\sqrt{2}} + \sqrt{2} \left[(\pi - \gamma) \cos \frac{\gamma - \beta}{\sqrt{2}} - \beta + \alpha \right] \sin \gamma$$

Then, the displacements on the crack are obtained can be obtained from the above results and the dimensionless crack tip opening displacement (CTOD) subjected to the splitting force can be expressed as

$$\delta = \frac{\sqrt{2}}{4}^{-1} \left[-A + C \cos \alpha - (0.5\alpha^2 + 1) \sigma_T \right] \quad (27)$$

Further, for the present load circumstance the full plastic condition on the cracked section is

$$\sigma_T = \frac{2}{\pi} \left[\arccos(0.5 \sin \alpha) - 0.5\alpha \right]$$

And

$$\beta = \gamma = 0.5(\pi + \alpha + \pi \sigma_T)$$

SOLUTIONS

The theoretical model proposed in the research is aiming to calculate the mechanical characteristic of the cracked damaged brace with a circumferential through crack lies at its boundary when the SEMI subjected to beam wave. At the beginning of the solutions, basic parameters such as parameters of the brace of SEMI, angle of the circumferential through crack and the splitting force should be input for the solution for plastic zones, elastic zones and CTOD of the cracked section.

As it's hard to find explicit solution from Eq. (26) to obtain the unknown parameters of the cracked section β and γ , numerical method should be used in this research. Firstly, assume an initial β_0 and initial γ_0 to start the calculation. And then, define two more parameters F and λ according to Eq. (26) following from

$$F = [B_1(\beta_0, \gamma_0)\sigma_T - N_1(\beta_0, \gamma_0)]^2 + [B_2(\beta_0, \gamma_0)\sigma_T - N_2(\beta_0, \gamma_0)]^2$$

$$\lambda = \frac{F(\beta_0, \gamma_0)}{\left[\frac{F(\beta_0 + 0.01, \gamma_0) - F(\beta_0, \gamma_0)}{0.01\beta_0} \right]^2 + \left[\frac{F(\beta_0, \gamma_0 + 0.01) - F(\beta_0, \gamma_0)}{0.01\gamma_0} \right]^2}$$

To guarantee to precision of the solution, verification is needed to see if $|F| < \zeta$ is satisfied, where ζ is a small specified quantity. If $|F| < \zeta$ does not appear, the assumed initial β_0 and initial γ_0 should be modified as

$$\beta = \beta_0 - \lambda \frac{F(\beta_0 + 0.01, \gamma_0) - F(\beta_0, \gamma_0)}{0.01\beta_0}$$

$$\gamma = \gamma_0 - \lambda \frac{F(\beta_0, \gamma_0 + 0.01) - F(\beta_0, \gamma_0)}{0.01\gamma_0}$$

After $|F| < \zeta$ is satisfied, the solution for plastic zones of the cracked horizontal brace is done. Then, the output of β and γ could be used to determine the 15 unknown parameters $a_p, b_p, c_p, d_p, a_R, b_R, c_R, d_R, A, C, G_p, G_R, P, Q, S$ and the crack tip opening displacement (CTOD) can be obtained from Eq. (27) too. Until now, the solutions of the mechanical characteristics of the cracked damaged brace of SEMI with a circumferential through crack that lies at the boundary are done.

EXAMPLES

To illustrate the proposed model with examples, a typical new-generation SEMI that suitable for drilling operations worldwide has been selected to analyze the variation tendency of the cracked brace's parameters. The geometrical dimensions of the main components of the SEMI are listed in Table 1.

As the ocean wave vary greatly under different wave frequencies. The wave frequency was considered as varying from 0.1 to 1.5 rad/s to reflect the actual wave frequencies most commonly seen in ocean areas, and an increment of

Tab. 1. Main geometrical dimensions of the SEMI

Component	Dimension(m)
Pontoon Length	114.07
Pontoon width	20.12
Pontoon Height	8.54
Distance between pontoons	58.6
Column length	17.4
Column width	17.4
Column height	21.4
Distance between longitudinal columns	58.6
Distance between transversal columns	58.6
Deck length	114.4
Deck width	74.4
Deck height	38.6

0.05 rad/s was used in the numerical simulations. In addition, the ocean wave was assumed to be a combination of infinite regular waves in this research, and the Jonswap spectrum was used to characterize random waves in the ocean.

Based on the numerical calculation, the response amplitude operator (RAO) of the swaying, surging and rolling of the SEMI under beam wave have been obtained, shown as in Fig. 3, Fig. 4 and Fig. 5. The RAO results obtained by the numerical calculation coincide with the white noise test and regular wave test under the beam wave.

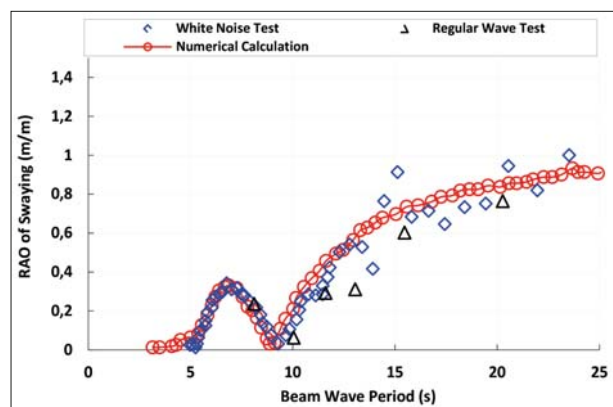


Fig. 3. RAO of swaying of the SEMI under beam wave

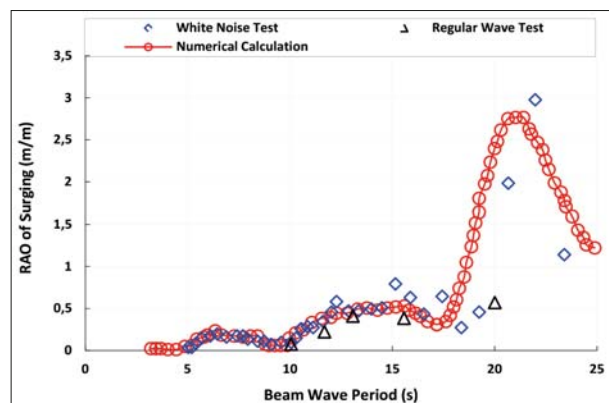


Fig. 4. RAO of surging of the SEMI under beam wave

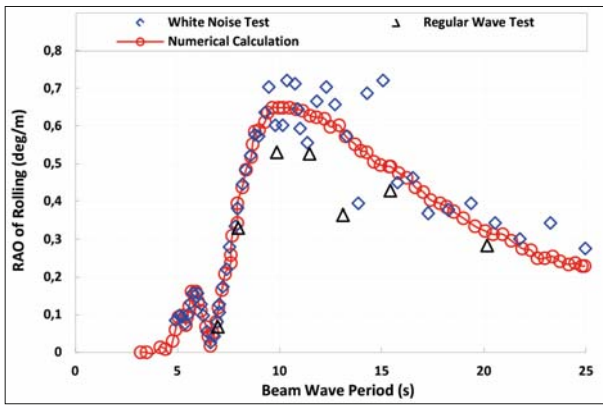


Fig. 5. RAO of rolling of the SEMI under beam wave

The circumferential through crack is assumed to be located at the boundary of the selected SEMI's brace and geometrical dimensions of the brace are listed in Table 2.

Tab. 2. Main geometrical dimensions of the brace

Component	Dimension
Quantity of the brace	4
Diameter of the brace	2.45m
Thickness of the brace	0.1m
Poisson's ratio	0.3
Young's modulus	210GPa
Yield stress of the material	400MPa

Different splitting forces could be loaded on the brace when the SEMI encounter different wave frequencies. According to the response amplitude operator (RAO) and long-term response (LTR) of the splitting force loaded on the chosen SEMI, shown as in Fig. 5 and Fig. 6, the largest splitting force loaded on the brace is 65×10^6 N when the beam wave frequency comes to 0.66 rad/s.

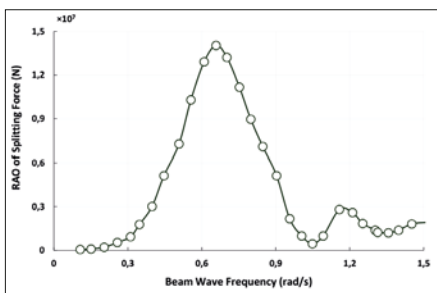


Fig. 6. RAO of splitting force loaded on the brace under beam wave

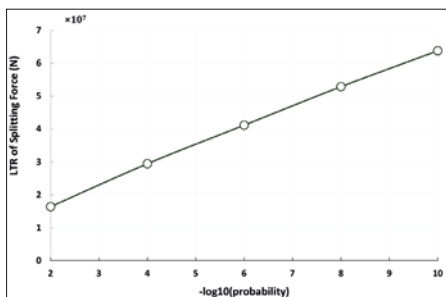


Fig. 7. LTR of splitting force loaded on the brace under beam wave

In order to estimate the variation tendencies of the crack tip opening displacement of the cracked section of brace, the crack tip opening displacement (CTOD) of crack under different splitting forces have been obtained by the method proposed in this research. Additionally, the initial circumferential through cracks have been assumed to be varying from $\pi/24$ to $10\pi/24$ with incensement of $\pi/24$ in this research to estimate the crack tip opening displacement of the cracked section under different circumferential through cracks. Shown as in Fig. 8, the values of the CTOD on the cracked section of brace increase smoothly when the cracked damaged brace loaded small splitting force and then increase dramatically when the brace loaded larger splitting forces. In addition, the cracked section of the brace has a larger CTOD while the brace locates a greater circumferential through crack at its boundary.

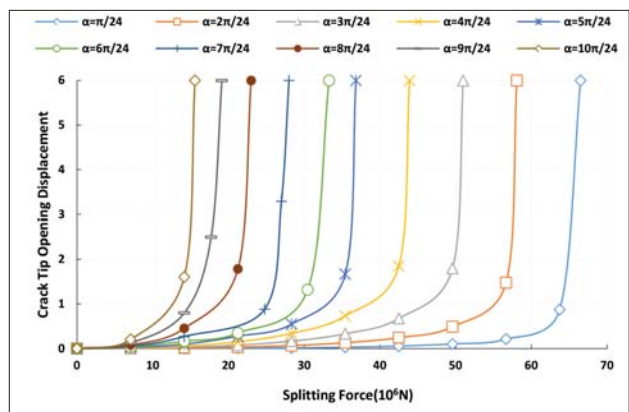


Fig. 8. Variations of crack tip opening displacement of the cracked section of brace

The variation tendency of the tensile plastic zone ($\beta-\alpha$) on the cracked section of MESI's brace is shown in Fig. 9. The tensile plastic zone on the cracked section increase with the splitting force loaded on the circumferential through crack-damaged brace and the values of crack's angle smoothly. Moreover, the cracked section of the brace with greater circumferential through crack has earlier appearance of the compressive plastic zone (parameter $\gamma < \pi$).

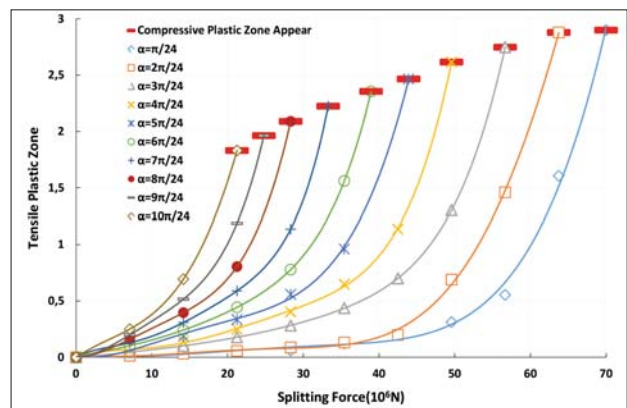


Fig. 9. Variations of tensile plastic zone on the cracked section of brace

The variation tendency of the elastic zone ($\gamma-\beta$) on the cracked section of MESI's brace is shown in Fig. 9. Contrary to the variation tendency of the tensile plastic zone on the cracked section, the elastic zone on the cracked section decrease with

the splitting force loaded on the brace and the values of crack's angle. In addition, the cracked section of the brace with greater circumferential through crack has sharper decrease with the splitting force.

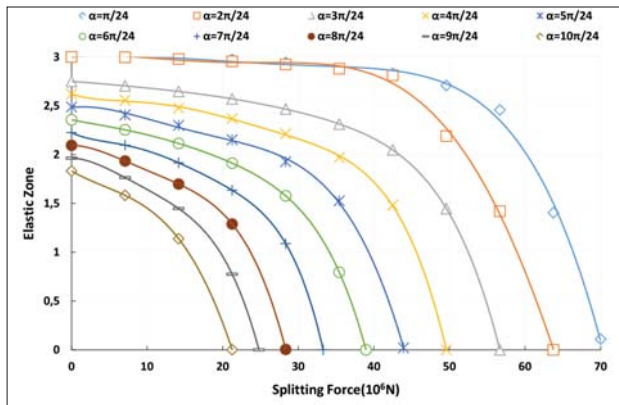


Fig. 10. Variations of elastic zone on the cracked section of brace

The cracked section of the brace would be in full plastic condition when the brace loaded a larger splitting force. Shown as in Fig. 11, the tensile plastic zone of the cracked section is much larger than the compressive plastic zone. However, the tensile plastic zone decrease with the angle of the circumferential through crack while the compressive plastic zone increase with the angle of the circumferential through crack of the brace smoothly.

Additionally, the larger circumferential through crack of the brace locates, the smaller splitting force has been loaded on the crack-damaged brace when the cracked section of brace is in full plastic condition.

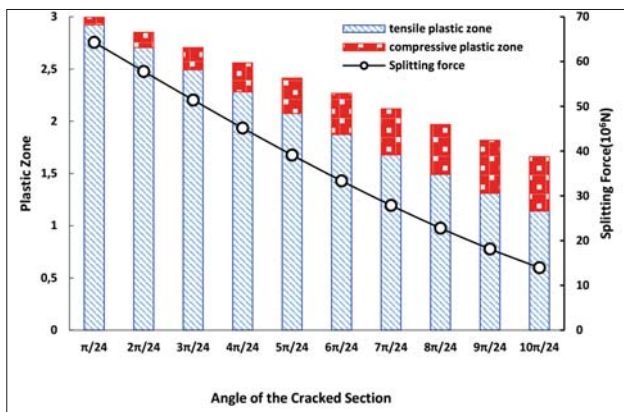


Fig. 11. Variations of tensile plastic zone and compressive plastic zone when the cracked section is in full plastic condition

CONCLUSIONS

An elastic-plastic method to analyze the variations of the crack tip opening displacement, elastic zone and plastic zone of the cracked section of the horizontal brace under beam wave has been proposed in this article. The brace of SEMI is assumed to be located a circumferential through crack at its boundary in this research. In addition, a typical new-generation SEMI that is in practical use was selected to analyze the variation tendency of the cracked brace's

parameters using the proposed model and some variation tendency has been got:

- (1) The values of the CTOD and tensile plastic zone on the cracked section of brace increase dramatically after a smoothly increase with the splitting force and circumferential through crack. In addition, the cracked section of the brace with greater circumferential through crack has earlier appearance of the compressive plastic zone.
- (2) The elastic zone on the cracked section decrease with the splitting force loaded on the brace and the values of crack's angle. In addition, the cracked section of the brace with greater circumferential through crack has sharper decrease with the splitting force.
- (3) The tensile plastic zone has a contrary variation tendency to the compressive plastic zone that increase with the angle of the crack of the brace smoothly when the cracked section is in full plastic condition. Moreover, the larger circumferential through crack of the brace locates, the smaller splitting force has been loaded on the crack-damaged brace.

ACKNOWLEDGMENT

The authors would like to acknowledge the support by scientific research starting project of SWPU (No. 2017QHZ010), China.

REFERENCES

1. Colin, H., Espen, F., Martyn, T. (2014). *Worldwide Offshore Accident Databank*, Det Norske Veritas, Oslo.
2. Moan, T. (2009). *Development of accidental collapse limit state for offshore structures*. *Structural Safety*, 31, 124–135.
3. Zaron, E., Fitzpatrick, P., Patrick J. (2015). *Initial evaluations of a Gulf of Mexico/Caribbean ocean forecast system in the context of the deep-water horizontal disaster*. *Frontiers of Earth Science*, 9, 605–636.
4. Giovani, D., Mariana, S. (2013). *Risk Based in Inspection Applied to a Semi-Submersible Platform*, Offshore Technology Conference, Rio de Janeiro, Brazil.
5. Sanders, J. L. (1987). *Dugdale model for circumferential through-cracks in pipes loaded by bending*. *International Journal of Fracture*, 34(1), 71–78.
6. Fei, W., Zheng, L. (2016). *Analytical solution for crack growth of semi-submersible platform's horizontal brace*. *Journal of Engineering Research*. 4(1), 146–158.
7. Brighenti, R. (2000). *Surface cracks in shells under different hoop stress distributions*, *International Journal of Pressure Vessels and Piping*, 77(9), 503–509.

8. Fei, W., Zheng, L. (2017). *Effects of wave loads on the strength of SEMI's horizontal brace*. Proceedings of the Institution of Civil Engineers: Maritime Engineering, 170(2), 163–172.
9. Alexandrov, S., Zerbst, U., Schwalbe, H. (1998). *Limit load solution for cracked tubular T-joints loaded in tension*. Fatigue & Fracture of Engineering Materials & Structures, 21(10), 1249–1257.
10. Lie, S., Chiew, S., Lee, C. (2004). *Fatigue Performance of Cracked Tubular T Joints under Combined Loads*. Journal of Structure Engineering, 130(4), 572–581.
11. Maier, G. (1985). *Case Histories in Offshore Engineering*, Springer Vienna Publishers.
12. Reason, J. (1997). *Managing the Risks of Organizational Accidents*, Ashgate Publishers.
13. Inge, L., Odd, O. (2005) *Risk assessment of loss of structural integrity of a floating production platform due to gross errors*, Marine Structures, 17(7), 551–573.
14. Moan, T., Berge, S., Holthe, K. (1981). *Analysis of the fatigue failure of the Alexander L. Kielland*. ASME Winter Annual Meeting, Washington, DC.
15. Nicholson, J.W., Weidman, S.T., Simmonds, J.G. (1983). *Sanders' energy-release rate integral for a circumferentially cracked cylindrical shell*. Journal of Applied Mechanics, 50(2), 373–378.
16. Sanders, J. L. (1972). *Closed form solution to the semi-infinite cylindrical shell problem*. Rotterdam Dam: Delft University Press.
17. Sanders, J. L. (1980). *On stress boundary conditions in shell theory*. Journal of Applied Mechanics, 47(1), 202–204.

CONTACT WITH THE AUTHOR

Fei Wang

e-mail: wangfei_swpu@126.com
 Southwest Petroleum University
 Xindu Road, 610500 Chengdu
CHINA

Xiong Deng

e-mail: hanshuichun1@126.com
 Southwest Petroleum University
 Xindu Road, 610500 Chengdu
CHINA

Yuqiong Li

e-mail: 472270582@qq.com
 School of Materials Science and Engineering
 Southwest Petroleum University
 Xindu Road no. 8 , 610500 Chengdu
CHINA

STUDY OF LOSSES AND ENERGY EFFICIENCY OF HYDROSTATIC DRIVES WITH HYDRAULIC CYLINDER

Grzegorz Skorek

Gdynia Maritime University, Poland

ABSTRACT

Energy efficiency of hydrostatic transmissions, and especially efficiencies of drives with motor speed controlled by throttle, as well as efficiency of hydraulic servomechanisms can in fact be higher than the efficiency values most frequently given by the respective literature in this field. With the progress achieved in recent years in the development of hydraulic systems it is becoming necessary to develop methods for precise energy efficiency calculation of such systems. It is difficult to imagine that more and more, better and better machines and control elements could be used without the possibility of a mathematical tool at our disposal to enable an accurate analysis and assessment of behavior of the system in which such machines and control elements have been applied. The paper discusses energy savings using mathematical model of losses in elements, the energy efficiency of the system. There are possibilities to reduce energy losses in proportional control systems (in the pump, in the throttle control unit, especially in the cylinder), and thus to improve the energy efficiency of the throttling manifold. The considerations allow for comparison of the loss power resulting from the applied hydraulic control structure of the hydraulic cylinder and the power consumed by the pump from the electric motor that drives it, the power necessary to provide pump-driven hydraulic cylinder. The article shows the impact on the output (useful) power consumed in the considered systems, and the impact on the power consumed of the loss power in the individual elements. The paper presents also formulas of loss power, formulas of energy efficiency connected with investigated hydrostatic drives, two schematic diagrams of hydraulic systems, their principle of operation and problems of studying losses in elements and energy efficiency characteristics of systems consisting of a feed assembly, control set and cylinder. It also includes a subject matter connected with an energy loss power of hydrostatic systems with hydraulic cylinder controlled by proportional directional control valve. Diagrams of loss power of two hydraulic systems worked at the same parameters of speed and load of a cylinder, which were different due to structure and ability of energy saving, were presented and compared.

Keywords: energy losses, energy efficiency, hydrostatic system, control structures, proportional directional control valve, cylinder

INTRODUCTION

The hydrostatic systems play a very important role in modern machines. A great number of the machines constructed nowadays has more or less developed hydrostatic or electric-hydrostatic drive systems and in many cases those systems are the most important parts of the machines. Component elements – hydraulic linear motors (cylinders) – are widely applied in machines used on land and aboard ships. Unquestioned advantages of cylinders are: capability of performing the translational motion, reliability, simple

construction, the effective force to weight ratio [2]. A control system with a directional control servo valve or a proportional directional throttling control valve, controlling a linear hydraulic motor (cylinder) is used in the ship steering gear drive, in the controllable pitch propeller control, in the variable capacity pump control system for hydraulic deck equipment motors or fixed pitch propellers in small ships (e.g. ferries) [1].

The electro-hydraulic system as one of the fundamental components has been applied in many other equipment too, such as construction machines, agricultural machines, and

airplanes. Common to these applications is that high power is often required to perform the desired work, for example moving material or lifting heavy weights. The power for such drives is often generated by a centralized source, usually an internal combustion engine or a high power electric machine. Using fluid power systems the power is easily distributed via hydraulic lines to either linear or rotary drives. It is estimated that by the year 2000, the world market of electro-hydraulics is about 30–35 billion dollars per year, and is in steady growth. Meanwhile, energy saving concerning a hydraulic system has been raised with the numerical application of heavy equipment. The electro-hydraulic system mounted equipment often works around the clock and outputs high power in handling heavy loads. The energy consumption and the waste gas emission of such systems therefore stays high. Take one of the most popular construction machines, 20-t load sensing controlled hydraulic excavator as an example. Such excavator type usually requires a diesel engine of more than 110 kW, which consumes at least 33 liters fuel in an hour. The amount of NOx and CO emitted by this machine is considerable. But only 30% of the consumed energy is used for moving loads. While more than 60% of the energy is consumed in power losses and driving of hydraulic systems. Therefore, even a small improvement in the hydraulic system efficiency will have a significant impact on the total energy efficiency of the machine [16].

There are uninvestigated areas connected with behavior of elements in hydraulic systems with different structures. Unawareness of proportions of the energy, volumetric, pressure and mechanical losses in elements is often the case. Problems connected with energy efficiency are essential for improvement of functionality and quality of hydrostatic drive systems, characterized by unquestioned advantages but also by relatively low efficiency in comparison with other types of drive. Energy efficiency of hydrostatic transmissions, particularly those with throttling control of the motor speed, and also efficiency of the hydraulic servo-mechanism systems may be in fact higher than the values most often quoted in publications regarding the subject. At present, for instance, the efficiency of a system with a servovalve is still often presented incorrectly. Namely, the maximum efficiency of such a system (with ideal pump and hydraulic motor) is quoted to be equal to $\eta = 0,385$ at a motor supply pressure equal to $p = 2/3 p_{max}$. Such an approach leads to the use of higher than required pump unit, operation at lower efficiency, increase in costs of the system itself and its operating costs. In too low efficiency systems there is an increase in load, mainly in pump load, and this can lead to a greater risk of failure, the necessity of repair or replacement and also to decrease of operating life of the system. Too low system efficiency resulting most often from intensive throttling of liquid flow is also the source of quick deterioration of operating properties, mainly lubrication properties of hydraulic oil, due to too high operating temperature of the hydrostatic transmissions. Possibility of calculating the real value of the hydraulic system overall efficiency as a function of many parameters influencing it, becomes a tool of complete evaluation of the designed system quality [3].

The paper presents definitions of power losses and energy efficiencies occurring in two hydraulic systems. It compares laboratory investigated efficiencies of systems with cylinder proportional control and efficiency of the system with volumetric control by a variable capacity pump. Presented are also two schematic diagrams of these hydrostatic systems, their principle of operation and problems of studying losses in elements of systems consisting of a feed assembly, control set and cylinder. The analysis was performed comparing the selected parameters of operation of the hydraulic cylinder power lines of energy losses in the elements of these structures.

In searching for the energy saving solutions, computer-aided methods of calculating the energy efficiency of systems have been developed and improved.

The required speed v_M and load F_M of the driven machine are a result of its operation cycle and tasks to be performed. The driven machine current speed and load values are independent of the type and structure of the machine driving system.

The current speed and load of the hydrostatic system driven machine have a direct or indirect impact on the mechanical, volumetric and pressure losses in the hydraulic motor, pump and other elements of the system with a given motor speed control structure, the losses resulting also from the hydraulic oil viscosity.

Laboratory verification of energy savings was concerned with two hydraulic systems controlled with a proportional directional control valve supplied with a constant capacity pump:

- a) with overflow valve – constant pressure structure [$p=cte$] (Fig. 1),
- b) using a pressure-controlled overflow valve from the cylinders' inlet line – variable pressure structure [$p=var$] (Fig. 2).

The most popular solution is a system (Fig. 1) where a throttling control valve is fed by a constant capacity pump cooperating with an overflow valve. This system, working with a constant pressure, achieves a high energy efficiency value η only at the point of maximum motor load coefficient \bar{M}_M and maximum motor speed coefficient $\bar{\omega}_M$. The pressure drop in the cylinder balances the load acting on the hydraulic cylinder. The proportional throttling valve generates two pressure drops at the inlet and outlet of the cylinder. The pump in the constant pressure system ($p=cte$) must generate pressure before the overflow valve, which will not be less than the pressure required by the hydraulic cylinder. The cylinder, which is an executive element in the system, may require pressure depending on its load, changing from zero to nominal value. When it reaches the nominal value of the load, the pressure drop in the throttle slots of the manifold tends to zero.

The unit, which consists of a pump and an overflow valve in constant pressure system $p=cte$ is ready to supply the system at maximum pressure and maximum capacity. However, it is not usually used to such an extent that the cylinder at the moment is loaded with force which requires a lower than nominal pressure drop.

This system achieves high energy efficiency, equal to the efficiency of the system without the throttling control, only at the point with the maximum values of the load coefficient \bar{M}_M and the speed coefficient $\bar{\omega}_M$. With decreasing engine load, especially with engine speed dropping, the efficiency η decreases rapidly [6].

There are possibilities to reduce energy losses in proportional control systems (in the pump, in the throttle control unit and in the hydraulic cylinder, and thus to improve the energy efficiency of the throttling control valve.

The hydraulic drive system and the proportional control of the hydraulic cylinder can be supplied with a constant capacity pump cooperating with an overflow valve stabilizing a pressure in proportional directional control valve to the nominal pressure level (Fig. 1), or a pump cooperating with a pressure-controlled overflow valve at the inlet to the receiver – hydraulic cylinder. The variable pressure system $p=\text{var}$ (Fig. 2) allows for the reduction of losses in the pump, in the control unit and in the hydraulic cylinder.

In the variable pressure system $p=\text{var}$, the structural pressure losses and structural volume losses in the throttle control unit, mechanical losses in the cylinder and pump, and volume losses in the pump can be seriously reduced. The mathematical description of loss and energy efficiency is presented in the paper.

The variable pressure structure $p=\text{var}$ represents the system with a constant-capacity pump cooperating with an overflow valve controlled by the cylinder supply pressure (Fig. 2). It is a cost-effective solution for both the cylinder and the pump as well as the entire control system. Variable pressure system $p=\text{var}$ with control overflow valve SPS, the actual throttling valve discharge pressure to the inlet chamber of the cylinder, allows the pressure level in the pump discharge line to be adjusted to the prevailing load of the cylinder so as to limit the pressure loss in the discharge opening of the distributor liquid to the tank. In addition, this system maintains a constant piston speed independent of the load. This is a result of keeping practically constant pressure drop Δp_{DE1} in the throttle slit of the proportional distributor (proportional directional control valve) [15].

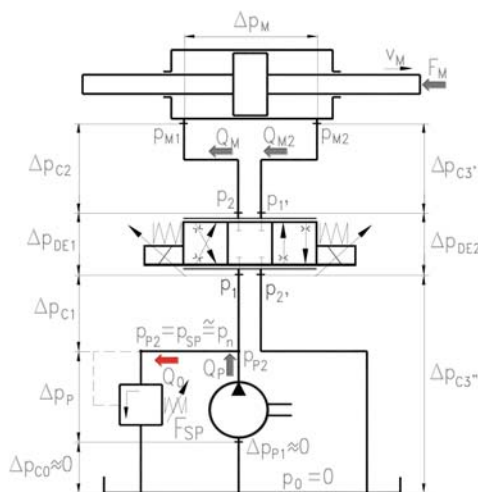


Fig. 1. Diagram of the test system fed at constant pressure – structure $p=\text{cte}$

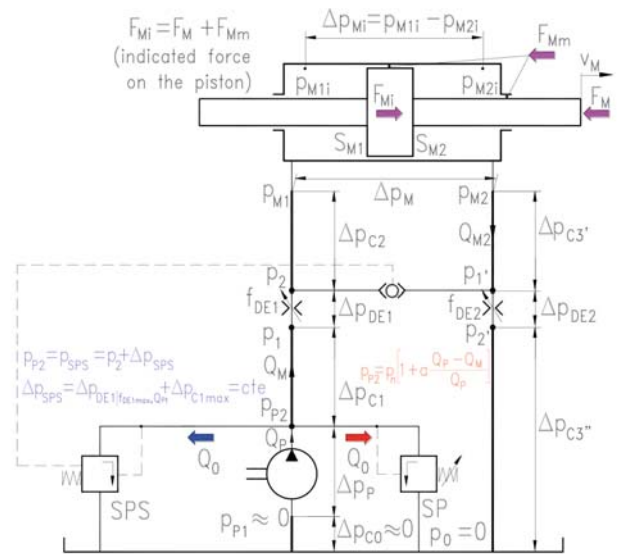


Fig. 2. Schematic diagram of a proportional valve system supplied by a constant capacity pump working with a controlled overflow valve in a variable-pressure system – $p=\text{var}$

The following components were used in the tested systems:

- axial piston pump with displaceable rotor HYDROMATIC type A7.VSO.58DR, operating with fixed theoretical capacity $Q_{Pt}=0,000805\text{m}^3\text{s}^{-1}$ ($48,30\text{dm}^3\text{min}^{-1}$),
- directional proportional control valve, REXROTH type 4WRA10E60-21/G24N9K4, with identical throttling slots $f_{DE1}=f_{DE2}$,
- double piston cylinder HYDROSTER type CD-63/36x500, piston diameter $D=63\text{mm}$ and piston rod diameter $d=36\text{mm}$,
- indirect operation overflow valve REXROTH type DBW10A3-52/315XU GE 62 4N9K4,
- controlled overflow valve REXROTH type ZDC10PT-23/XM (only in the variable pressure – $p=\text{var}$ system).

The nominal pressure of the tested systems was $p_n=16\text{MPa}$, the hydraulic oil Total Azola 46 was used with kinematics viscosity of $\nu=35\text{mm}^2\text{s}^{-1}$ (at the temperature $\vartheta=43^\circ\text{C}$) and volumetric mass of $\rho=873,3\text{kgm}^{-3}$.

The studied structures worked at the same parameters of the linear hydraulic cylinder, i.e. its load F_M and speed v_M .

The considerations allow for comparison of the loss power ΔP of the individual losses resulting from the applied structure supply and the power P_{PC} consumed by the pump from the electric motor that drives it, the power required to provide the unchanged useful power $P_{Mu}=F_M \cdot v_M$ for hydraulic cylinder.

DEFINITIONS OF POWER AND LOSS POWER OCCURRING IN SYSTEM COMPONENTS

Definitions of parameters of work, power and power of particular losses and the record of efficiency are the content of many articles, papers and monographs of prof. Z. Paszota [1÷13]. Model of loss and energy efficiency of a hydraulic drive with proportional control of the cylinder,

which would use a full description of loss and efficiency of the hydraulic motor itself, would become too complex. Therefore, pressure losses (flow resistance) in the inlet and outlet conduits of the cylinder are omitted, as well as negligible volume losses (leaks) in the cylinder.

The following describes the powers that characterize the operation of particular elements occurring in the tested hydrostatic drive systems.

The effective power of the cylinder on its piston rod is the product of the external load F_M and velocity v_M of the piston rod travel:

$$P_{Mu} = F_M v_M \quad [7]. \quad (1)$$

The P_{Mc} power consumed by the cylinder is the difference between the power of liquid in the inlet line and the power of liquid in the discharge line of the cylinder:

$$\begin{aligned} P_{Mu} &= P_{M1} - P_{M2} = Q_M p_{M1} - Q_{M2} p_{M2} \\ &= Q_M (p_{M1} - p_{M2}) \quad [7]. \end{aligned} \quad (2)$$

Power ΔP_{Mm} mechanical losses in the cylinder is the product of the velocity v_M of the piston and the force F_{Mm} of friction between the piston and the cylinder on one side and between the piston rod and the gland on the other hand:

$$\begin{aligned} \Delta P_{Mm} &= P_{Mc} - P_{Mu} = Q_M (p_{M1} - p_{M2}) - F_M v_M \\ &= F_{Mm} v_M \quad [7]. \end{aligned} \quad (3)$$

The useful power of the P_{pu} pump can be defined as the product of its Q_p capacity and pressure increase Δp_p (pressure p_{p2} when $p_{p1} = 0$):

$$\begin{aligned} P_{pu} &= Q_p \cdot \Delta p_p = Q_p \cdot (p_{p2} - p_{p1}) \\ &= Q_p \cdot p_{p2} \quad [7]. \end{aligned} \quad (4)$$

The P_{pc} power consumed by the pump on its drive shaft is the product of the moment M_p and the angular velocity ω_p :

$$P_{pc} = M_p \cdot \omega_p = 2\pi \cdot M_p \cdot n_p \quad [7]. \quad (5)$$

The power loss ΔP_p of the pump is the sum of the power ΔP_{pp} of the pressure losses, the power ΔP_{pv} of the volume losses and the power ΔP_{pm} of the mechanical losses in the pump:

$$\Delta P_p = \Delta P_{pp} + \Delta P_{pv} + \Delta P_{pm} \quad [7]. \quad (6)$$

Power ΔP_{pv} of pressure losses in the pump:

$$\Delta P_{pp} = Q_p p_{pp} = Q_p (\Delta p_{pp1} + \Delta p_{pp2}) \quad [7]. \quad (7)$$

Power ΔP_{pv} of volume losses in the pump:

$$\Delta P_{pv} = Q_{pf} \Delta p_{pi} = Q_{pf} (p_{p2i} - p_{p1i}) \quad [7]. \quad (8)$$

Power ΔP_{pm} of mechanical losses in the pump:

$$\Delta P_{pm} = M_{pm} \omega_p \quad [7]. \quad (9)$$

Power ΔP_C of pressure losses in conduits:

$$\Delta P_C = Q_M \Delta p_C \quad [7]. \quad (10)$$

DEFINITIONS OF ENERGY EFFICIENCIES

Problems connected with energy efficiency are of basic importance for improvement of functionality and quality of the hydrostatic drive systems, characterized by unquestioned advantages but also by relatively low efficiency in comparison with other types of drives. Publications describing the influence of particular design and operating parameters on the hydrostatic system efficiency are valuable. They make it possible to work out system configurations with losses reduced to a minimum [8].

Energy efficiency of hydrostatic transmissions, particularly those with throttling control of the motor speed, and also efficiency of the hydraulic servo-mechanism systems may be in fact higher than the values most often quoted in publications on the subject. Possibility of calculating the real value of the hydraulic system overall efficiency as a function of many parameters influencing it, becomes a tool of complete evaluation of the designed system quality. The capability of making such an evaluation is important because the hydrostatic control systems are used in various machines and equipment, and also due to increasing power of the hydrostatic drive at the time of constantly increasing costs of energy generation [5].

In a system with too low efficiency, the load of the pump increases, which leads to increased risk of failure and the necessary repair or replacement, as well as to a shorter service life. The too low system efficiency, most often resulting from intensive throttling of the stream of liquid, is also a source of rapid deterioration of operational characteristics, particularly the hydraulic oil lubricating properties, which is an effect, among other reasons, of too high temperature of the working liquid – the hydrostatic transmission power medium.

The energy efficiency of components and systems can be determined by the following formulas:

- mechanical efficiency η_{pm} of a pump:

$$\eta_{pm} = \frac{X + k_3(1 - k_1)^2(1 - k_2)^2}{k_{4.1} + (1 + k_{4.2})[X + k_3(1 - k_1)^2(1 - k_2)^2]^2} \quad [13], \quad (11)$$

where:

$$X = 1 + a[(1 - k_1)(1 - k_2) - \bar{Q}_M] \quad [13],$$

- pressure efficiency η_{pp} of a pump:

$$\eta_{pp} = \frac{1 + a[(1 - k_1)(1 - k_2) - \bar{Q}_M]}{1 + a[(1 - k_1)(1 - k_2) - \bar{Q}_M] + k_3(1 - k_1)^2(1 - k_2)^2} \quad [13], \quad (12)$$

- volume efficiency η_{pv} of a pump:

$$\eta_{pv} = 1 - k_1 \quad [13], \quad (13)$$

- overall efficiency η_p of a pump:

$$\eta_p = \frac{X(1 - k_1)}{k_{4.1} + (1 + k_{4.2})[X + k_3(1 - k_1)^2(1 - k_2)^2]} \quad [13], \quad (14)$$

where:

$$X = 1 + a[(1 - k_1)(1 - k_2) - \bar{Q}_M] \quad [13],$$

- total efficiency η_c of wires:

$$\eta_c = \frac{1 + a[(1 - k_1)(1 - k_2) - \bar{Q}_M] - k_5 \bar{Q}_M}{1 + a[(1 - k_1)(1 - k_2) - \bar{Q}_M]} \frac{k_{7.1} + (1 + k_{7.2}) \bar{M}_M}{k_{7.1} + (1 + k_{7.2}) \bar{M}_M + k_6 \bar{Q}_M} \quad [13], \quad (15)$$

- structural pressure efficiency η_{stp} :

$$\eta_{stp} = \frac{k_{7.1} + (1 + k_{7.2}) \bar{M}_M + k_6 \bar{Q}_M}{1 + a[(1 - k_1)(1 - k_2) - \bar{Q}_M] - k_5 \bar{Q}_M} \quad [13], \quad (16)$$

- structural volume efficiency η_{stv} :

$$\eta_{stv} = \frac{\bar{Q}_M}{(1 - k_1)(1 - k_2)} \quad [13], \quad (17)$$

- structural efficiency η_{st} :

$$\eta_{st} = \eta_{stp} \eta_{stv} = \frac{k_{7.1} + (1 + k_{7.2}) \bar{M}_M + k_6 \bar{Q}_M}{1 + a[(1 - k_1)(1 - k_2) - \bar{Q}_M] - k_5 \bar{Q}_M} \frac{\bar{Q}_M}{(1 - k_1)(1 - k_2)} \quad [13], \quad (18)$$

- overall efficiency η_M of the cylinder, equal to its mechanical efficiency η_{Mm} :

$$\eta_M = \eta_{Mm} = \frac{\bar{M}_M}{k_{7.1} + (1 + k_{7.2}) \bar{M}_M} \quad [13], \quad (19)$$

- overall efficiency η of the system:

$$\eta = \frac{P_{Mu}}{P_{Pc}} = \eta_p \eta_c \eta_{st} \eta_M = \frac{\bar{Q}_M}{1 - k_2} \frac{\bar{M}_M}{k_{4.1} + (1 + k_{4.2})[X + k_3(1 - k_1)^2(1 - k_2)^2]} \quad [13], \quad (20)$$

where:

$$X = 1 + a[(1 - k_1)(1 - k_2) - \bar{Q}_M] \quad [13], \quad (21)$$

FORMS FOR DETERMINING THE COEFFICIENTS “ k_i ” AND “ a ” AT THE REFERENCE VISCOSITY “ ν ”

Knowledge of the energy efficiency course of a positive displacement machine as an independent whole is not enough

to assess its energetic behavior in a hydrostatic drive system with a selected structure of hydraulic motor speed control. The energetic behavior of the positive displacement machine in the system results from the conditions created by the applied structure of the speed change of the hydraulic motor shaft, so it is different in different conditions. It is also required to describe it in the form of the function of current parameters of the operating system as well as the function of the speed coefficient $\bar{\omega}_M$ and load coefficient \bar{M}_M of the hydraulic motor in the system.

It is necessary to replace the previously used researches of energy efficiency of displacement machines with researches of energy losses in machines. The results of such researches

make it possible to assess the efficiency of the pump or hydraulic motor as an independent whole, as well as to evaluate the efficiency of the machine used in the drive system. Such possibilities are

offered by energy loss tests in the pump and in the hydraulic motor combined with the assessment of the coefficients of energy losses occurring in them. These coefficients were called “ k_i coefficients”.

Knowing the coefficients k_i of energy losses occurring in the hydrostatic system element (in the pump, in the hydraulic motor, but also in the conduits and in the motor speed control group) allows to build mathematical models of losses and energy efficiency of the element working in the system and energy efficiency of the system as a whole composed of elements. Mathematical model of losses and energy efficiency of an element in the system must take into account the conditions resulting from the applied structure of the system, from the level of assumed nominal pressure, from the rotational speed of the engine driving the pump shaft, from the viscosity change of the applied working fluid (hydraulic oil) [11].

The coefficients k_i describe the relative value of individual losses in the element. They allow to assess the proportions of losses and to assess the value of the energy efficiency of the element (volume, pressure, mechanical) resulting from losses occurring at the nominal pressure p_n of the system in which the element is used [4].

As a result, thanks to the knowledge of the coefficients k_i of individual losses, it is possible to determine losses and energy efficiency of components

operating in the drive system as well as the efficiency of the total system with a determined structure of the motor speed control as a function of the speed coefficient $\bar{\omega}_M$ and load coefficient \bar{M}_M of the hydraulic motor.

In order to compare losses and energy efficiency of two examined structures: constant pressure system $p=cte$ and variable pressure system $p=var$, consisting of the cylinder, conduits, proportional directional control valve, overflow valve SP ($p=cte$ and $p=var$ systems) and controlled overflow valve SPS (only $p=var$ system) and pumps, measurements were made using a laboratory computer and using the National Instruments LabView 6.0 program for this purpose. The

results of the measurements were processed in Excel program. The computer with measuring transducers was connected using a PCI 1713 Advantech measurement card. In this way, 4 signals from pressure transducers were recorded, the piston rod signal was signaled using a linear displacement transducer, on the basis of which its v_M speed was determined, and the signal of the F_M force loading the piston rod [14].

Each measurement cycle was started from oil heating to the temperature of $t=43^\circ\text{C}$, at which its kinematic viscosity is $\nu=35\text{mm}^2\text{s}^{-1}$.

At the beginning, the test cylinder performed reciprocating movements without load. Then, after starting the pump supplying the load cylinder, the load was systematically increased. When the measurement results were repeatable, i.e. stable, researches were started.

Thanks to the automated work of the systems, the hydraulic cylinders moved in both directions without interruption, while during the working movement the load cylinder loaded the tested cylinder. In the return movement, both cylinders moved independently. In this way, there are no air bubbles in the oil filling the cylinder chambers, which would adversely affect the measurement results.

In order to compare two hydraulic systems, the same series of speed v_M and piston rod loads F_M were assumed when testing them. During the measurements, the tested cylinder was loaded with the force of F_M equal to 0kN, 5kN, 10kN, 15kN, 20kN, 25kN, 30kN. On the other hand, the cylinder's piston moved at a speed v_M equal to 0.025m/s, 0.05m/s, 0.075m/s, 0.10m/s, 0.15m/s, 0.20m/s, 0.25m/s, 0.30m/s, 0.35m/s, 0.40m/s [14].

Thanks to the knowledge of the coefficients k_i of individual losses, it is possible to determine the losses and energy efficiency of components operating in the hydraulic system.

The following is a set of definitional formulas allowing to determine the coefficients k_i of energy losses in the elements of the hydraulic system and the value of the "a" coefficient of the overflow valve at the reference viscosity $\nu_n=35\text{mm}^2\text{s}^{-1}$.

A. THE PUMP

o Coefficients "k_i"

- k_1 – a coefficient of relative volumetric losses Q_{pv} per one shaft revolution of fixed capacity pump

$$k_1 = \frac{Q_{pv|\Delta p_{pi}=p_n}}{n_{p|\Delta p_{pi}=p_n}} \cdot \frac{1}{q_{pt}} \quad [12], \quad (22)$$

Therefore, based on the results obtained during laboratory researches, the coefficient "k₁" is:

$$k_1 = \frac{q_{pt} - q_{p|\Delta p_{pi}=p_n}}{q_{pt}} = \frac{32,20 - 30,35}{32,20} = 0,0574 \quad [14], \quad (23)$$

- k_2 – a coefficient of relative decrease Δn_p in pump rotational speed (Δn_p speed decrease is related to the rotational speed "n" characteristic as a function of the torque "M" of the driving motor – e.g. electric motor):

$$k_2 = \frac{n_{p0} - n_{p|\Delta p_{pi}=p_n}}{n_{p0}} = \frac{1500 - 1494}{1500} = 0,004 \quad [14], \quad (24)$$

- k_3 – a coefficient of relative pressure losses (flow resistance) in internal pump ducts, at theoretical pump delivery Q_{pt} :

$$k_3 = \frac{\Delta p_{pp|Q_p=Q_{pt}}}{p_n} \quad [9]. \quad (25)$$

According to the above formula, the coefficient k_3 of the tested pump is:

$$k_3 = \frac{0,38}{160} = 0,0024 \quad [14]. \quad (26)$$

- $k_{4.1}$ – a coefficient of relative mechanical losses $M_{Pm|\Delta p_{pi}=0}$ in the unloaded constant capacity pump, at $\Delta p_{pi} = 0$ (so at $M_{pi} = 0$) to the nominal moment M_{pn} :

$$k_{4.1} = \frac{2\Pi M_{Pm|\Delta p_{pi}=0}}{q_{pt} p_n} \quad [9]. \quad (27)$$

According to the above formula, the coefficient $k_{4.1}$ of the tested pump is:

$$k_{4.1} = \frac{3,21}{81,99} = 0,0391 \quad [14]. \quad (28)$$

- $k_{4.2}$ – a coefficient of relative increase of mechanical pump losses $\Delta M_{Pm|\Delta p_{pi}=p_n}$, at increase in pressure in pump working chambers:

$$k_{4.2} = \frac{\Delta M_{Pm|\Delta p_{pi}=p_n}}{M_{pn}} = \frac{2\Pi \Delta M_{Pm|\Delta p_{pi}=p_n}}{q_{pt} p_n} \quad [9]. \quad (29)$$

According to the above formula, the coefficient $k_{4.2}$ of the tested pump type A7VS0.58.DR is:

$$k_{4.2} = \frac{2\Pi \cdot 1,23}{32,20 \cdot 10^{-6} \cdot 160 \cdot 10^5} = 0,015 \quad [14]. \quad (30)$$

o Characteristics of basic pump types – approximate values of coefficients „k_i”

It is proposed to use, in the industrial energy calculations, approximate values of coefficients "k_i" of basic types of pumps.

For example, the approximate values of the "k_i" coefficients of axial piston pumps are shown below (Tab. 1):

Tab. 1. The approximate values of the "k_i" coefficients of axial piston pumps [1]

$p_n=10 \text{ MPa}$	$p_n=25 \text{ MPa}$
$k_1 = 0,01$	$k_1 = 0,02$
$k_3 = 0,01$	$k_3 = 0,01$
$k_{4.1} = 0,01$	$k_{4.1} = 0,05$
$k_{4.2} = 0,01$	$k_{4.2} = 0,02$

B. THE CONDUIT CONNECTING THE PUMP TO THE THROTTLE CONTROL UNIT

- k_5 – a coefficient of relative pressure losses (flow resistances) Δp_{C1} in the line joining the pump with throttle control unit, at theoretical pump delivery Q_{Pt} :

$$k_5 = \frac{\Delta p_{C1|Q_{Pt}}}{p_n} \quad [9]. \quad (31)$$

Thus, the value of the coefficient k_5 is:

$$k_5 = \frac{3,46}{160} = 0,0216 \quad [14]. \quad (32)$$

The coefficient k_5 represents the sum of the flow resistance (pressure loss) in the conduit and in the elements installed on this conduit (filters, check valves, connectors ...).

C. THE CONDUIT CONNECTING THE THROTTLE CONTROL UNIT WITH THE HYDRAULIC CYLINDER

- $k_{6.1}$ – a coefficient of relative pressure losses (flow resistances) Δp_{C2} in the line joining the throttle control unit with hydraulic motor, at theoretical pump delivery Q_{Pt} :

$$k_{6.1} = \frac{\Delta p_{C2|Q_{Pt}}}{p_n} \quad [9]. \quad (33)$$

Thus, the value of the $k_{6.1}$ coefficient is:

$$k_{6.1} = \frac{2,64}{160} = 0,0165 \quad [14]. \quad (34)$$

The coefficient $k_{6.1}$ represents, as above, the sum of the flow resistance (pressure loss) in the conduit and in the various elements that the conduit contains.

D. THE OUTLET LINE FROM THE HYDRAULIC CYLINDER

- $k_{6.2}$ – a coefficient of relative pressure losses (flow resistances) Δp_{C3} in hydraulic motor outlet line, at theoretical pump delivery Q_{Pt} :

$$k_{6.2} = \frac{\Delta p_{C3|Q_{Pt}}}{p_n} \quad [9]. \quad (35)$$

Thus, the value of the coefficient $k_{6.2}$ is:

$$k_{6.2} = \frac{2,75}{160} = 0,0172 \quad [14]. \quad (36)$$

The coefficient $k_{6.2}$ includes, as before, the sum of flow resistance (pressure loss) in the conduit and in the components installed on it.

E. A HYDRAULIC ROTATIONAL MOTOR

□ Coefficients “ k_i ”

- $k_{7.1}$ – a coefficient of mechanical losses $M_{Mm|M_M=0}$ in an unloaded hydraulic rotational motor with constant absorbcency per revolution:

$$k_{7.1} = \frac{M_{Mm|M_M=0}}{M_{Mn}} = \frac{2 \Pi M_{Mm|M_M=0}}{q_{Mt} p_n} \quad [10]. \quad (37)$$

- $k_{7.2}$ – a coefficient of mechanical loss increase $M_{Mm|M_M=M_{Mn}}$ in a hydraulic rotational motor with constant absorbcency per revolution:

$$k_{7.2} = \frac{M \Delta_{Mm|M_{Mi}=M_{Mn}}}{M_{Mn}} = \frac{2 \Pi \Delta M_{Mm|M_M=M_{Mn}}}{q_{Mt} p_n} \quad [10]. \quad (38)$$

- k_8 – a coefficient of pressure losses Δp_{Mp} in internal channels (and in the distributor, if any) of a hydraulic rotational motor:

$$k_8 = \frac{\Delta p_{Mp|Q_M=Q_{Pt}}}{p_n} \quad [10]. \quad (39)$$

- k_9 – a coefficient of volume losses Q_{Mf} in a hydraulic rotational motor:

$$k_9 = \frac{Q_{Mf|\Delta p_{Mi}=p_n}}{Q_{Pt}} \quad [10]. \quad (40)$$

□ Characteristics of basic types of hydraulic rotational motors – approximate values of coefficients “ k_i ”

As in the case of the pumps, it is proposed to introduce, for the energy calculations of hydraulic systems, approximate values of “ k_i ” coefficients of losses in basic types of motors. For example, the approximate values of the coefficients “ k_i ” of low-speed radial piston motors (with an internal cam – eccentric) are presented below (Tab. 2):

Tab. 1. The approximate values of the coefficients “ k_i ” of low-speed radial piston motors [1]

$p_n = 10 \text{ MPa}$	$p_n = 25 \text{ MPa}$
$k_{7.1} = 0.04$	$k_{7.1} = 0.02$
$k_{7.2} = 0.02$	$k_{7.2} = 0.02$
$k_8 = 0.02$	$k_8 = 0.01$
$k_9 = 0.02$	$k_9 = 0.03$

F. THE LINEAR HYDRAULIC MOTOR – CYLINDER

A measurement of friction forces F_{Mm} in the tested cylinder, operating at a constant speed, were made using the indirect method, as there is no device enabling the measurement to be carried out using the direct method. This made it necessary to use high quality transducers for measuring force and pressure.

□ Coefficients “k_i”

- k_{7,1} – a coefficient of mechanical losses in the unloaded cylinder:

$$k_{7,1} = \frac{F_{Mm|F_M=0}}{F_{Mn}} = \frac{F_{Mm|F_M=0}}{S_{M1} p_n} \quad [13]. \quad (41)$$

- k_{7,2} – a coefficient of mechanical loss increase in the cylinder:

$$k_{7,2} = \frac{F\Delta_{Mm|F_M=F_{Mn}}}{F_M} = \frac{F\Delta_{Mm|F_M=F_{Mn}}}{S_{M1} p_n} \quad [13]. \quad (42)$$

In the case of a cylinder, the coefficient k_{7,2} can be positive or negative; the latter case may result from the application of a throttle control at the outflow from the cylinder (an example of controlling the cylinder with a proportional directional control valve or servo valve).

- k₈ – a coefficient of pressure loss (flow resistance) in the internal channels of the cylinder:

$$k_8 = 0. \quad (43)$$

The picture of the loss and energy efficiency of the linear hydraulic motor – the cylinder – is more complicated compared to the case of a rotary hydraulic motor.

It was decided, therefore, to consider the energy efficiency problem of systems with the cylinder only for the case of the cylinder with pressure losses (flow resistance) Δp_{Mp} in the inlet and outlet channel, as well as with internal leakages Q_{Mf} negligible.

This is the case of the majority of cylinders, in which the pressure and volumetric energy losses are to be neglected in comparison with mechanical losses, and in particular in comparison with the power developed by the cylinder.

- k₉ – a coefficient of volume losses Q_{Mf} in the cylinder:

$$k_9 = 0. \quad (44)$$

- Characteristics of selected varieties and sizes of hydraulic cylinders with lip sealing rings – approximate values of coefficients k_{7,1} and k_{7,2} of mechanical losses in the cylinder (Tab. 3)

Conditions:

- a pressure p_{M2} in the cylinder outlet near the zero – p_{M2} ≈ 0,
- the piston rod is not loaded with transversal forces.

Variations of cylinders:

- K – double-acting, with one-sided piston rod,
- L – double-acting, with one-sided piston rod, with differential connection,
- R – double-acting, with double-sided piston rod.

H. THE PROPORTIONAL DIRECTIONAL CONTROL VALVE

- k₁₁ – a coefficient of relative pressure decrease Δp_{DE} in directional control valve (servovalve, proportional valve) demanded by a maximum throttling section f_{DEmax} for receiving flow intensity equal theoretical pump delivery Q_{Pt}:

$$k_{11} = \frac{p\Delta_{DE}|f_{DEmax}, Q_{Pt}}{p_n} = \frac{(p\Delta_{DE1} + p\Delta_{DE2})|f_{DEmax}, Q_{Pt}}{p_n} \quad [13]. \quad (45)$$

The coefficient k₁₁ corresponds to the sum of the pressure drops Δp_{DE} = Δp_{DE1} + Δp_{DE2} in the two slots of the throttle distributor. This coefficient for the proportional directional control valve type 4WRA 10 E60-21 / G24 N9K4 can be determined using equation (45). So, in this case:

$$k_{11} = \frac{0,592 \text{ MPa} + 0,592 \text{ MPa}}{16 \text{ MPa}} = \frac{1,184 \text{ MPa}}{16 \text{ MPa}} = 0,074 \quad [14]. \quad (46)$$

The choice of the size of the throttling valve is made in such a way that its nominal flow rate, while the hydraulic system is working, corresponds more or less to the maximum electric current (close to 100%). The application of this principle

Tab. 1. The approximate values of coefficients k_{7,1} and k_{7,2} of mechanical losses in the cylinder [4]

Push or pull movement (example):

Pulling motion									
D diameter of the piston [mm]	ρ – ratio of active surfaces of the piston	type K				type R			
		p _n = 10 MPa		p _n = 25 MPa		p _n = 10 MPa		p _n = 25 MPa	
		k _{7,1}	k _{7,2}	k _{7,1}	k _{7,2}	k _{7,1}	k _{7,2}	k _{7,1}	k _{7,2}
32÷50	1,4	0.05	0.07	0.03	0.05	0.06	0.07	0.03	0.06
	2	0.11	0.10	0.05	0.07	0.14	0.10	0.06	0.08
125÷200	1,4	0.04	0.05	0.02	0.03	0.04	0.05	0.02	0.03
	2	0.05	0.06	0.02	0.04	0.08	0.03	0.03	0.05
400÷630	1,4	0.02	0.02	0.01	0.02	0.02	0.02	0.01	0.02
	2	0.02	0.04	0.01	0.03	0.03	0.03	0.01	0.03

makes it possible to optimally use the size controlled by the throttling valve and their mild change during control.

If the nominal intensity of the throttling valve used is equal to the theoretical efficiency of the pump operating in the system, $Q_{DEn} = Q_{pt}$, then a specific numerical value of the k_{11} coefficient can be determined with the selected nominal pressure p_n of the system. For example, the size of the servo valve coefficient k_{11} , characterized by a nominal pressure drop $\Delta p_{DEn} = 7\text{MPa}$ and operating in a system with a nominal pressure $p_n = 20\text{MPa}$, will be equal to:

$$k_{11} = \frac{p\Delta_{DE|f_{DEmax}, Q_{pt}}}{p_n} = \frac{7\text{MPa}}{20\text{MPa}} = 0.35 \quad [9]. \quad (47)$$

As approximate values of the coefficient k_{11} , we can cite [4]: $k_{11} = 0.05 \div 0.50$ in the case of a servo valve, $k_{11} = 0.03 \div 0.06$ in the case of a proportional directional control valve.

J. AN OVERFLOW VALVE

A coefficient "a" of the pressure increase p_{SP} stabilized by an overflow valve (pressure limiter) in the constant capacity pump:

$$a = \frac{P_{SP|Q_0=Q_{pt}} - P_{SP0}}{P_{SP0}} = \frac{P_{SP|Q_0=Q_{pt}} - p_n}{p_n} \quad [9], \quad (48)$$

where:

$P_{SP|Q_0=Q_{pt}}$ – a pressure stabilized by the overflow valve at the flow rate Q_0 in the valve equal to theoretical pump capacity $Q_{pt} - Q_0 = Q_{pt}$, P_{SP0} [Pa] – the opening pressure of the overflow valve equal to the nominal pressure p_n of the system – $P_{SP0} = p_n$, obtained at the flow rate Q_0 in the valve equal to 0 – $Q_0 = 0$. Range of change of the coefficient "a":

$$a = 0 \div 0.20.$$

In order to determine the coefficient "a" of the pressure increase controlled by the overflow valve, installed on a test stand, researches were carried out. Thus, the coefficient "a" of the tested overflow valve type DBW 10 A3 – 52 \ 315XU 6E G2 4N9K4 from Rexroth is:

$$a = \frac{P_{SP|Q_0=Q_{pt}} - P_{SP0}}{P_{SP0}} = \frac{16,38 - 16,0}{16} = 0,023 \quad [14]. \quad (49)$$

EXAMPLES OF LABORATORY VERIFICATION OF ENERGY SAVING IN THE SYSTEM WITH A CONSTANT CAPACITY PUMP IN A VARIABLE PRESSURE SYSTEM $p=var$, IN COMPARISON WITH A CONSTANT PRESSURE SYSTEM $p=cte$

The test results, shown in Figures 3–9, allow for a comparison of the energy loss power values, expressed in Watts [W], in the $p=cte$ and $p=var$ system elements.

The most significant reduction of energy losses, when $p=cte$ system is replaced by a $p=var$ system, is obtained in the case of the structural pressure loss power ΔP_{stp} (Fig. 3) in the proportional directional control valve. With the cylinder load coefficient $\bar{M}_M = 0$ and speed coefficient $\bar{\omega}_M = 0,875$, the loss power is reduced from approx. 9800 W to approx. 1800W, i.e. by 7,5times. The pressure loss power ΔP_{stp} in both systems equalizes in the maximum cylinder load area (maximum \bar{M}_M values), i.e. in the area where the $p=var$ system begins to operate as a $p=cte$ system. The pressure structural loss power ΔP_{stp} in both systems is then relatively small – below 2300W.

The volumetric structural loss power ΔP_{stv} (Fig. 4), occurring in the overflow valve ($p=cte$ system) or in the controlled overflow valve and the overflow valve ($p=var$ system), decreases also when the $p=cte$ system is replaced by the $p=var$ system. However, the power reduction is not as significant as in the case of pressure structural loss power ΔP_{stp} .

With the cylinder coefficient $\bar{M}_M = 0$ and speed coefficient $\bar{\omega}_M = 0,063$, the volumetric loss power ΔP_{stv} is reduced from ca. 12000W to approx. 2400W, ie. 5 fold. The volumetric loss power ΔP_{stv} in both systems equalizes in the cylinder maximum load area (maximum \bar{M}_M values, i.e. in the area of the $p=var$ system operating as a $p=cte$ system). However, the same volumetric loss power ΔP_{stv} in both systems is at its maximum – it reaches 12000W at $\bar{\omega}_M = 0,063$ [15].

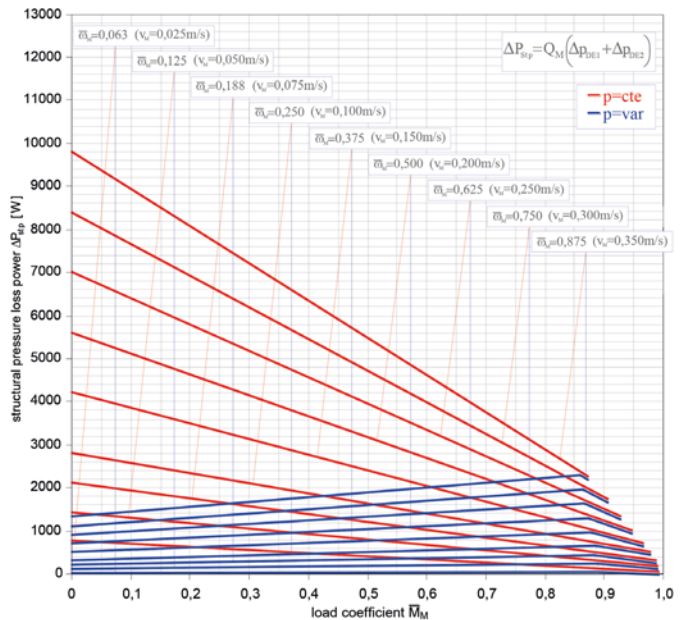


Fig. 3. Relation between the structural pressure loss power ΔP_{stp} (in the directional proportional control valve), in the constant pressure system ($p=cte$) and variable pressure system ($p=var$), and the load coefficient \bar{M}_M with different speed coefficients $\bar{\omega}_M$ of the cylinder [15]

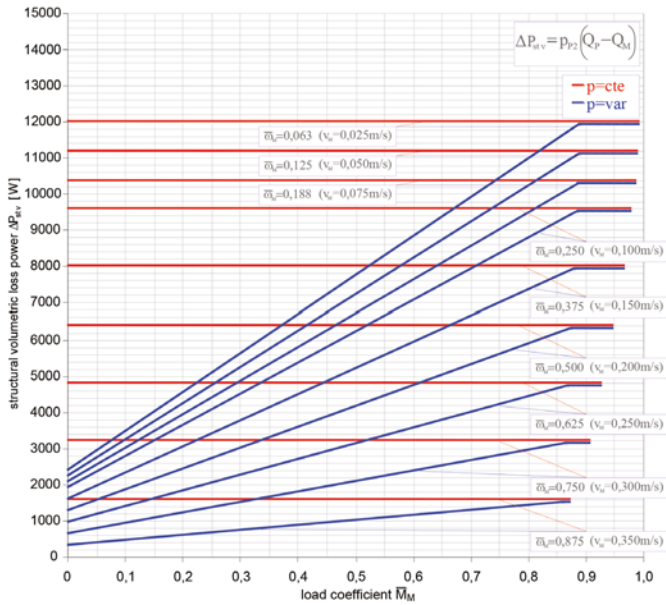


Fig. 4. Relation between the structural volumetric loss power ΔP_{stv} (in the overflow valve and in controlled overflow valve), in the constant pressure system ($p=cte$) and variable pressure system ($p=var$), and the load coefficient \bar{M}_M with different speed coefficients $\bar{\omega}_M$ of the cylinder [15]

The structural loss power ΔP_{st} is the sum of the structural pressure loss power ΔP_{stp} in the proportional distributor (proportional directional control valve) and the structural volume loss power ΔP_{stv} in the overflow valve or in the control overflow valve:

$$\Delta P_{st} = \Delta P_{stp} + \Delta P_{stv} \quad (50)$$

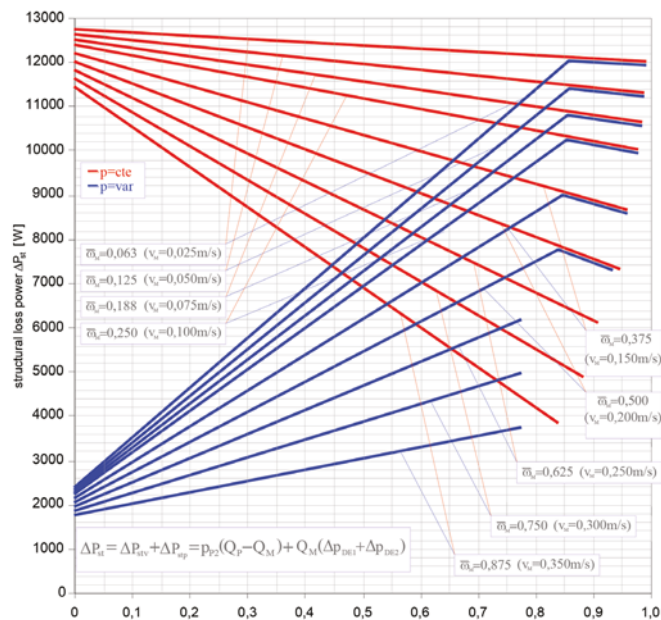


Fig. 5. Relation between the structural loss power ΔP_{st} in the throttle control unit (sum of structural pressure loss power ΔP_{stp} in the proportional directional control valve and the structural volume loss power ΔP_{stv} in the overflow valve and in the control overflow valve) in constant pressure system ($p=cte$) and variable pressure system ($p=var$) from the load coefficient \bar{M}_M at different speed coefficients $\bar{\omega}_M$ in hydraulic cylinder

Fig. 5 shows the diagram of structural loss power ΔP_{st} in constant pressure system ($p=cte$) and variable pressure system ($p=var$).

The structural loss power ΔP_{st} in the $p=cte$ system, with the determined values of the speed coefficient $\bar{\omega}_M$ of the cylinder decreases, as the load coefficient \bar{M}_M increases.

With the load coefficient $\bar{M}_M=0$ and the speed coefficient $\bar{\omega}_M=0,063$ ($v_M=0,025m/s$) of the cylinder, the loss power ΔP_{st} of the constant pressure system $p=cte$ achieves the greatest value of $\Delta P_{st}=12700W$. At the same speed value and with a maximum load coefficient of $\bar{M}_M=0,988$, the structural loss power ΔP_{st} in the $p=cte$ system drops to $\Delta P_{st}=12000W$. On the other hand, with the maximum values of speed and load of the cylinder, ΔP_{st} of the system $p=cte$ assumes the smallest value equal to $\Delta P_{st}=3815W$. This 3,3 times decrease of ΔP_{st} is mainly related to the decreasing pressure drop ΔP_{DE} in the proportional directional control valve and to the decreasing flow intensity Q_0 facing to the reservoir through the overflow valve [14].

After replacing the constant pressure system $p=cte$ with the variable pressure system $p=var$, the structural loss power ΔP_{st} is noticeable. This is due to the reduced pressure p_{p2} in the pump discharge line at lower load coefficients \bar{M}_M of the cylinder.

With a load coefficient $\bar{M}_M=0$ and a speed coefficient $\bar{\omega}_M=0,063$ ($v_M=0,025m/s$) of the cylinder, the structural loss power decreases from $\Delta P_{st}=12700W$ ($p=cte$) to about $\Delta P_{st}=2400W$ ($p=var$) and therefore 5,3 times. The structural loss power ΔP_{st} in both systems equate in the zone of maximum cylinder load (maximum values), ie in the zone where system $p=var$ works as $p=cte$. Then the structural loss power ΔP_{st} in both systems, at a minimum speed coefficient of $\bar{\omega}_M=0,063$, is high and is $\Delta P_{st}=12000W$.

In the $p=var$ system, when the hydraulic cylinder is operating at a high speed coefficient of $\bar{\omega}_M=0,875$ ($v_M=0,350m/s$), the structural loss power ΔP_{st} decreases markedly, changing from $\Delta P_{st}=1780W$ at $\bar{M}_M=0$ to $\Delta P_{st}=3800W$ at $\bar{M}_M=0,775$ [15].

In summary, the advantage of replacing the constant pressure structure $p=cte$ with the $p=var$ structure is most evident in the representation of the structural loss power ΔP_{st} in the studied systems in the aggregate diagram of these losses (Fig. 5). It follows that ΔP_{st} of the $p=cte$ structure decreases both with increasing speed and with increasing load of the cylinder. In $p=var$ system, ΔP_{st} increases with increasing load, and decreases with increasing speed of hydraulic cylinder.

RELATION BETWEEN LOSS POWER IN HYDRAULIC COMPONENTS AND POWER REQUIRED BY THE CONSTANT CAPACITY PUMP FROM USEFUL POWER OF CYLINDER IN $p=cte$ AND $p=var$ STRUCTURES

Test results shown in Fig. 6 allow for comparison depending on the amount of the loss power ΔP (expressed in watts [W]) occurring in the elements and the consumed power P_{pc} by

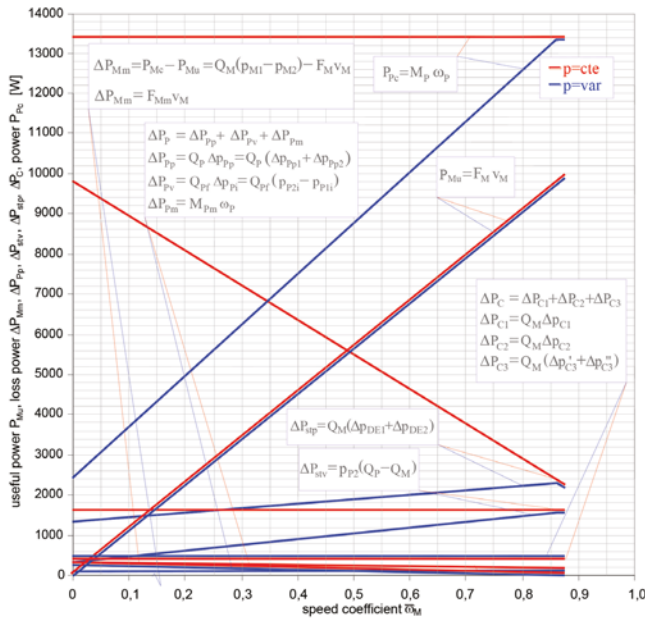


Fig. 6. The loss power ΔP of the system components and the power P_{pc} demanded by the pump in the constant pressure system ($p=cte$) and variable pressure system ($p=var$) from the load coefficient \bar{M}_M at the hydraulic cylinder speed coefficient $\bar{\omega}_M=0,875$ ($v_M=0,35m/s$); The useful power P_{Mu} of the hydraulic cylinder is resulted from the product of the current load F_M (\bar{M}_M) and the actual speed v_M ($\bar{\omega}_M$) of the cylinder required by the driven device [14]

the pump from the useful power P_{Mu} of cylinder controlled in a constant pressure system $p=cte$ and variable pressure system $p=var$ at the speed coefficient of the cylinder $\bar{\omega}_M=0,875$ ($v_M=0,350m/s$).

The graph in Fig. 6 shows that the charts of the consumed power P_{pc} of the pump (at the same useful power P_{Mu} of the cylinder) are different for the two investigated systems. In the constant pressure system, the consumed power P_{pc} is constant throughout range of change of the load coefficient and is 13380W. On the other hand, in the case of a variable pressure system, the power P_{pc} varies, depending on the load of the cylinder, in the range of 3200W at $\bar{M}_M=0$ to 13380W at $\bar{M}_M=0,875$. The useful power P_{Mu} of the cylinder increases over the whole load coefficient range, is equal to zero at $\bar{M}_M=0$ and 9900W at $\bar{M}_M=0,875$.

Fig. 7 shows the dependence of the power P_{pc} demanded by the pump from the output useful power P_{Mu} in the constant pressure system ($p=cte$) and variable pressure system ($p=var$). The power P_{pc} required by the pump and the power P_{Mu} of the cylinder are shown here as a function of the load coefficient \bar{M}_M at different cylinder speed coefficients $\bar{\omega}_M$.

At the smallest speed v_M of the cylinder ($v_M=0,025m/s$), the power P_{pc} required by the pump is greatest in the constant pressure system $p=cte$. This is related to the operation of the overflow valve SP. With increasing speed v_M of the cylinder, the pressure p_{p2} decreases as the overflow valve sets the lower pressure p_{sp} . Consequently, the power P_{pc} required by the pump decreases.

On the other hand, the useful power of the cylinder, which is the product of the speed v_M of the cylinder and its force loading F_M , is independent of the system. The speed and load of the cylinder are independent of the control structure.

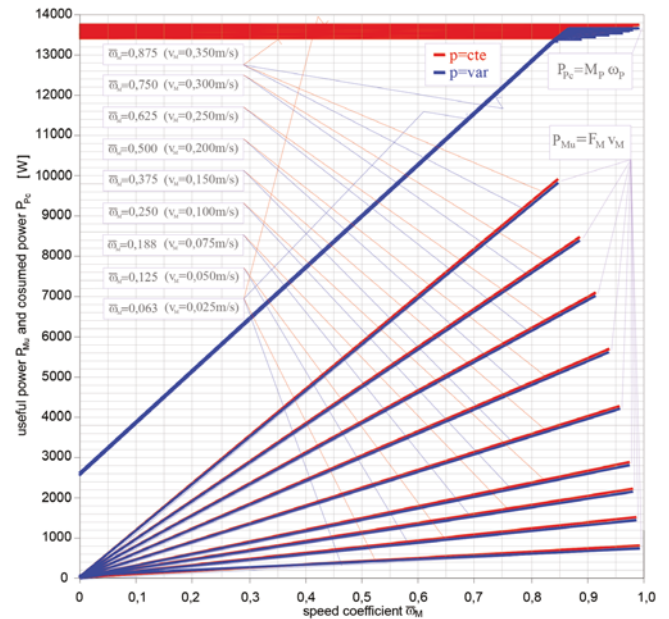


Fig. 7. Relation of power P_{pc} demanded by the pump in the constant pressure system ($p=cte$) and variable pressure system ($p=var$) from the load coefficient \bar{M}_M at the different speed coefficient $\bar{\omega}_M$ (So this is the dependence the consumed power P_{pc} from the useful power P_{Mu} of the hydraulic cylinder) [14]

Consequently, all loss power ΔP that occur in $p=cte$ and $p=var$ systems are a function of the useful power P_{Mu} and the quality of these components (ie loss power in these components). The loss power ΔP , on the other hand, depends on the current useful power P_{Mu} and above all on the current load F_M and the current speed v_M of the cylinder.

The useful power must be supplied by the investigated systems with the same load F_M and speed v_M and is the same. The useful power P_{Mu} will increase as load and speed increase.

The power P_{pc} demanded by the pump results from the useful power P_{Mu} of the cylinder and all the loss power ΔP occurring in the system.

In conclusion, the power P_{pc} demanded by the pump depends on the useful power P_{Mu} , the structure of the circuit, and the loss power ΔP that are present in the system components.

COMPARISON OF THE ENERGY EFFICIENCY OF VARIOUS SYSTEM VERSIONS

Investigations of the efficiency of elements and systems, taking into account detail analysis of the sources of particular energy losses, may be included in the basic scope of research into the hydrostatic drive and control systems.

The energy efficiency, one of the most important system characteristics, is defined as the ratio of, by the driven device currently demanded, useful power P_{Mu} of the hydraulic motor to the power P_{pc} , corresponding to P_{Mu} , obtained by the pump on its shaft from the (electric or combustion) motor driving the pump. In case of improper choice of the system type, the

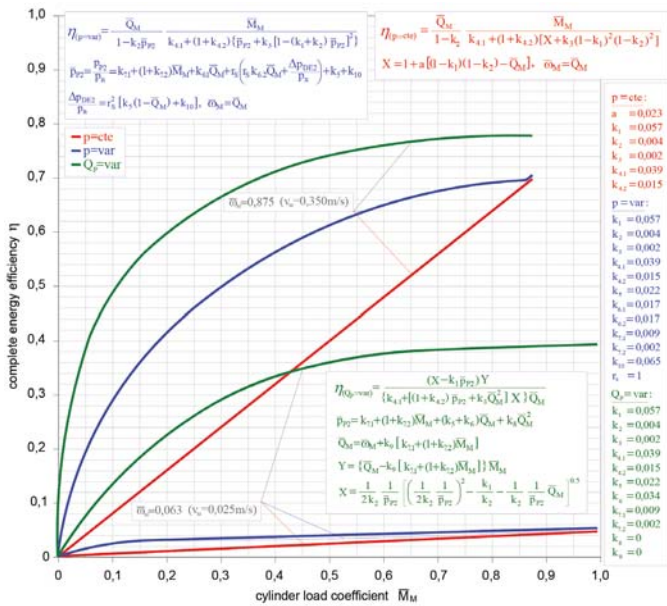


Fig. 8. Relation of the overall efficiency η of a constant pressure ($p=cte$) and a variable pressure ($p=var$) system with proportional control and a system with volumetric control by a variable capacity pump ($Q_p=var$) to the load coefficient \bar{M}_M at different values of the cylinder speed coefficient $\bar{\omega}_M$ (efficiency determined by simulation from experimentally obtained k_i coefficient; the $v_M = 0,350\text{m/s}$ ($\bar{\omega}_M = 0,875$) speed was the highest cylinder speed used during the tests) [15]

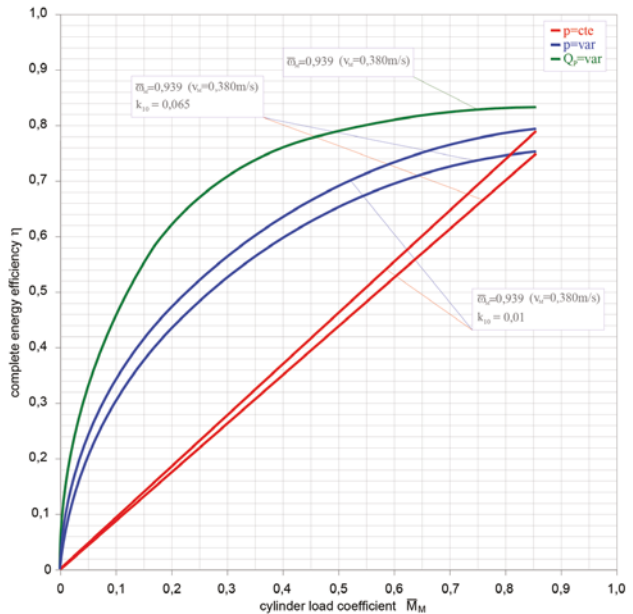


Fig. 9. Relation of the overall efficiency η of a constant pressure ($p=cte$) and a variable pressure ($p=var$) system with proportional control, with the used proportional directional valve coefficient $k_{10}=0,065$ and with possible use of a bigger proportional directional valve with $k_{10}=0,010$, as well as a system with volumetric control by a variable capacity pump ($Q_p=var$), to the load coefficient \bar{M}_M at the value of the cylinder speed coefficient $\bar{\omega}_M=0,939$ ($v_M = 0,380\text{m/s}$) resulting from the maximum pump capacity Q_{pmax} . Maximum η_{max} values of the three considered systems are closer to one another [15]

consequence may be increased hydraulic oil temperature, i.e. decreased oil viscosity and, in turn, lower efficiency of the system elements, and also an impact on the system run characteristics. Therefore, the energy efficiency may be a decisive factor for usability of a system in a specific case. Its detailed analysis quite often leads to design improvements of the system elements. However, improving the quality of hydrostatic systems does not consist exclusively in the improvements of their elements [10].

Fig. 8 and 9 present the overall efficiency η of a constant pressure ($p=cte$) and a variable pressure ($p=var$) system with proportional control and a system with volumetric control by a variable capacity pump ($Q_p=var$) as a function of the load coefficient \bar{M}_M at different values of the cylinder speed coefficient $\bar{\omega}_M$.

In the case of a system with volumetric control by a variable capacity pump ($Q_p=var$), increasing the cylinder load coefficient \bar{M}_M causes rapid increase of the system overall efficiency η (Fig. 8). However, efficiency of structures with the series throttling control fed by a constant capacity pump is, with small value of the $\bar{\omega}_M$ coefficient, distinctly lower than the volumetric control efficiency with the same value of $\bar{\omega}_M$, because the structural losses are high [15].

Increase of the cylinder speed causes a proportional increase of efficiency of the $p=cte$ and $p=var$ systems, but with an increase of the cylinder speed v_M the relative increase of efficiency of the system fed by a variable capacity pump is smaller (Fig. 8).

It can be seen in Fig. 8 that a 14-fold increase of the cylinder speed in the investigated structures causes about 14-fold increase of their efficiency. As a comparison, a 14-fold increase

of the cylinder speed in a $Q_p=var$ structure causes about 2-fold increase of its efficiency (from $\eta=0,39$ at $\bar{\omega}_M=0,063$ and $\bar{M}_M=0,875$ to $\eta=0,78$ at $\bar{\omega}_M=0,875$ and $\bar{M}_M=0,875$).

Fig. 9 presents efficiency η of a constant pressure ($p=cte$) and a variable pressure ($p=var$) system with proportional control, with the used proportional directional valve coefficient $k_{10}=0,065$ and with possible use of a bigger proportional directional valve with $k_{10}=0,010$, as well as a system with volumetric control by a variable capacity pump ($Q_p=var$), as a function of the load coefficient \bar{M}_M at the value of the cylinder speed coefficient $\bar{\omega}_M=0,939$ ($v_M = 0,380\text{m/s}$) resulting from the maximum pump capacity Q_{pmax} [15].

In the maximum cylinder speed range, i.e. with the full use of the pump capacity, efficiency values of the $p=cte$ and $p=var$ systems with throttling control become close to the efficiency of the $Q_p=var$ system with volumetric control.

SUMMARY AND CONCLUSIONS

There are possibilities to reduce energy losses in proportional control systems (in the pump, in the throttle control unit, especially in the cylinder), and thus to improve the energy efficiency of the throttling manifold. The considerations allow for comparison of the loss power resulting from the applied hydraulic control structure of the hydraulic cylinder and the power consumed by the pump from the electric motor that drives it, the power necessary to provide pump-driven hydraulic cylinder. Presents the impact on the output (useful) power consumed in the considered systems, and the impact on the power consumed of the loss power in the individual

elements. Instantaneous useful power of the cylinder, which is determined by the product of force and speed of the cylinder rod is independent of all losses. There are mechanical loss power in the cylinder, loss power in the conduits, the structural volume and pressure loss power that are associated with the throttling control and loss power in the pump: pressure, volumetric and mechanical which have to be added to the useful power. As a result, the sum of the effective useful power and the loss power of all system is the instantaneous value of the power consumed by the pump from the electric motor that drives it.

This article presents a comparison of the loss power of the two systems – $p=cte$ and $p=var$. Diagrams show how the power lines P_{Mu} of the cylinder are running, the power lines ΔP of the loss power in the components and the power line P_{Pc} taken by the pump from the motor that drives it. The energy gains associated with the introduction of a variable pressure $p=var$ compared to the $p=cte$ pressure system are also presented.

The influence of power P_{Mu} on the power P_{Pc} in the systems under consideration as well as the influence on the P_{Pc} of the loss power ΔP on the individual components are presented. The P_{Mu} momentary power of the cylinder, which is determined by the product of the force F_M and the speed v_M of the cylinder rod, is independent of all losses. For the useful power P_{Mu} comes the mechanical loss power ΔP_{Mm} in the cylinder, the loss power ΔP_C in the conduits, the structural volume loss power ΔP_{stv} and the structural pressure loss power ΔP_{stp} associated with the throttling control and the losses in the pump: pressure loss power ΔP_{pp} , volume loss power ΔP_{pv} and mechanical loss power ΔP_{pm} . As a result of the sum of the useful power P_{Mu} and all loss power ΔP in the system, the instantaneous power P_{Pc} value that the pump requires from the electric motor driving it is obtained. Changing the structure from $p=cte$ to $p=var$, with the same useful power P_{Mu} , results in a significant decrease in structural loss power ΔP_{st} (Fig. 5).

The maximum achievable values of efficiency of systems with proportional (i.e. series throttling) control and of a system with volumetric control by a variable capacity pump are approximately similar. The compared systems were assembled from elements with the same k_i coefficients of energy losses.

By applying a variable pressure ($p=var$) system, a significant increase of the energy efficiency η can be achieved with smaller cylinder loads.

With small cylinder speed values, the effect of using a $p=var$ system is little, mainly due to volumetric losses connected with draining the excess liquid to the tank.

Optimization of hydrostatic systems means, among other aspects, a possibility of foreseeing the behaviour of an energy system in various conditions of its operation, as a function of speed and load of the hydraulic motor, working liquid viscosity, losses in the elements and particularly as an effect of the system structure. The common acceptance and use of the objective, experimentally verified methods of determining the system energy efficiency, looking at the efficiency of entire combined system, can clarify many misunderstandings, e.g. those pertaining to the problem of maximum efficiency of specific structures.

The Author intends to carry out further investigations of systems with proportional control, aimed at determining the influence of the working liquid (oil) viscosity on the energy efficiency.

NOMENCLATURE

- a – coefficient of pressure increase in the overflow valve or in the controlled overflow valve
- cte – constant
- f_{DE1} – throttling slot at the cylinder inlet
- f_{DE2} – throttling slot at the cylinder outlet
- F_M – hydraulic linear motor (cylinder) load, current force required of a linear motor
- F_{Mi} – force indicated on the piston of the hydraulic linear motor (cylinder)
- F_{Mm} – hydraulic linear motor mechanical losses
- F_{SP} – force of spring in the overflow valve
- k_1 – coefficient of relative volumetric losses per one shaft revolution of fixed capacity pump
- k_2 – coefficient of relative decrease in pump rotational speed
- k_3 – coefficient of relative pressure losses (flow resistance) in internal pump ducts, at theoretical pump delivery Q_{Pt}
- $k_{4.1}$ – coefficient of relative mechanical losses in pump, at $\Delta p_{pi}=0$
- $k_{4.2}$ – coefficient of relative increase of mechanical pump losses, at increase in pressure in pump working chambers
- k_5 – coefficient of relative pressure losses (flow resistances) in the line joining the pump with throttle control unit, at theoretical pump delivery Q_{Pt}
- $k_{6.1}$ – coefficient of relative pressure losses (flow resistances) in the line joining the throttle control unit with hydraulic motor, at theoretical pump delivery Q_{Pt}
- $k_{6.2}$ – coefficient of relative pressure losses (flow resistances) in hydraulic motor outlet line, at theoretical pump delivery Q_{Pt}
- $k_{7.1}$ – coefficient of relative mechanical losses in hydraulic motor – cylinder, at a force $F_M=0$
- $k_{7.2}$ – coefficient of relative increase of mechanical losses in motor – cylinder, at increase of force F_M
- k_8 – coefficient of relative pressure losses (flow resistances) in internal ducts of hydraulic motor, at theoretical pump delivery Q_{Pt}
- k_9 – coefficient of relative volumetric losses in hydraulic motor
- k_{10} – coefficient of relative minimum pressure decrease in 2-way flow control valve, which still ensures the flow regulation, or coefficient of relative pressure decrease in 3-way flow control valve
- k_{11} – coefficient of relative pressure decrease Δp_{DE} in directional control valve (servovalve, proportional valve) demanded by a maximum throttling section f_{DEmax} for receiving flow intensity equal theoretical pump delivery Q_{Pt}

\overline{M}_M – hydraulic motor relative load coefficient $\overline{M}_M = F_M / F_{Mn}$
 p_0 – the reference pressure in the oil reservoir
 p_1 – pressure at the cylinder feed proportional valve inlet
 p_2 – pressure in the outlet conduit from proportional valve to the cylinder
 $p_{1'}$ – pressure in the inlet conduit to the proportional valve from the cylinder
 $p_{2'}$ – pressure in the outlet conduit from proportional valve to the oil reservoir
 p_n – nominal (rated) working pressure of hydrostatic transmission (hydraulic system)
 p_{M1} – pressure in the inlet conduit to the cylinder
 p_{M2} – pressure in the outlet conduit from the cylinder
 p_{M1i} – pressure in the inlet chamber of the cylinder
 p_{M2i} – pressure in the cylinder discharge chamber
 p_{P1} – pressure in the pump inlet
 p_{P2} – pump supplying pressure
 p_{SP} – operating pressure overflow valve
 p_{SP0} – opening pressure overflow valve for ($Q_0=0$)
 p_{SPS} – operating pressure overflow valve controlled by the receiver inlet pressure
 Δp_{C0} – pressure drop in the inlet conduit to the pump
 Δp_{C1} – pressure drop in the inlet conduit to the control unit
 Δp_{C2} – pressure drop in the line between the control unit and cylinder
 $\Delta p_{C3'}$ – pressure drop in the outlet conduit from cylinder to the proportional valve
 $\Delta p_{C3''}$ – pressure drop in the outlet conduit of the cylinder from the proportional valve
 Δp_{DE1} – pressure drop in the proportional directional valve throttling slot f_{DE1} (at the cylinder inlet)
 Δp_{DE2} – pressure drop in the f_{DE2} proportional valve throttling slot (at the cylinder outlet)
 Δp_M – decrease of pressure (pressure drop) in hydraulic linear motor (cylinder)
 Δp_{Mi} – pressure drop indicated between inlet and outlet chamber of the cylinder
 Δp_P – increase of pressure in the pump
 Δp_{Pp1} – pressure drop in the inlet channel pump (and the distributor, if any)
 Δp_{Pp2} – pressure drop in the pump outlet duct (and the distributor, if there is one)
 Q_0 – intensity of flow directed through the overflow valve to the oil reservoir
 Q_M – hydraulic linear motor absorbing capacity, intensity of flow to hydraulic linear motor
 Q_{M2} – intensity of flow from the hydraulic linear motor (cylinder)
 Q_P – pump delivery
 η – energy efficiency
 S_{M1} – effective area of the hydraulic linear motor piston in its inlet chamber
 S_{M2} – effective area of the hydraulic linear motor piston in its outlet chamber
 SP – overflow valve

SPS – overflow valve controlled by the receiver inlet pressure
 var – variable
 v_M – hydraulic linear motor speed
 $\overline{\omega}_M$ – hydraulic linear motor speed coefficient – ratio of instantaneous speed to the nominal one of a hydraulic linear motor – $\overline{\omega}_M = v_M / v_{Mn}$

REFERENCES

1. Paszota Z.: *Energy-saving structures of hydrostatic drives for ship deck machines*. Polish Maritime Research, Vol. 7, No 1, 2000, pp. 3–9.
2. Paszota Z.: *Energy efficiency of hydraulic cylinders in servo-mechanism. Conference proceedings*. International XIX Scientific Conference of Naval Architects and Marine Engineers “Marine Technology on the Theshold of XXI Century – Marine Technology 2000”. May 4–6, 2000, Szczecin-Dziwnówek, Poland. Szczecin Technical University, Pol. Acad. Sci., Soc. Pol Naval Arch. Marine Eng. KORAB. 2000, pp. 139–147.
3. Paszota Z.: *Hydraulic proportional control of the cylinder with a variable pressure overflow valve – a model of the energy efficiency of the system*. Chapter in the monograph: “Research, design, manufacturing and operation of hydraulic systems”, Edward Palczak editor, “Cylinder” Library (in Polish), Centrum Mechanizacji Górnictwa „Komag”, Gliwice 2001, pp. 55–67.
4. Paszota Z.: *Energy – Saving Supply Structures of the Throttling Directional Control Valve in the System of Proportional Control of the Linear Hydraulic Motor*. [Proceedings] Viertes Deutch – Polnisches Seminar “Innovation und Fortschritt in der Fluidtechnik”, Sopot, 20–21 September 2001, Technische Universitat Warszawa, Fakultat fur Mechatronik, Institut fur Automatik und Robotik, pp. 90–100.
5. Paszota Z.: *Energy aspects of hydrostatic drives*. Polish Maritime Research, Vol. 10, No 2 2003, pp. 18–20.
6. Paszota Z.: *An Energy Behaviour Comparison of two Kinds of Hydrostatic Drive of Ship Deck Machines*. Brodogradnja – Journal of Naval Architecture and Shipbuilding Industry, Brodarski Institut Zagreb, Vol. 52, No 3, 2004, pp. 213–222.
7. Paszota Z.: *Model of losses and energy efficiency of a hydraulic system with proportional control of the cylinder fed by a constant capacity pump in a variable pressure system*. Chapter in the monograph: “Research, design, manufacturing and operation of hydraulic systems”, Edward Palczak editor, “Cylinder” Library (in Polish), Centrum Mechanizacji Górnictwa „Komag”, Gliwice, 2005, pp. 145–162.

8. Paszota Z.: *Energy Saving in a Hydraulic Servomechanism System – Theory and Examples of Laboratory Verification*. Brodogradnja, Journal of Naval Architecture and Shipbuilding Industry, Zagreb, Vol. 58, No 2, 2007, pp. 146–157.
9. Paszota Z.: *Power of energy losses in the hydrostatic drive system elements – definitions, relations, change ranges, energy efficiencies. Part II – Conduits, throttling control assembly, pump*, Chapter in the monograph: “Research, design, manufacturing and operation of hydraulic systems”, Andrzej Meder and Adam Klich editors, “Cylinder” Library (in Polish), Centrum Mechanizacji Górnictwa „Komag”, Gliwice, 2007, pp. 121–139.
10. Paszota Z.: *Graphical presentation of the power of energy losses and power developed in the hydrostatic drive and control system elements. Part I – Systems with the series throttling control of the hydraulic rotational motor speed*, Chapter in the monograph: “Research, design, manufacturing and operation of hydraulic systems”, Adam Klich, Edward Palczak and Andrzej Meder editors, “Cylinder” Library (in Polish), Centrum Mechanizacji Górnictwa „Komag”, Gliwice, 2008, pp. 121–139.
11. Paszota Z.: *Losses and energy efficiency of hydraulic motors and drive systems (in Polish)*. Drive and Control, No. 5, 2013, pp. 82–90.
12. Paszota Z.: *Losses and energy efficiency of drive motors and systems. Replacement of the Sankey diagram of power decrease in the direction of power flow by a diagram of power increase opposite to the direction of power flow opens a new perspective of research of drive motors and systems*. Polish Maritime Research, Vol.20, No 1 (77), 2013, pp. 3–10.
13. Paszota Z.: *Energy losses in hydrostatic drive. Monography*, LAP Lambert, Academic Publishing, 2016.
14. Skorek G.: *Energy characteristics of the hydraulic system with proportional control of cylinder, fed by a constant capacity pump in a constant pressure and variable pressure system (in Polish)*. Doctor dissertation. Gdansk University of Technology, Faculty of Ocean Engineering and Ship Technology, 2010.
15. Skorek G.: *Energy efficiency of a hydrostatic drive with proportional control compared with volumetric control*. Polish Maritime Research, Vol. 20, No 3 (79), 2013, pp. 14–19.
16. Quan Z., Quan L., Zhang J.: *Review of energy efficient direct pump controlled cylinder electro-hydraulic technology*. Renewable and Sustainable Energy Reviews, Elsevier, Vol. 35, 2014, pp. 336–346.

CONTACT WITH THE AUTHOR

Grzegorz Skorek

e-mail: grzesko@am.gdynia.pl

Phone: +48-58-55-86-484

Department of Engineering Sciences

Faculty of Marine Engineering

Gdynia Maritime University

Morska 81–87, 81-225 Gdynia

POLAND

A CONCEPT OF DETERMINING THE RELATION BETWEEN LOAD AND WEAR OF TRIBOLOGICAL SYSTEMS OF SHIP MAIN SELF-IGNITION ENGINES BY USING PROBABILISTIC APPROACH

Jerzy Girtler

Department of Land and Marine Power Plants, Faculty of Ocean Engineering and Ship Technology
Gdansk University of Technology

ABSTRACT

This paper presents a proposal of simultaneous consideration of load and wear associated with it, of tribological systems of ship main engines (intended for ship propulsion). Based on results of investigations it was assumed that both the load Q (i.e. a cause of wear) and the wear Z (i.e. an effect of load occurrence) considered in a given time t ($0 \leq t \leq t_n$) are random variables Q_t and Z_t , respectively. There was characterized operational principle of ship main engines in definite external conditions (WZ) as well as consequences of excessive load of engines. Three hypotheses highlighting relations existing between load and wear of the above mentioned systems, have been proposed. The first of them deals with explanation of stochastic relation between load and wear, the second highlights why it is possible to assume that the load Q_t and the wear Z_t are positively correlated, and the third – why it is possible to assume that coefficient of correlation between Q_t and Z_t may be taken close to one.

Keywords: combustion engine load, probability, stochastic process, self-ignition engine, random variable, statistical relation, stochastic relation

INTRODUCTION

Durability and reliability of any ship main engine depend first of all on wear of its crucial tribological systems such as main and crankshaft bearings as well as friction pairs of pistons and cylinder liners. Many factors affect such systems, but thermal and mechanical load applied to them [5, 11, 12, 13, 16, 18, 28, 29] are most important. Especially unfavourable effect onto wear of the systems results from excessive load generated during ship voyage in stormy weather conditions. Such loading may lead to extensive failures of the tribological systems of ship main engines in question, called damages [4, 12, 18, 27, 29]. It mainly concerns pistons and cylinder liners when the engine is forced to work with maximum output as well as main and crankshaft bearings in case when maximum combustion pressure values reach 18MPa and more and the

mean pressure rate of rise ($\varphi_{p(sr)}$) exceeds 1,2MPa/°OWK [18, 21, 22]. There is possible to predict an excessive wear of elements of the engines in question and consequently their failures by applying appropriate diagnosing systems intended for the generating of complete diagnoses, i.e. such which cover also a forecast of their technical state. The working out of such forecast requires a. o. to determine loads which may appear during service of the engines. Today the loads of combustion engines are usually analyzed by using deterministic approach, and less often – probabilistic one. In the last case they are very simplified and as a rule limited only to statistical analyses with application of point estimation of their expected values [1, 2, 11, 14, 17, 18, 23]. However, loads on ship combustion engines are random variables appearing in determined instants t which are not random variables. Therefore the loads considered in subsequent instants t ($0 \leq t \leq t_n$) as the

random variables Q_t form the loading process $\{Q(t) : t \geq 0\}$. Hence during their examination it is necessary to take into account that the loads following in succession form the stochastic process $\{Q(t) : t \geq 0\}$ whose values are the above mentioned random variables Q_t [1, 2, 4, 16, 29, 30]. Taking into consideration the random features of loads on ship combustion engines it is worthwhile initiating actions leading to determination of probabilistic relations between load and wear of the tribological systems in question, resulting in consequence of acting loads. Hence, the wear of such systems should be considered to be the stochastic process $\{Z(t) : t \geq 0\}$ whose values in arbitrary instants t ($0 \leq t \leq t_n$) are the random variables Z_t . As results from investigations, it is not possible to unambiguously determine values of wear (random variable Z_t), if value of random variable Q_t is known. It is necessary to assume that a stochastic relation exists between randomly varying loading (Q_t) and wear (Z_t), in an arbitrary instant t .

CAUSES AND CONSEQUENCES OF RANDOM VARIABILITY OF LOADING

The ship main engine (1) is able to transfer, by the propulsion shaft (2), kinetic energy from the screw propeller (3) whose task is generating the demanded thrust force T (Fig. 1). The force depends on the effective power (N_e) produced by the engine (1), and its rotational speed (n), hence also – on the rotational speed of screw propeller and ship hull resistance [20, 24, 25, 29]. The resistance overcome by the propeller thrust force T depends on the external conditions WZ (Fig. 2) randomly varying in a given instant t , and formed by such random factors as [6, 19, 25, 29]:

- 1) hydro-meteorological conditions: wind force and direction as well as sea state (height, length, speed and propagation direction of waves),
- 2) features of water area: its breadth and depth, the lay and kind of seabed (rocky, sandy),
- 3) kind of ship voyage: free moving, towing a ship,
- 4) ship hull position against water surface: draught, trim, heel,
- 5) state of underwater surface of ship hull: fouling of hull surface and its wear.

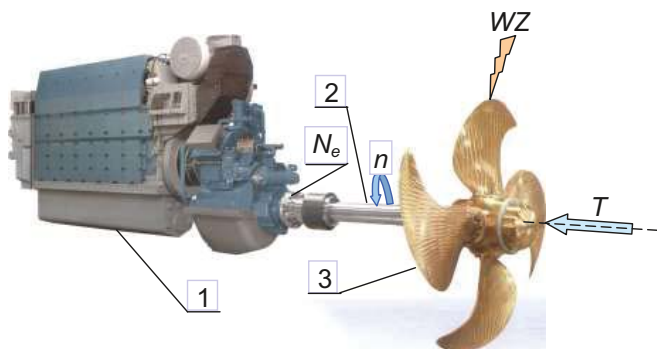


Fig. 1. Image of a ship propulsion system without reduction gear: 1 – ship main combustion, self-ignition engine, 2 – propeller shaft, 3 – screw propeller, N_e – effective power of the engine, n – rotational speed of the engine, WZ – external conditions, T – thrust force.

Energy conversion in working spaces of the ship main engine is aimed at developing the demanded effective power N_e as well as the rotational speed n of the engine and reaching such value of the propeller thrust force T in a given external conditions as to ensure a demanded speed of the ship. Large values of loads Q (mutually implicating thermal and mechanical ones) of engine tribological systems are then generated. The loads depend on ship speed and external conditions (mainly hydro-meteorological) in which transport tasks of the ship are executed. With increasing the rotational speed (n) of the engine and its effective power (N_e) and getting the external conditions (WZ) worse, the load on the engine increases. It is clearly illustrated in Fig. 2 where main engine speed characteristics (external, screw-propeller and governor ones) are presented. They made it possible to show an example change in the effective power (N_e) of the engine and its rotational speed (n) in accordance with the governor characteristics ($NR_{nom} = idem$). According to the characteristics, the power N_e and speed n will undergo a change from the point A to point B when the external conditions get worse from the state WZ_2 into WZ_3 . In the case when the conditions (WZ) get better from the state WZ_2 into WZ_3 , the engine power N_e and its rotational speed n will be determined by the point C. The above mentioned screw-propeller characteristics may be interpreted as follows: the external conditions WZ_3 are deemed the heaviest ones (stormy weather), WZ_2 – deal with less harsh ones, and WZ_1 – favourable conditions which may be formally written in the form of the inequality: $WZ_3 > WZ_2 > WZ_1$. Both the engine power N_e and its rotational speed (n) are random variables which characterize its loading [6, 7, 25, 29].

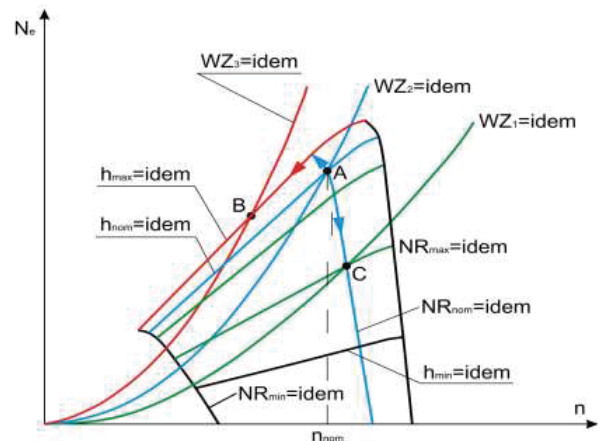


Fig. 2. Example characteristics of the main engine, which illustrate changes in engine load according to the governor characteristics $NR_{nom} = idem$: N_e – engine effective power, n – engine rotational speed, WZ – external conditions ($WZ_3 > WZ_2 > WZ_1$), NR_{min} – minimum setpoint of the governor, NR_{nom} – nominal (rated) setpoint of the governor, NR_{max} – maximum setpoint of the governor, h_{max} – maximum setpoint of the injection pump, h_{nom} – nominal (rated) setpoint of the injection pump, h_{min} – minimum setpoint of the injection pump, n_{nom} – nominal (rated) rotational speed of the engine.

In external conditions (WZ) varying from the most favourable (WZ_1) up to stormy ones (WZ_3), engine-propeller interaction within the range shown in Fig. 2 will run from

the point B to A and back in compliance with the governor characteristics $NR_{nom} = idem$ [4, 20, 24, 25, 29].

Ships very rarely sail in calm water. Usually during voyage ship rolling appears due to wind and wave action and in consequence many unwanted and dangerous phenomena follow, such as: drop of ship's speed and rise of ship hull resistance in waves, shipping of water, screw propeller emerging etc. This leads to increasing load on main engines and often their overloading which results in failures of their tribological systems, especially the cylinder liner-piston systems and rings as well as crankshaft bearings and crossheads [12, 30, 31]. Examples of such failures in ship main slow-speed large-output engines are presented in Fig. 3 ÷ 6.

Fig. 3. shows the damaged surface of piston and its sealing rings due to excessive friction wear of piston ring surface and significant damage of piston rings.



Fig. 3. Image of a piston damaged due to excessive friction wear of piston ring surface and significant damage of piston rings [30]

Fig. 4. shows the damaged surface of cylinder liner due to an excessive friction wear resulting from the seizing of piston in the cylinder.



Fig. 4. Image of the damaged surface of cylinder liner due to an excessive friction wear resulting from the seizing of piston in the cylinder [30]

Fig. 5. presents the damaged surface of crosshead pin resulting from an excessive wear due to friction and corrosion.



Fig. 5. Image of the damaged surface of crosshead pin resulting from an excessive wear due to friction and corrosion [30]

Fig. 6. illustrates the damaged surface of sliding coat of crank-end bearing sleeve due to its excessive friction wear.



Fig. 6. Image of the damaged surface of sliding coat of crank-end bearing sleeve due to its excessive friction wear [30]

Such damages endanger safety of ship at sea, especially when it executes transport tasks in stormy weather conditions. In the conditions extensive waving occurs, that makes keeping the proper course by the ship difficult. Therefore, the damages of the so crucial tribological systems as the crankshaft and crosshead system bearings and piston-ring-cylinder – liner friction pairs are, do not allow to deliver an appropriately large amount of power to the screw propeller. As a result, the screw propeller is not able to produce the demanded thrust force T . Lack of the force leads first to loss of course keeping (ship's capability of ensuring desirable direction of motion, e.g. perpendicular to wave direction) and then to its possible capsizing and sinking. Such situations may be prevented only in case of application of appropriate algorithms for prediction of technical states of the above mentioned tribological systems. However, such algorithms must have programs containing relations between wear of tribological systems of main engine and its load [3, 15, 28, 30].

RELATION BETWEEN WEAR OF TRIBOLOGICAL SYSTEMS OF MAIN ENGINE AND ITS LOAD

During ship voyage the external conditions WZ are varying (Fig. 2), and in extreme case, stormy weather conditions may be encountered. Fig. 7 illustrates such heavy weather conditions in which a ship continues navigation.



Fig. 7. Illustration of sea state in which a ship continues navigation

Random features of load and wear of a. o. tribological systems of ship main engines and their impact onto change of their technical state are generally presented in [8]. There was possible to demonstrate that the theory of semi-Markov processes may be applied to working out a four-state model of changes in technical states of the engines in question, which are crucial for safety of the entire ship. However, for diagnostic purposes to present more strict relations between load and wear of the engines is necessary. First of all, to formulate such relations there should be taken into account the fact that between the load Q and the wear Z mutual cause-effect relations do exist. For instance, the load Q (as a cause) results in the wear Z (i.e. an effect), but when it is important not to allow for occurrence of a failure in a tribological system (hence in the engine itself), then the wear Z (being now a cause) forces the engine's operator to mitigate the load Q (being now an effect). Because of the randomness of the load, the wear Z of tribological systems shows also random nature [9].

Interpretation of the wear occurring in such systems is presented in Fig. 8, based on Lorence curve [8, 28].

In Fig. 8. there are presented with thin lines various wear realizations $z(t)$ of five tribological systems, according to the publications [3, 9, 10, 12, 16, 23, 27]. As results from this figure, in an arbitrary instant t the wear of such systems is the random variable Z_t . Therefore, to every instant t , the random variable Z_t of the expected value $E(Z_t)$, depending on t -value, can be attributed. It means that the wear considered in function of time t is the random function $Z(t)$ forming a set of the random variables Z_t . The function is hence the stochastic process $\{Z(t) : t \geq 0\}$. The expected value $E[Z(t)]$ of the process is distinguished with bold line in this figure. The value is determined by a set of the expected values $E(Z_t)$ for every instant t . Worth mentioning that the expected value $E[Z(t)]$ of the stochastic process $\{Z(t) : t \geq 0\}$ depends on the time t , because the values $E(Z_t)$ are different for different instants t . However, it is not possible to take the expected value $E[Z(t)]$ to be random function since for a given value t the values $E(Z_t)$ are constant, i.e. for a definite value t the value $E(Z_t) = \text{const}$ [2, 4, 14, 16, 17].

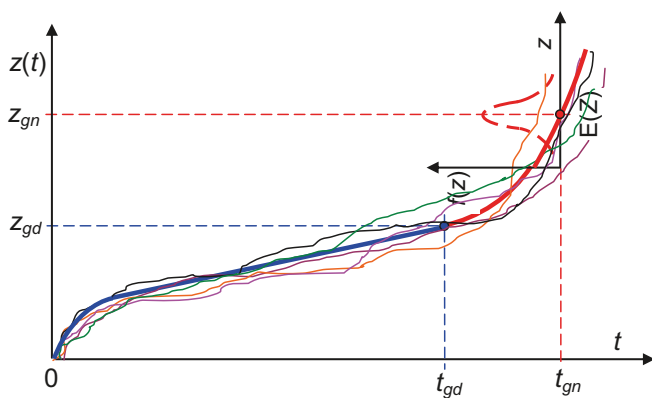


Fig. 8. Example interpretation of tribological system wear: z – wear; z_{gn} – impermissible limit wear; z_{gd} – permissible limit wear; t_{gn} – time to occurrence of z_{gn} ; t_{gd} – time to occurrence of z_{gd} ; t – operational time of tribological system, $f(z)$ – density function of wear, $E(Z)$ – expected value of wear

The loading process of the tribological systems of the engine $\{Q(t) : t \geq 0\}$ on which the mentioned process $\{Z(t) : t \geq 0\}$ depends, may be considered in a similar way [9].

In case if it were possible and reasonable to take into account all factors affecting the load Q and wear Z resulting from it, then the relation between Z and Q could be described by algebraic equations. Then the dependence of Z on Q would be a functional relation.

However such case is not possible to occur for the following reasons, a. o.:

- not all the factors affecting load and wear of engine's tribological systems are known and not all – measurable quantities,
- the taking into account a large number of factors may complicate considerations to such a degree that it would be impossible to carry out them even with using contemporary computer technique.

In this case a combined consideration of the load Q and wear Z implicated by it, requires to consider the random variable U which is a two-dimensional random variable (Q, Z) . In view of that measurements are conducted from time to time only the random variables Q and Z are step like (not continuous), whose realizations are q and z , respectively. Hence, the pair (q, z) is the realization of the random variable (Q, Z) . Therefore the variable takes values (q, z) with a definite probability $p(q, z)$, i.e. the probability of simultaneous occurrence of the events: $Q = q$ and $Z = z$.

The set of the mentioned probabilities $p(q, z)$ constitutes the two-dimensional distribution of the random variable (Q, Z) , which satisfies the following condition [1, 9, 1]:

$$\sum_{i=1}^r \sum_{j=1}^r p(q, z) = 1 \quad (1)$$

The boundary distribution of the random variable Q is the following:

$$p(q) = \sum_{j=1}^r p(q, z) \quad (2)$$

And, the boundary distribution of the random variable Z has the following for:

$$p(z) = \sum_{i=1}^r p(q, z) \quad (3)$$

In view of that the load (Q) and wear (Z) considered in the instant t ($0 \leq t \leq t_n$) are random processes it can be concluded that a stochastic relation between their values Q_t and Z_t should be expected. In order to highlight the relation, the following hypothesis H_1 may be formulated: „a stochastic relation exists between the load Q_t and wear Z_t of an arbitrary tribological system of ship main engine because definite variants of one of the random variables are accompanied by different

variants of the second variable". Hence it can be concluded that the relation between the load $Q(t)$ and wear $Z(t)$ cannot be described by algebraic equations. The conclusion seems to be true as the load depends on a large number of factors including also those which cannot be measured [4, 5, 13, 16, 18, 26]. A degree of dependence between the variables essential in this case, i.e. intensity (strength) of stochastic relation between Q and Z can be determined by using Czuprow convergence coefficient (4). Therefore during empirical investigations the strength of the stochastic relation between Q and Z may be determined by making use of the following relation [1]:

$$T_{MC}^2 = T_{CM}^2 = \frac{\chi^2}{N\sqrt{(k-1)(l-1)}} \quad (4)$$

where:

k – number of variants of the variable Q ; l – number of variants of the variable Z , N – limit number of variants of the variable Q or Z , χ^2 – a value calculated from the chi-square formula, $T_{(0)}^2$ – Czuprow convergence coefficient. It can be proved, [14], that T_{MC} takes values from the interval $[0,1]$. The coefficient is equal to zero ($T_{MC} = 0$) when there is no relation between values (Q and Z) of the process, while the coefficient equal to one ($T_{MC} = 1$) demonstrates that such relation exists. To state if the random variables Q and Z are dependent is possible by examining the probabilities defined by the formulae (1) ÷ (3).

The necessity of searching for stochastic relation between Z and Q may be substantiated also graphically by using the example stochastic relation between the load q and wear z , presented in Fig. 9.

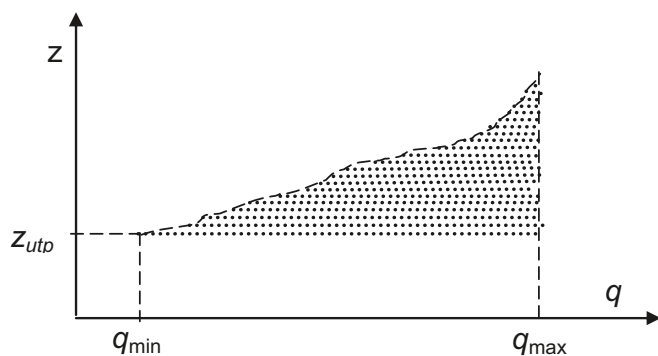


Fig. 9. Graphical interpretation of the example stochastic relation between the load q and wear z ; z_{utp} – wear (small) resulting from oxidation during liquid friction, q_{min} – minimum load, q_{max} – maximum load

Investigation of a stochastic relation between load (Q) and wear (Z) may be very difficult when their distributions (also conditional ones) greatly differentiate to each other by variability, concentration and asymmetry. In such case it is better to examine a statistical relation between Q_t and Z_t . Then it is possible to assign, to particular values of one of the variables, mean value of the other variable [14].

Analyzing values of states of the processes $\{Q(t): t \geq 0\}$ and $\{Z(t): t \geq 0\}$ in an arbitrary instant t , one is able to state that there exists stochastic relation between value (state) of the load Q_t and value (state) of the wear Z_t (being random variables in the instant t). The fact that such relation between the random variables exists does not mean that knowing a value of the random variable Q_t (cause) one is able to unambiguously determine a value of the random variable Z_t (effect). Such unambiguous dependence could be stated only in the case of existence of a dependence of these variables in usual sense or by assuming that Q_t and Z_t are random variables which constitute values (states) of the deterministic processes $Q(t)$ and $Z(t)$, i.e. those having prediction error equal to zero.

A stochastic dependence between the variables Q_t and Z_t should be meant as an influence of one of the variables, e.g. Q_t on distribution of the other variable, i.e. Z_t or vice versa, namely – an influence of the variable Z_t on distribution of the variable Q_t . It means that a correlation between the random variables exists.

In the case if the random variables Q_t and Z_t were not independent then their boundary distributions would not differ from conditional ones. In view of that the load Q_t and the wear Z_t are measurable in an arbitrary instant t ($0 \leq t \leq t_n$), they can be considered to be step-like random variables. They can be considered this way because both the measurement operations performed to find their values and the measuring instruments make it possible to obtain discrete values from the measurements. In view of that, to state independence of the random variables Q_t and Z_t it is possible to use conditional probabilities and unconditional ones by employing the following relations [1, 14, 17]:

$$p(q_i/z_j) = p(q_i); \quad p(z_j/q_i) = p(z_j) \quad (5)$$

hence

$$p(q_i/z_j) = p(q_i)p(z_j) \quad (6)$$

Therefore in case if the random variables Q_t and Z_t fulfil the condition (6) it will mean that they are stochastically independent random variables, otherwise they must be considered stochastically dependent, i.e. correlated.

The random variables Q_t and Z_t may be also considered continuous random variables. Then, in case of their independence, the following formulae are obtained [1, 14, 17]:

$$f(q/z) = f(q) \text{ oraz } f(z/q) = f(z) \quad (7)$$

hence

$$f(q, z) = f(q)f(z) \quad (8)$$

and

$$f(z) = \int_{\beta}^{\infty} f(q, z) dq \quad (9)$$

$$\text{where } \beta = \begin{cases} -\infty & \text{for oscillating loads} \\ 0, & \text{for pulsating loads} \end{cases}$$

The conditional expected values for a definite instant t : $E(Q/z)$ and $E(Z/q)$ are then equal to the unconditional expected values, namely [1, 14, 17]:

$$E(Q/z) = E(Q) = m_{1Q}; \quad E(Z/q) = E(Z) = m_{1Z} \quad (10)$$

Also, the conditional variances $D^2(Q/z)$ and $D^2(Z/q)$ are then equal to respective unconditional variances, i.e.:

$$D^2(Q/z) = D^2(Q) = \delta_Q^2; \quad D^2(Z/q) = D^2(Z) = \delta_Z^2 \quad (11)$$

And, the covariance is then equal to zero, i.e.:

$$\text{Cov}(Q, Z) = K(Q, Z) = E(Q, Z) - E(Q)E(Z) = 0 \quad (12)$$

Making use of the formulae (6) and (8) one can show that when the random variables Q and Z are independent to each other, then:

$$E(Q, Z) = E(Q)E(Z) \quad (13)$$

i.e. according to the formula (12):

$$K(Q, Z) = 0 \quad (14)$$

When the random variables Q and Z are independent then, taking into account their features, one can also write that [1, 16]:

$$D^2(Q + Z) = D^2(Q) + D^2(Z) \quad (15)$$

The relations (12)-(15) may be also applied in the case when value of the wear Z is signalled by a diagnostic symptom of the wear which is a physical quantity not susceptible to changes in values of the load Q . When the conditions (6) and (12) are not fulfilled, i.e. when the conditional distributions of the random variables Q and Z are differ from the boundary distributions, then it means that the random variables are correlated to each other (i.e. a stochastic relation exists between them). In such case the conditions (10) and (11) are also not fulfilled. Therefore, the following relations exists:

$$E(Q/z) = F(z) \quad (16)$$

$$E(Z/q) = F(q) \quad (17)$$

$$D^2(Q/z) < D^2; \quad D^2(Z/q) < D^2 \quad (18)$$

$$K(Q, Z) = E(Q, Z) - E(Q)E(Z) \neq 0 \quad (19)$$

The relation (16) is a regression equation of the variable Q against the variable Z , whereas the relation (17) is a linear equation of regression of the variable Z against the variable Q . In the case of the maximum coupling of the random variables Q and Z their regression lines coincide. If they are straight lines (i.e. when influence of the load Q on conditional expected value of the wear Z is constant), they form one straight line of the slope factor $\delta = \frac{\sigma_Z}{\sigma_Q}$. In the case when the variables Q and Z are σ_Q independent then the regression lines (being straight lines) are parallel to coordinate axis and cross the point of the coordinates (m_{1Q}, m_{1Z}) . Fig. 10 shows an example course of the regression lines.

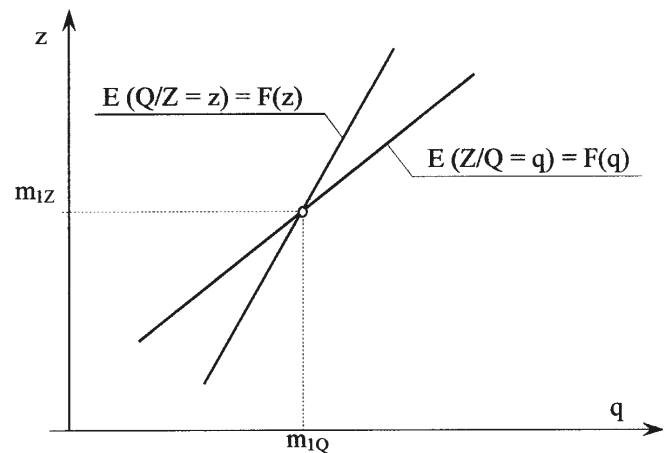


Fig. 10. Graphical illustration of the course of regression straight lines: $m_1 - 1^{st}$ order zero moment (expected value), $m_{1Z} = E(Z)$, $m_{1Q} = E(Q)$, respectively; $E(Q/Z=z)$ - expected value of the variable Q dependent on the value z of the variable Z , $E(Z/Q=q)$ - expected value of the variable Z dependent on the value q of the variable Q , z - realization of the variable Z (wear), q - realization of the variable Q (load).

As a correlation measure (mutual dependence) of the random variables Q and Z the correlation coefficient r_{QZ} (i.e. covariance of the standardized random variables Q^* and Z^*) determined by using the relation [1, 3, 14, 17], may also serve:

$$r_{QZ} = \frac{K(Q, Z)}{\sigma_Q \sigma_Z} \quad (20)$$

and:

$$Q^* = \frac{Q - E(Q)}{\sigma_Q}, \quad Z^* = \frac{Z - E(Z)}{\sigma_Z}$$

The use, in addition, of the correlation coefficient makes it possible to determine whether the correlation is positive or negative. As results from the presented considerations it should be positive.

In the case when the random variables Q and Z are independent, then $r_{QZ} = 0$. For the random variables Q and Z the coefficient takes values from the interval $(0, 1]$, i.e.:

$$0 < r_{QZ} \leq 1 \quad (21)$$

if generally increasing value of the wear Z is associated with increasing values of the load Q . The occurrence of such case means that a positive correlation between the load Q and the wear Z exists.

Hence, the following hypothesis H_2 may be postulated: **the load of an arbitrary tribological system of engine, in the time t , constitutes the random variable Q_t positively correlated with its wear, i.e. the random variable Z_t , because with the load increasing the wear of the engine grows.**

The presented hypothesis may be considered equivalent to the following hypothesis H_3 : **the wear of a tribological system of engine and its load are, in an arbitrary instant of its working time (t), random variables between whose such relation exists that the correlation coefficient $r_{QZ} \approx 1$, because the engine wear increases first of all with increasing the load.**

As results from the considerations, correlation (stochastic dependence) between random variables which stand for the load Q and the wear Z may be determined by using:

- a) regression lines which illustrates the dependence of mean value of one of the variables on value of the other of the variables in question, i.e.: $E(Q/Z = z)$ and $E(Z/Q = q)$;
- b) correlation coefficient defined by the relation (20).

Achievement of zero-value of the correlation coefficient ($\rho_{QZ} = 0$) is a prerequisite, but not a sufficient condition to deem the random variables Q and Z to be independent on each other if their distributions are different from normal. Zero- value of the coefficient does not prove that the random variables are independent if they do not have normal distributions. Possession of zero-value of the correlation coefficient ρ_{QZ} is the sufficient condition for considering random variables independent only if their distributions are normal [2, 14, 17].

FINAL REMARKS AND CONCLUSIONS

In this paper there was undertaken an attempt to determine relation between load and wear of tribological systems of an arbitrary ship main engine (intended for ship propulsion) by applying probabilistic approach. It was justified that application of such approach is necessary in view of a random character of load exerted on ship main engine by ship screw propeller driven by the engine. There were presented examples of excessive wear suffered by selected tribological systems of such engines, in consequence of their loading in highly unfavourable (stormy weather) conditions. It was signalled that the load depends on many factors, mainly hydrological conditions, which results in that a stochastic relation between load and wear of the mentioned tribological systems, exists. For examination of intensity (force) of the stochastic relation it was proposed to use Czuprow convergence coefficient.

In this paper it was proved that in investigations of tribological systems of an arbitrary ship main engine in an arbitrary instant t it should be strived to express probabilistically relations which occur between their load Q and wear Z .

It was proposed to consider the load Q and wear Z to be a two-dimensional random variable (Q, Z) by assuming that the variables Q and Z are step – like (non-continuous) variables or continuous random variables; however it was also mentioned that to examine a relation between step-like variables is simpler.

In the presented considerations it was proved that load and wear in an arbitrary instant t should be considered to be realizations of the load process $\{Q(t): t \geq 0\}$ and the wear process $\{Z(t): t \geq 0\}$. The realizations $(Q_t$ and $Z_t)$ should be examined assuming that they are random variables. In the case of the process $\{Q(t): t \geq 0\}$ its realizations are the random variables Q_t of the expected value $E(Q_t)$ and variance $D^2(Q_t)$, while in the case of the process $\{Z(t): t \geq 0\}$ its realizations are the random variables Z_t of the expected value $E(Z_t)$ and variance $D^2(Z_t)$. Hence, the variables are values (states) of these stochastic processes.

There were proposed the hypotheses highlighting the facts that a stochastic relation between load and wear exists and that it is possible to assume that the load Q_t and wear Z_t are positively correlated to each other with a correlation coefficient whose value may be taken close to one.

BIBLIOGRAPHY

1. Benjamin J. R., Cornell C. A.: Probability calculus, mathematical statistics and decision theory for engineers (in Polish). WNT, Warsaw, 1977.
2. Firkowicz S.: Statistical assessment of quality and reliability of electron tubes (in Polish). WNT, Warsaw, 1963.
3. Gercbach I.B., Kordonski Ch.B.: Reliability models of technical objects (in Polish). WNT, Warsaw, 1968.
4. Girtler J.: Steering the operation process of ship combustion engines on the basis of diagnostic decision model (in Polish). Zeszyty Naukowe AMW, No. 100A, Gdynia, 1989.
5. Girtler J.: Stochastic model of load spectrum of self-ignition engine (in Polish). Zagadnienia Eksploatacji Maszyn. PAN quarterly, iss. 1/97, 1994.
6. Girtler J., Kitowski Z., Kuriata A.: Safety of ship at sea. System approach (in Polish). WKiŁ, Warsaw, 1995.
7. Girtler J., Kuzmider S., Plewiński L.: Selected issues of operation of sea-going ships in the aspect of safety of navigation (in Polish). A monograph. WSM (Szczecin Maritime University), Szczecin, 2003.
8. Girtler J.: Features of load and wear of main propulsion devices on sea-going ships with piston combustion engines and their impact on changes in technical states of the systems. Polish Maritime Research. No. 4(96), Vol. 24, pp.57-66.

9. Girtler J.: Identification of damages of tribological associations in crankshaft and piston systems of two-stroke internal combustion engines used as main propulsion in sea-going vessels and proposal of probabilistic description of loads as causes of these damages. Polish Maritime Research. No. 2(86), Vol 22, pp. 44-54.
10. Jaščericyn P.I., Skorynin Ju.V.: Rabotosposobnost' uzlov trenija mašin (in Russian) . Nauka i Technika, Minsk,1984.
11. Karpov Ł.N.: Nadežnost' i kaczestwo sudovych dizelej (in Russian) . Transport, Moscow, 1985.
12. Kondratev N.N.: Otkazy i defekty sudovych dizelej (in Russian). Transport, Moscow, 1985.
13. Kozłowiecki H.: Bearings of piston combustion engines (in Polish). WKiŁ, Warsaw,1982.
14. Krzysztofiak M., Urbanek D.: Statistical methods (in Polish). PWN, Warsaw, 1979.
15. Michlin V.M.: Prognozowanie techničeskogo sostojanija mašin (in Russian) . Kołos, Moscow,1976.
16. Niewczas A.: The rudiments for stochastic model of friction wear in issues of durability of machine elements (in Polish) . Zeszyty Naukowe, Mechanika No. 19, Politechnika Radomska, 1989.
17. Pawłowski Z.: Mathematical statistics (in Polish). PWN, Warsaw, 1980.
18. Piotrowski I.: Ship combustion engines (in Polish). WM, Gdańsk, 1971.
19. Rudnicki J.: Application issues of the semi-Markov reliability model. Polish Maritime Research. No. 1(85)/2015, Vol. 22, pp. 55 – 64.
20. Urbański P.: The rudiments of ship propulsion (in Polish). Fundacja Rozwoju Akademii Morskiej, Gdynia, 2005.
21. Wajand J.A.: Self-ignition engines (in Polish). WNT, Warsaw 1980.
22. Wajand J.A., Wajand J.T.: Piston combustion engines of medium – and high – speed (in Polish). WNT, Warsaw, 2005.
23. Włodarski J.K.: Piston combustion engines .Tribological processes (in Polish) . WKiŁ, Warsaw, 1981.
24. Wąsowicz J.: Ship power plants. Part 1 (in Polish). AMW, Gdynia, 1972.
25. Wojnowski W.: Ship combustion power plants. Part 1 and 2. (in Polish). AMW, Gdynia, 1999.
26. Voinov A.N.: Sgoranie v bystrochodnych poršnevych dvigateljach (in Russian). Mašinostroenie, Moscow, 1977.
27. Voznickij I.B., Ivanov Ł.A.: Predotvraščenie avarij sudovych dvigatelej vnutrennego sgoranija (in Russian). Transport, Moscow, 1971.
28. Zwierzycki W. at al.: Selected issues of the wearing-out of materials in slide units of machines (in Polish). PWN, Warsaw-Poznań, 1990.
29. Girtler J.: Identification of working conditions of piston – crankshaft systems of ship main engines . (in Polish). Stage report from realization of the research project, titled: „Decision steering the operation process of piston – crankshaft systems of ship main engines with the use of technical diagnostics as well as with taking into account safety and environment protection”, conducted in the frame of the project No. N N509 494638 finacially supported by MNiSW. Supervisor: Prof. J. Girtler. Research report No.1/10 /PB. Faculty of Ocean Engineering and Ship Technology, Gdansk University of Technology, Gdańsk, 2010.
30. Girtler J., Łosiewicz Z: Analysis of features of a diagnostic model of of piston – crankshaft systems of engines, which is adjusted to needs of the rational steering of operation of the engines in the aspect of ship safety and sea environment protection (in Polish). Stage report from realization of the research project, titled: „Decision steering the operation process of piston – crankshaft systems of ship main engines with the use of technical diagnostics as well as with taking into account safety and environment protection”, conducted in the frame of the project No. N N509 494638 finacially supported by MNiSW. Supervisor: Prof. J. Girtler. Research report No.61/10 /PB. Faculty of Ocean Engineering and Ship Technology, Gdansk University of Technology, Gdańsk, 2010.
31. Włodarski J. K. at al.: Analysis of failure frequency of crankshafts and their bearings in A25 engines (in Polish). WSM, Gdynia,1987. Unpublished.

CONTACT WITH THE AUTHOR

Jerzy Girtler

e-mail: jgirtl@pg.gda.pl

Department of Land and Marine Power Plants
Faculty of Ocean Engineering and Ship Technology
Gdansk University of Technology
G. Narutowicza 11/12
80-233 Gdańsk
POLAND

RELIABILITY BASED ANALYSIS AND DESIGN OF A TRIPOD OFFSHORE WIND TURBINE STRUCTURE ASSURING SERVICEABILITY PERFORMANCE

Jianhua Zhang¹

Won-Hee Kang²

Chunwei Zhang^{3,2}

Ke Sun¹

¹ Harbin Engineering University, Harbin, China

² Western Sydney University, Sydney, Australia

³ Qingdao University of Technology, Qingdao, China

ABSTRACT

Typical tripod foundations are designed using deterministic computational models according to relevant standards and codes. However, for more cost-safety balanced design, uncertainties in significant parameters should be considered in preliminary design to ensure meeting a specific probabilistic safety target in the context of the complex configuration of a tripod structure. In this article, uncertainties associated with design parameters and modelling errors are considered using Monte Carlo simulations, in order to determine the key structural design parameters, and to determine the optimal balance between design parameters and design requirements. A Spearman rank-order correlation based analysis is carried out to understand the effects of design variables on maximum deformation, total weight, and natural frequency, and to have insight about important design parameters for improvement of a preliminary design. It is found that the tower diameter has the most significant effect on the maximum displacement on the hub as validated through engineering case studies. In addition, a statistical framework, which identifies influential design parameters and provides reliability evaluation, is proposed for the structural design of a tripod OWT system. The design cases considered in this study indicate that a simple deterministic design check cannot guarantee the required reliability level of the structure, and the cost-safety balance can be achieved by a reliability analysis with the consideration of the uncertainties in the structure.

Keywords: Offshore wind turbine; tripod foundation; serviceability limit state; statistical correlation analysis; reliability analysis

INTRODUCTION

An offshore wind turbine (OWT) is the main device to generate energy in wind farms. It consists of a long slender column, a heavy mass, and a rotating mass at the top. The foundation is a supporting structure for an OWT, which transfers all loads from the OWT to the ground with allowable deflection. The allowable deflection is considered in the serviceability limit state (SLS) in the design of an OWT, and the tilt at the hub lever should be controlled according to the allowable limit stipulated in engineering codes such as DNVGL-ST0126 [1] and API [2]. If the tilt exceeds the allowable limit, an OWT needs to be shut down.

Foundations for OWTs are generally classified into fixed and floating types, and most of the currently installed and operating turbines are mounted on a fixed foundation [3]. The fixed foundation includes gravity-based, mono-pile, tripod, jacket and suction bucket. Among them, tripod foundations show good potential for OWTs due to their good stability and overall stiffness in water depth ranging from 20 to 40 m. For example, they were successfully installed in Borkum West 2, Global Tech 1, and Alpha Ventus wind farms [4].

To achieve a cost-safety balance for the structural design of the foundations of OWTs, a significant amount of studies in terms of analysis and design of tripods have been carried out in recent years including the following studies: Haskell et al. [5] adopted a pseudo-static analysis

method to explore the effects of statistical variation of the model parameters on the predicted pile response by means of sensitivity analyses. Lozano-Minguez et al. [6] used a systematic assessment methodology to select the most preferable configuration among a mono-pile, a tripod, and a jacket considering environmental and economic aspects. In order to minimize the damage to a tripod type OWT-substructure caused by collisions with a boat, the influence of impact on the structure and the performance of a rubber fender for impact prevention were investigated by Lee [7]. Yu et al. [8] conducted a group of earthquake centrifuge tests on a physical model of a wind turbine with tripod foundation. They mentioned that the tripod foundation can provide better resistance in the lateral displacement and structural settlement under earthquake loading. Yeter et al. [9] carried out a spectral fatigue damage prediction and an assessment of tripod offshore wind turbine support structure subjected to combined stochastic waves and winds.

It is unavoidable to consider uncertainties in the design of a support structure, which exist in the strength and stiffness due to natural randomness of materials, in the resistance prediction model, and in the environmental loads. The modeling of uncertainties can be achieved by using fully probabilistic approaches [10] or semi-probabilistic approaches [11]. Consequently, the structural response of the support structure needs to be probabilistically analyzed or, at least, it is desired to investigate the effects of uncertain input parameters, to determine the most significantly affecting parameters [12, 13], and to reduce the number of uncertain variables which leads to improving design efficiency. In this regards, Andersen et al. [14] developed a methodology considering the uncertainties of the soil properties to estimate the natural frequency of a simple OWT model on a mono-pile foundation. Nour El-Din and Kim [15] investigated the sensitivity of the seismic response with respect to the uncertain modeling variables of a jacket platform using Tornado diagram and first-order second-moment techniques. Lee et al. [16] presented a reliability-based optimization method for a mono-pile transition piece in an offshore wind turbine system. Yang et al. [17] proposed a reliability based design optimization methodology for a tripod of OWTs considering dynamic response requirements to decrease weight and cost of a foundation. Vahdatirad et al. [18] considered the uncertainties regarding soil properties and proposed an asymptotic sampling method to estimate the probability distribution of stiffness for the OWT on a mono-pile foundation. However, the uncertainties related to the model and structural properties were not considered in that study.

By practically extending these previous studies on reliability analysis and deterministic parameter prioritizing analysis to the structural design of an OWT, this study proposes a statistical framework for a structural design of a tripod OWT foundation system, which includes the reliability evaluation of the structure and the statistical correlation analysis for design parameters. The proposed framework highlights a reasonable engineering judgment

and understanding for structural design of tripod foundation. This study is a significant extension of a preliminary study in Zhang et al. [19], which combined nonlinear finite element method and Monte Carlo simulations to perform sensitivity analysis of key design parameters on the mechanical behavior of a tripod foundation.

DESCRIPTION OF SUPPORT STRUCTURES

TRIPOD GEOMETRIES

Fig. 1 shows a sketch of a tripod structure for a 3MW OWT. The tripod structure is analyzed at a water depth of 20 m, and it consists of a central column, three pile sleeve legs, three top braces, and six mud braces. Piles are installed at the legs to anchor the tripod to the seabed. The tripod top and bottom are 10 m and -20 m above the mean sea level (MSL). The base of the tripod has the area of 22 m × 22 m. The upper conical tower mounted on the tripod is 79.5 m high, and the hub elevation is 89.5 m above the MSL. The turbine is modeled according to the conventional upwind, variable speed, and collective pitch horizontal axis.

UPPER TOWER STRUCTURE

For convenient transportation and erection, the entire tower is designed as an assembly of four sections, as shown in Fig. 1(c), which shows four pieces of thin-wall cylindrical and conical parts. The pieces have diameters of 4740 mm at the base and 2860 mm at the top. The diameters linearly vary along the height. Each piece has a different thickness as indicated in Fig. 1(c). Circular stiffeners are placed at regular intervals along the height of the tower, and they are welded together along their perimeters.

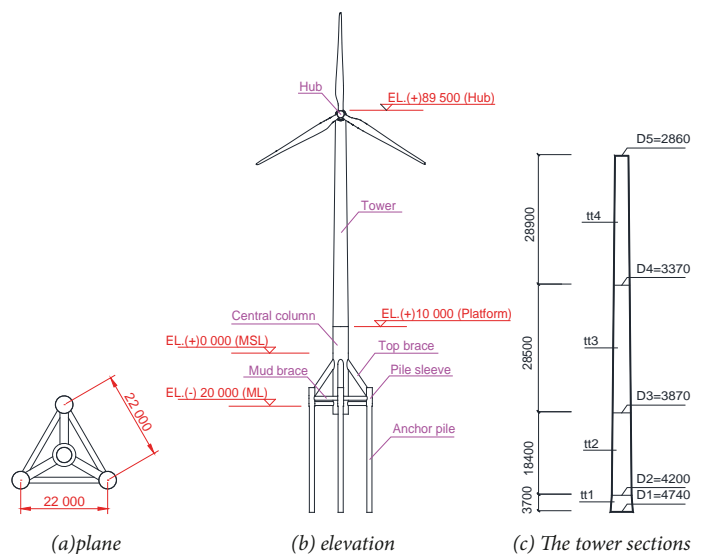


Fig. 1. Sketch map of tripod foundation

FINITE ELEMENT MODELING

A Finite Element (FE) model of the tripod is created in a commercial nonlinear FE code ANSYS, as shown in Fig. 2. *Pipe 59* element is chosen for pile sleeve, mud brace, top brace, and central column. *Beam 188* is chosen for the tower part; and *Mass* element is chosen for nacelle and rotor. Young's modulus, yield strength and Poisson's ratio of steel are 210 GPa, 355 MPa and 0.3 respectively. The pile-soil interaction (PSI) is simulated using *Combine 39* element and soil-pile springs, along the pile penetration length. The model simplifies the interaction between soil and pile by assuming that there is no dependency between the displacements of springs. The lateral soil stiffness is modeled using the p - y curve approach, which is described in API [2]. In this curve, the nonlinear relationship between lateral soil reaction (p) and lateral pile displacement (y) can be established and defined in *Combine 39* element by force-deformation (F - D) relationship where F is the total force applied along the length of the pile. The lateral stiffnesses of soil from -8 m to -14 m depth are calculated using p - y curves as shown in Fig. 3.



Fig. 2. FE model of the tripod

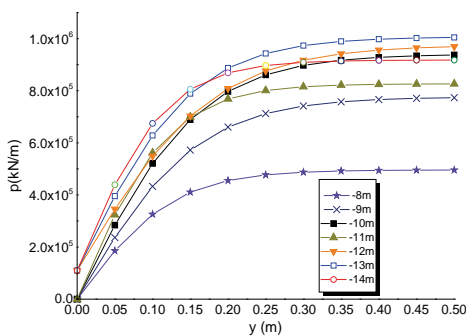


Fig. 3. P-Y curve for soil between -8 m and -14 m

APPLIED LOADS

OWTs are often exposed to the harsh marine environment, and load combinations required for limit states such as ultimate limit state (ULS) and serviceability limit state (SLS) need to be rigorously considered in the design phase. Essential information regarding the selection of characteristic

loads is described in standards and regulations such as DNVGL-ST0126 [1] and IEC [20]. In this study, the primary loads including wind load, wave, current load, and gravity are considered, and load simplifications have been made as provided in the following sub-sections.

Wind loads

Wind loads include loads on the rotor and the tower. The wind loads on an impeller can be obtained from the blade element theory and dynamic stall, dynamic wake model. Aerodynamic properties of blades were obtained from reference [21].

The wind loads distribution along the altitude of the tower is expressed as follows:

$$f(z) = \frac{1}{2} C_d \rho D V^2(z) \quad (1)$$

where ρ is the density of air, which is 1.225 kg/m^3 , C_d is drag coefficient, D is the diameter of the tower, and $V(z)$ is wind speed (in meters per second) at height z (in meters) and can be calculated using the following formula:

$$V(z) = \left(\frac{z}{z_{ref}}\right)^m V(z_{ref}) \quad (2)$$

where $V(z_{ref})$ is the known wind speed at the reference height z ; the exponent m is an empirically derived coefficient that varies depending on the stability of the atmosphere. In this study, m is taken to be 0.143.

Wave loads

For a slender structure such as a pile in a tripod, a diffraction effect is negligible for waves, and the Morison formula can be applied to the wave force. The horizontal force applied to the element of the cylinder at level z is expressed as:

$$dF = dF_m + dF_d = C_m \rho \pi \frac{D^2}{4} \dot{u}_w dz + C_d \rho \frac{D}{2} |u_w| u_w dz \quad (3)$$

where the first term (dF_m) is an inertia force, and the second term (dF_d) is the drag force. C_m and C_d are the inertia and quadratic drag coefficients, respectively. ρ is the water density, and D is the diameter of a structural member. \dot{u}_w and u_w are the horizontal acceleration and velocity of water, respectively. The positive force direction is the wave propagation direction. The resulting force can be derived by integrating the force over the length of the structure from the seabed to the MSL. In this study, $C_m = 1.0$ and $C_d = 2.0$.

Current loads

The current loads are affected by the angle between the wave and current directions, and the wave and current loads reach the maximum values when the wave and current are in same directions [21]. In this study, the maximum current is considered.

Gravity

The weight of each of nacelle, rotor, and turbines is simplified to a mass point, and the point is located 2.5 m away from the center line of the tower, as shown in Fig. 4. The mass of the tower and foundation is considered to have a gravity acceleration of 9.8 m/s^2 .

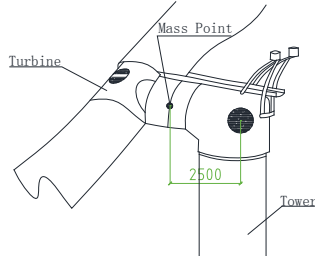


Fig. 4. Schematic diagram of mass point

DETERMINISTIC ANALYSIS AND RESONANCE CHECK

In the phase of preliminary design, the dimensions of the tripod and the tower are determined based on the requirements in codes of practice such as DNV and API and experts' experience. The details of the dimensions are listed in table 1.

Tab. 1. Schematic diagram of mass point

Components	Size (diameter × thickness)	Unit
Pile	ø 2000 × 40	mm
Pile sleeve	ø 2200 × 30	mm
Mud brace	ø 1500 × 30	mm
Top brace	ø 2200 × 40	mm
Central column	ø 4500 × 40	mm
Tower	ø 2860 × 20 to ø 4740 × 50	mm
Nacelle and rotor	163.3	ton

First, to check the occurrence of resonance, a modal analysis is performed to get the natural frequencies of the structure. Fig. 5 shows the three modes shapes for the support structure system. The deformation and natural frequency are computed using ANSYS.

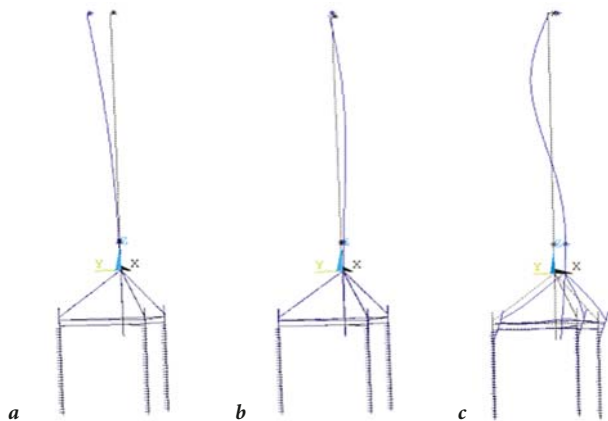


Fig. 5. First three mode shapes of tripod structure (a) 1st frequency=0.342Hz; (b) 2nd frequency=2.065Hz; (c) 3rd frequency=3.891Hz

A constant speed for the turbine is assumed in the analysis. The constant rotational speed is the first excitation frequency, and the second excitation frequency is the blade passing frequency NP , in which N is the number of rotor blades. In this study, a three-blade V90-3 MW (Vestas) wind turbine has an operational interval between 8.6 rpm and 18.4 rpm. The rotor frequency (termed $1P$) lies in the range of 0.143 Hz to 0.306 Hz, and the corresponding $3P$ frequency lies in the range of 0.429 Hz to 0.920 Hz. The DNVGL-ST-0126 code [1] suggests that the first natural frequency should not be within the 10% of the $1P$ range and the 10% of the $3P$ range. It is confirmed from Fig. 5 that the first natural frequency in the designed tripod is not within 10% of $1P$ and $3P$ ranges, and the structure does not resonate. In the support structure, the bending is predominant in vibration.

One of the main aims of the support structure is to transfer all the loads from the wind turbine to the ground bearing allowable deformation to assure a safe operation of turbines. The DNVGL-ST-0126 code [1] specifies a 0.25 degree limit on tilt at the hub level in SLS criteria. Fig. 6 shows the total rotation vector of the support structure. It is seen that the maximum rotation on the hub level is 5.825×10^{-3} rad, that is, the tilt of 0.33 degree, which is greater than the allowable title of 0.25 degree specified in DNV.

In summary, the natural frequency of the support structure preliminary design lies outside of the excitation frequencies, which avoids resonance. However, the deformation at the hub level exceeds the required threshold value. Therefore, it is required to refine the design by increasing the stiffness of the support structure to meet the deformation requirement. It requires the selection of key parameters that mostly affect the performance of the structure. The statistical correlation analysis and the reliability based design procedure introduced in the next sections are necessary for this process.

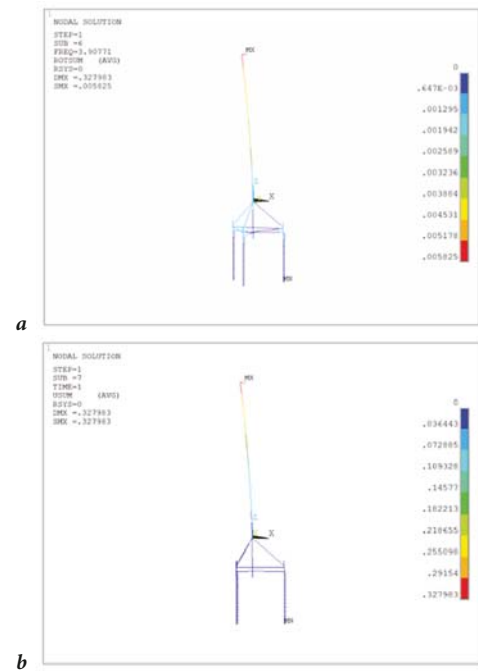


Fig. 6. Deformation of support structure (a: the total rotation vector; b: total displacement vector)

STATISTICAL CORRELATION ANALYSIS FOR KEY DESIGN PARAMETER SELECTION

STATISTICAL PARAMETER SELECTION USING THE CONCEPT OF A CORRELATION COEFFICIENT

This section proposes to use a statistical correlation analysis that helps to identify the statistical relation between the design parameters and the structural performance. In this study, the randomness of the design parameters is considered, and its effect on the structural performance is measured using the statistical correlation coefficient.

The structural response of the target tripod can be expressed as follows:

$$Y = g(x_1, x_2, x_3 \dots x_n) \quad (4)$$

where Y is the structural response such as deformation, stress, and natural frequency; $x_1, x_2, x_3 \dots x_n$ are input variable; and g is the function, which represents the analysis carried out by the finite element model in this study. In this study, the Spearman rank-order correlation coefficient (SROC) is chosen to represent the statistical correlation between the structural response and the design input variables. The SROC is calculated to be

$$SROC = \frac{COV(Y, x_i)}{\sigma_{x_i} \sigma_Y} \quad (5)$$

where $COV(X, x_i)$ is the covariance of Y and x_i , and σ_{x_i} and σ_Y are the standard deviations of x_i and Y , respectively. $SROC$ represents the degree of a linear statistical relationship between two variables. The values of $SROC$ range between -1 and $+1$, and the absolute value of $SROC$ represents the strength of the relationship. As the absolute value of $SROC$ approaches 1, the relation between two variables becomes a linear deterministic relation. As the value of $SROC$ approaches 0, the relation between two variables becomes purely random. The sign of $SROC$ indicates the direction of the linear relationship, and the positive sign indicates that an increase in one variable is associated with an increase in the other variable, while the negative sign indicates that an increase in one variable is associated with a decrease in the other variable.

Among various methods for estimating $SROC$, the Monte Carlo simulation (MCS) is chosen in this study due to its straight-forwardness in implementation and its accuracy upon the convergence of the result. Latin Hypercube Sampling [22] is a representative advanced MCS method to reduce the number of iterations required for the crude MCS.

In this study, applied loads including wind, wave and current are considered for extreme cases. Considering that loads are already based on a conservative assumption, the uncertainties of the resistance of the structure are of interests. In MCS analysis, geometric parameters including the thickness and diameters of structural components and material property parameters are considered as design

variables. These variables are considered as random variables, and their statistical distributions are provided in Table 2 with references. The maximum displacement at the hub level D_{max} and the frequencies are taken as output variables. From a convergence test, the sample size of 5000 was selected in this study.

Tab. 2. Random input variable specifications

Random input variables	Symbol	Mean	C.o.v	Distribution type	Ref.
Elastic modulus (GPa)	TM	210	7.6%	Normal	[23]
Yield strength (MPa)	YS	355	6.8%	Lognormal	
Outer diameter of central column (mm)	D1	5200	10%	Normal	[24] [25]
Thickness of central column (mm)	T1	60	10%	Normal	
Outer diameter of top brace (mm)	D2	2200	10%	Normal	
Thickness of top brace (mm)	T2	40	10%	Normal	
Outer diameter of pile sleeve (mm)	D3	2000	10%	Normal	
Thickness of pile sleeve (mm)	T3	30	10%	Normal	
Outer diameter of mud brace (mm)	D4	1500	10%	Normal	
Thickness of mud brace (mm)	T4	30	10%	Normal	
Outer diameter of anchorage pile (mm)	D5	1800	10%	Normal	
Thickness of anchorage pile (mm)	T5	38	10%	Normal	
Outer diameter of tower bottom (mm)	TD1	4700	10%	Normal	
Thickness of tower segment 1 (mm)	TT1	60	10%	Normal	
Thickness of tower segment 2 (mm)	TT2	38	10%	Normal	
Thickness of tower segment 3 (mm)	TT3	30	10%	Normal	
Thickness of tower segment 4 (mm)	TT4	24	10%	Normal	

ANALYSIS RESULTS AND DISCUSSIONS

The statistical correlation analysis results using $SROC$ are shown in Fig. 7(a), where the $SROC$ between the maximum lateral deflection and the parameters for structural geometry and material property are provided. It is seen that the diameter of the tower bottom (TD1) has the most significant effect to the lateral deflection of the hub showing the $SROC$ of -0.88 . The negative value means that the increase in the diameter of the tower bottom results in the decrease in displacement. The other parameters having a significant effect include the elastic modulus (EM), the diameter of the central column of the tripod (D1), and the thickness of tower segment 2 (TT2). The other parameters such as D2, T1, D5, TT3, T2 and D4 have a little influence to the maximum deflection.

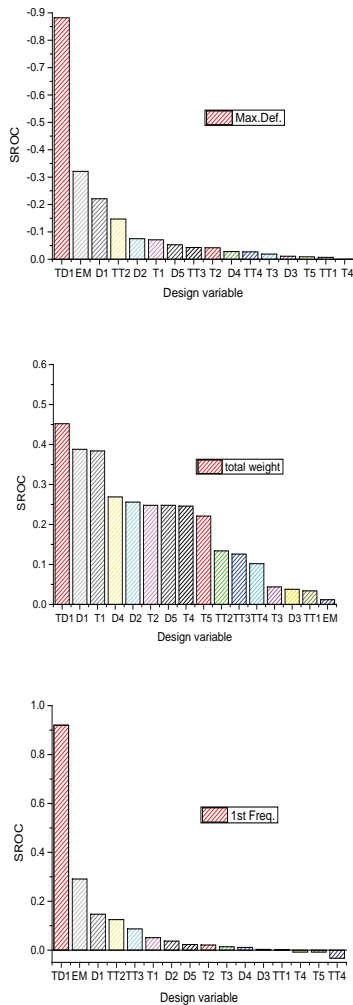


Fig. 7. SROCs of design variables to maximum deflection (a) total weight (b) and the first natural frequency (c)

To consider the effect of each design parameter to the total cost, the SROC between each parameter and the total weight is estimated. The weight is chosen as a cost measure as it is related to the amount, transportation, and installation of construction material. Fig. 7(b) shows the SROC between each of the parameters and the total weight. It shows that the design variable with the greatest effect on the total weight is TD1, and the variable with the second greatest effect is the diameter of the central column of the tripod, D1. Variables TT2, TT3, TT4, T3, D3 and TT1 have a negligible contribution to total weight.

Compared to traditional offshore structures, OWT foundations impose a stricter requirement for the natural frequency to avoid resonance, and therefore, it is important for designers to know the correlation of natural frequency and design parameters. Fig. 7(c) presents the SROC of the first-order natural frequency of the tripod foundation to diameter, thickness and elastic module of the structure. The natural frequency of tripod is highly dependent on the thickness of tower bottom (TD1) and elastic module (EM). In other words, an adjustment of the thickness of the tower bottom is recommended if natural frequency of foundation structure

does not meet the design requirements. On the other hand, TT1, T2, D3, T3, D4, T4, D5 and T5 show no significant effect on the first-order natural frequency, and they do not significantly affect the design.

A statistical correlation analysis helps to identify important parameters, and it is also useful in reducing the size of problems with a large number of random variables because only a few variables generally have a significant effect on the structural response. For instance, there are 17 random variables in the probabilistic structural analysis, and only 8 variables have effects on the deflection (Fig. 7(a)) from which 3 variables (TD1, D1 and D2) whose SROCs are greater than 0.2, other variables have insignificant effects on maximum deflection and they can be neglected in preliminary design.

VALIDATIONS OF STATISTICAL CORRELATION ANALYSIS RESULTS

The results of the statistical correlation analysis are summarized in Table 3 for ranks 1–4 and 13–16. In addition, the variation rates of the maximum deflection, the total weight and the 1st natural frequency are provided according to the 10% increase of TD1, D1, TT1, which show good agreement with the results of SROC. It is seen from Fig. 8 that the maximum deflection, the total weight, and the 1st natural frequency change by 17.5%, 12.1% and 3.0%, respectively, when increasing the 10% of TD1, while they change by 2.9%, 2.6% and 0.2% when increasing the 10% of TT1. It means that, when the deflection or natural frequency does not meet the code requirements, it is effective to modify parameters that are highly dependent on the structural response and to neglect insignificant parameters.

Tab. 3. Ranks of sensitive design parameters

Rank	Maximum deflection	Total weight	1st natural frequency
1	TD1	TD1	TD1
2	EM	D1	EM
3	D1	T1	D1
4	TT2	D4	TT2
13	D3	T3	TT1
14	T5	D3	T4
15	TT1	TT1	T5
16	T4	EM	TT4

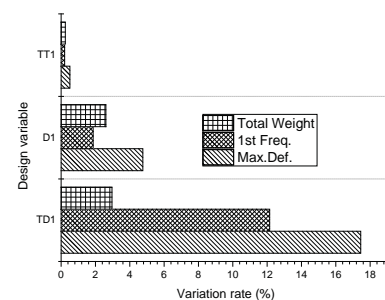


Fig. 8. Variations rate of structural responses due to changing a design variable

RELIABILITY ANALYSIS

RELIABILITY ANALYSIS USING MCS

After identifying significant parameters for the improvement of structural design, it is necessary to perform a reliability analysis and check if the proposed design provides the best cost-safety balance meeting the target reliability level.

In this study, for reliability analysis, the MCS method is used because it does not involve the calculation error due to approximation, and the computational cost of MCS is affordable especially for serviceability reliability analysis as the target reliability level for the serviceability limit state is not too high. The reliability is often represented by the reliability index β that is related to the probability of failure P_f in the following relation:

$$\beta = -\Phi^{-1}(P_f) \quad (6)$$

where $-\Phi^{-1}(\cdot)$ is the inverse standard normal cumulative distribution function [25]. Although P_f can be estimated using either approximations or statistical simulations, approximations such as the first-order reliability method have limitations in handling highly nonlinear limit state functions. According to MCS, the probability of failure is estimated as follows:

$$P_f = \frac{N_f}{N} \quad (7)$$

where N_f is the number of simulations in the failure domain, and N is the total number of random simulations. The accuracy of the simulation depends on convergence that is represented by the coefficient of variation (C.o.v) of the estimated probability of failure as follows [26]:

$$C.o.v_{P_f} = \delta_{P_f} \approx \sqrt{\frac{1-P_f}{NP_f}} \quad (8)$$

In this study, Latin hypercube sampling (LHS) has been used to get improved convergence using a stratified sampling technique [26].

RELIABILITY ANALYSIS FOR THE TARGET STRUCTURE

This study mainly considers a serviceability limit state because it directly affects the operation of OWTs and has more frequency than the ultimate limit state. The serviceability criteria are defined based on the tolerance requirements for the operation of the wind turbine. Typically these tolerances are specified in some codes of practice (e.g. DNV) or a design specification supplied by turbine manufactures. Examples of the specific requirements are as follows: the limiting value for lateral deflections for a cantilever beam is given as $H/100$ in the DNV GL-ST-0126 code [1], which is related to the straight line joining the support. Here, H is the projecting

length. The limiting lateral deflection is also advised to be controlled within $1/200 \sim 1/125$ of tower height H based on their operating experience [27].

In this study, five thresholds values for lateral deflection including $H/200$, $H/175$, $H/150$, $H/125$ and $H/100$ are considered in the reliability analysis to investigate the effect of a range of threshold values, which are determined based on a combination of the provisions of design standard and practical engineering experience. Simultaneously, to investigate the effect of modeling error, parameter ϵ is introduced and multiplied to the variation of Ex to amplify the variation of the overall result. Thereby, the 10% increase in the value of ϵ results in roughly 10% decrease in the variation of the deflection.

Table 4 lists the probability results for the five different threshold values for deflection. The analysis results are computed by the combination of Finite Element Method (FEM) and the LHS method.

Effects of thresholds

From the results provided in table 4, it is apparent that failure probability decreases for greater thresholds. It is also observed that the selection of SLS criteria impacts the foundation design and costs. The threshold value should be carefully chosen considering the balance in the operation cost and safety.

Effects of Ex

To see the effect of additional uncertainties such as the modeling uncertainties, additional variations are put to the important parameter Ex manually. The additional variation has been multiplied to the C.o.v of Ex . From the data in table 4, it is apparent that failure probability increases with increasing the Elastic Module Ex variation. As an example, for the threshold $H/200$, the failure probability changes from 2.0906×10^{-1} to 2.6987×10^{-1} when Ex factor changes from 1 to 1.1.

Tab. 4. Probabilistic results of different thresholds in 5 cases (5,000 MCS)

Case	Factors of $Ex(\epsilon)$	Threshold	Failure probability P_f	Reliability index β
1	1	H/200	2.0906×10^{-1}	0.8097
		H/175	1.1095×10^{-1}	1.2215
		H/150	4.6992×10^{-2}	1.6747
		H/125	1.5439×10^{-2}	2.1586
		H/100	3.9230×10^{-3}	2.6586
2	1.05	H/200	2.5910×10^{-1}	0.6461
		H/175	1.3862×10^{-1}	1.0865
		H/150	5.7291×10^{-2}	1.5779
		H/125	1.8729×10^{-2}	2.0807
		H/100	4.7086×10^{-3}	2.5965
3	1.1	H/200	2.6987×10^{-1}	0.6132
		H/175	1.4112×10^{-1}	1.0753
		H/150	5.8688×10^{-2}	1.5659
		H/125	1.9463×10^{-2}	2.0650
			4.7145×10^{-3}	2.5961

In addition, it is also noted that some of the serviceability criteria do not meet the reliability level specified in current international codes. The target reliability index for the serviceability limit state provided in international codes including EN 1990 [28] and ISO 2394 [29] are 1.5. That corresponds to the failure probability of 6.6807×10^{-2} . For example, for Case 1, the calculated failure probability of H/200 is 2.0906×10^{-1} , which is greater than the target failure probability 6.6807×10^{-2} . However, in the deterministic analysis in section 2.5, it is shown that the maximum lateral deformation of the structure is 327 mm (H/243) in Fig. 6, which satisfies the deflection limit H/100 in DNVGL-ST-0126 [1]. This example shows that the optimal cost-safety balance can be achieved by a careful reliability analysis rather than a simple deterministic check.

PROPOSED RELIABILITY BASED DESIGN FRAMEWORK

This study proposes to use a reliability based framework to design an OWT structure by combining the statistical correlation analysis procedure and the reliability analysis procedure presented in the previous sections. A flowchart for this framework is presented in Fig. 9, which includes the following four stages: structural configuration, deterministic analysis, statistical correlation analysis, and reliability analysis. In the preliminary design of the tripod, first, the structural configuration including tower and foundation geometries is determined based on the estimations of design conditions and the engineers' experience. Generally, the tower height is decided by the wind turbine diameter and the speed at the tower height in the wind farm and the foundation height is related to the water depth. The base layout (the distance of the anchored pile) should consider the structural stability to avoid overturning subject to horizontal loads including wind, wave, and current loads. Since the diameters and thicknesses of the components in a tower and a foundation are massive and are difficult to be determined directly from engineering estimations, they need to be determined through some iteration processes. For their initial approximate values determined based on engineering experience, the structural responses such as stress and deformation need to be estimated using an FE analysis to check SLS stipulated in code and practice. If the results are satisfied, a further step of the reliability analysis needs to be carried out, where the target probability in MCS is taken as criteria for judging the response whether the reliability requirements are met. In the reliability analysis, the uncertainties of geometry and material properties need to be considered. If the results do not meet the reliability requirement, the important design parameters identified from the statistical correlation analysis need to be altered to improve the structural design to meet the design requirement. The iterations updating the tripod model are repeated until the final robust design is obtained.

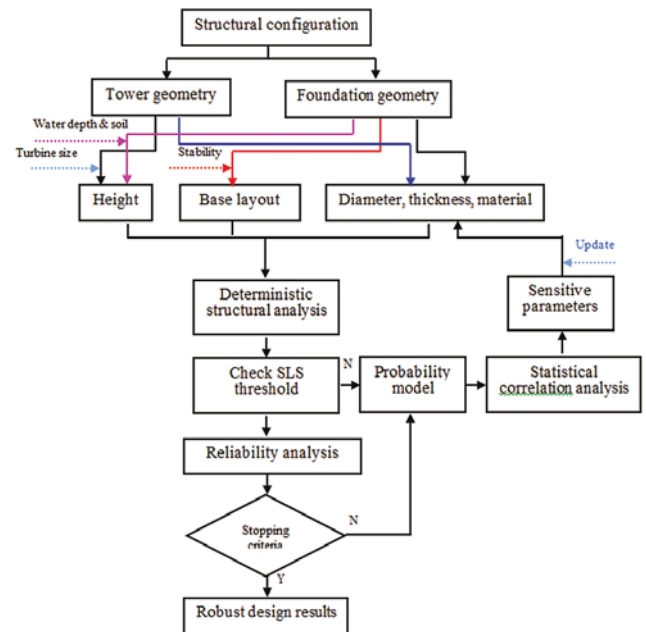


Fig. 9. SA flow chart of reliability based preliminary design of tripod in SLS

Case study

As can be seen from the deterministic analysis results in case 1, the failure probability for threshold H/200 is greater than the target value of 6.6807×10^{-2} , while that for H/100 is smaller than the target value. These two cases indicate that the structure is conservative or unsafe. In either case, to achieve the target probability, the deformation should be controlled by adjusting important parameters identified from the statistical correlation analysis until meeting the target reliability level. It should be also mentioned that the natural frequency and total weight of new design will also change according to the change of design parameters.

To demonstrate the proposed framework, we take threshold H/200 in Case 1, and the failure probability for the current design proposal is 2.0906×10^{-1} . This means that the support structure stiffness is not sufficient, and the design parameters need to be adjusted to increase the stiffness of the structure. According to the steps in the flow chart, to reach target failure probability $P_f = 6.6807 \times 10^{-2}$, the preferred options for adjusting design parameters based on the statistical correlation analysis results in Section 3 are to increase TD1, to increase D1, or to increase TT2. For these three options, the variation rates of total weight and the 1st natural frequency due to updating TD1 are summarized in Table 5.

Table 5 describes the changes of the values of the three parameters TD1, D1 and TT2. In the three options, TD1 has the most significant effect on the deflection of the support structure. To satisfy the deflection criterion in terms of the reliability level, the diameter of TD1 is increased by 10%. It should be noted that to obtain a similar level of reliability, D1 and TT2 need to be increased by 150% and 195%, respectively. The order of the effectiveness of the change of these parameters exactly agrees with the order obtained in the statistical correlation analysis results.

In addition, while making the change in the values of these three parameters, the total weight and natural frequency will change due to the changes in diameter and thickness. Among them, option 1 gives the smallest weight and the natural frequency that is still outside of the 10% of 1P and 3P ranges. Therefore, changing the most significant parameters TD1 is the most effective and economical option for the design of the target structure.

Tab. 5. Variation rate of geometry, total weight and 1st natural frequency to meet probability level

Option	Variation	Total weight	1st natural frequency	Failure probability P_f	Reliability index β
TD1		+2.9 %	0.384	0.0566	1.5840
D1	+150%	+10.4%	0.372	0.0903	1.3389
TT2	+195%	+13.0%	0.362	0.0782	1.4173

CONCLUSIONS

A reliability based structural design framework for a 3 MW OWT tripod foundation was proposed in this study. The proposed framework combined the statistical correlation analysis and the reliability analysis, which were carried out based on a finite element model. First, the statistical correlation analysis was based on the Spearman rank-order correlation analysis to give insight into important design parameters in a preliminary design phase. It was found that the diameter of the tower bottom, the material properties, and the outer diameter of the central column showed a strong effect on the maximum displacement of the tower in the order of significance. These parameters showed a considerable impact on the improvement of structural design compared to the other not-important parameters. Second, in the reliability analysis, the MCS with Latin Hypercube sampling technique was used to consider the uncertainties in structural geometries and modeling errors. The effects of thresholds and uncertainties were discussed through multiple reliability analyses. The reliability analysis results showed that a simple deterministic analysis result does not guarantee the achievement of the required reliability level of the structure, and it is necessary to perform reliability analysis to achieve the best cost-safety balance in a structural design.

ACKNOWLEDGEMENTS

This research was financially supported by the National Natural Science Foundation of China (No. 51409065, 51678322 and 51650110509); Provincial Science Foundation of Heilongjiang (No. E2015051); the Fundamental Research Funds for the Central Universities (No. HEUCFG201817); and Harbin Special Study Fund for Technological Innovation (No. 2014 RFQXJ017 and No. 2015RQXJ014). The authors are grateful for their support.

REFERENCES

1. DNV G. ; *Support structures for wind turbines* DNV GL AS, Høvik, Det Norske Veritas 2016.
2. API RP2A-WSD. *Recommended practice for planning, designing and constructing fixed offshore platforms-working stress design*. American petroleum institute, Washington (DC), American 2014.
3. Knowledge L. *List of offshore wind farms*. Available at: <http://www.lorc.dk/offshore-wind-farms-map/list>.
4. Karimirad M. *Offshore Energy Structures For Wind Power, Wave Energy and Hybrid Marine Platforms*, Springer International Publishing, Cham 2014.
5. Haskell JJM, Cubrinovski M and Bradley BA. *Sensitivity analysis and its role in pseudo-static design of pile foundations*. Soil Dynamics and Earthquake Engineering 2012, 42, pp. 80–94.
6. Lozano-Minguez E, Kolios AJ and Brennan FP, *Multi-criteria assessment of offshore wind turbine support structures*. Renewable Energy 2011, 36, pp. 2831–2837.
7. Lee K, *Effects on the various rubber fenders of a tripod offshore wind turbine substructure collision strength due to boat*. Ocean Engineering 2013,72, pp. 188–194.
8. Yu H, Zeng X and Wang X, *Seismic centrifuge modelling of offshore wind turbine with tripod foundation*, IEEE Energytech, Energytech 2013.
9. Yeter B, Garbatov Y and Guedes Soares C. , *Evaluation of fatigue damage model predictions for fixed offshore wind turbine support structures*. International Journal of Fatigue 2016, 87, pp. 71–80.
10. Cullen AC, Frey HC, and Frey CH, *Probabilistic techniques in exposure assessment: a handbook for dealing with variability and uncertainty in models and inputs*. Springer Science & Business Media 1999.
11. Pająk M, *Fuzzy modeling of cardinal features of a complex technical system in Risk, Reliability and Safety: Innovating Theory and Practice: Proceedings of ESREL 2016 (Glasgow, Scotland, 25–29 September 2016)*. CRC Press, 2016, pp. 2762–2767.
12. Borgonovo E, *A new uncertainty importance measure*. Reliability Engineering & System Safety 2007, 92, pp. 771–784.
13. Pająk, M. *Identification of the operating parameters of a complex technical system important from the operational potential point of view*. Proceedings of the Institution of Mechanical Engineers, Part I: Journal of Systems and Control Engineering, 2018, 232, pp. 62–78.

14. Andersen LV, Vahdatirad MJ, Sichani MT, et al. *Natural frequencies of wind turbines on monopile foundations in clayey soils-A probabilistic approach*. Computers and Geotechnics 2012, 43, pp. 1–11.
15. Nour El-Din M and Kim J. *Sensitivity analysis of pile-founded fixed steel jacket platforms subjected to seismic loads*. Ocean Engineering 2014, 85, pp. 1–11.
16. Lee YS, Choi BL, Lee JH, et al. , *Reliability-based design optimization of monopile transition piece for offshore wind turbine system*. Renewable Energy 2014, 71, pp. 729–741.
17. Yang H, Zhu Y, Lu Q, et al. , *Dynamic reliability based design optimization of the tripod sub-structure of offshore wind turbines*. Renewable Energy 2013, 78, pp. 16–25.
18. Vahdatirad MJ, Bayat M, Andersen LV, et al, *Probabilistic finite element stiffness of a laterally loaded monopile based on an improved asymptotic sampling method*. Journal of Civil Engineering and Management 2015, 21, pp. 503–513.
19. Zhang JH, Xie YQ and Gao DW, *Sensitivity Analysis of Structural Behaviors on Key Design Parameters of Tripod for Offshore Wind Farm*. The Twelfth ISOPE Pacific/Asia Offshore Mechanics Symposium. Australia 2016.
20. Commission IE. *Wind Turbines—Part 3: Design Requirements for Offshore Wind Turbines*. No. IEC61400-3, 2009.
21. Zhang L, Zhao J and Zhang JH, *Analysis of Environmental Loads on Pile Foundation of Offshore Wind Turbines*. International conference on marine science and technology for green shipping 2009, pp. 69–77.
22. Pilger GG, Costa JFC and Koppe JC. *Improving the efficiency of the sequential simulation algorithm using Latin Hypercube Sampling*. Geostatistics Banff 2004. Springer 2005, pp. 989–998.
23. Hess PE, Bruchman D, Assakkaf IA, et al, *Uncertainties in material and geometric strength and load variables*. Naval Engineers Journal 2002, 114, pp. 139–165.
24. ASTM A. A500-93, *Standard Specification for Cold-Formed Welded and Seamless Carbon Steel Structural Tubing in Rounds and Shapes*, ASTM, West Conshohocken, PA 2003.
25. Code JPM, *Joint committee on structural safety*. 2001 URL: www.jcss.ethz.ch.
26. Nowak AS and Collins KR. *Reliability of structures*: CRC Press 2012.
27. Wang F, Chen Q and Yu GC, *Research on large scale wind driven generator group tower rigidity*. New Energy and Technology 2005, 20, pp. 38–39.
28. Gulvanessian H, Calgaro J-A and Holický M. *Designer's guide to EN 1990: eurocode: basis of structural design*: Thomas Telford 2002.
29. ISO I. 2394. *General Principles on Reliability for Structures*. Zurich: ISO 2015.

CONTACT WITH THE AUTHOR

Jianhua Zhang

e-mail: zjh@hrbeu.edu.cn

Harbin Engineering University
No.145 Nantong Str. Nangang Dist.
150001 Harbin

CHINA

Won-Hee Kang

e-mail: w.kang@westernsydney.edu.au

Western Sydney University
56 Second Avenue
2747 Sydney

AUSTRALIA

Chunwei Zhang

e-mail: Chunwei.zhang@westernsydney.edu.au

Qingdao University of Technology
11 Fushun Rd, Si Fang Qu
266033 Qingdao

CHINA

Western Sydney University
56 Second Avenue
2747 Sydney

AUSTRALIA

Ke Sun

e-mail: sunke@hrbeu.edu.cn

Harbin Engineering University
No.145 Nantong Str. Nangang Dist.
150001 Harbin

CHINA

DEGRADATION OF THE CONCRETE RAILWAY TRACK BED LOCATED IN THE VICINITY OF THE LOADING WHARF

Maciej Niedostatkiewicz

Gdańsk University of Technology, Faculty of Civil and Environmental Engineering, Poland

ABSTRACT

The following article describes the damages of the concrete railway track bed at the place of unloading petroleum products located in the immediate vicinity of the cargo berth. The concrete of the track bed has been a subject to degradation as a result of many years of exploitation resulting, inter alia, in its cyclical flooding of petroleum products during the unloading and loading of rail tankers. Repairs carried out in the previous period involving the reprofiling of the top part of the board proved to be ineffective. Methods of repairing existing damages have been proposed. Due to the need to limit the time of excluding the track from operation, the repair works were divided into two stages - ad hoc, intended for urgent implementation, and target, to be carried out as a major overhaul.

Keywords: concrete corrosion, damage to the concrete substructure, concrete repair

INTRODUCTION

Petrochemicals have a negative effect, both on the natural environment resulting in contamination of the area [3], [7]-[19], [21] -[23], as well as a destructive one on concrete structural [1], [4], [20], [24] and finishing elements of building objects. It should be noted that the reasons for the destruction of the concrete structure by petroleum substances are very complex and until now have not been fully understood and explained. In the technical literature four basic mechanisms of concrete destruction are defined: biological (1), chemical (2), physical (3) and physicochemical (4). In most cases, these mechanisms occur simultaneously, however, their quantitative share in the process of concrete destruction is diversified.

The purpose of the article is to describe the influence of oil derivatives known as so-called heavy hydrocarbons, on the properties of concrete and the impact of said changes on the technical condition of the track bed. The article also presents a proposal for repairing existing damages.

GENERAL INFORMATION

The 100 m long reinforced concrete track bed was located in the vicinity of the wharf and used for loading and unloading petroleum materials for rail tankers. The railway track was laid on a reinforced concrete track bed. The plate consists of three elements: the main part of the track bed, the drainage channel and the sewage tray (Fig.1 and Fig.2).

In the past, the reinforced concrete track bed, in the middle part at the length of ~ 40 m has undergone repair works, consisting in reprofiling and securing the top surface of the track bed with PCC mortars.

In addition, a sectional reconstruction of the outflow channel was carried out, replacing damaged concrete channels and damaged steel drains.

PRZEKRÓJ POPRZECZNY UTWARDZENIA
1: 20

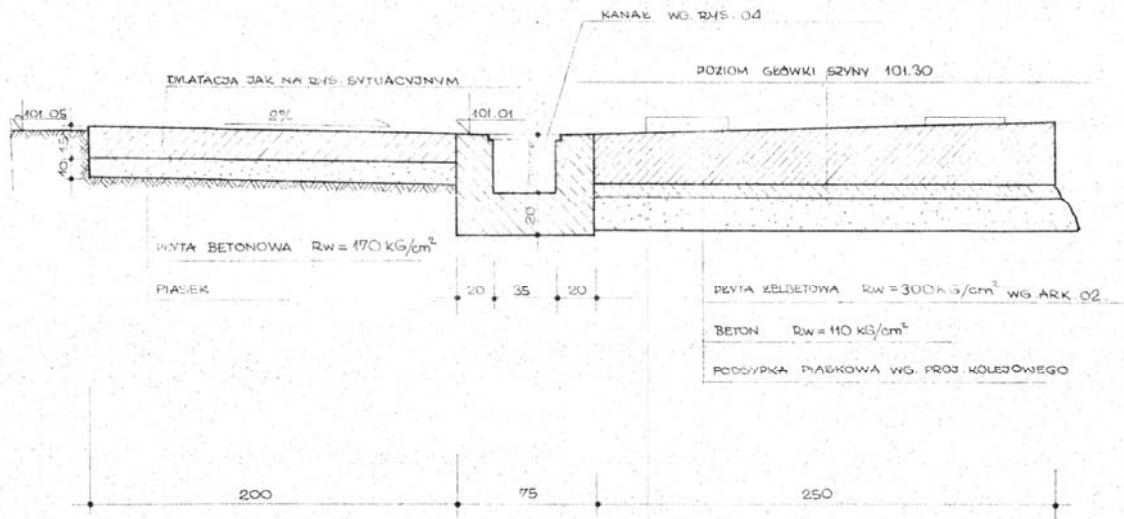


Fig. 1. The design solution of the concrete railway subgrade-cross-section (based on archival project documentation)

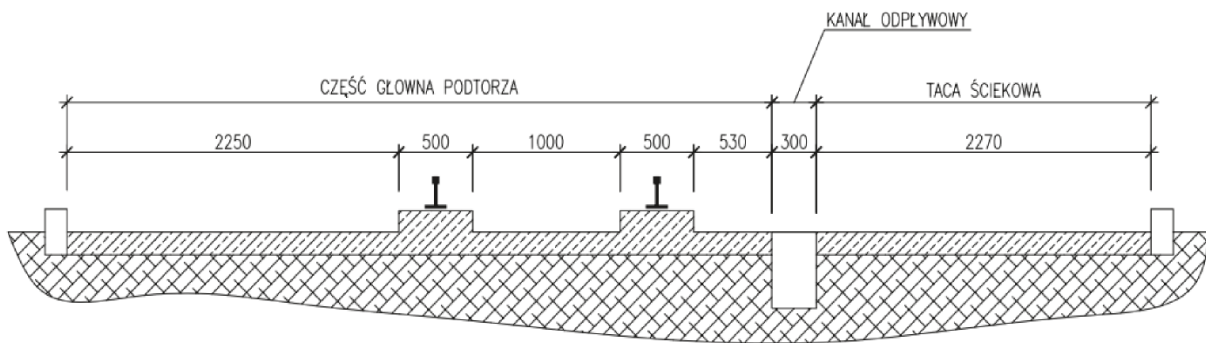


Fig. 2. Diagram of the concrete structure of the railway subgrade-stocktaking

DESCRIPTION OF DAMAGE TO THE CONCRETE RAILWAY TRACK BED

The most intense damage occurred at the length of the middle part of the track bed with a length of about 40 m. In this part the most damaged element was the middle section of the plate located between the rail heads (Fig.3a and Fig.3b). In the main part of the track bed the following damage to the upper surface of the board was found: separation of the PCC layer from the cracking ground, scratches and oil saturation of the concrete slab and PCC. Made in the past (~ 2 years ago), the layer was intensely fractured and carried traces of freezing (frosty scratches). Open pits ascertained that oil-based liquids gathered (by inflowing) from the sub-surface of the subgrade due to unloading of railway tanks (Fig. 3c). The depth of damage to the concrete layer was up to 6 cm, and structural reinforcement bars were visible. The drainage channel located along the road, located between the main part of the track bed and the drainage tray (Fig.2) was

deformed in an intensive manner. The concrete had extensive damage along drainage grates - a sectional drainage channel was replaced ~ 2 years ago as part of the works related to the reprofiling of the substrate. Despite the application of systemic repair solutions (built-in reinforced concrete, prefabricated elements of linear drainage) along the channel, the joints of the channel profiles were found to be broken and the surface layer of the concrete damaged (Fig.3d).

ANALYSIS OF THE TECHNICAL CONDITION OF THE CONCRETE RAILWAY SUBGRADE IN TERMS OF THE EXTENT OF ITS DAMAGE

The approximate mechanism of biological (1) and chemical (2) destruction (corrosion) of concrete lies in the destructive action of acids and bacteria. Often, both mechanisms are described together due to their simultaneous occurrence.



Fig. 3. Track with track bed: a) general view, b) damage to the main part of the track bed, c) open pit in the middle of the track between the rails, d) damage to the drainage channel, e) open pit - control hole, f) the interior of the control hole

In oily concrete, bacteria (aerobic and anaerobic) develop in the presence of water, while organic acids, hydrogen sulphide are produced and the pH of the water decreases. In oiled concrete durability decreases compared to the condition before oil formation - there is the phenomenon called concrete softening, and the long-term impact of organic acids results in a decrease in the mass of concrete, as a result of the dissolution of the cement binder and increase in its porosity. As a result of the dissolution of the binder, the durability of the concrete decreases significantly. The drop in concrete strength depends on the type of oil and the time of exposure of the concrete to oiling [3-4] (Fig.4).

The physical (3) and physicochemical (4) mechanism of destruction (corrosion) of concrete, which took place in the analyzed substructure, is related to the destruction of the concrete structure by the freezing water located in the concrete pores. The change in the pore pressure leads to the formation of micro-scratches in the concrete, which over time lead to the formation of macro-scratches and destruction of the concrete structure.

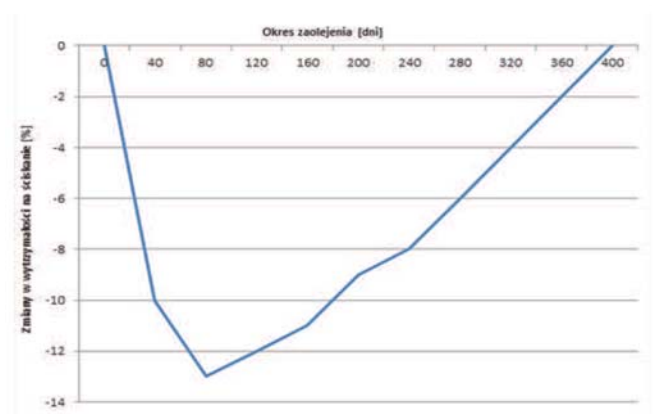


Fig. 4. Change in compressive strength of concrete (vertical axis-%) contaminated with diesel oil versus (horizontal axis-time (days)) (Błaszczczyński 1995)

In order to extend the durability of concrete exposed to petroleum products, it is necessary to apply mineral-structural, surface-as well as structural protection. On the surface of the concrete it is necessary to use a multi-layer external coating, e.g. epoxy, acrylic, alkyl, vinyl, chlorinated

rubber or oil-resin. An important parameter affecting the durability and effectiveness of protection is the thickness of these coatings, which should depend on the expected mechanical factors and it is recommended that it should not be less than 0.15÷0.20 mm for elements with low mechanical load and > 3,0 mm for components loaded with high mechanical load. The effectiveness of surface restorations, eg with PCC mortars, depends to a large extent on the adhesion of the selected repair system (resin) to the substrate (concrete).

In the described case of a concrete railway subgrade, soil saturation with petroleum products was found, based on the conducted ground tests. The soil did not soften despite the contamination. The homogeneity of concrete in the made-out pits was sufficient for surface repairs - the concrete had a compact structure [2], [5]-[6]. Also on the concrete surface, after removing the damaged PCC trip layer, no crayfish or caverns were found (Fig.3e and Fig.3f). The maximum depth of damaged concrete was 6 cm.

The direct cause of damage to the concrete substructure structure, including the PCC repair mortar layer, was the poor quality of the works performed and the use of materials not intended for use in the aggressive operating environment (with agents negatively affecting the concrete). The repair materials used did not provide the designed durability and resistance of the concrete railway sub-floor.

THE PROPOSED METHOD OF REPAIRING THE CONCRETE RAILWAY SUBGRADE

Due to the range of damages, renovation works had to be carried out in the STAGE system.

STAGE 1 (for urgent implementation) included:

I) ad hoc removal of loose fragments of the PCC and concrete,

II) initial geodetic surveying of rectilinearity and inclination of the track rails as well as running control measurements of the subgrade at regular intervals. It was recommended to perform geodetic measurements at intervals of 4 weeks in winter and at intervals of 2 weeks in the spring and summer. During the measurements, particular attention should be paid to the measurement of linearity, verticality and inclination of the heads of the rails with respect to each other,

III) sub-division of the subgrade to working plots and execution of works including:

- a) pressure washing with water and detergents,
- b) priming washed concrete surface: for matt-damp concrete applying a protective layer of epoxy resin for oily floors and sprinkling it with quartz sand (annealed with fire),
- c) making buffer layer of epoxy resin and sprinkling it with quartz sand,
- d) reprofiling the upper surface a mortar based on epoxy resin mixed with quartz aggregate,
- e) applying a support layer of resin resistant to petroleum products.

At the same time, work related to the repair of dilatation had to be carried out in parallel with the work related to the construction of the strain, buffer and putty layers.

STAGE 2 (for the final implementation during the overhaul) included reconstruction of the main part of the track bed and the sewage tray based on systemic prefabricates made of polymer concrete resistant to oil-based liquids - in the newly designed subgrade layer system horizontal damp insulation was to be designed, also fulfilling the role of anti-oil insulation laid on the foundation layer of lean concrete B15 (C12 / 15). As insulation material, it has been recommended to use, for example, oil and bitumen protective foil with a minimum thickness of 2 mm..

CONCLUSIONS

The concrete platform bed exposed to a prolonged exposure of petroleum liquids (diesel oil, gasoline, rapeseed oil, alcohol, fatty acid esters), despite the repairs carried out in the past, was quickly destroyed. The direct cause of the damage occurred was the long-term operation period and the lack of periodic repairs carried out regularly, as well as the lack of major overhaul of the track and track bed. The lack of damp proofing which would fulfill the role of anti-oil insulation under the board resulted in concrete moisture caused by the phenomena of capillary moisture rising from the ground substrate, which contributed to the increase of damage and soil contamination.

BIBLIOGRAPHY

1. Błaszczczyński T. *Destrukcyjna betonu pod wpływem produktów ropopochodnych*. Wydawnictwo Politechniki Poznańskiej, 133, 1995.
2. Bukowski B. *Morfologia rys w konstrukcjach betonowych i żelbetowych*. Archiwum Inżynierii Lądowej, 3, 4, 1957.
3. Cywińska C., Sitkowski J. *Zabezpieczenie gruntu na stacjach paliw i bazach produktów naftowych*. Paliwa płynne, 3, 1994.
4. Detwiler R.J., Mehta P.K. *Chemical and physical effects of silica fume on the mechanical behaviour of concrete*. Journal of ACI Materials, 86, 3, 609-614, 1989.
5. Flaga K. *Naprężenia skurczowe i zbrojenie przypowierzchniowe w konstrukcjach betonowych*. Wydawnictwo Politechniki Krakowskiej, Kraków, 2004.
6. Godycki-Ćwirko T. *Morfologia rys w konstrukcjach z betonu*. Wydawnictwo Politechniki Białostockiej, Białystok, 1992.

7. Izdebska-Mucha D. *Wpływ zanieczyszczeń ropopochodnych na wybrane geologiczno-inżynierskie właściwości gruntów spoistych*. Przegląd Geologiczny, 53, 9, 766-769, 2005.
8. Jaskóła P. *Jak powstaje skażenie gruntu i wód podziemnych produktami naftowymi*. Paliwa płynne, 2, 1994.
9. Kondras M., Czępińska-Kamińska D. *Zanieczyszczenie środowiska glebowego przez oleje mineralne w otoczeniu stacji paliw na terenie aglomeracji warszawskiej*. Ochrona środowiska i zasobów naturalnych, 41, 624-630, 2009.
10. Muszyński A., Karwowska E., Kaliszewski M. *Bioremediacja gleby z produktów ropopochodnych przy zastosowaniu mikroorganizmów immobilizowanych na nośnikach stałych*. Gaz, woda i technika sanitarna, 8, 1996.
11. Nowak J. *Bioremediacja gleb z ropy i jej produktów*. Biotechnologia, 1, 80, 97-108, 2008.
12. Onabolu O.A. *Some properties of crude oil-soaked concrete-II. Exposure at ambient temperature*. Journal of ACI Materials, 86, 3, 205-213, 1989.
13. Pietraszek E., Ślosorz Z., Rakowska J. *Praktyczne aspekty usuwania zanieczyszczeń ropopochodnych z gruntów i powierzchni utwardzonych*. Monografia pt. *Usuwanie substancji ropopochodnych z dróg i gruntów*. Wydawnictwo Centrum Naukowo-Badawczego Ochrony Przeciwpożarowej im. Józefa Tuliszkowskiego-Państwowy Instytut Badawczy, Józefów k/Otwocka, 45-64, 2012.
14. Pużak T. *Beton odporny na oddziaływanie paliw ropopochodnych oraz cieczy lekkich*. Budownictwo, Technologie, Architektura, 3, 39, 60-62, 2007.
15. Radwan K. *Wydawnictwo Centrum Naukowo-Badawczego Ochrony Przeciwpożarowej im. Józefa Tuliszkowskiego-Państwowy Instytut Badawczy, Józefów k/Otwocka, 9-15, 2012*.
16. Radwan K., Ślosorz Z., Rakowska J. *Ocena skuteczności usuwania substancji ropopochodnych z gruntów i powierzchni utwardzonych*. Monografia pt. *Usuwanie substancji ropopochodnych z dróg i gruntów*. Wydawnictwo Centrum Naukowo-Badawczego Ochrony Przeciwpożarowej im. Józefa Tuliszkowskiego-Państwowy Instytut Badawczy, Józefów k/Otwocka, 107-126, 2012.
17. Rakowska J. *Wpływ środowiska na zachowanie się substancji ropopochodnych w gruncie*. Monografia pt. *Usuwanie substancji ropopochodnych z dróg i gruntów*. Wydawnictwo Centrum Naukowo-Badawczego Ochrony Przeciwpożarowej im. Józefa Tuliszkowskiego-Państwowy Instytut Badawczy, Józefów k/Otwocka, 20-22, 2012.
18. Suchorab P. *Wpływ produktów pochodzenia naftowego na cechy fizyczno-mechaniczne betonu*. Monografia pt. *Usuwanie substancji ropopochodnych z dróg i gruntów*. Wydawnictwo Centrum Naukowo-Badawczego Ochrony Przeciwpożarowej im. Józefa Tuliszkowskiego-Państwowy Instytut Badawczy, Józefów k/Otwocka, 37-44, 2012.
19. Surygała J. *Ropa naftowa a środowisko przyrodnicze*. Wydawnictwo Politechniki Warszawskiej, Poznań, 272, 2001.
20. Szydło A., Mackiewicz P. *Nawierzchnie betonowe na drogach gminnych*. Poradnik. Wydawnictwo Polski Cement, Kraków, 2005.
21. Ślosorz Z., Suchorab P., Łudzik M. *Usuwanie zanieczyszczeń ropopochodnych z gruntów i powierzchni utwardzonych*. Monografia pt. *Usuwanie substancji ropopochodnych z dróg i gruntów*. Wydawnictwo Centrum Naukowo-Badawczego Ochrony Przeciwpożarowej im. Józefa Tuliszkowskiego-Państwowy Instytut Badawczy, Józefów k/Otwocka, 86-106, 2012.
22. Włostowska E. *Olej a środowisko*. Paliwa oleje i smary w eksploatacji, 7, 1993.
23. Zieńko J., Karakulski K. *Substancje ropopochodne w środowisku przyrodniczym*. Wydawnictwo Politechniki Szczecińskiej, Szczecin, 181, 1997.
24. Ziółko J. *Ochrona przed skażeniem gruntu w nowoczesnych zbiornikach stalowych na paliwa płynne*. Inżynieria i Budownictwo, 10, 563-567, 1996.

CONTACT WITH THE AUTHOR

Maciej Niedostatkiwicz
e-mail: maciej.niedostatkiwicz@pg.edu.pl

Gdańsk University of Technology
Faculty of Civil and Environmental Engineering
11/12 Narutowicza St.
80 - 233 Gdańsk
POLAND